Electro-Optic Propagation Through Highly Aberrant Media

A Thesis submitted to the University of Adelaide as a requirement for the degree of Doctorate of Philosophy in Mechanical Engineering

by

William Martin Isterling

B.Eng. (Hons) M.Eng. (Electronics)

March 2010

Centre for Energy Technology
School of Mechanical Engineering
Faculty of Engineering, Mathematical and Computer Sciences
The University of Adelaide, Australia

Preface

This document is the culmination of many years of study, and is the thesis submitted for the award of Doctoral of Philosophy. The topic of research is electro-optic propagation through highly aberrant media. The effect of a high temperature, high turbulence gas medium on the propagation of various laser beams is studied. The propagated beams are imaged using focal plane array cameras and the images analysed to determine spatial and temporal degradations. The work importantly supports the laser beam defense of aircraft. A better understanding of laser beam propagation through high temperature and turbulence regimes was needed to provide better assessment of the capability of on-board laser systems (DIRCM) to defend aircraft from infrared seeking missile attack when scenarios dictate that the laser beam must propagate through the jet engine exhaust gases. The work improves the understanding of laser beam propagation in high temperature and turbulence regions, thereby allowing better optimization of the operation and design of life-saving DIRCM systems.

Abstract

Infrared guided, or “heat seeking” missiles, have posed a threat to aircraft ever since their inception. However, the proliferation of man portable shoulder launching infrared guided missiles has increased the threat level against both military and civilian aircraft. Furthermore, advanced variants of the missiles are less susceptible to decoy against traditional countermeasures such as flares. To counter the threat, advances in laser technology have allowed the development of small, robust and powerful infrared lasers that have been developed into laser defence systems that can be fitted to aircraft. These systems, Directed InfraRed CounterMeasures (DIRCM), detect the incoming missile and direct modulated infrared energy, in the form of a laser beam, on to the missile sensor to disrupt the missile’s guidance.

The defence system works well in laboratory settings, and through normal atmosphere, but effects of a highly aberrant propagation path on the laser beam’s temporal and spatial quality need to be considered. In particular, scenarios may arise where the laser beam must pass through the hot, turbulent gases of the engine exhaust, the plume. Some initial system studies highlight the problem but have not reported on the individual effects of the various laser and flow parameters in this high temperature, high turbulence environment. Furthermore, laser beam propagation has traditionally been studied at atmospheric temperatures and often in the visible spectrum to support geodesy.

The thesis incorporates a system level study in collaboration with the Defence Science Technology Organisation, Australia, and the Defence Science and Technology Laboratories, UK. The study showed general properties of the propagation but did not allow detailed analysis of the effect of the various flow and beam parameters on the laser beam propagation.

To further contribute to the knowledge in this field, the thesis took a novel approach to the study of laser beam propagation by using an experimental apparatus to produce high temperature, high turbulent flows in the laboratory for the purpose of studying the laser beam degradation while

controlling flow and beam parameters. This approach allowed the individual effects of flow and beam parameters; such as turbulence intensity, eddy scales, species concentration, wavelength, beam diameter and temperature, to be isolated analysed.

High temperature turbulent flows were generated by combusting a lean mixture of hydrogen and air, while applying perforated plates of various hole diameters and blockage ratios to the jet nozzle to condition the flow. The resulting flow was traversed by 632.8 nm and 4.67 μm wavelength laser beams of varying beam diameter. The resultant laser beam was recorded using visible and infrared detecting focal plane array cameras. The temporal and spatial properties of the propagated beams were analysed and linked to the flow conditions. The flow was characterised in terms of integral length scale and turbulence intensity using Particle Image Velocimetry (PIV) as the diagnostic tool.

The study found temperature, eddy size, beam diameter and wavelength to be parameters that significantly affected the laser beam propagation. For example, the beam displacement, for both wavelengths, was found to increase as the beam diameter was decreased, closely following the inverse third root of the beam diameter. Further, there was a difference in beam displacement related to wavelength. It was found that the 632.8 nm beam would need to be 8/7ths times greater in diameter than the 4.67 μm beam to produce the same beam displacement variance.

The experiment has extended the data range used to develop existing models and has allowed correlations to be observed at the higher temperatures found typically in jet engine plumes. These results show existing models that link beam diameter and wavelength to beam displacement at these higher temperatures are still valid.

The role of path length, although seen to be significant, was not able to be quantified using the experimental set-up, while the presence of carbon dioxide was found through theory and measurement to not be significant at the wavelengths studied.

A significant finding of the work has been the quantifying of the effects of high temperature on laser beam propagation. New data has provided correlations between beam displacement and temperature. The change in the increase in beam displacement variance with high temperature was found to be related to the inverse square of temperature. Beam displacement variance tended towards an asymptote at around 600°C for both wavelengths studied. However it was notable that the beam displacement variance was found to be related to wavelength, with the visible beam exhibiting a notably greater variance than the infrared beam at temperatures above 400°C. The new correlations have shown beam displacement models need to represent the effects of wavelength. This is required for the displacement variance to be correctly modelled as the temperatures increase to levels found in a jet engine plume.

Measurements also showed that as temperature increased, mean and variance of the spot size and the irradiance variance all increased. This data is reported in the thesis and can be used to estimate the energy being directed onto the sensor of an incoming missile under various flow conditions.

The findings and approach presented in this thesis has meant the impact of hot turbulent exhaust flows on the propagation of the DIRCM laser beam can be confidently predicted under a range of conditions. These results provide certainty for those designing DIRCM systems.

Declaration

NAME: William Martin Isterling PROGRAM: PhD

This work contains no material which has been accepted for the award of any other degree or diploma in any university or other tertiary institution and, to the best of my knowledge and belief, contains no material previously published or written by another person, except where due reference has been made in the text.

I give consent to this copy of my thesis, when deposited in the University Library, being available for loan and photocopying, subject to the provisions of the Copyright Act 1968.

I also give permission for the digital version of my thesis to be made available on the web, via the University's digital research repository, the Library catalogue, the Australasian Digital Theses Program (ADTP) and also through web search engines, unless permission has been granted by the University to restrict access for a period of time.

SIGNATURE: DATE:

Acknowledgements

This thesis has been made possible thanks to the support of many people. Primarily I would like to acknowledge my supervisors A/Prof Bassam Dally, Dr Peter Kalt and Dr Zeyad Alwahabi who provided invaluable guidance and teaching throughout the various stages of the thesis. Thank you.

I am also extremely grateful to the optical and turbulence instruction received from Prof David Titterton, Dr Laurence Cox, Dr Miro Dubovinsky and Michael Gillyon.

The friendship and advice of Dr Paul Medwell and Dr Darren Bachmann has helped keep me on track many times. Thanks.

I would like to acknowledge the assistance given by the Department of Defence. The first year of research was funded by the 2005 Secretary of Defence Scholarship. Later years work was supported by the Defence Science and Technology Organisation (DSTO). Thanks to Mark Pitt for supporting this research.

The DSTO experimentation laboratory was kindly provided by Dr Michael Stringer and Dr Lakshmanan Krishnamoorthy, while Ted Keytes, Dion Schutz and other staff at the Science and Engineering Services Division provided manufacturing support.

Daniel Wright provided programming support for the thesis, without your help Daniel the work could not have advanced so quickly. Also thanks to Troy Tobin, who helped in the initial development of the image processing software.

Thank you to the staff at the Mechanical and Electronic Engineering workshops at The University of Adelaide who manufactured the final apparatus and provided sensor calibration support.

Finally, thank you to my family and friends for your interest and support during this work.

Contents

List of Figures

List of Tables

Chapter 1

Introduction

1.1 Importance of Lasers in Missile Defence Systems

Man-portable shoulder launched missiles are a threat to aircraft operated by both the military and civilian authorities. These missiles are guided by sensing the infrared (IR) energy emitted from hotspots, generally engines or engine emissions, belonging to the targeted aircraft. Traditionally, the military counters such missiles using a deployment of flares, in an attempt to present alternative infrared targets and hence disrupt the missile guidance. Flares, as a countermeasure to IR-guided missiles, are limited in their ability to provide protection against newer seekers due to continuously evolving missile counter-countermeasures and advanced imaging and pseudo-imaging seeker technology. These same advances in imaging array technology as well as laser technology over the last decade have offered an alternative, or additional, method for protecting aircraft from IR missile attack. Directed infrared countermeasure systems (DIRCM) have been developed to detect and track a missile and then direct modulated IR energy in the form of a laser beam on to the missile's IR seeker to disrupt the missile's guidance.

One potential deficiency of the DIRCM is the degradation of the laser beam over its propagation path. In particular, little is known about the effect on the laser beam when transmitting through a hot engine exhaust plume. One requirement of self-protection laser systems is to direct and maintain modulated

IR energy on to the detector of a small, fast-moving, incoming IR-guided missile threat. Propagation degradation effects that result in beam spread, beam wander and beam attenuation, all reduce the energy and the exposure time, hence reducing the defence effectiveness. Temporal degradation effects will also corrupt the jamming code and limit the performance. These effects would be most significant during take-off as the DIRCM may be required to operate through a largely plume obscured area if protecting from a rear aspect missile attack. Placing the DIRCM laser turret at the tail may help but does not remove the problem as modern missiles can also detect sufficient IR signature from the front aspect of the aircraft to enable them to engage in the forward hemisphere. Figure 1.1 shows the extent of the exhaust plumes IR signature.

Figure 1.1: A mid-infrared signature showing the extent of the exhaust effect [1].

1.2 The Research Problem

Laser beam propagation in the mid-IR region through hot turbulent gases has not been well studied, probably due to the limited situations where these conditions are encountered. DIRCM systems, however, are becoming more widely used due to their decrease in cost, improvement in laser technology, advancements in missile technology and the proliferation of man portable IR anti-aircraft missiles [2].

Missing from the literature is significant analysis of the propagation of a mid-IR band laser through an environment such as that generated by an engine. Factors such as the effect of temperature, turbulence, and species (exhaust gas constituents) concentrations on the laser beam wander and "dispersion" require further study.

The influence of the shear layer induced by the co-axial coflow, typical of jet engines, on beam propagation is not well understood either.

1.3 Objective

The key objective of the research is to provide new data on laser beam propagation effects at temperatures typical of those found in jet engine exhaust plumes. By collecting data-sets at temperatures above those found in normal atmospheric conditions, this work is extending the range of existing data. Effects on the propagated beam will be correlated with the flow and beam characteristics. These new correlations will be used to verify models, which have been developed using data derived from atmospheric conditions. The research will therefore provide a significant contribution, both to the development of experimental infrastructure and procedure, and the collection of data sets and correlations, for these higher temperatures.

1.4 Specific Aims

An aim of the research is to study the effect on laser beam propagation in a simulated exhaust plume due to factors such as: gas temperature; species concentration; laser radiation wavelength; turbulence and length scales.

Previous work on modelling the refractive index of air has concentrated on wavelengths in the visible region and temperatures near ambient, because the principal need for such models has been in metrology. By extending the region of modelling into the mid-infrared, with far higher concentrations of water vapour and carbon dioxide and to temperatures over 100°C, this thesis makes a significant extension to the scientific knowledge in this field.

1.5 Thesis Layout

New research in the area of IR laser beam propagation through highly aberrant media is reported in this thesis. The research focus is on the propagation of beams through flows, such as those found in jet engine exhausts, where the temperature is far greater than atmospheric temperatures, the turbulent intensity is considered strong and levels of H_2O and CO_2 exceed those found in normal atmospheric conditions.

In Chapter 2 an overview of previous work on laser beam propagation through highly turbulent and hot environments is presented. The chapter begins with an overview of existing work on refractive index modeling that pertains to laser beam propagation. An outline of characteristics of turbulent flow is given along with a description of various flow characterization techniques. Next, research on infrared laser beam propagation is highlighted with emphasis on highly turbulent conditions. Previously documented experiments on laser beam propagation through jet engine exhausts are summarized and related modeling methodologies are reviewed.

A full scale jet engine experiment in which a laser beam is propagated through the engine exhaust of a ground mounted engine is reported in Chapter 3. In the experiment the laser beam is passed at various heights and angles through the exhaust gases for a number of engine thrust conditions. The results are analyzed and presented.

In Chapter 4 a jet parametric study conducted in the laboratory is described. In the experiment, data are obtained on laser beam propagation through a path of known temperature, species concentration, turbulence intensity and length scales. Laser spot instances as the laser pulses pass through the hot, turbulent gases are used to assess the effect of the flow conditions. Beam and flow parameters are varied to determine the effect on the laser beam propagation. The characterization of the experimental set-up is documented in this chapter and the methodology is also outlined. Particle Image Velocimetry (PIV) is used to characterize the flow for various flow conditions encountered by the laser beam in the study.

Chapter 5 reports the results of the jet parametric study described in Chapter 4. The results show the effect of the flow and laser beam parameters on the laser beam quality after propagation through the flow. Image processing techniques are used to assist in measuring the effect of the parameters on the laser beam propagation. The data obtained is compared with existing models to determine validity of the models at higher temperatures.

The parametric effects determined from the simple jet and the full scale jet engine studies are further discussed in Chapter 6. Additional analysis is conducted to better interpret the experimental findings and compare the new data to existing data and models. The findings are discussed with reference to DIRCM performance.

Finally, general conclusions and recommendations are reported in Chapter 7.

Chapter 2

Background Literature

2.1 Introduction

The majority of the work on optical transmission through turbulent flows is related to atmospheric conditions and in particular to astronomical seeing [3-5]. These studies have generated valuable knowledge which is relevant to this research. In this chapter a review of key issues such as: refractive index formulations; turbulence and mixing; flow diagnostic techniques; known effects on a laser beam propagating through turbulence and current modeling approaches used to model laser beam propagation are presented and discussed.

2.2 Refractive Index

2.2.1 Introduction

Refractive index values depend on the wavelength of the light passing through the medium, its temperature and gas composition.

The refractive index, *n*, quantifies the phenomenon which occurs due to variations in the speed of light as it passes from one medium to another. The phenomenon is described as the bending of light as it passes through the interface between two different media, provided the phase front of the light wave enters the media at different times. In a gas mixture, the propagation speed of the laser radiation will change as different temperatures, and concentrations of gases are encountered. A

higher value of refractive index indicates a slowing down of the wave's phase velocity [6]. This is evident in equation (2-1) which defines the relative refractive index between two media;

$$n = \frac{v_1}{v_2} \tag{2-1}$$

where v_1 is the speed of light in media 1 and v_2 is the speed of light in media 2.

Different wavelengths of light may travel at different velocities through a medium. This is due to the electro-magnetic resonance properties of the particles within the medium. The electro-magnetic light wave is delayed by a time that depends on the electro-magnetic properties of the particle it encounters. The particle will absorb the light's energy and then some time later releases this energy. Most energy is not scattered and maintains its original direction but with a resulting phase delay on the electromagnetic light wave. Thus, the phase velocity, that is the velocity of the movement of the crests, is altered. The refractive index phenomenon can be seen as either normal dispersion or anomalous dispersion [6]. These dispersive effects are described in the following sections.

2.2.1.1 Normal Dispersion

In the case of normal dispersion, the refractive index increases as the wavelength decreases. That is, short wavelengths are "bent" more than long wavelengths. The particles, mostly the electrons of the atom, are slow to respond, by oscillating, to a high frequency wave. Normal dispersion, as the name would suggest, is the normal way in which refraction occurs. However, for certain wavelengths of radiation, anomalies appear in the behaviour of the refractive index, with the index increasing as the wavelength increases. The frequencies at which this occurs are said to be resonant [6].

2.2.1.2 Anomalous Dispersion

Anomalous dispersion is present at all resonant frequencies of a molecule. These resonant frequencies are attributes of the individual molecules and can be observed in the absorption spectra

of that molecule. These spectra are produced by changes in the molecule's energy state. It is the absorption of the radiation which causes these anomalies in the refractive index to appear. This is because the radiation does not propagate as expected; the radiation is absorbed, with a molecule gaining the energy of the radiation, and then retransmitted in accordance with the reduction of the energy state of the molecule. The reduction can occur in any number of state transitions and thus the resultant radiation is altered and dispersed [7].

The effect of the anomalous dispersion on the refractive index for various wavelengths of light propagating through air containing a 3% volume of carbon dioxide is shown in the Figure 2.1. The formulation for anomalous dispersion given in equation (2-6) (which will be introduced later) was used in the calculations. Note that the resonant lines for carbon dioxide at 4.2586 µm and 4.27965 µm were used in the calculation.

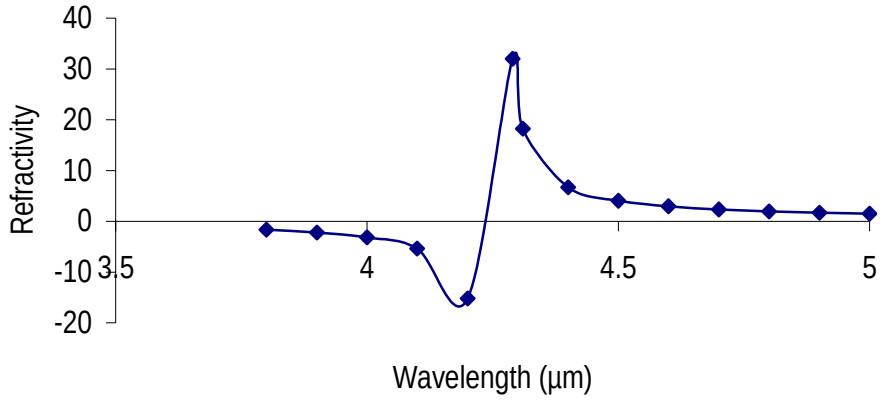

Figure 2.1: Change in calculated refractivity (defined as 10^6 (n-1)) due to the 4.25686 µm and 4.27965 µm CO_2 absorption lines, calculated using 3% CO_2 per volume in air.

It is clear from Figure 2.1 that to the left of the absorption band the refractive index decreases as the wavelength approaches the absorption band, while approaching the right hand side of the absorption band the refractive index increases.

2.2.2 Review of Refractive Index Calculations

Expressions to determine refractive index under a variety of conditions have been evolving through theory and experimentations since the phenomenon was first noted. More specifically, the phenomena of dispersion, that is, refractive index as a function of wavelength, was noted by Cauchy in 1835 [8]. Cauchy was the first to publish a mathematical representation of dispersion. Cauchy's work was based on the assumption that the medium through which the light travelled is discontinuous and consists of molecules with mutual attraction. A disturbed molecule thus transmits the disturbance to its neighbour. Cauchy proposed a formula for the refractive index change with wavelength (see equation (2-2)). The formula represents the visible spectrum well but fails to represent the infrared spectrum and anomalous dispersion [9].

$$n - 1 = A + \frac{B}{\lambda^2} + \frac{C}{\lambda^4} \tag{2-2}$$

where *A*, *B* and *C* are constants and λ is the wavelength in vacuum. The coefficients are usually stated to match a wavelength in units of μm.

Sellmeier in 1871 considered gas molecules to be attached to a surrounding ether. He hypothesised that they were free to vibrate, with limits, and consequently developed mathematical models to describe this concept. The results matched well experimental observations and better explained the phenomenon of anomalous dispersion. A form of Sellemier's equation (equation (2-3)) is as follows [10];

$$n^2(\lambda) = 1 + \sum_i \frac{B_i \lambda^2}{\lambda^2 - C_i} \tag{2-3}$$

where each term of the sum represents an absorption resonance of strength B_i at a wavelength $\sqrt{C_i}$. The wavelength $\sqrt{C_i}$ represents the wavelength of a resonance.

At long wavelengths, far from the absorption peaks, the value of *n* tends to;

$$n \approx \sqrt{1+\sum_i B_i} \approx \sqrt{\varepsilon_r} \tag{2-4}$$

where ε_r *i*s the relative dielectric constant of the medium.

There are many forms of the Sellmeier equation, with modifications made to allow the equation to be valid over a larger range of wavelengths and at different temperatures. One such form of the Sellmeier equation, incorporating only two absorption peaks, is given in equation (2-5).

$$n^2(\lambda) = A + \frac{B_1\lambda^2}{\lambda^2 - C_1} + \frac{B_2\lambda^2}{\lambda^2 - C_2} \tag{2-5}$$

where the coefficient *A* is an approximation of the short-wavelength (e.g. ultraviolet) absorption contributions to the refractive index at longer wavelengths.

The equation does however break down at, and near, the absorption peak and in these wavelength regions another representation is required.

Close to each absorption peak, the equation gives unreal values of $n = \pm\infty$, and in these wavelength regions a more precise model of dispersion must be used.

A widely accepted formulation to represent refractive index changes near absorption peaks is given by Born and Wolf [7] and is shown in equation (2-6);

$$n^2 - 1 = \frac{Ne^2}{\varepsilon_0 m}\sum_s \frac{f_s}{\omega_s^2 - \omega^2} \tag{2-6}$$

where f_s is the resonance strength parameter, ω_s the resonance frequency, ω the frequency of the propagating signal, *N* is the number of oscillators and the other symbols have their usual meanings.

2.2.2.1 Formulations to Determine the Refractive Index at Various Conditions

In 1858 Dale and Gladstone [11] published their findings on the influence of temperature on the refraction of light. Studying various materials and gases they noted a decrease in refractive index as the temperature increased. They also noted that in some gases dispersion decreased while in others it was augmented by the rise in temperature [12]. Since that time, many expressions derived from experiments were published that describe the refractive index under various conditions, such as; wavelength, gas temperature range, gas composition and pressure [13-31]. Table 2.1 lists the various published works and the refractive index expressions they have proposed.

It is clear that as time went by the formulations were refined further and further. Notable, however, that the data used in all these experiments had gas temperatures below 100°C.

As described in Section 1.3, one objective of this work is to investigate the effects of both water vapour and carbon dioxide on laser beam propagation. It is notable that Penndorf [27] showed that the effect of water vapour has a minor influence on the refractive index of air as compared with the effect of temperature. Penndorf considered water vapour corrections were considered not necessary for most applications, unless in the cm-wavelength region of the spectrum. Further, Edlén [32], when working in the visible region, found that the effect of carbon dioxide was notably less than that of water, with the refractive index of carbon dioxide calculated to be an order of magnitude less than water vapour.

The effect of temperature and pressure on the refractive index at optical wavelengths can be estimated using the formulation (see equation (2-7)) given by Ishimaru [33];

$$n_1 = n - 1 = \frac{77.6P}{T} \times 10^{-6} \tag{2-7}$$

where T is the temperature of the air in Kelvin and P the pressure of the air in millibars.

Table 2.1: A sample of refractive index formulations until the early 1970's.

Year	Formulation	Comment	Authors
1918	$(n-1)_0 \times 10^7 = 2875.66 + \frac{13.412}{\lambda^2 \times 10^{-8}} + \frac{0.3777}{\lambda^4 \times 10^{-16}}$ $(n-1)_{15} \times 10^7 = 2726.43 + \frac{12.288}{\lambda^2 \times 10^{-8}} + \frac{0.3555}{\lambda^4 \times 10^{-16}}$ $(n-1)_{30} \times 10^7 = 2589.72 + \frac{12.259}{\lambda^2 \times 10^{-8}} + \frac{0.2576}{\lambda^4 \times 10^{-16}}$	Near-IR to mid-IR spectral region, 2218 to 9000 cm^{-1} 0°C, 15°C and 30°C	Meggers & Peters [25]
1920	$n-1 = \frac{5517160 \times 10^{-8}}{199.5534 \times 10^{-8} \lambda^2} + \frac{48803 \times 10^{-8}}{43.8193 \times 10^{-8} \lambda^2}$	Visible to UV	Traub [31]
1924	$n^2 - 1 = 57642 \times 10^8 + \frac{327.7 \times 10^8}{\lambda^2 - {\lambda_0}^2}$	λ = 0.436 µm to 8.68 µm for air at 0°C	Koch [22, 34-36]
1966	$(n-1)_s \times 10^8 = 8342.14 + \frac{2406030}{130 - \sigma^2} + \frac{15997}{38.9 - \sigma^2}$	Standard air; where σ is the vacuum wavenumber in μm^{-1}	Edlén [32]
1966	$(n-1)_{tp} = (n-1)_s \times \frac{0.00138823\,p}{1 + 0.003671t}$	Accounting for temperature and pressure in laboratory atmospheric conditions	Edlén [32]
1966	$n_{tpf} - n_{tp} = -f\left(5.722 - 0.0457\sigma^2\right) \times 10^{-8}$	Where *f* is the amount of water vapour present in units of torr	Edlén [32]
1966	$(n-1)_x = [1 + 0.540(x - 0.0003)](n-1)_s$	*x* parts by volume carbon dioxide	Edlén [32]
1967	$R_i = \frac{(n_o)_i^{\,2} - 1}{(n_o)_i^{\,2} + 2} \frac{1}{(\rho_o)_i}$	Density dependence and updated Edlén formulations	Owens [37]
1971	$(n-1)10^5 = \frac{0.154489}{0.0584738 - \sigma^2} + \frac{8309.1927}{210.92417 - \sigma^2} + \frac{287.64190}{60.122959 - \sigma^2}$	Refractivity of CO_2; 0.4801260 µm to 1.8172 µm. 1 atm 0°C	Old et al. [38]
1972	$(n-1) \times 10^8 = \frac{5791817}{238.1085 - \sigma^2} + \frac{167909}{57.362 - \sigma^2}$	Replaced Edlén using extra measurements; 0.23 to 1.69 µm	Peck & Reeder [39]

More recent work on the refractive index published by Birch [40] allows the determination of the refractive index based on the gas constituents. Birch documented the development of an experimental apparatus and a technique to measure the refractive index of various gases at different wavelengths, temperatures and pressures. A number of results were tabulated and checked against two forms of the Lorentz-Lorenz [7] equation. The equations were found to be valid for air over the temperature and pressure ranges studied; namely 10 - 30˚C and 20 – 115 kPa. Birch's results showed that adding molar refraction to determine the refractive index of a gas mixture proved reliable. The Lorentz-Lorenz formulation shown in equation (2-8) was used.

$$\frac{n^2-1}{n^2+2}\frac{1}{\rho}=R' \tag{2-8}$$

where n is the refractive index, R' is the specific refraction and the density, ρ, is equal to $pm(ZRT)^{-1}$ where p is the atmospheric pressure, m is the molar mass of the gas, Z is the compressibility factor for the gas, R is the universal gas constant, and T is the absolute temperature.

The molar refraction is;

$$[R] = R'M \tag{2-9}$$

where M is the molecular weight of the constituent atoms or molecules.

Equations (2-8) and (2-9) are rearranged to produce equation (2-10);

$$n=\left(\frac{2A+1}{1-A}\right)^{1/2} \tag{2-10}$$

where $A=[R]\rho/M$.

The refractive index of any gas can therefore be derived from the molar refraction, density and molecular weight of its constituent atoms or molecules. Birch and Downs [41] presented molar refraction of a number of gases, including CO_2 and O_2, measured at a pressure of 101325 Pa and at a temperature of 15˚C. Furthermore, assuming moderate pressures, the refractive index of a mixture can be determined using an additive expression (see equation (2-11)).

$$[R] = \frac{n^2 - 1}{n^2 + 2}\frac{M}{\rho} = \sum_K x_K [R]_K \tag{2-11}$$

where $[R]$ is the molar refraction of the mixture and n, M, and ρ are the refractive index, the molecular weight, and the density of the mixture respectively, while x_K and $[R]_K$ are the molar fraction and the molar refraction of each of the respective components in the mixture.

Born and Wolf [7] showed that the Lorentz-Lorenz equation can be expressed in several ways;

$$\frac{n^2 - 1}{n^2 + 1} = \frac{4\pi}{3} N\alpha = A\frac{N}{N_A} = A\frac{\rho}{M} = \frac{AP}{RT} = K\frac{P}{T} = L \tag{2-12}$$

where α is the average molecular polarizability, A the molar refraction, N the molecular concentration, N_A is Avogadro's number, ρ the density, P the pressure, T the absolute temperature, K a constant and L the specific refraction.

This section has shown that the refractive index formulations have been refined over the years. The formulations include the development of method to calculate the refractive index of any gas composition by knowing the refractive indices of the constituent gases and their concentrations in a flow. This method is used as the basis of the refractive index calculations within the thesis, in conjunction with Ciddor's refractive index formulations presented in the next section.

2.2.2.1.1 Ciddor –Refractive Index Formulation

Ciddor's work provides the most used formulation of the refractive index of air [42]. Ciddor [43] extended the work of Birch and Downs [44] by combining dispersion and density equations and measurements from a number of sources in order to account for a wider range of atmospheric conditions and wavelengths. Ciddor used two approaches.

In one approach Ciddor determines the refractivity of dry air and water vapour at a standard condition then multiplies by the relative density of each to obtain a partial refractivity of each. The effects of each component are combined to determine a net effect. Carbon dioxide is accounted for by assuming each CO_2 molecule replaces an O_2 molecule and has the same molecular refractivity. To determine the refractivity of dry air Ciddor uses the equation from Peck and Reeder [39]; for water vapour an extension of Erickson's equation [16] with a correction to Barrell and Sears's absolute value of the refractivity of pure water vapour [45].

Thus for standard air;

$$10^8\left(n_{as}-1\right)=\frac{k_1}{\left(k_0-\sigma^2\right)}+\frac{k_3}{\left(k_2-\sigma^2\right)} \tag{2-13}$$

where n_{as} refers to the refractivity of standard air at 15˚C, 101,325 Pa and 0% humidity with 450 ppm of CO_2. Here σ is the wavenumber in units of μm^{-1}; k_0 = 238.0185 μm^{-2}; k_1 = 5792105 μm^{-2}; k_2 = 57.362 μm^{-2} and k_3 = 167917 μm^{-2}.

To describe the effect of carbon dioxide on the refractivity;

$$\left(n_{axs}-1\right)=\left(n_{as}-1\right)\left[1+0.534\times10^{-6}\left(x_c-450\right)\right] \tag{2-14}$$

where n_{axs} refers to the refractivity when there is x_c ppm of CO_2.

For water the refractivity n_{ws} is given by;

$$10^8(n_{ws}-1) = cf\left(w_0 + w_1\sigma^2 + w_2\sigma^4 + w_3\sigma^6\right) \tag{2-15}$$

where *cf* (=1.022) is a correction factor that is found when fitting the calculations to the measurements, w_0 = 295.235 μm^2; w_1 = 2.6422 μm^2; w_2 = -0.032380 μm^4; w_3 = 0.004028 μm^6.

Then combining all refractivity effects and correcting for density, one can determine the total refractivity, n_{prop};

$$n_{prop} - 1 = \left(\frac{\rho_a}{\rho_{axs}}\right)(n_{axs} - 1) + \left(\frac{\rho_w}{\rho_{ws}}\right)(n_{ws} - 1) \tag{2-16}$$

where ρ_{axs} is the density of dry air at 15˚C, 101,325 Pa, x_w = 0, and a fractional CO_2 content of x_c, and ρ_{ws} is the density of pure water vapour at 20˚C, 1333 Pa , and x_w = 1. Similarly ρ_a and ρ_w are the densities of the dry air component and water vapour component of moist air for the actual conditions. Ciddor also presents the density calculations required to calculate ρ_a and ρ_w.

In the second approach Ciddor uses the additivity of the Lorentz-Lorenz relation [43];

$$L = \frac{n_i^2 - 1}{n_i^2 + 2} \tag{2-17}$$

where n_i is either the refractive index of air (*a*) or water (*w*). Then,

$$L = \left(\frac{\rho_a}{\rho_{axs}}\right)L_a + \left(\frac{\rho_w}{\rho_{ws}}\right)L_w \tag{2-18}$$

and the combined refractive index is

$$n_{LL} = \left[\frac{(1+2L)}{(1-2L)}\right]^{1/2} \tag{2-19}$$

Both methods are said to agree [43] to within a few times 10^{-10} in the refractive index under ordinary laboratory conditions. Even for H_2O saturated at 60˚C the agreement is stated to be within $2x10^{-9}$.

2.2.2.1.2 Specific Absorption Lines Considerations

Hill, Clifford and Lawrence [46] considered the effect of temperature, pressure and humidity when determining a method for calculating refraction and absorption fluctuations. They considered the refractive index to be the sum of anomalous absorption effects on a continuous refractive index. In their work they calculated the refractive index for air with water as the contributor to the anomalous absorption effects. The nett refractive index is then a summation of the continuous refractive index effect of dry air and the continuous refractive index effect due to water, plus the anomalous absorption effects of water on the refractive index. The continuous refractive index formula they employ is derived from Goody [47] based on Edlén's original dispersion formula. For dry air;

$$N_d = \frac{0.3789P}{T} N_o\left[1 + (5.337 - 0.0157T)\times 10^{-6} P\right] \tag{2-20}$$

where N_d is the continuous refractive index for dry air, N_o is the continuous refractive index for dry air at 15°C and 760 Torr, P is the total atmospheric pressure in Torr and T is the temperature in Kelvin.

N_o, the continuous refractive index for dry air at 15°C and 760 Torr, is given in equation (2-21).

$$N_o = 64.328 + \frac{29498.1}{146 - \lambda^{-2}} + \frac{255.4}{41 - \lambda^{-2}} \tag{2-21}$$

where λ is wavelength in µm.

The continuous water contribution is given by;

$$N_w = -1.765\times10^{-18}\left(1-0.0109\lambda^{-2}\right)Q \tag{2-22}$$

where Q is the concentration of water vapour in molecules/cm^3.

Anomalous dispersion contributions are summed in using;

$$N_{ai} = \frac{S_i Q}{4\pi^2 \nu_i} f \times 10^6 \tag{2-23}$$

where ν_i is the line frequency in cm^{-1}, S_i is the line strength in cm^{-2} per concentration (i.e.: cm^{-2} /(molecules cm^{-3})), and f is the line-shape factor.

For a Lorentzian line shape;

$$f = \frac{\nu_i - \nu}{\left(\nu_i - \nu\right)^2 + \alpha_i{}^2} \tag{2-24}$$

where α_i is the line width in units of cm^{-1}.

N_{ai} is summed over all the spectral lines to obtain the total anomalous contribution.

Temperature affects the line strength value as the line strength has a dependency on temperature arising from the difference of two Boltzmann distributions and the partition function, Q_{PART}. The temperature is related to pressure and concentration via the ideal gas law.

The line strength, S_i, is proportional to;

$$\frac{e^{\left(-E_i^L/CT\right)} - e^{\left(-E_i^U/CT\right)}}{Q_{PART}} \tag{2-25}$$

where E_i^L and E_i^U are the values of lower and upper energy state responsible for the spectral line *i*, *C* is a constant (*C* = K_B/hc; where K_B is the Boltzmann constant, *h* is the Plank constant and *c* the speed of light), *T* is the temperature and Q_{PART} is the partition function.

The line width is also dependent on pressure, concentration and temperature;

$$\alpha_i(P,T,Q) = \alpha_{oi}\frac{P + 4K_B QT}{P_0}(T_0/T)^b \tag{2-26}$$

where *b* = 0.62, α_{0i} is the width of the line *i* at the reference pressure P_0 and temperature T_0, K_B is the Boltzmann constant.

Hill and Lawrence [48] furthered their work by choosing nine wavelengths in the region 7.8 to 19.0 µm that were not affected by nearby IR resonances of water molecules. They then performed a line-by-line summation over all IR water molecule resonances from radio frequencies into the visible. The refractive index was then calculated at 10˚C temperature steps from -40˚C to +40˚C using the full temperature dependence of the line strength. The following equation was then found by fitment to the calculated summation;

$$\left[n_{(\lambda)} - 1\right]\times 10^6 = Q\frac{1 - 0.97\theta^{0.4}(x-1)}{1.03\theta^{0.17} - 19.8x^2 + 8.2x^4 - 1.7x^8} \tag{2-27}$$

where $\theta = \frac{T}{273.16}$, $x = \nu/1000$ cm^{-1} = 10 µm/λ, *Q* is the water-vapour density in g m^{-3}, *T* is the absolute temperature, λ is the wavelength and ν is the frequency.

Hill and Lawrence [48] suggested that the use of equation (2-27) be supplemented by the addition of any significant resonant refractivity, due to absorption lines, around the wavelength of interest.

2.2.2.1.3 HITRAN: Absorption Lines and Temperature

HITRAN (a high-resolution transmission molecular database) may be used to quantify the anomalous absorption effects. To account for absorption effects, Šimečková et al. [49] presented expressions for line intensity defined for either a unit pressure (P in atm), unit volumetric density (ρ in g cm^{-3}) or for one molecule per unit volume (N in molecule cm^{-3}). The relationship between each was presented so that the HITRAN database, which presents line intensity as one molecule per unit volume, can be used to derive the other line intensity relationships. Line intensity is expressed as follows;

$$S_v^N(T) = \frac{P}{N} S_v^P(T) \tag{2-28}$$

where S is the line intensity, v is the wave number in units of cm^{-1}, P is pressure in atm, N is molecules per unit volume in molecule cm^{-3} and T is temperature in Kelvin.

Šimečková et al. then applied the ideal gas law and the Loschmidt number to derive the following conversion formula;

$$S_v^N(T) = \frac{P_0}{L(T_S)} \frac{T}{T_S} S_v^P(T) \tag{2-29}$$

where T_S is the standard temperatures (T_S = 273.15K), $L(T_S)$ is the Loschmidt number ($L(T_S)$ = 2.68676x10^{19} molecule cm^{-3}) and P_0 the pressure unit (equal to 1 atm).

Šimečková et al. [49] also presented, by derivation, an expression for the line intensity by considering the molecule distribution between two energy levels, E_2 and E_1, such that;

$$S_v^N(T) = \frac{g_2}{Q_{tot}(T)} \frac{A_{21}}{8\pi c v_o^2} e^{-c_2 E_1/T} \left(1 - e^{-c^2 v_o/T}\right) \tag{2-30}$$

where g_2, or degeneracy factor, is the statistical weight of molecules in energy level 2 (the upper level); Q_{tot} is the total internal partition sum; A_{21} is the Einstein A-coefficient, a first-order decay constant, for spontaneous emission (units s^{-1}) from energy level 2 to 1; E_1 and E_2 is the energy at level 1 and 2 respectively; $v_0 = E_2 - E_1$ is the wave number (units of cm^{-1}) of the resulting emission line; c is the speed of light; c_2 is the second radiation constant ($c_2 = hc/k_B$ where h is the Planck constant, c is the speed of light and k_B is the Boltzmann constant); T is the temperature in Kelvin.

The total internal partition sum at temperature, T, is given by [50];

$$Q_{tot}(T) = \sum_{\eta} g_{\eta} e^{-c_2 E_{\eta}/T} \tag{2-31}$$

where η is the number of energy states, g is the statistical weight of molecules in an energy state, E is the energy state and T is the temperature in units of Kelvin.

The equation gives the line intensity for a pure gas, whereas in HITRAN, the line intensity is defined at a reference temperature T_0 = 296 K for an isotropic abundance, I_a. The HITRAN line intensity is called S_{HIT}. The conversion to the Einstein coefficients from S_{HIT} is given by;

$$A_{21} = \frac{8\pi c \upsilon_0^2 Q_{tot}(T_0) S_{HIT}}{e^{-c_2 E_1/T_0}(1 - e^{-c_2 v_0/T_0}) I_a g_2} \tag{2-32}$$

S_v^N can now be calculated using quantities found within the HITRAN or HITEMP (a database of high temperature spectroscopic absorption parameters) database. To obtain a temperature conversion of the line intensity a ratio of the S_v^N expression at different temperatures gives;

$$S_v^N(T) = S_v^N(T') \frac{Qtot(T')}{Qtot(T)} e^{-c_2 E_1((1/T)-(1/T'))} \left[\frac{1 - e^{-c_2 v/T}}{1 - e^{-c_2 v/T'}} \right] \tag{2-33}$$

The dimensionless oscillator strength, or f-value, can be obtained using the following relationship between oscillator strength and the Einstein A-coefficient;

$$f_{12} = \frac{g_2}{g_1} \frac{\varepsilon_0 mc}{2\pi e^2 \nu_0^{\ 2}} A_{21} \tag{2-34}$$

where *e* and m are the charge and the mass of the electron respectively.

Note that $g_1 f_{12}$ is the weighted oscillator strength.

2.2.3 Refractive Index of Exhaust Gases

The refractive index of the efflux forming the jet plume and the entrained air surrounding it depends on two factors. The first is the gas temperature and the second is the species concentrations. The effect of pressure on refractive index can be ignored for sub-sonic jets because the plume is fully expanded, so their pressure is the same as local atmospheric pressure and the variation of this with time does not affect a propagating laser beam [51].

Previous studies of air refractive index by Edlen [32], Ciddor [43] and Barrel and Sears [45] have concentrated on the visible and very near infrared regions (≤1700 nm). At longer infrared wavelengths, the absorption bands of water vapour and carbon dioxide modify the refractive index of air. For normal atmospheres, the concentrations of water vapour and carbon dioxide are small, so this modification is usually ignored. However, in an engine exhaust the concentrations are significant (3% by volume at the core of the plume for both CO_2 and H_2O [52]). This is about one hundred times higher than in the normal atmosphere [53].

Measurements of refractive index in the 3-5 μm band will be affected primarily by the water absorption bands at 2.6 μm and 6.0 – 7.0 μm and by the carbon dioxide absorption band at 4.2 μm; these are not only the nearest absorption bands but also very strong bands [54]. The CO_2 band at 15 μm and the H_2O bands at 1.4 μm and 1.9 μm will have some effect but these are both weaker and further away from the wavelengths (3-5 μm) of interest.

One report [46] did compute the refractive index of air for propagating wavelengths from radio waves to 5 µm. However, the results shown were for 23°C and only the contribution of H_2O to the anomalous absorption was calculated. In the jet engine the core temperature will be much higher (> 500°C) with the presence of other species (e.g. CO_2, CO). The strength of an absorption band is proportional to the number of electrons in the lower state of the transition (since these are the only ones that can absorb photons) and the temperature will affect the energy state of the electrons [7]. The equations developed show that temperature and species concentrations will affect the refractive index of the medium. The methodology presented by Hill et al. [19, 46] and Šimečková et al. [49] can be applied, using HITEMP to provide data on energy levels, to calculate the line strengths based on electron distributions due to temperature effects.

Ignoring the effects of anomalous absorption, refractive index equations for dry air or moist air exist in the literature, but appear to only to have been developed for lower temperatures (< 100°C) [32, 43, 55]. There appears to be a gap in the literature of validated equations of refractive index at higher temperatures and high concentration of added species.

2.2.4 Summary

The refractive index calculations have been refined over the last century to enable very precise calculations of the refractive index under certain conditions. However the conditions tested, and hence represented by the equations, are for ordinary atmospheric temperatures as they have generally been developed for geodesy applications. These equations have not been tested for temperatures >100°C found in the jet engine exhaust and their accuracy in this range is not known. The equations developed by Ciddor [47, 56-58] are presently the most accurate and applicable for determining the refractive index encountered by a laser beam passing through the hot exhaust plume. The dominant absorption features (closest to 632.8 nm, 2.0 µm, 4.0 µm and 4.67 µm laser lines) found in the jet engine exhaust are the combustion by-products water and carbon dioxide. The equations presented by Ciddor cover these wavelength ranges, with the dominant 4.3 µm carbon dioxide absorption line [56] being accounted for in the refractive index equation, originally presented by Old et al. [38].

The increased temperature will affect the refractive index, not only as the molecular spacing increases, but as the electron distribution in the energy states within the molecules change.

Hill et al. [57] outline a procedure for calculating the effect of temperature on the anomalous component of the refractive index. The theoretically derived equations presented by Šimečková et al. [49] demonstrate how the effect of temperature on the anomalous dispersion line can be evaluated using parameters contained within the HITRAN and HITEMP databases.

2.3 Fluid Mechanics Overview

2.3.1 Introduction to Turbulence

A turbulent flow is one which is characteristically unsteady, irregular and seemingly chaotic. The time and space variation of the velocity field within the turbulent flow is significant and is irregular. Common everyday examples of turbulence may include fast running water in a river, smoke from a chimney or simply wind [58].

The turbulence is a result of instabilities in a flow due to the fluid's viscosity not having a sufficient damping effect [59]. To cause turbulence to occur in the first place there must be a perturbation that would cause a flow to respond. Failure of the flow to suppress an initial fluctuation may result in random velocity fluctuations, or turbulence. Low velocity flows may be able to damp out a perturbation. However, at high velocity the system may not respond in time and perturbations may become manifest on the entire flow causing the flow to become turbulent in its response [60].

Turbulence can be thought of as consisting of eddies of different sizes. Turbulent mixing of gases of different temperature will lead to randomly distributed pockets of air, each having a characteristic temperature. Since the refractive index is a function of temperature, this gives rise to seemingly "randomly" (there is some spatial and temporal correlation) distributed pockets of varying refractive index [61].

A flow may be predicted to be turbulent based on the flow's Reynolds number, *Re*. The Reynolds number relates the viscous and inertial forces, and is defined as;

$$\mathrm{Re} = \frac{Ulp}{\mu} = \frac{Ul}{\nu} \tag{2-35}$$

where *U* is the velocity, *l* is the characteristic length, *p* is the fluid density, μ is the dynamic viscosity and *v* is kinematic viscosity. For a pipe flow *l* is taken as the diameter.

Generally, a pipe flow is considered laminar when Re_D < 2300, turbulent for Re_D > 4000 and transitional for values in-between [58]. A flow may also be characterized by measuring the variation in velocity at a point within the flow. For a turbulent flow the velocity at a point within the flow will be variable. The degree of variation of a point from the mean velocity at the point is a measure of the turbulence intensity. Turbulence intensity is given by;

$$I = \sigma u / U = u' / U \tag{2-36}$$

where σ is the standard deviation, *u* is the instantaneous velocity, *u'* is the root-mean-square of the turbulent velocity fluctuations and *U* is the mean velocity.

2.3.1.1 Kolmogorov's Turbulence Theory

Kolmogorov's turbulence theory assumes that energy is fed to the system at a rate ε per unit mass and generates large eddies (characteristic length L_O, velocity V_O) called the outer scale. The energy is then fed into progressively smaller eddies (length *l*, velocity *v*) until at the inner scale (length l_o, velocity v_o) energy is dissipated by viscous friction. The region $l_o < l < L_O$ is called the inertial range, and it is within this range that Kolmogorov's theory is applicable. A feature of turbulence is that it looks the same regardless of the scale, providing it is in the inertial range. In this way it has fractal characteristics [62].

Kolmogorov predicts the distribution of eddy currents with a spatial power spectral density (PSD) of $n_1(\vec{\kappa})$, denoted $\Phi_n^K(\vec{\kappa})$. For a three dimensional flow the PSD is given in equation (2-37) as;

$$\Phi_n^K(\vec{\kappa}) = 0.033 C_n{}^2 \kappa^{-11/3} \tag{2-37}$$

where $\vec{\kappa}$ is the spatial wave number vector with orthogonal components (κ_x, κ_y, κ_z), *K* superscript indicates a Kolmogorov spectrum, C_n^2 is the structure constant of the refractive index (units $m^{-2/3}$) and characterises the strength of the fluctuations.

The structure constant of the refractive index, C_n^2, is often used as a measure of turbulence strength. The refractive index structure constant, for locally homogeneous and isotropic temperature fluctuations, may be calculated using the temperature and pressure difference between two points, separated by a distance, *r*, within the flow [3, 63] as shown in equation (2-38).

$$C_n{}^2 = C_T{}^2 \left(\frac{7.9x10^{-5} p}{T^2} \right)^2 \tag{2-38}$$

where *p* is the pressure in mbars, *T* is the absolute temperature and C_T^2 is the temperature structure parameter, shown in (2-39).

$$C_T{}^2 = \left(\frac{\langle T(x) - T(x+r) \rangle^2}{r^{2/3}} \right) \tag{2-39}$$

where *r* is the separation vector.

Kolmogorov's theory assumes that the medium is incompressible and that turbulence is homogeneous and isotropic. These assumptions are not rigorously satisfied in the real world, but Kolmogorov's model, with some adjustments, seems to work well in practice [64]. The adjustments needed are outside the region of l_0 and L_0 where Kolmogorov's theory no longer holds. It can be seen

how Kolmogorov's law breaks down around the inner and outer scales as shown in Figure 2.2. Kolmogorov's law is valid when $2\pi/L_O < k < 2\pi/l_O$ [65].

NOTE:
This figure is included on page 28 of the print copy of the thesis held in the University of Adelaide Library.

Figure 2.2: Kolmogorov's -5/3 power law, relating power to spatial frequency (Reproduced from Turbulence & Symmetry, Berkeley University [65]).

The problem with the Kolmogorov spectrum is that it is not applicable outside the inertial range and also has a non-integrable pole at $k = 0$. The von Karman spectrum, given by equation (2-40), attempts to remedy this;

$$\Phi_n^V(k) = \frac{0.033.C_n^2}{(k^2 + k_0^2)^{11/6}} \exp(-\frac{k^2}{k_m^2}) \qquad (2\text{-}40)$$

where $k_0 = 2\pi/L_0$, $k_m = 5.92/l_0$ and the superscript V indicates the von Karman spectrum.

The parameters k_0 and k_m allow for deviation from the Kolmogorov spectrum at the inner and outer scales. The exponential term reduces the spectrum near the inner scale, and the $(k^2 + k_0^2)$ term at the outer scale, while retaining the Kolmogorov spectrum in the inertial scale (Figure 2.3). The degree and location of the reduction can be selected by adjusting the values of k_0 and k_m. Various other modifications can be made to the von Karman spectrum to fit experimental results and allow for in-

homogeneities [66]. If the turbulence strength varies as a function of distance then we can substitute $C_n^2(z)$, $\Phi_n^K(k,z)$ and $\Phi_n^V(k,z)$ for C_n^2, $\Phi_n^K(k)$ and $\Phi_n^V(k)$ respectively.

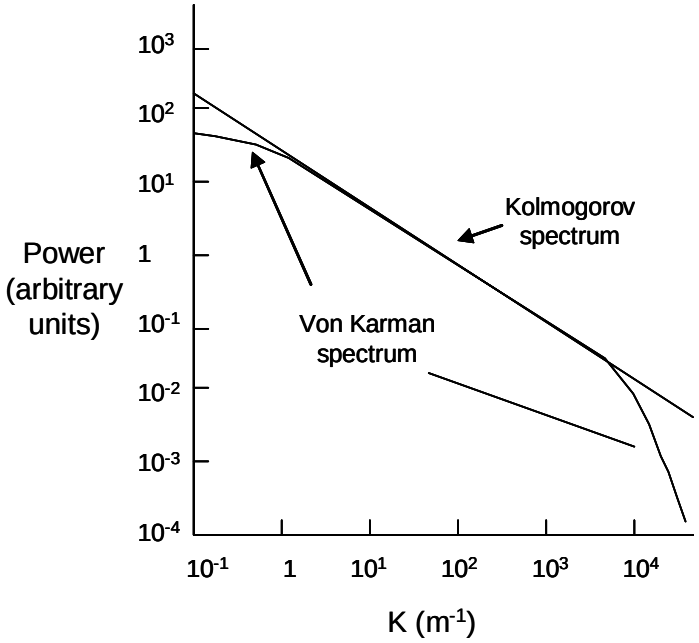

Figure 2.3: Schematic of Kolmogorov and von Karman power spectral densities.

Atmospheric studies of turbulence data have shown a peculiar 'bump' in the spectrum at high wave numbers, near $1/l_o$, though it appears not to be understood. However, Hill [67] developed second-order differential expressions to model this phenomena and Andrews [68] converted the numerically solvable equations of Hill into an analytical expression given in equation (2-41);

$$\Phi_n(\kappa) = 0.033 C_n^2 \left[1 + 1.802(\kappa/\kappa_l) - 0.254(\kappa/\kappa_l)^{7/6}\right] \frac{\exp(-\kappa^2/\kappa_l^2)}{(\kappa^2 + \kappa_0^2)^{11/6}} \tag{2-41}$$

where $\kappa_l = 3.3/l_0$, $\kappa_0 = 1/L_0$ and C_n^2 is the refractive index constant.

It is unknown whether the same spectrum exists for jet engine turbulence.

2.3.2 Turbulence Length Scales

Turbulence is often described in terms of the distribution and range of eddy sizes in the flow. For example, Kolmogorov's equation (see (2-37)) holds for a range of eddy currents (l_o *to* L_o) where L_o is the outer scale and l_o the inner scale. Overall the flow can be considered to consist of a series of eddies of different size, structure and orientation [61]. The eddy current size can be characterised by a length scale. The turbulence length scales measure the eddy scale sizes in the turbulent flow. There are a number of categories of length scale.

The largest scales represent the upper bound of the eddy size within the turbulent flow. Often the physical dimensions of the system, rather than the properties of the flow, dictate this dimension. The largest scales are referred to as the "energy-containing" range as they contain the most kinetic energy [60].

The intermediate scales are known as the inertial sub-range scales. These scales lie between outer an inner scales, the L_o and l_o respectively, referred to when discussing Figure 2.2. It is in the inertial sub-range that turbulence kinetic energy is conserved as it is transferred from larger to smaller scales. The mechanism for the transfer is known as vortex stretching and the rate at which the energy is passed to a smaller eddy is generally in the order of the turnover time of the larger eddy [69].

The energy containing eddies, existing in the intermediate and largest scales, may be defined as integral length scales. These scales measure the largest separation distance over which components of the eddy velocities at two distinct points are correlated. Integral length scales characterise the energy containing range of eddy length scales [70].

At the smaller scales, where viscous dissipation begins to affect the eddies, the scales are referred to as the Taylor micro scale, l_λ .This scale is related to the mean rate of strain and marks the transition from the inertial sub-range to the dissipation range [71].

The smallest scales are referred to as being at the Kolmogorov micro scale. At these scales the eddy sizes are in the dissipation region where the rate of energy being supplied equals the rate at which it is dissipated by viscosity. The length scale is related to the ratio of the viscosity to the rate of dissipation [72], see (2-42).

$$\eta = \left(\frac{\nu^3}{\varepsilon} \right)^{0.25} \tag{2-42}$$

where η is the Kolmogorov length scale, ε is the dissipation rate and v is the kinematic viscosity.

Note that there may be several orders of magnitude difference between the mixing scales of a turbulent flow and the dissipation scales. Consider that the diffusion scale for air at standard conditions is 6×10^{-8} m as measured by the mean free path with 10^{-10} s mean time between successive collisions, while in most flows the smallest length scale is 10^{-4} m, with a time scale of 10^{-6} s [58].

2.3.3 Grid or Perforated Plate Generated Turbulence

Turbulence can be affected by placing a grid or perforated plate into the flow. The grid, like a perforated plate, obstructs the flow with only the holes to allow the transmission of the gas. The gas flow is broken-up by the turbulence generator to produce a series of small jets and wakes which interact with each other. At a certain distance down-stream the turbulence may be considered homogeneous and approximately isotropic [73].

Application of the grid or perforated plate acts as a turbulence generator, enabling the turbulence to be increased without increasing the net flow rate. The level of turbulence generated, the energy to drive it arises from the pressure drop through the grid [74], depends on the solidity ratio (area fraction of the solid portion) of the turbulence generator. Controlling the solidity ratio and hole-sizes has been seen to affect both the turbulence intensity and the eddy scales with the turbulence [73, 75, 76].

The change of the turbulence intensity as a function of distance down-stream and hole-dimension has been discussed by many authors [76-78]. For grid turbulence the general expression that describes the power law decay of turbulence intensity with distance down-stream is;

$$\frac{\overline{u}^2}{U^2} = A\left(\frac{x}{M}\right)^{-n} \tag{2-43}$$

where $\overline{u}^2$ is the mean square fluctuating stream-wise velocity, U^2 is the square of the mean stream-wise velocity, M is the hole size, x is the distance down-stream and A and n are constants. The turbulence intensity down-stream and its rate of decay are set by experimentally determined coefficients, A and n.

The expression, equation (2-43), is only valid for a region down-stream from the turbulence generator known as the power-law region. The power-law region is the region where the resulting small jets and wakes from the turbulence generator have merged to become nearly homogenous. In the initial distance down-stream the flow is still considered developing, while past the power-law region the turbulence finally decays as the viscous effects dissipate the energy.

Mohamed and LaRue [76] studied the turbulence intensity profiles of the flow after passing through various grids. The decay exponent, n, was found to be equal to 1.3. They cite reported n values ranging from 1 to 1.3. Mohamed and LaRue found the decay exponent had *no* dependence on solidity, mesh size and Reynolds number over the range of Reynolds numbers (6000 to 68000), grid sizes (2.54 cm and 5.08 cm) and solidities (0.34 and 0.44) tested. In contrast the decay coefficient, A, was found to be a function of these initial conditions, though no quantitative trend was given. Further, the distance downstream that the power-law region commenced, and the spatial extent of the power law region, was found to be related to the Reynolds number and the turbulence generator hole-size, though no quantitative reporting could be found.

Liu et al. [73, 75] reported on the turbulence intensity produced by the insertion of perforated plates into the flow, in what appears to be a wind tunnel, of various blockage ratios and hole sizes. They observed that by holding the down-stream distance and plate solidity constant, the normalised

turbulence intensities remained nearly unchanged for various Reynolds numbers. They reported that the turbulence intensity increased with increasing plate solidity.

Length scales within the turbulent flow were also seen [73, 75] to be affected by the hole size of the turbulence generator. The length scale, *L*, increased as the hole size, *D*, increased and also *L/D* increased with plate solidity for a fixed hole diameter, and with distance down-stream; a result also reported by Checkel [79].

After reviewing work by others [77, 79, 80, 82, 83], it is concluded that changing the solidity of the turbulence generator, while fixing the hole-size, primarily affects the turbulence intensity at a given point down-stream, though does have some effect on the length scale. Similarly, changing the hole-size, while fixing the solidity, also has an effect on both the length scale and turbulence intensity at a given point downstream. The conclusion is that length scale at a point down-stream is a function of solidity and hole-size, as too is turbulence intensity a function of solidity and hole-size. However, the relationships between the parameters hole diameter, solidity, distance down-stream, turbulence intensity and length scale have not been found to be represented in a mathematical function.

2.4 Flow Measurement Techniques

To determine the characteristics of the flow, such as turbulence intensity and length scale, a number of techniques are available. The flow characterisation techniques may be separated into those techniques that use a laser to interrogate the flow and those that do not.

Most non-laser based techniques involve the introduction of a sensor into the flow, which disturbs the flow. For example a pitot-static tube may be used to measure pressure, and hence velocity fluctuations, but has in the past been not suitable for highly turbulent flows due to the long response time. However, miniaturised multi-hole pressure probes are now available with response time less than one millisecond, making this technique a viable option for measuring the turbulence intensity and length scales within a turbulent flow. Hot Wire Anemometry (HWA) has traditionally been better suited to turbulent flows due to its ability to measure velocities well above the speed of sound, but HWA is not a good option for high temperature flows as calibration is problematic. HWA requires the

measurement of the heat transfer between the sensing element, usually a heated piece of wire, and the surrounding medium, the flow being measured.

Laser based flow diagnostic techniques such as Laser Doppler Anemometry (LDA) and Particle Image Velocimetry (PIV) are frequently used to measure fluid flow velocities. Both LDA and PIV make use of the electromagnetic scattering properties of particles. It is the scattering properties of particles that form the basis of the most elementary laser diagnostic techniques. The scattering of the laser light from particles in the flow can be characterised as either: Mie, Rayleigh or Raman scattering.

2.4.1 Mie Scattering

Mie scattering occurs when light is reflected from particles in the flow. The scattering process occurs when the particles are of sizes larger than the wavelength of the incident light. Beyond this criterion, Mie scattering is not strongly wavelength dependent, as seen in Equation (2-44) [80].

$$\sigma_{Mie} = \left(\frac{2\pi}{k^2{}_{med}} \right) \sum_{n=1}^{\infty} (2n+1) \left(|a_n|^2 + |b_n|^2 \right) \tag{2-44}$$

where $k_{med} = 2\pi n_{med}/\lambda_0$ and the coefficients a_n and b_n are described by Bessel and Hankel functions and the magnetic permeability of the sphere and the surrounding medium.

In Mie scattering the scattered light remains at the same frequency of the incident light. The intensity of received scattered light, for example captured on an imaging camera, is directly proportional to the concentration of the scattering particles. The scattering is predominately scattered forward. Mie scattering can be used to image flows by introducing, or seeding, particles into the flow if there are not sufficient naturally occurring scatters already in the flow. The results of the imaging can be used to infer particle number density and can be used in Particle Image Velocimetery (PIV) (which is discussed later in Section 2.4.5).

2.4.2 Rayleigh Scattering

Rayleigh scattering, like Mie scattering is elastic, but unlike Mie scattering, occurs when light is scattered from objects smaller than the wavelength of the light. Rayleigh scattering is often used to describe light scattering from molecules but also describes particle scatter [81]. Each molecular species, or particle size, will scatter the light to varying degrees. The amount of scattering can be related to the Rayleigh cross-section of the particle or molecule. The Rayleigh cross-section is essentially a measure of the amount of light a particular object will scatter. An analytic function to determine the Rayleigh cross-section of a particle is [80];

$$\sigma_{ray} = \frac{8\pi}{3}\left(\frac{2\pi n_{med}}{\lambda_0}\right)^4 a^6 \left(\frac{m^2-1}{m^2+2}\right)^2 \tag{2-45}$$

where λ_0 is the vacuum wavelength, a is the particle radius and $m = n_{sph}/n_{med}$ is the ratio of the refractive index of the particle to that of the surrounding medium.

It is apparent that the Rayleigh cross-section is proportional to $(\lambda_0)^{-4}$ and for molecular Rayleigh scattering the wavelength relationship is the same. The Rayleigh cross-section of a species i for detection at 90° to the incident light, assuming no de-polarisation, is given by [82];

$$\sigma_i = \frac{4\pi^2(\eta_i - 1)^2}{\lambda^4 N_0{}^2} \tag{2-46}$$

where σ_i is the Rayleigh cross-section of species i (cm^2/sr), η_i is the refractive index of species i, λ is the laser wavelength (cm) and N_0 is the Loschmidt number (2.687×10^{19} cm^{-3}).

The received signal is related to the density of the various scattering species present in the flow. Using Rayleigh scattering, it is possible therefore to determine the density or temperature in the flow by illuminating a flow with laser light and recording images of the scattered light [83].

2.4.3 Raman Scattering

Raman is similar to Rayleigh scattering but the scattering is in-elastic. In Rayleigh scattering the electrons in the atoms, molecules or small particles radiate like dipole antennas when they are forced to oscillate by an applied electromagnetic field [81]. In Raman scattering the same process occurs but in this case the incident photons interact in such a way that energy is either lost or gained resulting in the scattered photons being shifted in frequency. The incident photons can cause a polarisable molecule to be excited into a vibrational mode resulting in scattered photons whose energy is diminished by the vibrational transition energy. The scattered energy resulting from this process is considerably weaker than the elastically scattered energy and can be hard to detect experimentally. Raman scattering is primarily used to measure species within the flow.

2.4.4 Laser Doppler Anemometry

Laser Doppler Anemometry (LDA) measures particle velocities by utilising the Doppler Effect that occurs when laser light is scattered from the particles. To characterise a flow using LDA will therefore usually require the particles to be introduced, or 'seeded', into the flow. The Doppler Effect occurs when there is a small shift in frequency of the scattered beam, with respect to the incident beam, that is linearly proportional to the particle velocity. The velocity can be determined by splitting the laser beam and analysing the beat frequency which results from superimposing the two resulting wave-trains; one with the particle shifted frequency and one without. Best results are obtained by intersecting the beams at a point at the beams waists providing two planar wavefronts that interfere to produce interference fringes, Figure 2.4.

Figure 2.4: Fringes at the point of intersection of two coherent beams [84].

The spacing distance of the fringes is related to the laser wavelength and the intersection angle, while the intensity of the light reflected from a particle moving through the measuring volume varies with a frequency proportional to the x-velocity component, u_x, of the particle;

$$f_D = \frac{u_x}{\delta_f} = \frac{2\sin(\theta/2)}{\lambda} u_x \tag{2-47}$$

where f_D is the Doppler frequency, u_x is the x-velocity component of the particle, δ_f is the distance between the fringes, θ is the angle between the incoming lasers and λ is the laser wavelength.

LDA is susceptible to errors when the laser beams do not intersect at the beam waists, resulting in curved wavefronts and non-constant fringe spacing. The Doppler frequency is then no-longer only directly proportional to the particle velocity, depending also on the particle position. Another limitation of LDA is that it can only be used to measure the velocity in the flow at one point, resulting in limited spatial resolution, typically 100 µm x 1 mm [84].

2.4.5 Particle Image Velocimetry

Particle Image Velocimetry (PIV) is a flow diagnostic technique that, like LDA, usually requires the flow to be seeded as the technique relies on laser light scattered from particles to measure the flow characteristics. However, unlike LDA, PIV can be used to determine the velocity of multiple points in the flow at the same time. To achieve this larger spatial resolution the laser beam illuminating the flow is conditioned by optics to produce a thin sheet of laser light. The light is scattered by the particles it encounters in the flow. The light scattered from each particle can be recorded using a photon counting camera, such as an intensified Charge Coupled Device (CDD) multi-pixel array. In order to see one instance of the flow, the capture time of the camera is reduced so that the recording time is such that the particles have not moved more than a pixel on the camera array during image capture. To determine the velocity of the particles, two images or instances of the particles are needed. This is achieved by successive imaging of the scattered light, allowing time for the particles to be displaced by the flow before the second image is captured. Often two co-linear pulsed laser

beams are used to illuminate the flow. One laser provides illumination for the first image and the second laser the second image. This is necessary to achieve the high luminance necessary for image capture, as pulse energy from one laser is not usually sufficient if its second discharge must occur too soon after the first discharge.

To achieve accurate measurements of the instantaneous flow velocity, the time between the exposures should be small compared to the time scales in the flow, and the spatial resolution of the imaging camera should be small compared to the length scales in the flow [84].

A camera imaging the flow can either be set to capture both illuminations on the same image or on separate images. The particle movement is tracked using correlation algorithms. An auto-correlation algorithm is used when the scattered light for both instances of illumination is recorded on one image. A cross-correlation algorithm is used when comparing the particle movement using two recorded images. Figure 2.5 shows the PIV layout with the cross-correlation processing.

Figure 2.5: Layout of a PIV System [84].

The cross-correlation method is preferred as it removes any direction ambiguity which can arise with both exposures captured on the one image.

Other considerations involve the choice of particles and the method of seeding. The particles chosen for seeding the flow will need to be large enough to produce enough scattered light, but small enough to follow, and not alter, the movement of the flow. Ideally the particles should be neutrally buoyant. Furthermore, if the flow is heated or combusting, the particles must have sufficient thermal resistance so that they do not 'burn-up' in the flow. Typical particles when using PIV to characterise high temperature flows are Aluminium Oxide, Al_2O_3 and Titanium Oxide, TiO_2 [85].

There are many types of seeding configuration. Melling [86] details a number of seeders. To seed into a gas flow, generating particles from powders, a seeder design incorporating either fluidized beds and/or cyclonic action is recommended. A fluidized bed describes a configuration where the powder rests on a porous plate that allows air to pass up through the plate to disperse the particles from the powder. A cyclonic aerosol generator essentially is a container holding the powder with an inlet port and outlet port. Design features can be added to improve the cyclonic action of the air. The action of the unit is to aggregate the powder and disperse particles into the flow. A combination of both designs may produce more even particle distribution in the flow. Melling also cites that the addition of small beads into the powder bed has also been reported to assist in the breakdown of powder coagulation.

2.5 Electro-Optical Propagation

The propagation of the electro-magnetic wave, in the visible and infrared spectrums, has been of interest in atmospheric physics and communications. Many publications report on the effect of the atmosphere on a propagating wave, which were determined both mathematically and experimentally [87-95]. However, the complex nature of the changing atmosphere means that statistical representations of these effects are required when considering propagation in real-world applications. Models have been presented to represent these effects under a variety of conditions [62, 63, 87, 96-104]. The models have been refined by considering the measured data from the many atmospheric laser beam propagation studies. In the case of a laser beam propagating through strong turbulence

at high temperatures, such as in a jet engine exhaust, there are fewer studies available [102, 105-112]. The studies that are available have been system levels studies that have not aimed to isolate and quantify the effect of individual parameters, such as temperature, on the propagating beam through the highly turbulent and hot region. Section 2.5 therefore reviews some relevant studies of electro-optical propagation through various media and the equations developed to represent the effects on the propagating wave. The work recently undertaken on laser beam propagation through jet engine exhausts is presented in Section 2.6.2.

2.5.1 The Propagating Wave

Laser beams are generally Gaussian beam waves (disregarding unstable resonator systems) and are often approximated as spherical waves. At the beam waist, or if the beam is considered 'perfectly' collimated, they may also be modelled as planar waves [5]. The coherent laser beam, in the atmosphere or through a jet engine exhaust, must propagate through random inhomogenieties which result in random fluctuations in the refractive index. The light is then distorted, bent and modulated, with an eventual loss of coherence across the wavefront. The result is a time and spatial variation in the energy of the laser at the receiver, some distance from the source. The time and spatial variation of the laser beam can be measured as scintillation, beam wander or beam spread. Scintillation describes the temporal variation in energy at a point receiver. Beam wander describes the angular movement of the centroid of the beam energy and beam spread describes the spatial distribution of the beam energy [113].

The entire propagation path, including the laser beam, can be modelled. The electro-magnetic wave can be represented mathematically, including diffraction effects. The medium can be characterised in terms of the size distribution of the turbulent pockets of gas (using length scales), and the refractive index variations (using the refractive index structure parameter). The medium may also be represented by statistics to model the random events. The accuracy of the modelling is validated, or verified, by comparison with measurable effects such as scintillation and beam wander and spread.

2.5.2 Scintillation

Scintillation refers to the intensity fluctuations experienced by the propagating electro-magnetic wave [64]. The cause of scintillation is primarily the refractive index changes in the transmission path brought about by variations in temperature along the path, and across the beam front of the propagating wave. The wave encounters the refractive index changes in the form of eddy current cells, or pockets of air with varying temperature and size. The largest cells act as lenses to either focus or defocus the beam. The smallest cells can act to scatter the wave through the process of diffraction. Generally cells smaller than the first Fresnel zone, $\sqrt{L/k}$ (where *L* is the path length and *k* is the wavenumber), or smaller than the coherence radius, *ρ*, whichever is smallest, contribute to small scale fluctuations of the beam amplitude. The larger turbulent cells contribute to the large scale fluctuations. Large cells are generally considered to be those greater than either the Fresnel zone or the "scattering disk", $L/k\rho_0$, whichever is largest. Andrews et al. [5] state that the scattering disk, $L/k\rho_0$, is defined by the refractive cell size l at which the focusing angle $\theta_F \sim 2l/L$ is equal to the average diffractive angle $\theta_D \sim \lambda/\rho_0 \sim 1/k\rho_0$. Figure 2.6 illustrates the definition of the scattering disk.

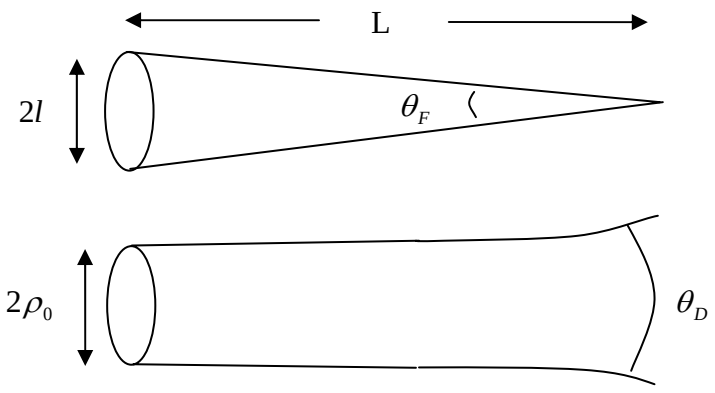

Figure 2.6: Schematic to illustrate the focusing angle and the diffraction angle. The scattering disk is the scale size l at which these angles are equal.

The scintillation can therefore be viewed as a contribution of both diffractive scattering, caused by small turbulence cells, and refraction, caused by large turbulence cells.

One way the measured fluctuation at a receiver can be modelled is by choosing a mathematical expression to represent the propagating wave and applying statistical distributions to represent the fluctuations caused by the path. Early published literature by Tatarski [95] evaluated the variance of the log-amplitude fluctuations of a spherical wave propagating horizontally over a path assuming uniform statistics of turbulence. Fried [114] also derived the log-amplitude covariance, variance and phase structure function for a propagation path over which the statistics of turbulence are constant. Fried took Schmeltzer's [115] results and reduced the beam size to an infinitely small diameter, to represent a point source, and hence a propagating spherical wave. Schmeltzer had published the formulations that described the statistical behaviour (phase and log-amplitude fluctuations) of an initially coherent beam of focused light (focused in the measurement plane) propagating in a medium which, while isotropic, was characterised by a random point function representing the refractive index. The derivations considered the refractive index function to be a function of position in space, and thus the statistics of turbulence were non-uniform. The equations were complex and not readily useable. Together with Seidman, Fried [89] determined workable equations for log-amplitude variance for a propagating beam that is focused on a measurement plane and for a beam that is collimated. The derivations were in good agreement with Tartaski's results [95] for a spherical wave. Equation (2-48) shows the log-amplitude variance for a spherical wave propagating through a fluctuating medium;

$$C_l(0) = 0.124 k^{7/6} z^{11/6} C_n^{\ 2} \tag{2-48}$$

where k is the wavenumber ($k=2\pi/\lambda$), z is the propagation distance and C_n^2 is the refractive index structure constant.

Note that an expression for the log-amplitude variance of a spherical wave travelling through the atmosphere that considers variation in the C_n^2 values through-out the path length has been presented by Beland [4];

$$\sigma_{\chi}^{2}(L) = 0.56k^{\frac{7}{6}}\int_{0}^{L} C_{n}^{2}(\eta)\left(\frac{\eta}{L}\right)^{\frac{5}{6}}(L-\eta)^{\frac{5}{6}}d\eta \tag{2-49}$$

where *k* is the optical wavenumber given by $k = \frac{2\pi}{\lambda}$ and *L* is the path length.

Variations in intensity appear to follow a log-normal distribution. As a result it can be shown [4] that the normalised intensity variance $\sigma_I^{\,2}$ is defined by and satisfies;

$$\sigma_I^2 = \exp\left(4\sigma_{\chi}^2\right) - 1 \tag{2-50}$$

Schmeltzer's results [115] represented the propagation of a laser-like beam, as well as the fluctuating medium. Gebhardt and Collins [99] used Schmeltzer's results, but to derive an expression for the log-amplitude mean value, $\langle l \rangle$, of a Gaussian beam propagating along a horizontal path in a turbulent atmosphere. In both the collimated beam and focused beam cases considered, the log-amplitude mean value was expressed as;

$$\langle l \rangle = Y\left(8.16/8\pi\right)k^{7/6}z^{11/6}C_n^{\,2} \tag{2-51}$$

where: *Y* is a complex expression that changes between the collimated and focussed beam cases and the value of *Y* depends on the beam diameter, wavelength and propagation distance; *k, z* and C_n^2 are the wavenumber, the propagation distance and the refractive index structure constant respectively.

Gebhardt and Collins also combined Schmeltzer's and Fried's results to calculate the mean on-axis irradiance;

$$\langle I \rangle = I_0 \exp\left\{2\left[\langle l \rangle + C_l(0)\right]\right\} \tag{2-52}$$

where *l* is the random log-amplitude ratio that is normally distributed with mean $\langle l \rangle$ and variance $C_l(0)$ and I_0 is the irradiance observed in the absence of turbulence effects.

The mean on-axis irradiance determined by Gebhardt and Collins was then used to calculate the mean spot size resulting from the beam transmission through the turbulence (further discussed in Section 2.5.3). Kolmogorov's (1942) power spectrum for the refractive index fluctuations was used to represent the turbulence. The equations derived are valid but under limited conditions; that is, for ranges, *z*, less than the Rayleigh range of the source or for values of Ω, the normalised beam size, greater than one. For example, in the case of a collimated beam the mean-value results were most accurate in the near field.

2.5.3 Spot Size

The resulting spot size of a transmitted laser beam is dependent on the medium through which the light travels and is related to the wavelength of the light. Banish et al. [116] state that contributions to the blurring of the optical image may be due to; large scale turbulence, jitter of the optical platform or turbulence field (as in the case of a jet engine plume) and gross image steering at refractive index boundaries where the refractive index pocket is greater in dimension than the optical beam front. In general, turbulent cell sizes greater than the wavelength and less than the beam diameter have the greatest influence on the resulting spot size.

Gebhardt and Collins [99] calculated the mean spot size resulting from the beam transmission through the turbulence. For a collimated beam, the average beam size in the measurement, α_t, divided by the source beam size, α_0, is given by;

$$\alpha_t / \alpha_0 = \frac{\left(1+\Omega^2\right)^{0.5}}{\Omega} \exp\left(-\left[\langle l \rangle + C_l(0)\right]\right) \tag{2-53}$$

where Ω is the normalised beam size, $\Omega = k\alpha_0^{\,2}/z$, k is the wavenumber, z is the propagation distance, $\langle l \rangle$ is the mean of the random-log amplitude ratio and $C_l(0)$ is the variance.

While for a focused beam, the average beam size in the measurement divided by the source beam size is given by;

$$\alpha_t / \alpha_0 = \left(\frac{1}{\Omega}\right)\exp\left(-\left[\langle l \rangle + C_l(0)\right]\right) \tag{2-54}$$

Equations (2-53) and (2-54) show the effect of wavelength, source-beam size and range on the resulting spot size. Further, they show that for a focused beam, a smaller average spot size can be obtained, within diffraction theory limits, by using a larger aperture, or shorter range, regardless of the strength of the turbulence induced scintillation (measured as $C_l(0)$).

2.5.4 Aperture Averaging

At this point it is worth noting the effect that the aperture size of the collecting area has on the determination of the scintillation and spot size. The previous discussion indicated that using a larger collecting aperture decreases the scintillation for both collimated and focused beams. Andrews et al. [5] state that the decrease in scintillation with increasing telescope collecting area, known as aperture averaging had been noted in astronomical measurements in the 1950's. There is a shift to lower frequencies of fluctuation because as the aperture size increased fast fluctuations are reduced. A measure of the aperture averaging is given by Andrews [117] who describes the aperture averaging factor, *A*, as being the ratio of the irradiance flux variance obtained by a finite-size receiver lens to that obtained by a point detector. For a spherical wave and a circular aperture the aperture averaging factor, *A*, is;

$$A = \frac{\sigma_I^2(D)}{\sigma_I^2(0)} = \frac{16}{\pi}\int_0^1 b_I(Dx)\left(\cos^{-1}x - x\sqrt{1-x^2}\right)x\,dx \tag{2-55}$$

where $\sigma_I{}^2(D)$ is the irradiance flux variance over the circular aperture with diameter *D*, $\sigma_I{}^2(0) = B_I(0)$ is the scintillation index for a point aperture (*D* = 0) and $b_I(\rho) = B_I(\rho)/B_I(0)$ is the normalised covariance function of irradiance fluctuations for a spherical wave. For a spherical wave, under very general irradiance fluctuations, the irradiance flux variance can be approximated by;

$$\sigma_I^2(D) = \exp\left[\frac{0.49\sigma_I^2}{\left(1+0.18d^2+0.56\sigma_I^{12/5}\right)^{7/6}} + \frac{0.51\sigma_I^2\left(1+0.69\sigma_I^{12/5}\right)^{-5/6}}{1+0.90d^2+0.62d^2\sigma_I^{12/5}}\right] - 1 \tag{2-56}$$

where

$$d = \sqrt{\left(\frac{kD^2}{4L}\right)} \tag{2-57}$$

Note that the aperture averaging effect is still seen if the entire image is captured on a CCD array. Perlot and Fritzsche [118] show the effect of aperture averaging by changing the array size of data used when processing an image captured using a CCD camera.

2.5.5 Beam Wander

The transmission of the laser beam through a medium of varying pockets of refractive index can result in beam wander. Andreev and Gel'fer [119] characterised these fluctuations in the propagation of a light beam through a turbulent media by considering the position of the "centre of gravity" of the beam intensity. It was shown that the mean square of the angular displacement of the light centre of gravity can be expressed as a single formula irrespective of whether the beam is collimated, focused

or diverging; provided $\rho_e / f << 1$ where ρ_e is the effective beam width and f is the radius of curvature of the wavefront. The formula is given in equation (2-58).

$$\left\langle \beta^2 \right\rangle = 0.48\alpha C_n^2 L\left(2\rho_\rho\right)^{-1/3} \tag{2-58}$$

where: β is the angular displacement; α, a coefficient, equals 1 for $\lambda L/\pi\rho_e^2 >> 1$ and equals 2 for $\lambda L/\pi\rho_e^2 << 1$; C_n^2 is the structure constant; L is the path traversed by the wave in the turbulent atmosphere and ρ_e is the effective beam width.

Equation (2-58) gave results for C_n^2 to within 10% of values obtained by experiments with a 532 nm laser beam through 1.5 kilometres of turbulent atmosphere.

Chiba [87] also analysed the angular variation of a propagating beam through the atmosphere and derived the degree of spot dancing using the ray equation (see (2-59)).

$$\left[d\left(ns\right)/dl\right] - \nabla n = 0 \tag{2-59}$$

where s is the unit vector tangent to the ray, dl is the differential length along the path, and n is the refractive index.

Chiba used a correlation function based on the Kolmogorov spectrum to represent the refractive index variations between points in space, constrained between the inner and outer turbulence scales. Mean square deviation was determined theoretically to be;

$$\overline{\Delta\theta^2} = 5.7Cn^2\Delta l\left(\omega_0{}^{-1/3} - L_0{}^{-1/3}\right) \tag{2-60}$$

where Cn^2 is the structure constant, Δl is a section of the path length, ω_0 the beam size and L_0 the outer scale of turbulence.

If Cn^2 and ω_0 are assumed to be constant along the entire path length then Δl becomes L, a fixed path length, the variance of the angular deviation was shown [87] to be given by;

$$\sigma_\theta{}^2 = 5.7Cn^2 L\omega_0{}^{-1/3}\left(1 \mp \frac{1}{6}\theta\frac{L}{\omega_0}\right) \tag{2-61}$$

where L is the path length, ω_0 the beam size, Cn^2 the structure constant, $+\theta$ the divergent angle of the beam and $-\theta$ the convergent angle of the beam. It is assumed $\theta L/\omega_0 < 1$.

The beam displacement is considered to result from the differential coefficient of the angular variation along the path multiplied by the path length to the receiving plane [87]. The result is;

$$\sigma_\rho{}^2 = \frac{1}{3}\sigma_\theta{}^2 L^2 \tag{2-62}$$

where $\sigma_\rho{}^2$ is the variance of spot position, $\sigma_\theta{}^2$ is the variance of angular deviation and L is the path length.

Experiments measuring the angular deviation resulting from transmitting a He-Ne laser over 480 m and 1380 m path lengths, 20 m above the ground where compared with theoretical estimates by Chiba. Cn was determined by measurement of the temperature variations between two points separated by a distance r at the transmitter end;

$$C_T = \left[\overline{(T_1 - T_2)^2}\right]^{1/2} r^{-1/3} \tag{2-63}$$

$$C_n = \left(79P/T^2\right)10^{-6} C_T \tag{2-64}$$

where P is the pressure in millibars and T is the temperature in Kelvin.

The experimental findings were found to be in strong agreement with the theory [87]. A strong correlation between Cn^2 levels and beam displacement was observed.

Note that Kuriger [120] proposed an alternative technique for measuring laser beam pointing fluctuations. The technique required a laser beam to be modulated such that the modulation phase varied with position across the beam. Reflecting the modulated laser beam from a target then gives an indication of the position of the target within the beam using the relative modulation phase of the return signal.

Cook [121], when reviewing some ray optic beam propagation methods, also proposed an alternative method for measuring beam fluctuations, based on Ehrenfest's theorem, which did not require the wave equation to be solved. The method overcomes the limitation that is present in previous ray optic methods, namely over estimating the motion of the beam centroid. Chiba's method [87] also overcame this limitation but was simplified in that it applied a definite cut-off scale size. The base assumption was that only refractive-index scale sizes larger than the beam diameter contributed to the beam wander. Cook found, applying Ehrenfest's theorem, that the centroid of the beam can be shown to propagate as a paraxial ray in an 'effective' refractive index that depends on the irradiance profile of the beam.

Churnside and Lataitis [88] later developed a simple, analytic expression for the beam wander variance using a geometrical optics formulation applied to a finite, uniform beam propagating through a weak refractive turbulence characterised by the Kolmogorov spectrum. Provided $\sqrt{\lambda L}$ and $\lambda L/\rho_0 \leq D << L_0$ where L is the path length, D is the beam diameter, λ is the wavelength and ρ_0 is the spherical wave coherence length, then, the expression obtained is found to be a good approximation (within 5% of the exact result).

For a collimated beam the single-axis variance of beam wander is;

$$\sigma^2{}_{COL} = 0.97 C_n{}^2 D^{-1/3} L^3 \tag{2-65}$$

For a focused beam the single-axis variance of beam wander is;

$$\sigma^{2}{}_{FOC} = 1.10 C_n{}^{2} D^{-1/3} L^{3} \tag{2-66}$$

A diverging beam produces less wander than a collimated beam.

Andrews et al. [113] noted that the far-field angular spread of a free-space propagating beam of diameter $2W_0$ is of order $\lambda/2W_0$. They also noted that in the presence of turbulence the beam will experience random fluctuations. These fluctuations were seen as a movement of the beam off-boresight in the receiver plane with a displacement of the point of maximum irradiance (the 'hot-spot') within the beam. The wandering beam, in fact, they stated, becomes highly skewed from Gaussian. Large-scale turbulence effects can result in a wander of the beam. However, as the size of the beam approaches the outer-scale of turbulence, theoretical modelling performed by Andrews et al. [122] predicts that the beam wander nearly vanishes. For a collimated beam, with a finite outer scale present, the root mean square of the beam movement is;

$$\left\langle r_c{}^{2} \right\rangle = 2.42 C_n{}^{2} L^{3} W_0{}^{-1/3} \left[1 - \left(\frac{\kappa_0{}^{2} W_0{}^{2}}{1 + \kappa_0{}^{2} W_0{}^{2}} \right)^{1/6} \right] \tag{2-67}$$

where C_n^2 is the structure constant, κ_0 is the outer scale, W_0 is the beam radius and L is the path length.

2.5.6 Beam Jitter

Andrews et al. [122] define another phenomenon, named beam jitter, as being the movement of the beam around its unperturbed position in the receiver plane with a resulting beam-tilt significantly smaller than that occurring during beam wander. Banish et al. [116] also describe this phenomena and relate it to gross jitter of the turbulence cells (as in a jet engine plume waving). The jitter induced pointing variance is calculated, employing geometrical optics approximations, for a collimated beam, to be;

$$\sigma_{pe}^2 = 0.48\left(\frac{\lambda L}{2W_0}\right)^2\left(\frac{2W_0}{r_0}\right)^{5/3}\left[1-\left(\frac{C_r^2 W_0^2 / r_0^2}{1+C_r^2 W_0^2 / r_0^2}\right)^{1/6}\right] \quad (2\text{-}68)$$

where C_r is a scaling constant of the order 2π, W_0 is the beam radius, L is the path length and r_0 is Fried's parameter for a reciprocal propagating spherical wave defined by;

$$r_0 = \left(0.16 C_n^2 k^2 L\right)^{-3/5} \quad (2\text{-}69)$$

where k is the wavenumber, C_n^2 the structure constant and L the path length.

Andrews et al. determine that increased scintillation resulting from beam wander is seen as a pointing error. Note that the beam wander model is simplified as it removes the effect of beam broadening resulting from scale sizes smaller than the beam. The pointing error effects are shown to be negligible for a collimated beam but significant for a focused beam.

2.5.7 Fante's Summary

In 1975 and 1980 Fante [96, 97] published comprehensive summaries of the effects of a turbulent medium on electromagnetic beam propagation by reviewing previous work on the topic. Fante considered the effect of the propagation path on a beam as being measurable by observing a subsequently generated beam spot. The spot can be analysed by considering the beam spread and spot movement. Short-term beam spread is represented by ρ_S and the long term spot size, the blurred spot, as ρ_L. The beam centroid is represented by ρ_C. Fante summarised other's work on beam movement and spread for a number of cases.

Case 1: $\rho_0 << D < L_0$ and $x \leq kL^2$. That is, when the coherence length (that is the distance transverse to the propagation axis over which the wave is coherent) of the beam is a lot smaller than the beam diameter and the beam diameter is smaller than the largest distance over which fluctuations in the index of refraction are correlated. Also, case 1 requires the displacement to be less than the product of the laser beam wavenumber and L, which is either the beam diameter or coherence length

(whichever is smaller). Note that lateral coherence length is $\rho_0 = \lambda/\varphi$, where φ is the beam divergence. For case 1 he found that the beam centroid is represented by;

$$\left\langle \rho_C{}^2 \right\rangle \cong \frac{2.97x^2}{k^2 \rho_0{}^{5/3} D^{1/3}} \tag{2-70}$$

Case 2: If $\rho_0 \sim D$ and $x \leq kL^2$ Fante did not find any simple expression for the beam centroid and short term spot spread.

Case 3*: If* $\rho_0 >> D$ *and* $x \leq kL^2$ there is very little beam wander with short and long term spreads approximately equal. If x is a lot less than $(k^2 Cn^2 (l_0)^{5/3})^{-1}$ then;

$$\left\langle \rho_L{}^2 \right\rangle \cong \frac{4x^2}{k^2 D^2} + \frac{D^2}{4}\left(1 - \frac{x}{F}\right)^2 + \frac{4x^2}{k^2 \rho_0{}^2} \tag{2-71}$$

where the beam has initial diameter D, with a radius of curvature $-F$, and lateral coherence length given in equation (2-72).

$$\rho_0 = \left[1.46k^2 x \int_0^1 d\xi (1-\xi)^{5/3} C_n{}^2(\xi x)\right]^{-3/5} \tag{2-72}$$

While if x is a lot greater than $(k^2 Cn^2 (l_0)^{5/3})^{-1}$ then;

$$\left\langle \rho_L{}^2 \right\rangle \cong \frac{4x^2}{k^2 D^2} + \frac{D^2}{4}\left(1 - \frac{x}{F}\right)^2 + \frac{6.6x^3 \int_0^1 (1-\xi)^2 C_n{}^2(\xi x) d\xi}{l_0{}^{1/3}} \tag{2-73}$$

Case 4: If $x >> kL^2$ then the beam will be broken-up into a number of patches with negligible wander of the beam centroid. The beam centroid motion is negligible in comparison to the variation in the size of the blurred sport. The blurred spot, or the square radius of the region where the bright patches will be formed, can be calculated using (2-71).

Fante [97] stated that in strong turbulence very little of the long-term-averaged beam spread is due to beam wander. This is because the beam wander saturates. In other words, increasing the path length or turbulence strength no longer increases the mean square beam centroid position.

2.6 Laser Beam Propagation through a Turbulent Medium

Laser beam propagation is effected by changes to the refractive index of the medium through which the beam travels. Traversing a high temperature gas medium of homogeneous temperature, pressure and density will not produce beam movement. Continual mixing of the hot gas with gas of a different temperature would produce dynamic temperature gradients across the gas medium. A propagating beam could be significantly affected. The exhaust from a jet engine, mixing with the surrounding air, produces such a situation. Similar, though less extreme, conditions exist within the atmosphere. The characterisation of the turbulence structure can be done optically, as shown in the following sections.

2.6.1 Measuring Inner Scale of Turbulence

The inner scale of turbulence describes the smallest length scale in the inertial range and is used as a measure to characterise the turbulence and the resulting effects on a propagating laser beam. Knowledge of the inner scale value is therefore useful. Many methods have been presented that may give a measure of the inner scale. For example, Livingston [123] presents a number of existing methods for measuring the inner scale of a turbulent atmosphere. One existing method involved plotting the log of the temperature and power spectra. The graph produced has a straight line with a -5/3 slope between the frequencies associated with the inner and outer scale of turbulence. However, at the inner scale the power level is 3-4 orders of magnitude lower than at the outer scale and consequently is susceptible to noise obscuring the inner scale breakpoint. Additional methods are discussed but both required the measurement of the refractive index structure constant, Cn^2. Livingston also suggested a solution which allowed the determination of the inner scale by using the ratio of outputs from two scintillometers placed at different ranges. The new method did not require

an independent measurement of Cn^2. The method works because the spectrum of refractive turbulence changes sharply at the spatial wave numbers near the inverse of the inner scale.

Hill and Ochs [90] also described an optical technique for measuring the path-averaged value of the turbulence inner scale. In their technique a laser was used as the transmitter source with two scintillometers used to detect and collect the transmitted energy. One scintillometer acted as a point receiver with an aperture smaller than both $\sqrt{\lambda L}$ and l_0. They used a large aperture receiver as the second scintillometer. In this case, although the light received was incoherent, large spatial wavelengths within the inertial range could be measured. The receiver needed to have an aperture much larger than both $\sqrt{\lambda L}$ and l_0. The inner scale was determined by measurement of the variances of the measured intensity from both scintillometers. The point receiver was used to record the spherical-wave log-intensity variance, σ^2_{LNI}, which was normalized by $0.5k^{7/6}L^{11/6}C_n^2$ and plotted versus $\sqrt{\lambda L / lo}$. The large aperture receiver also recorded the log-intensity variance and a ratio of the normalised variance from both receivers was obtained. The ratio was proportional to the normalised log-intensity variance previously reported (Figure 4, Hill and Clifford [19]) and hence $\sqrt{\lambda L / lo}$ could be read from Figure 4 [19] and l_o obtained. Hill and Ochs [90] stated that scintillation saturation may still occur during extreme atmospheric turbulence and that there was a limitation present on the minimum value of l_0 measurable as σ^2_{LNI} becomes insensitive to l_0 for $\sqrt{\lambda L} >> l_0$. Their technique offered three advantages. Firstly, the apertures, and hence optical paths, could be almost coincident. Secondly, as the optical path they used was short, there was less chance for error from scintillation saturation. Lastly, their work used a more accurate model of the spectrum of atmospheric refractive index fluctuations. Their technique was proven to be reliable when they compared the results with those obtained by a simultaneous measurement of the inner scale using a hot-wire anemometry technique.

An alternative method for measuring the inner scale is described by Consortini and O'Donnell [124]. Their method involves the use of two thin parallel laser beams. The difference of the two correlation functions describing the beam wandering is a maximum value at the inner scale. The maximum occurred when the distance between the beams is equal to the value of the inner scale. To determine the inner scale the measurements needed to be made at a number of beam separations.

Hill [125] discussed a number of methods for determining the inner scale of turbulence, including that presented by Livingston [123] which used measured variances at various different path lengths. Hill concluded that a bi-chromatic method, using two wavelengths, has advantages when $l_0 \leq 0.6\sqrt{L/k}$, whilst when $l_0 \geq 0.6\sqrt{L/k}$, the method that used variable aperture sizes was best. However, all methods only applied to weak turbulence as the Rytov approximation (which is only valid when the variance of logarithmic amplitude variations is less than unity [126]) is employed during their formulations. Livingston's method suffered from any inhomogeneities in the horizontal path as well as scintillation saturation over longer paths while the bi-chromatic method must also consider the dispersion effects on the wavelengths being employed.

Consortini et al. [127] subsequently presented a new method for measuring the inner scale and structure constant of atmospheric turbulence. The method considers the intensity variance of a spherical wave (a diverging beam) and the lateral-displacement variances of a narrow laser beam (collimated). The transverse displacement of the laser beam is given by;

$$\left\langle (\delta x)^2 \right\rangle = 2.2 {C_n}^2 L^3 {l_0}^{-1/3} \tag{2-74}$$

where the brackets denote the average and L is the path length, provided $\lambda L << (l_0)^2$.

The mean-square of the log-amplitude fluctuations of a spherical wave is given by;

$$\left\langle (\chi)^2 \right\rangle = 0.32 {C_n}^2 L^3 {l_0}^{-7/3} \tag{2-75}$$

Assuming the same C_n^2 value, an expression to determine l_0 can be obtained.

The method is sensitive because the fluctuations of both intensity and position are proportional to the third power of the propagation distance. The technique can be performed over a short-path length and over a short time period. It appears, however, the technique does require the thin laser beam to

be within the inner scale dimension so that the beam does not break-up across the wavefront precluding measurement of the beam wander.

Yi et al. [128] also described a method for measuring the inner scale of turbulence over a range of paths lengths, including intermediate path lengths (tens of metres). Previous methods [124, 127] are only sensitive over short path lengths (beam wandering depends on path length L as L^3). Yi et al. proposed a variation on their previous work [127] that used measurements of intensity and angle of arrival. In the new approach they propose a pin-hole to be used to allow the angular arrival measurement to be realised as a displacement measurement. Experiments showed the results in good agreement with previous measurements. The method is less sensitive (as angle of arrival fluctuation variance depends on L as L^2) but applicable to intermediate ranges.

The techniques used for the measurement of inner scale can therefore be seen to make use of the known atmospheric frequency spectrum and its relationship to the inner scale. The recording of the variances of the measured energy incident on a receiver appear to be common in all the measurement techniques. The variance of the received energy is related to the path length, the wavelength, inner scale and the diameter of the receiver. It is by making measurements at various conditions that enables a solution for the inner scale parameter to be obtained.

2.6.2 Laser Beam Propagation through Jet Engine Exhausts

Barrett and Budni [105] were perhaps the first to measure the effect of strong turbulence (C_n^2 values of up to $3\text{x}10^{-9}$ $m^{-2/3}$) in a jet engine exhaust on laser beam propagation. The temperature in the exhaust was around 650°C. A 904 nm laser beam with 180 ns long pulses at 5 kHz, having a beam diameter of 4 cm and divergence of 0.3 mrad, was passed at an angle through the exhaust gases. The size of the beam was considered to be a direct measure of the turbulence as the size increased when the engine power was increased. Beam wander was also observed. The beam was broken-up by the turbulence and the result was a number of irregular patches of energy falling onto the detector array. In order to measure the beam spread the energy was collected to produce a long-term average distribution of beam irradiance;

$$I = A\exp\left[-(x - x_0)^2 / \sigma^2\right] \qquad \text{2-76}$$

where σ is the width, x_0 is the peak irradiance position and A is the peak amplitude.

The spot size went from 8.66 cm (no plume) to 15.86 cm (90% power). In addition, the beam was seen to deflect up to 2 cm over the 80 m range. Beam centroid movement was also measured with the beam found to wander over approximately 4 cm RMS.

Hogge and Visinsky [129] passed a 632 nm, 30 mm diameter, 10 mW laser beam through the exhaust of a jet engine and estimated the structure constant to be in the order of 10^{-5} $m^{-1/3}$ by considering the beam spread of focused and collimated beams [129]. The experimental methodology presented was based the work of Gebhardt and Collins [99]. Taking scintillations measurements using a 10.6 µm beam, the structure constant was also estimated to be in the order of 10^{-5} $m^{-1/3}$ and by measurement in the exhaust with a hot-wire anemometer, 10^{-6} $m^{-1/3}$.

More recently Sirazetdinov et al. have published a number of papers [106-109, 111, 130] related to on-ground testing of laser beam propagation through a jet engine. Their experiments used an R-25-300 jet engine, which is fitted to some variants of the Mig-21 fighter plane. The jet velocity was 170 m/s at the nozzle exit and its temperature was 650 K (on axis, 1 m from the nozzle). Values of the structure constant, C_n^2 were of the order of 10^{-9} $m^{-2/3}$. Beams with diameters of 10 and 30 mm were passed through the plume at angles between 10 and 90 degrees. At a distance of 80 m a lens system and CCD camera recorded the far field intensity distribution. The experimental results and analysis are quite extensive and the following provides a brief overview.

In one set of experiments using laser radiation at 0.53 and 1.06 µm, the jet off (no plume) beam radii (1/e points) were of the order of 30 µrad. For the jet on, the 0.53 µm beam radii varied from about 400 to 500 µrad for a 90º intersection angle with the plume to about 700 to 950 µrad for a 10º angle. For the 1.06 µm beam the radii varied from about 140 to 220 µrad for a 90º intersection angle to about 320 to 400 µrad for a 10º angle. The difference between the half and one micron case was stated as unexpected, as an estimate based on the power spectrum predicted only a 20% difference. There was also asymmetry in beam radius, the broadening normal to the plume axis being 20 to 40% larger

than along the plume axis. In addition scattering needed to be taken into account for the 0.56 μm beam, but had a relatively weak impact at 1.06 μm.

Beam centroid RMS wander was about 10 to 20 μrad for the jet off case. For the jet on, the 0.53 μm beam wander varied from about 100 to 200 μrad for a 90º intersection angle to about 250 μrad for a 10º angle. For the 1.06 μm beam the beam wander varied from about 50 to 130 μrad for a 90º intersection angle to about 130 to 190 μrad for a 10º angle. The degree of wander was greater normal to the plume axis than along it.

Experiments using 10.6 μm laser radiation were conducted with the transmission orthogonal to the beam axis. The jet off case gave beam RMS half widths of about 515 to 630 μrads, for the 10 and 30 mm beams. With the jet on the corresponding radii were 530 and 670 μrads. RMS beam wander was about 20 μrad with the jet off and 160 and 190 μrad for the 10 and 30 mm cases with the jet on.

From these experimental results, Borisova et al. [106] modified a von Karman spectrum to account for high and low frequency components in the spatial frequency range $\geq 10^3$ m^{-1}. She also included terms to represent asymmetry. A phase screen was derived to account for the lowest to highest frequencies, about 10^4 harmonics were needed. This resulted in a $10^4 x 10^4$ array which was computationally impractical for 2D Fourier Transforms, particularly as many replications were needed to be generated. However, they found it was possible to use two sequential phase screens. This gave good agreement between experimental and simulated results. Structure functions were also derived and used to derive algorithms for beam wander and divergence. An extensive range of algorithms for estimating the effects of turbulence on the laser beams were provided. Good agreement with experimental results was obtained by choosing parameters that defined the functions near the inner and outer scales, and made allowance for asymmetry.

Recently Sjöqvist et al. [112] have also reported on laser beam propagation through a jet engine exhaust. They presented the results of an experiment that studied the effect on a 1.55 μm laser beam propagating through the exhaust gases of a downscaled jet engine. The experimental results were compared with a model. They claimed the structure constant could be modelled using;

$$C_n^2 \approx 2\sigma_T^2 \left|\frac{dn}{dT}\right|^2 L_0^{-2/3} \tag{2-77}$$

where σ_T^2 is the temperature variance, $\left|\frac{dn}{dT}\right|$ is the gradient of the refractive index and $L_0^{-2/3}$ is the outer scale of turbulence. Their phase-screen model used an average value of structure constant corresponding to an effective propagation length.

The variance of the beam centroid motion was determined using an expression derived by Sirazetdinov at al. [107] that used a modified von-Karman spectrum that takes into account observed anisotropy;

$$\sigma_{c,x(y)}^2 = 2.84 C_n^2 L D^{-1/3} \left\{ 1 - 0.1 \left(\frac{D^2}{L_{0,x(y)} L_{0,y(x)}} \right)^{1/6} \left(3 \left[\frac{L_{0,x(y)}}{L_{0,y(x)}} \right]^2 + 1 \right) \right\} \tag{2-78}$$

where $L_{0,x(y)}$ denotes the outer scale length in the *x* any *y* directions respectively.

Beam centroid motion was also predicted using both (2-79) and (2-81);

$$\left\langle \sigma_c^2 \right\rangle \cong \frac{2.97 z^2}{k^2 \rho_0^{5/3} D^{1/3}} \tag{2-79}$$

where *z* is the propagation distance, *D* the aperture diameter and ρ_0 the transversal coherence length, defined as;

$$\rho_0 = \left[1.46 k^2 \int_0^L \left(1 - \frac{\eta}{L} \right) C_n^2(\eta) d\eta \right]^{-3/5} \tag{2-80}$$

where λ is the wavelength, $k=2\pi/\lambda$ is the wavenumber and *L* is the total propagation distance.

And, using a simplified geometrical optics model by Churnside and Lataitis [88] ;

$$\left\langle \sigma_c^{\,2} \right\rangle \sim 0.97 C_n^{\,2} D^{-1/3} L^3 \tag{2-81}$$

The experimental results for the 1.55 µm beam profile were analysed before and after propagation along the jet engine exhaust. An increase in beam diameter of approximately 20-30% was reported after propagating through the exhaust. Similarly beam wander increased, with a ten-fold increase reported. A scenario was studied where a co-flow was also applied once the engine was running. The results indicated a further increase in beam wander by around 25% when compared to no co-flow.

The measured results were used as input into equations (2-78), (2-79) and (2-81) in order to estimate an average value for the refractive index structure constant. A phase screen model, using either the von Karman spectrum or the fast Fourier transform method, was then used to predict the beam movement. The model output under-predicted the beam movement, they supposed because these phase screen methods do not account for low spatial frequencies.

Further results and experiments from Sjöqvist et al. have also been published [131, 132]. One experiment [132] using 3.5 µm and 1.57 µm lasers was reported where the beams propagated along the jet axis. The RMS beam wander for both lasers were found to be between 60 µrad to 150 µrad, with a maximum deflection of around 400 µrad. There was a refraction angle of around 200 µrad that was towards the jet axis. Beam wander for the 3.5 µrad laser, being sampled at over 600 Hz, was found to be 50% correlated at 3.5 ms. The data set was limited, which meant no definite conclusion on the dependence of different parameters could be made.

Another experiment co-propagated 1.52 µm and 3.56 µm laser beams along the plume while a 532 nm visible laser beam was propagated across the plume. Beam break-up was notably more severe for the 1.52 µm beam compared to the 3.56 µm beam. For both IR beams the beam wander decreased as the beams were propagated at increasing distance from the jet's centre axis. The range of values recorded for different geometries and conditions varied from 75 µrad to 228 µrad. It was noted that although the centroid movement was similar for both beams, the movement of the highest value within the recorded beam image was greater for the 1.52 µm beam. The scintillation

index of the 1.52 µm beam varied from 0.58 to 1.36 compared with 0.12 to 0.36 for the 3.56 µm beam, a factor or around 4 for the same conditions. In the case of the 532 nm laser beam crossing the exhaust the beam break-up was severe, with a beam wander that ranged from 50 µrad to 120 µrad for the various engine settings.

2.6.3 Laser Beams Propagation through Laboratory Generated Turbulence

Studies of laser beam propagation through controlled turbulence in a laboratory environment were performed by Joia et al. [133, 134] using on a planar heated gas jet and a visible laser. These were the only laboratory studies of laser beam propagation identified in the literature review. In the work by Joia el al. the gas jet, with a nozzle 1 cm by 100 cm, had a Reynolds number of $3x10^4$ and was heated to up to 18°C above ambient room temperature. The jet velocity profile was previously well characterised. Joia et al. described how they used a HeNe laser to measure the phase spectrum of a planar heated gas jet by splitting the beam and passing each beam through different paths, but with homogenous turbulence, and finally combining the beams to record the resulting intensity measurement. The phase difference was extracted from intensity measurements by considering the minimum and maximum intensity values. The phase spectrum was found to be proportional to $k^{-8/3}$ at high wavenumbers. The phase fluctuations depended on local fluctuations in the refractive index, which in turn depended on the velocity fluctuations. A change in gas temperature was found to cause a change in the variance of the phase difference.

Joia et al. also considered intensity fluctuations resulting from of the laser beam propagating through the turbulent medium. The beam front would traverse the turbulent flow, which has a refractive index that varies in space and time, and undergo a phase modulation, which also varies in space and time. The phase fluctuations would then result in amplitude fluctuations, due to the process of diffraction, as the beam continued past the turbulent media. An experiment was conducted in which the time spectrum of fluctuations was measured. The measurements were analysed and it was seen that the low-frequency part of the spectra followed a power law with an exponent of -1. The higher frequencies followed a power law with an exponent of -8/3. The measured values agreed with those calculated theoretically. The break-point between the two transitions was related to distance, with experimental measurements matching theoretically calculated values.

2.7 Modelling of Laser Beam Propagation

Laser beam propagation models, numerical and analytical, are commonly employed in modeling laser beam propagation through the atmosphere. However, the accuracy of these models is under question when considering the temperatures and turbulence present in jet engine exhausts. Laser beam propagation studies done by Shapiro [135] suggested that the temperature predictions, and hence refractive index structure, in an aircraft's wake are not isotropic and do not fit Kolmogorov's [101] energy spectra at large scales, predicting larger than expected beam wander. Further, Barrett & Budni [105] measured the beam spread and wander for a 904 nm laser passing through a jet exhaust. The beam wander was over two times that calculated from existing models, which were only developed for weak to moderate turbulent flows.

Hogge & Visinsky [129] used lasers to probe the engine exhaust to determine the average structure constant values along propagation paths. They used methods and data [89, 99] based on Schmeltzer's studies of beam propagation [115]. However, their results used modeling data that assumes a Kolmogorov spectrum, which does not represent correctly the low and high frequencies within the exhaust turbulence [134].

Sirazetdinov et al. [107-109, 111, 130] conducted an extensive study in the jet engine exhaust region, probing with 0.53, 1.06 and 10.6 μm lasers. They developed algorithms for determining beam wander and divergence based on an estimation of the turbulence structure. A modified von Karman spectrum was used to take into account anisotropic features of strong turbulence. Calculated results, which unfortunately required input estimations of scale lengths and turbulence strength, were matched to experimental results. More recently, Sjöqvist et al. [112] studied laser propagation using a 1.55 μm beam fired parallel to a scaled-down jet engine exhaust. A model of the propagation was developed using phase screens, an approach also used by Borisova et al. [106] and which is discussed in the following section. To apply this method they used estimates of the refractive index structure constant to define the level of turbulence. The approach involved running the model for different structure constant values, comparing the results with experimental results until a match was found. The obvious limitation is that the simulations required parameters derived from the experimental data.

Developing a model for different engine conditions would not be readily realised using this approach as experimental results would be required for each engine condition.

2.7.1 Modelling using Phase screens

In atmospheric physics it is assumed that the initial plane wave is perturbed by turbulent layers at various heights in the atmosphere (Figure 2.7). In the simplest approach these are modelled as infinitely thin layers which perturb the phase, but do not affect the amplitude or change the direction of the wave-front. Hence the effect can be aggregated into one, infinitely thin, phase screen. The first order treatment [65] assumes that all points of the waveform are advanced or retarded in phase by the phase screen. This is represented by φ(x,y), which defines phase variation from the mean;

$$\phi(x,y) = \frac{2\pi}{\lambda}\int_{o}^{h} \Delta n(x,y)dz \tag{2-82}$$

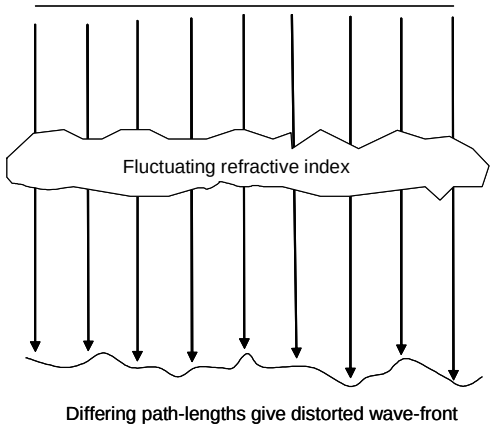

Figure 2.7: Schematic of phase front distortion.

Between phase screens propagation is in free space and can be represented by the Helmholtz equation [106];

$$\nabla^2 U + k^2 U = 0 \tag{2-83}$$

where *U* is the field and *k* is the wave number. Restricting the direction to *z* (the parabolic approximation) gives;

$$U(x.y.z) = \psi(x, y, z)e^{-ikz} \tag{2-84}$$

representing a plane wave travelling in the *z* direction. The effect of the phase screen is then;

$$W(x.y.z) = U(x.y.z)\exp(i\phi(x, y)) \tag{2-85}$$

where *W(x,y,z)* is the wave-front after passing through the phase screen, $\phi(x, y)$ is the phase change in the screen. Because of the assumption that the phase screens are infinitely thin, multiple phase screens can be aggregated into a single screen by adding the phase perturbations of the individual screens.

The aim of phase screen modelling is to generate a grid of sample points which have the same phase statistics as the turbulence induced phase fluctuations. Each individual phase screen is a sampled grid of these statistics. Numerous methods have been developed to determine a representative phase screen using experimentally obtained data to match up the statistical representation. This approach is limited because of the reliance on experimentally obtained data that is used to describe the turbulence being modelled.

2.8 Summary

Chapter 2 has provided an overview of aspects relevant to the study of laser beam propagation through highly aberrant media such as jet engine exhaust plumes. Firstly, a reliable method for determining the refractive index of a gas mixture has been identified, though it has only been validated for temperatures up to 100°C. Also, a method for calculating the effects of anomalous absorption, including correcting for temperature effects, at particular wavelengths has been identified.

An overview of turbulence was given. Grid generated turbulence was identified as a method for varying the turbulence conditions. Changing the hole dimensions and blockage ratio both affect the downstream development of turbulence. A discussion of others' findings describing the turbulence produced for various grid conditions was reviewed and summarized. Furthermore, the chapter has also presented methods for characterizing a turbulent flow and its compositional structure. These included: Mie; Rayleigh and Raman scattering; Laser Doppler Anemometry and Particle Image Velocimetry.

Various aspects of Electro-Optic propagation have also been presented. These have included a discussion on the effects of the transmitting media on the laser beam covered topics such as: scintillation, spot area, aperture averaging and beam wander. Characteristics of the transmission media were described by terms such as: structure constant and inner and outer scales. Such terms have been discussed and equations that use these parameters to derive the effect on the propagating beam have been shown.

Previous studies of laser beam propagation through jet engine exhausts have been summarized and discussed. The majority of the work has been done by either Sirazetdinov et al. [107-111] or Sjöqvist et al. [102, 112]. The studies have been system level studies where control and understanding of turbulence has been limited. Engine settings have been used to change the turbulence while the turbulence was characterized by analyzing the laser beam movement and solving modified atmospheric models to derive the structure functions or scales of the turbulence. Laboratory studies of laser beam propagation through well characterized turbulent flows appear scarce. Only one study, at low temperature, was found in the literature.

Finally, Chapter 2 has provided an overview of the various modeling approaches that have been used to predict laser beam degradation. Analytical and numerical models exist, and are used primarily for atmospheric propagation. To predict the beam degradation through jet engine exhausts a number of attempts have been made to modify the existing analytical equations to take into account noted anisotropy and the small scale fluctuations of the turbulence.

The review undertaken has highlighted the need to undertake a controlled laboratory experiment to study the effect of the various parameters related to the turbulence and resulting beam degradation of a laser beam transmitted through a hot, turbulent flow. As a result, the effect on the laser beam degradation due to a change in various key parameters will be studied. The parameters identified include: turbulence intensity; path length; laser beam diameter; laser beam wavelength; gas constituents (eg: CO_2) concentration and the temperature of the flow.

Experiments will be conducted to isolate the effect of each parameter on, for example, the angular divergence and beam wander of the laser beam. The results can be compared with existing analytical models. In this way a model may be generated that uses the understanding derived from the controlled experiments. This model could be used to predict the effect on the laser beam under a wide range of conditions.

In the Chapter 3 a jet engine study is documented. The study was used to assess the impact of a real jet engine exhaust plume on laser beam propagation.

Chapter 3

Jet Engine Study

3.1 Introduction

This study is concerned with the practical evaluation of the effects of a jet engine's efflux on the propagation characteristics of energy from a laser jam source. Laser beam propagation is assessed when a laser beam is passed through the efflux of a ground-based jet-engine for various engine settings, set-up geometries and laser beam conditions. In the study often multiple, and sometimes unknown, parameter changes are occurring from one scenario to another. Consequently, the end-to-end performance is assessed. The study therefore provides an estimation of the effects on the laser beam degradation when propagating through a jet engine exhaust.

One purpose of this study is to investigate the impact of a zone of highly turbulent hot exhaust plume on the propagation characteristics of a mid-IR laser beam passing through it. The study involved the use of a turbojet operated, with and without by-pass, at various speeds to investigate the impact on the laser beam.

Other measurements made during the study included near- and far-field angular displacements and far-field measurements of laser modulation waveforms using radiometers.

3.2 Experimental Setup and Considerations

The jet engine test laboratory was situated in a defence establishment in the United Kingdom and provided access to an experimental configuration that represented a by-pass jet engine. Two kerosene engines were used; the Rolls Royce manufactured Gnome 1000 and Gnome 1200 engines. The Gnome 1000 was used to drive a turbo-compressor to provide the by-pass air, whilst the Gnome 1200 provided the core flow. The bypass air is delivered through four flexible metal pipes to the annular bypass nozzle. These pipes are fed from a rectangular manifold (Figure 3.1) to provide the primary engine with bypass air having minimum swirl. A mass flow of over 5 kg/s could be obtained with a thrust of 3 kN and an exhaust temperature of 685°C.

The laser beam was directed through various parts of the highly turbulent engine efflux region to measure the impact on the spatial characteristics of a propagating mid IR laser beam. Schematics of the experimental set-up are shown in Figure 3.2 and Figure 3.3.

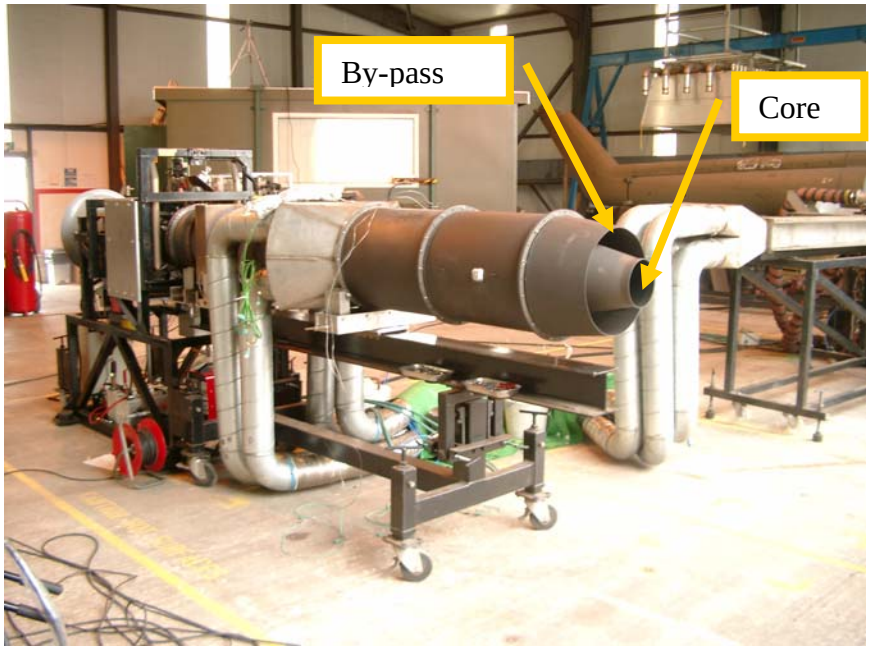

Figure 3.1: The Gnome 1200 engine showing the core and bypass nozzles.

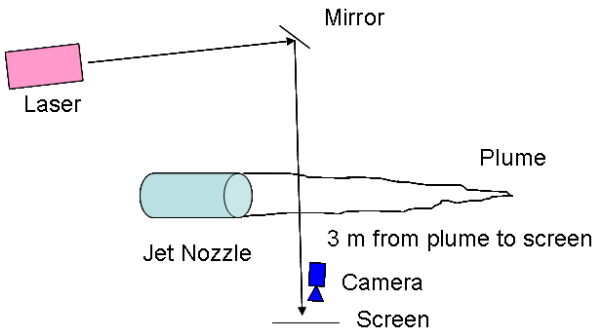

Figure 3.2: Plan view schematic of the near-field experimental set-up for the jet engine study.

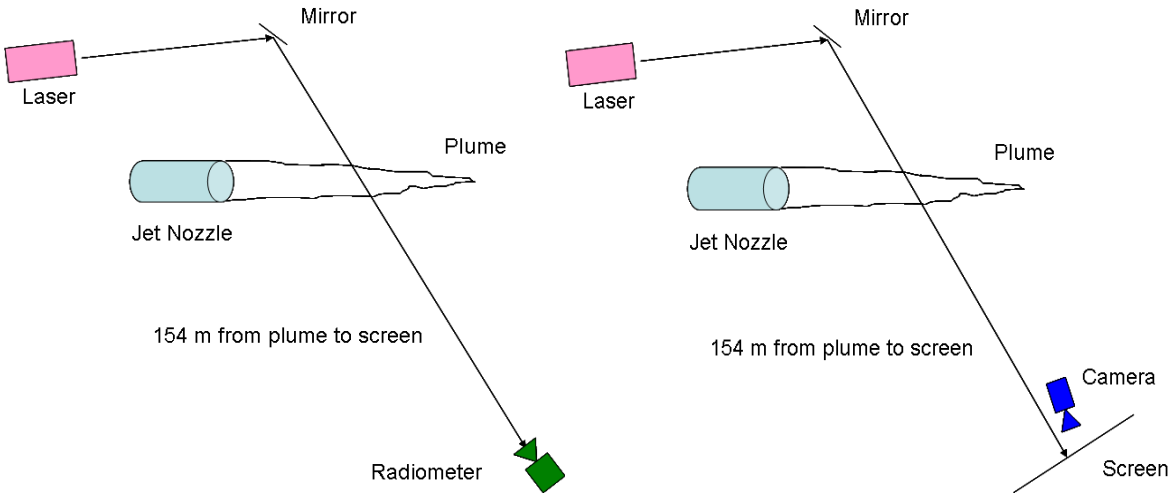

Figure 3.3: Plan view schematic of the far-field experimental set-up for the jet engine study. The radiometric measurement set-up is shown on the left, while the camera set-up is shown on the right.

The engine producing the core flow was run at a range of speeds, both with and without bypass air from the secondary engine, to provide a range of likely operating conditions. Measurements of the laser beam's spatial position were made when the flow had stabilised at a selected operating point.

The measurements of laser beam motion used a frequency-doubled CO_2 laser, 4.67 µm, which could be modulated at frequencies up to 133 kHz. The laser model was Mid-IR–2, developed under contract by DeMaria ElectroOptics Systems, Inc. The laser was mounted on masonry block pillars to minimise the effects of vibration. Camera integration time was set to capture one pulse per frame.

A Focal Plane Array (FPA) camera was used to image the laser beam that was projected onto a sight board after propagating through the plume. A black-body source located behind the target board, which acted as a position reference point, gave a means of measuring the change in position of the beam centroid with engine power as well as the standard deviation of the frame-to-frame centroid motion.

Laser propagation paths were selected to provide a range of intersection points along the plume axis and normal to it. Measurements were made of the laser beam motion through the plume over short distances (< 3 metres) and long distances (~150 metres) for identical geometries and engine settings. A list of the experiments performed is given in Table 3.1. At the longer range the effect of turbulence on the beam was assessed using a radiometer to measure the resulting signal.

Tests on the engine (Figure 3.4) showed that its turbine exit temperature changed little between 14,000 and 22,000 RPM, whilst its axial thrust increased monotonically. Data points were taken for a number of engine settings over this range with the intention that the effects of gas temperature and gas velocity could be separated more easily. The beam centroid position with the engine off was measured prior to the start of each run in order to provide a baseline.

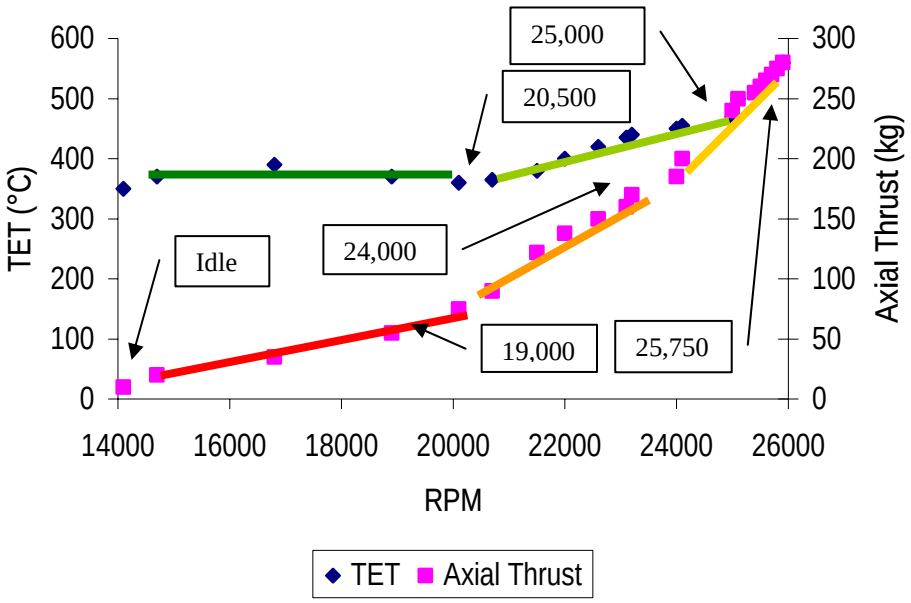

Figure 3.4: Engine Turbine Exit Temperature (TET) and Axial Thrust as a function of RPM [136].

Table 3.1: Jet engine experimental conditions

Distance from nozzle when beam intersects plume core (m)	Engine Configuration	Engine (RPM)	Crossing height above plume core (m)	Crossing angle (°)	Distance from plume to sensors (m)	Camera Used	Radiometer Used
0.5 1.0 1.5	Turbofan Turbojet	Off 14,000 (idle) 20,000 22,000 24,000 25,000 25,750	0.0	22.5 45 90	3	Yes	No
1.0	Turbofan Turbojet	Off 14,000 (idle) 20,000 22,000 24,000 25,000 25,750	0.0 to 0.24 in steps of 0.04	90	3	Yes	No
1.0	Turbojet	Off 25,750	0.0	22.5	154	Yes	Yes

3.2.1 Turbulence Dependence on Engine Setting and Type

The gas turbine engine has the characteristics shown in Figure 3.4 when operated as a pure turbojet (zero bypass). The Turbine Exit Temperature (TET) is used as a surrogate for plume temperature when defining the operation conditions.

The choice of 14,000, 17,000, 20,000, 22,000, 24,000, 25,000 and 25,750 RPM settings was made to allow determination of the extent to which the laser centroid motion depends on the temperature of the gas and the extent to which thrust is related to the gas velocity. The link to the gas temperature is easiest to understand, because of the inverse relation between gas temperature and density, and hence refractive index. Thrust should also have an effect, because the motion of the gas in the plume provides the energy to drive turbulent mixing. It is easier to separate effects of temperature and gas velocity by making measurements at 14,000 and 20,000 RPM and at 17,000 and 22,000 RPM where the TETs are nearly equal but where the thrusts differ by a factor of 7 and a factor of 3.5 respectively.

The second area that was investigated was whether the turbulent mixing was affected by the core flow being surrounded by a flowing annulus of cooler air (by-pass air). The tests with the turbojet engine, with and without by-pass, were done with a by-pass ratio of 1:1.

3.2.2 Vibration Control

Vibration effects were minimised by mounting all equipments on concrete blocks. However, it became apparent that although the process of changing the height of the masonry block pillar that supported the target board by adding further courses of blocks worked well, it did slow down the process of taking data. As a result an alternative approach was tried (see Figure 3.5) in which the target board was mounted on the X-Y stage. This also proved adequate and was used for all the remaining tests.

It was expected that the camera may be affected by vibration; this was one reason for using the black-body source behind the target board, the arrangement of the tripod with the legs spread as wide as possible proved to be very stable. Measurements of the apparent black body position

showed variations of a few hundredths of a pixel during a single data capture and just over a tenth of a pixel during an entire engine run. These effects were deemed negligible and were ignored.

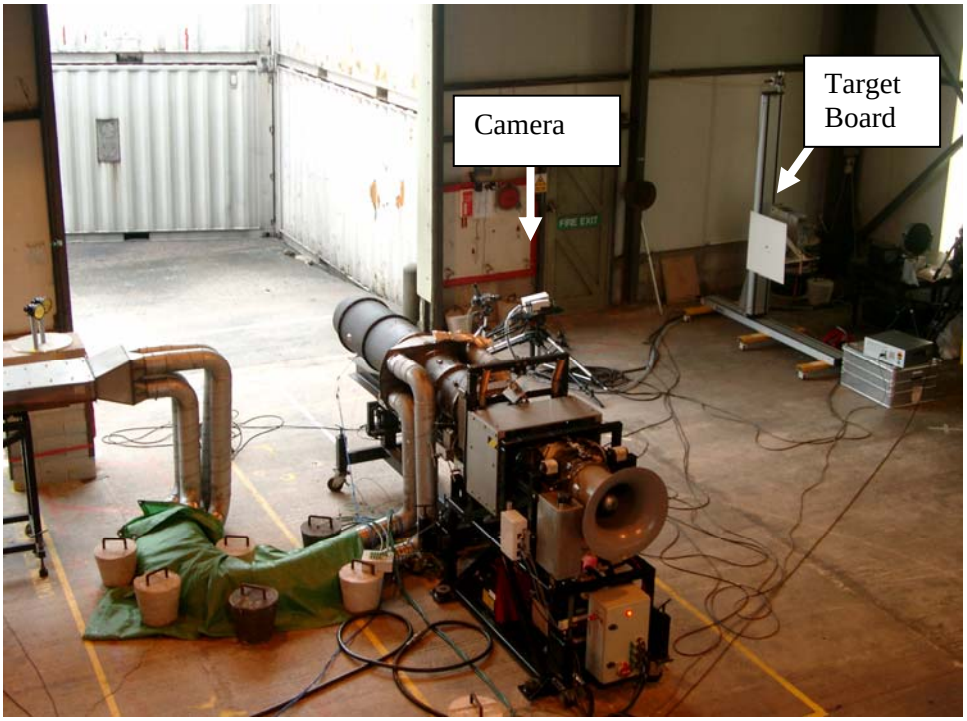

Figure 3.5: The set-up for measurements through the plume.

3.2.3 Turbulence Spectrum

The measurement of the turbulence spectrum using data collected by the high frame-rate FPA camera was an experimental objective. Consider that the highest frequency of centroid movement is dictated by the transit time of a parcel of gas across the laser beam. It is possible that effects on the laser beam displacement at frequencies up to 50 kHz (velocity of gas / laser beam diameter = 500 $m.s^{-1}$ / 10 mm) could be seen. However, this is well beyond the maximum frequency that can be achieved by reducing the size of the readout area of the FPA camera. Accordingly, a composite approach was followed. To study the lower frequencies, the camera was run at a series of different frame rates from 100 Hz up to about 1300 Hz (above this the frame rate setting was not reliable and could result in the camera only collecting alternate frames).

To determine the high frequency components the camera was also set at a single frame rate (100 Hz) and the integration time varied to change the number of 4.67 µm laser pulses collected in each integration time. If the effect of the engine plume on successive laser pulses is uncorrelated then the apparent centroid motion will be reduced by a factor of $\sqrt{N}$ [137], where *N* is the number of laser pulses in the integration time. On the other hand, if the pulses are correlated, then the centroid motion will not be reduced.

3.2.4 Data Analysis Methods

Data was collected using either the radiometer or the imaging camera. The radiometric data was output to data acquisition software and the histogram of the energy received over the frames was determined. The camera data was analysed after pre-processing the images. Background pixel noise was removed by subtracting an averaged background image with no laser beam present. Further noise was filtered out by setting to zero pixels with count levels less than 13.5% of the maximum pixel count in the frame. Centroid displacement was calculated by using the weighted sum of the pixels in the frame. The mean and variance was determined over the 1000 frames recorded.

3.2.4.1 Scaling Measurements of Centroid Motion

Measurements were taken with a camera having a pixel field-of-view of 30 µm and a lens with 50 mm focal length. This was at a distance of 2.23 m from the screen for the cases where the beam intersected the plume at 1.0 m from the nozzle and 2.27 m from the screen when the beam intersected 0.5 metre from the nozzle. This gives a length at the screen of 1.34 – 1.36 mm per pixel. The distance from the plume axis to the screen was 4.90 metres in the 1.0 m case and 4.86 m for the 0.5 m case. This gives angles at the plume for 1 pixel of centroid motion of 270 µrad at 1.0 m and 280 µrad at 0.5 m. This scaling is accurate to better than 10% for all vertical positions of the beam passing through the plume. Appendix A gives a more detailed calculation of scaling for all the beam positions in the plume.

3.3 Results

In this section the key results are documented. The results include the effect of engine configuration, turbofan versus turbojet, on the laser beam propagation. Other results show the laser beam propagation as a function of axial and vertical position in the plume and the effect of crossing position and angle. The turbulence spectrum characterization using the high-frame rate FPA camera and radiometric measurements of the beam in the far field are also included.

3.3.1 Laser Beam Propagation as a Function of Axial Position in the Plume

The centroid motion in the y direction for a turbojet plume measured at 90° to the plume axis and 0.5 m from the nozzle is plotted in Figure 3.6. The data in Figure 3.7 is measured under the same conditions except at 1.0 m from the nozzle. The differences between the two are that the peak in the centroid motion around the idle condition has disappeared, but the absolute levels of centroid motion at engine settings above about 20,000 RPM are almost the same, and the reduction in centroid motion for the 20 and 24 cm positions is much less than for the shorter distance.

At a distance of 0.5 m from the nozzle, where there is still an unmixed plume core (refer to Figure 3.11 introduced later), the centroid motion in the cross plume (y) direction peaks around the idle setting (14,000 RPM) and then decreases before increasing to a maximum at the maximum continuous setting (25,750 RPM). This is because the low thrust at idle means that there is more effective mixing of the exhaust and the surrounding air.

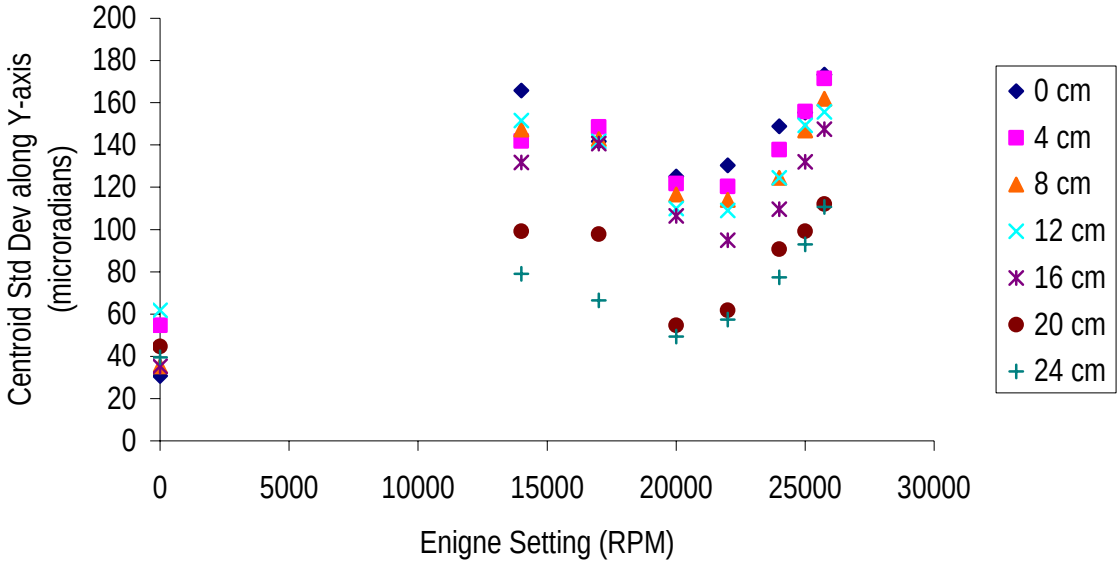

Figure 3.6: Centroid motion for the laser beam propagating 0.5 metres from the nozzle at 90° in a turbojet configuration at different crossing heights and over a range of engine conditions.

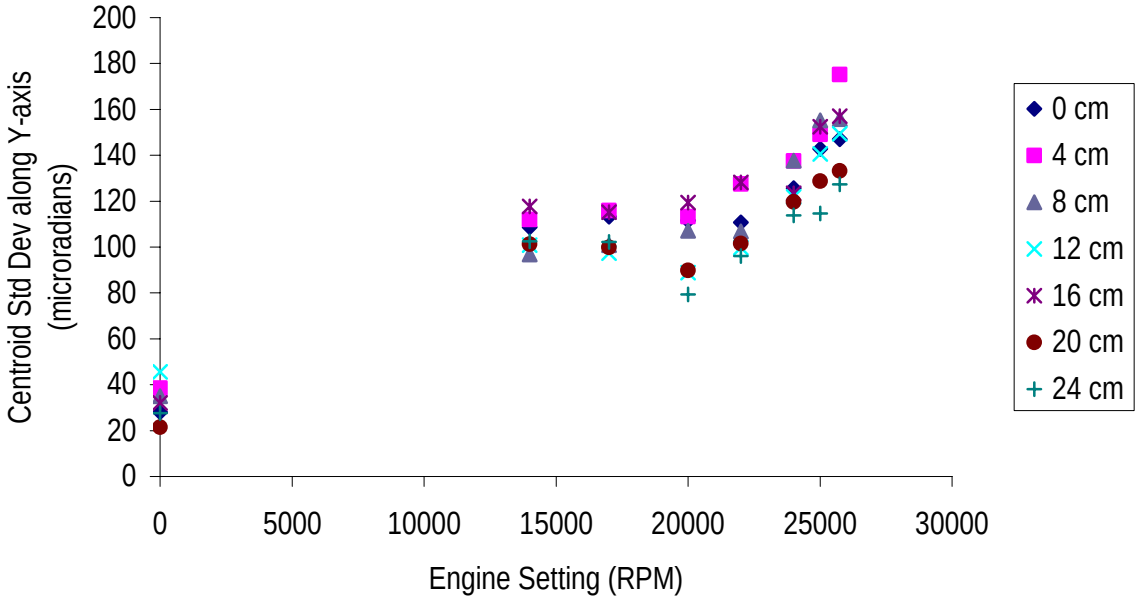

Figure 3.7: Centroid motion for the laser beam propagating 1 metre from the nozzle at 90° in a turbojet configuration at different crossing heights and over a range of engine conditions.

At a distance of 1.0 m from the nozzle, the dip between the idle setting and the maximum continuous setting has almost disappeared, except for the measurements farthest from the plume axis. By this distance, the plume is almost fully mixed and there is little evidence of any dependence of centroid motion on thrust.

3.3.2 Laser Beam Propagation as a Function of Vertical Position in the Plume

Figure 3.8 and Figure 3.9 show the centroid motion as a function of height above the axis for both the turbofan and turbojet configurations. The diameter of the inner nozzle (turbojet) is 160 mm and of the outer nozzle (bypass) is 395 mm. The measurements at 8 cm above the axis represent the centre of the boundary between the core and bypass flows, whilst the measurements at 20 cm above the axis represent the boundary between the bypass flow and entrained air.

In each vertical crossing height configuration a number of measurements of the beam displacement were made with the engine off. This enabled an error bar to be added to the engine off data to indicate the run-to-run variability in the measurements. In Figure 3.8 and Figure 3.9 the error bar is plotted to indicate the standard deviation in beam centroid position for the engine off cases at each vertical position. The error bar represents ±1 standard deviation of these measurements.

The results plotted in Figure 3.8 and Figure 3.9 indicate that there is a slight decrease in beam displacement variance as the beam intersection point moves radially from the plume core for all engine settings.

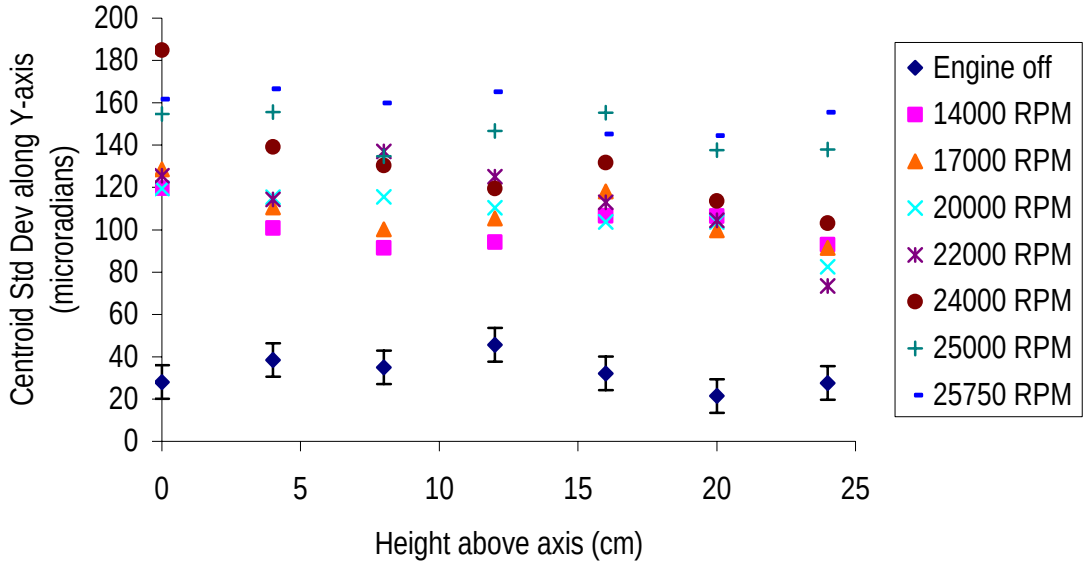

Figure 3.8: Centroid motion for the laser beam propagating 1 metre from the nozzle at 90° at different crossing heights and over a range of engine conditions for the turbofan configuration.

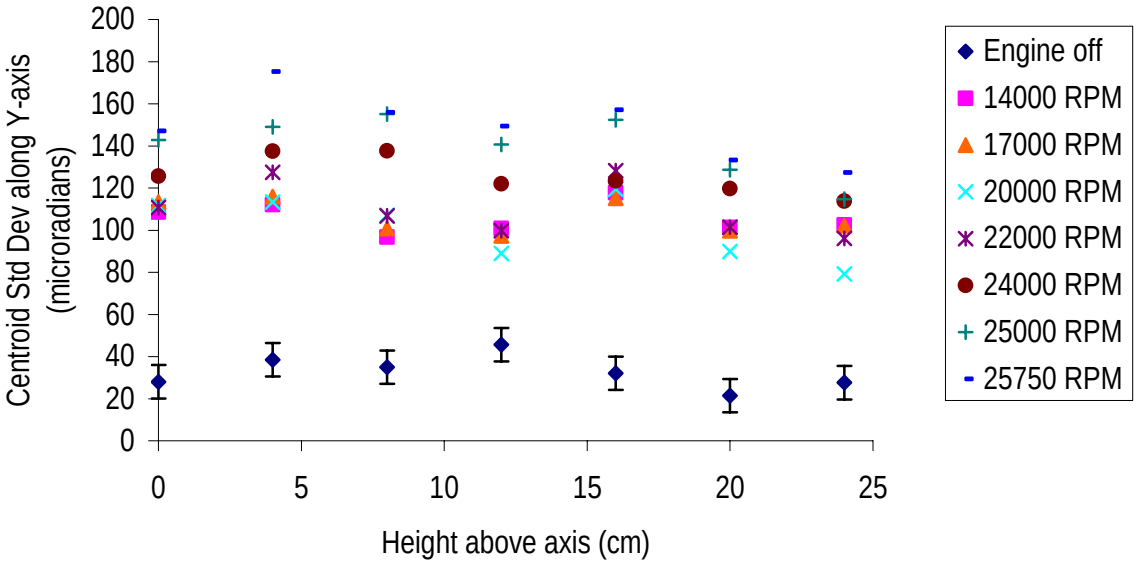

Figure 3.9: Centroid motion for the laser beam propagating 1 metre from the nozzle at 90° at different crossing heights and over a range of engine conditions for the turbojet configuration.

3.3.3 Laser Beam Propagation as a Function of Engine RPM

Figure 3.6 and Figure 3.10 show the centroid motion standard deviation for a turbojet and turbofan in the direction perpendicular to the plume axis (the y direction). The peak in centroid motion around the idle condition, and the dip before the increase near maximum power, suggests that the increased thrust (and therefore increased gas velocity) is having a negative rather than a positive effect on the level of centroid motion. The increased mixing with the cooler surrounding air results in an increase in the refractive indices within the gas mixture. Subsequently there is a decrease in the refractive index gradient along the beam path and a decrease in beam movement would therefore occur.

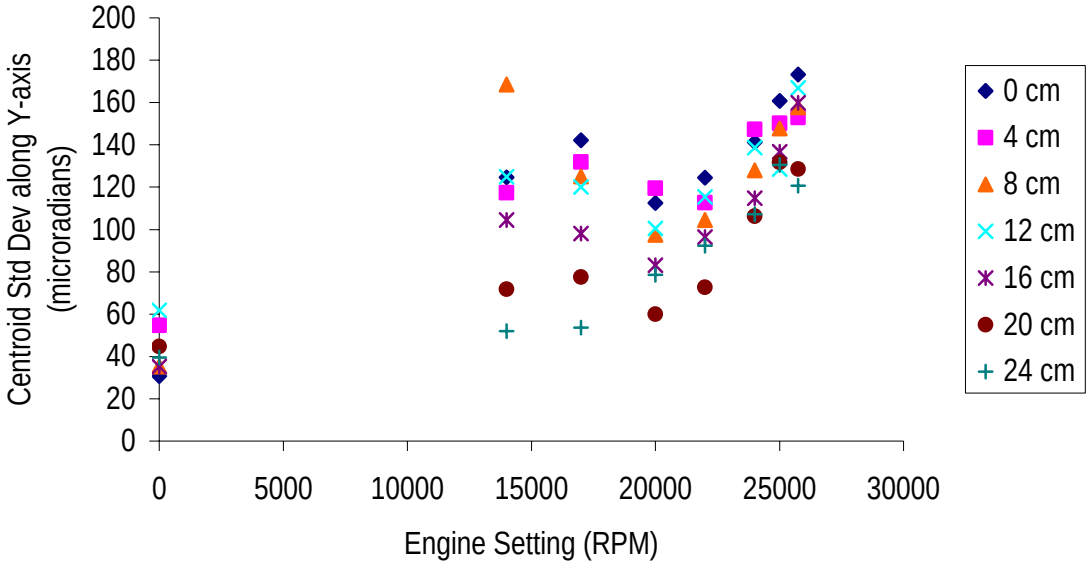

Figure 3.10: Centroid motion for a turbofan (1:1 bypass) plume in the y-direction for different propagation heights and as a function of engine setting for a laser beam propagating 0.5 metres from the nozzle at 90°.

3.3.4 Differences between turbojet (zero bypass) and turbofan (1:1 bypass)

The turbofan plume (Figure 3.10) has a slightly lower peak at the idle condition than the turbojet plume (Figure 3.6) but has higher values at the 20 and 24 cm positions above the axis at maximum engine RPM.

Data were supplied by Cox [136] from the engine operators for typical plume temperature profiles for the turbojet engine. The temperature profile for the turbojet is plotted in Figure 3.11. From Figure 3.11 it is clear that for the 0.5 m location there is a jet core, while at 1.0 m the mixing zone has reached the centre of the plume. It was stated by Cox [136] that the corresponding profile for a turbofan is similar except that the core is smaller at 0.5 metres. It is assessed that the differences between the turbojet and turbofan (1:1 bypass ratio) engine conditions are insignificant apart from at 0.5 m from the nozzle.

For the turbofan configuration, the decreased beam movement at 0.5 m from the nozzle is due to the mixing of the cooler surrounding air with the jet. The decreased refractive indices produce decreased beam movement. In the turbojet, the decrease in beam movement at the 20 and 24 cm positions above the jet centre is also due to decreased refractive indice gradients. In this case, the beam is propagating through a region where the surrounding air has not been sufficiently mixed with the hot core temperatures.

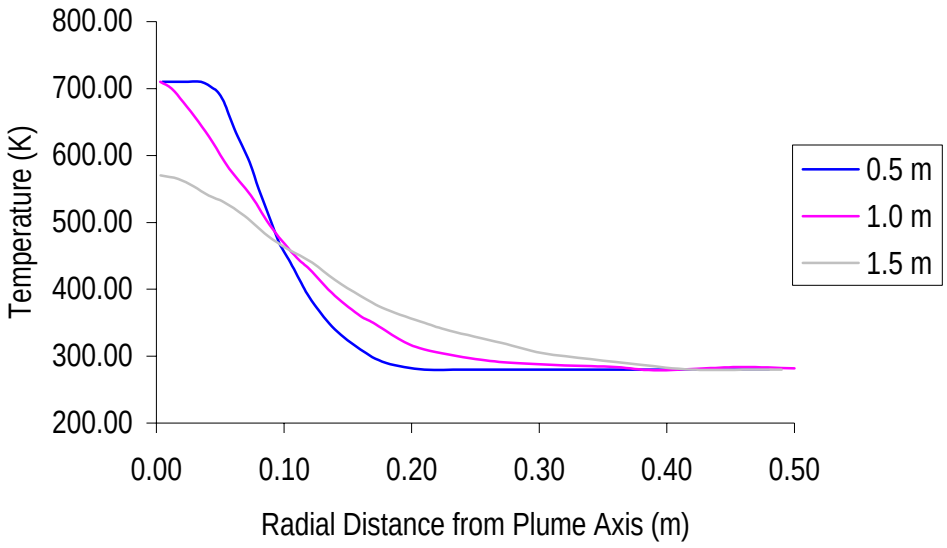

Figure 3.11: A typical plume temperature profile as a function of distance from the nozzle where the turbojet is at maximum continuous engine setting [136].

3.3.5 Turbulence Spectrum and Sampling Time

Inverting the measured centroid motion as a function of integration time gives an (crude) indication of the frequency spectrum of the exhaust. The results are plotted in Figure 3.12.

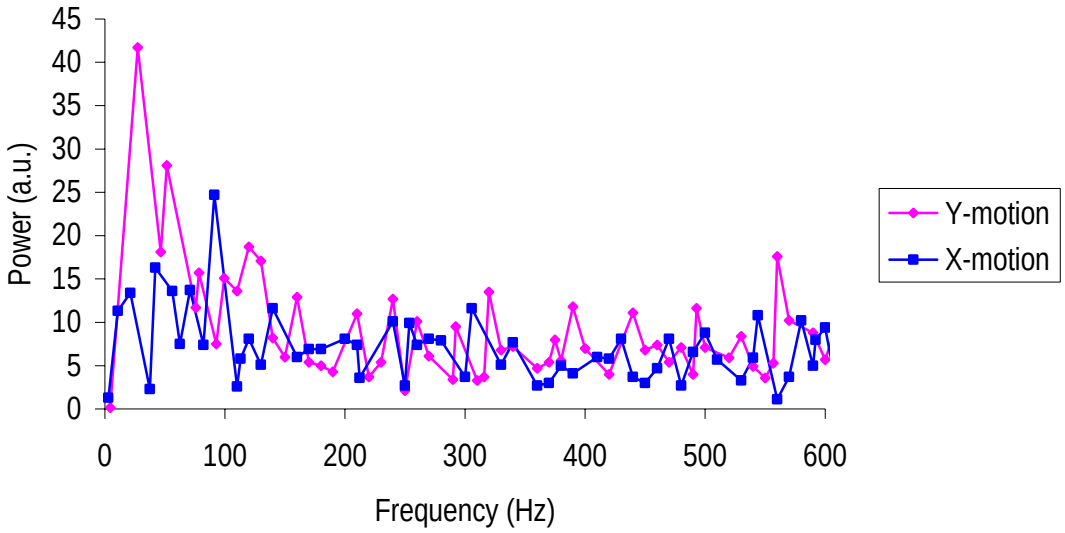

Figure 3.12: Low frequency measurements of turbulence spectrum.

Figure 3.12 shows the power spectrum of the centroid motion for frequency up to 600 Hz. The x-direction is along the plume axis and the y-direction at right-angle to the plume axis. In the x-direction the power spectrum is quite flat, with a single 'spike' at about 88 Hz (which may be aliased from a frequency above 600 Hz). In contrast, the y-direction power falls steeply up to about 150 Hz. It is then flat out to the highest frequency measured. This implies that there is a higher likelihood of beam movement due to larger and slower structures moving vertically within the flow.

In Figure 3.13 and Figure 3.14 the effect of varying the integration times on the measured standard deviations for two engine settings, idle and 20,000 RPM, is plotted. In both cases, a function of $\sqrt{1/t}$ (where *t* is the integration time) has been fitted to the x-direction curve, showing that below about 100 - 150 μs the effects of the plume on successive laser pulses are correlated. This is about a factor of five to seven longer than the time taken for a parcel of gas to cross the laser beam. The variation of

centroid motion with integration time is slower than $\sqrt{1/t}$ showing that there is some degree of correlation for times longer than 150 μs. The corresponding measurements at an engine speed of 20,000 RPM show a similar dependence on integration time, but with indications that the break occurs at a lower integration time, as would be expected for a faster-moving jet plume.

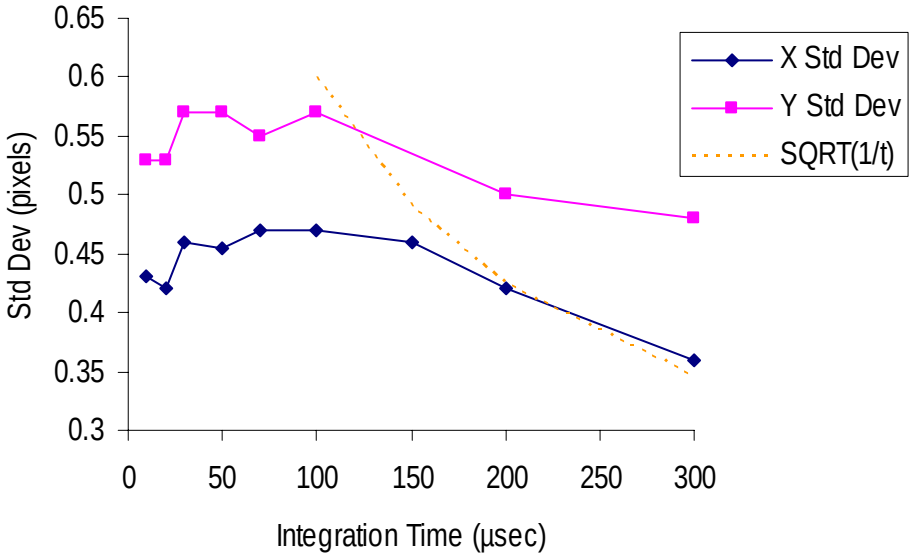

Figure 3.13: Measured centroid motion for different integration times at engine idle setting.

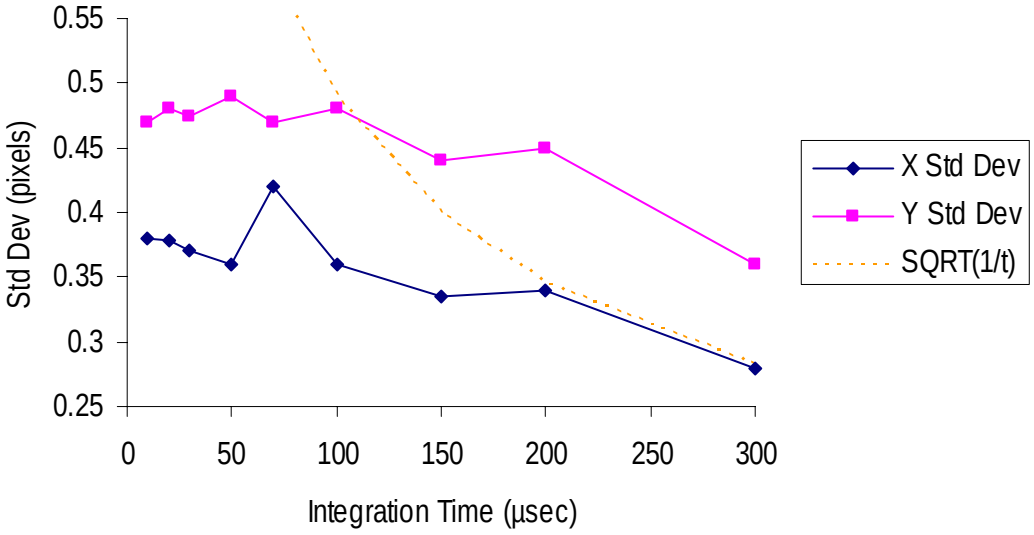

Figure 3.14: Measured centroid motion for different integration times at engine 20,000 RPM setting.

It can also be concluded that there is no need to use very short integration times on the camera for these measurements. The results of the measurements indicate that there is no significant variation for timescales shorter than 50-100 μs, depending on the laser beam diameter. The laser can still be run at high repetition rate, to give multiple pulses within the integration time.

3.3.6 Near and Far Field Measurements

The far-field measurements clearly demonstrate the severity of the refractive index variations caused by the jet, as illustrated by the two mosaics in Figure 3.15 and Figure 3.16. Both mosaics show the first six laser pulses captured by the camera looking at the target board at 154 metres from the plume. The picture with the jet off (Figure 3.15), whilst showing a degree of speckle, shows very little variation in the beam structure from pulse to pulse. The largest structures appear to be about the same size as the aperture in the centre of the plate. The arrow in the bottom right-hand corner image of Figure 3.16 points to the aperture in the centre of the target board. This is 25 mm in diameter and can be used to assess the scale of the beam structure.

In contrast to the jet-off setting, the picture (Figure 3.16) with the jet at its maximum continuous setting shows structure on a rather coarser scale, and this structure changes significantly from pulse to pulse. The structure is around 100 mm in size (21 pixels) at the target board.

The near-field measurements are not plotted here and compared to the far-field measurements; this is for two reasons. Firstly, the laser used has a non-Gaussian beam profile. At a range of 8 metres from the transmitter (the position of the target board inside the building), it has not developed its far-field characteristic fully and could be mistaken for a Gaussian (TEM_{00}) profile apart from its non-circular shape. At a range of 160 metres from the laser (Figure 3.15) it is clearly not in a TEM_{00} mode. The beam profile shows a similarity to a TEM_{01} mode but the two lobes (above and to the right of the centre of the target board, and below and to the left of the centre) are unequal in intensity. This makes comparing the effects of the plume in the near and far-field cases more difficult, because it cannot be assumed that the measurements of centroid motion in the x and y-axes in the near-field and far-field correspond as the beam shapes are different.

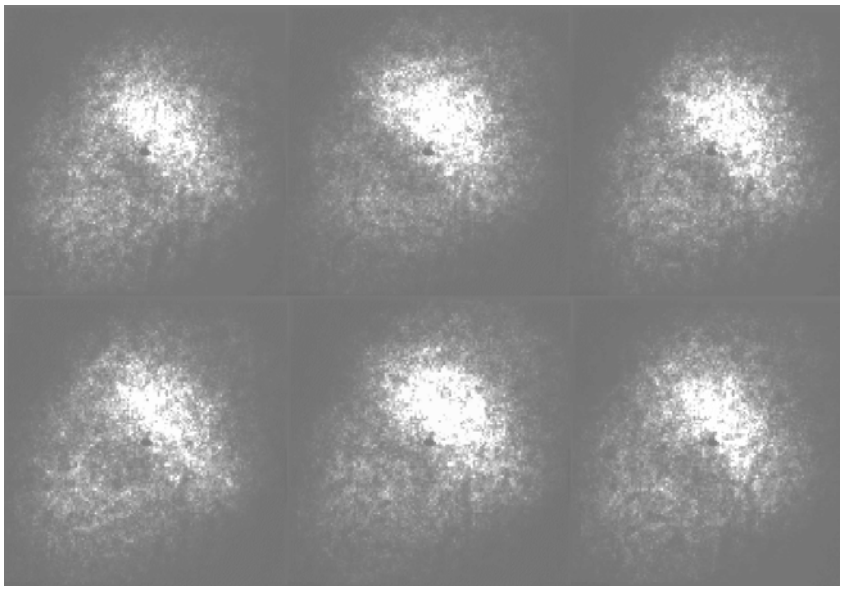

Figure 3.15: Six consecutive laser pulses recorded with the jet off.

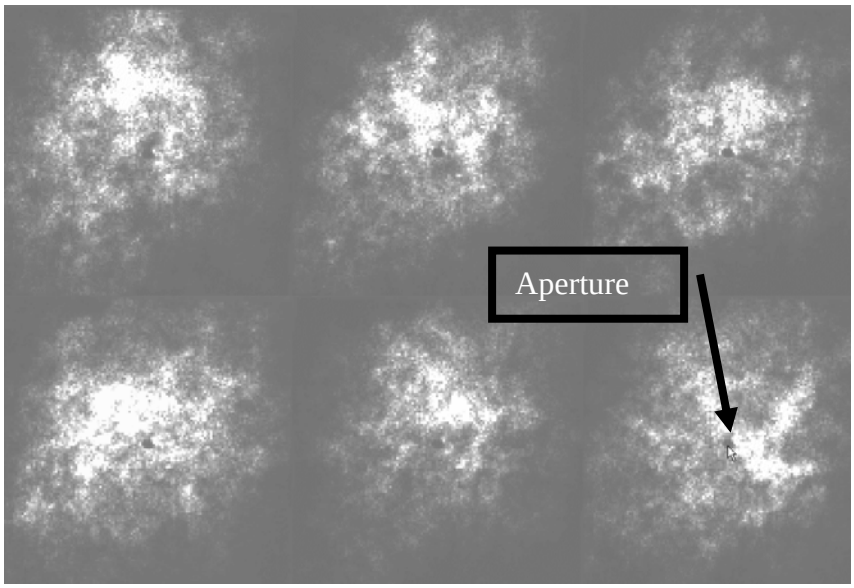

Figure 3.16: Six consecutive laser pulses recorded with the jet at maximum RPM.

Secondly, because of the building and measurement infra-structure the same intersection angle between the laser beam and the plume could not be obtained for the near and far-field measurements. This meant that centroid displacements could also not be directly compared.

3.3.7 Radiometric Measurements

The radiometer was used to sample the beam energy in the far-field. Figure 3.17 and Figure 3.18 show that the irradiance functions for the engine off and the engine at maximum continuous power have similar structure; a comparison of the probability distributions shows that both are a good fit to a Gaussian profile (Figure 3.19 and Figure 3.21). This matches the known energy distribution resulting from laser beam propagation through the atmosphere, where the irradiance function shows a log-normal distribution [138].

The camera image was also used to determine the laser irradiance distribution. Figure 3.20 and Figure 3.22 show the distribution of the logarithm of laser irradiance for the approximately 280 frames in which the laser beam was visible. The 13x13 square area was chosen as being the nearest to the area of the radiometer aperture (calculated as 177 pixels). Both the jet off condition and the jet at maximum power condition produced distributions that were less good approximations to a Gaussian distribution than the radiometer results, showing a distinct skewness.

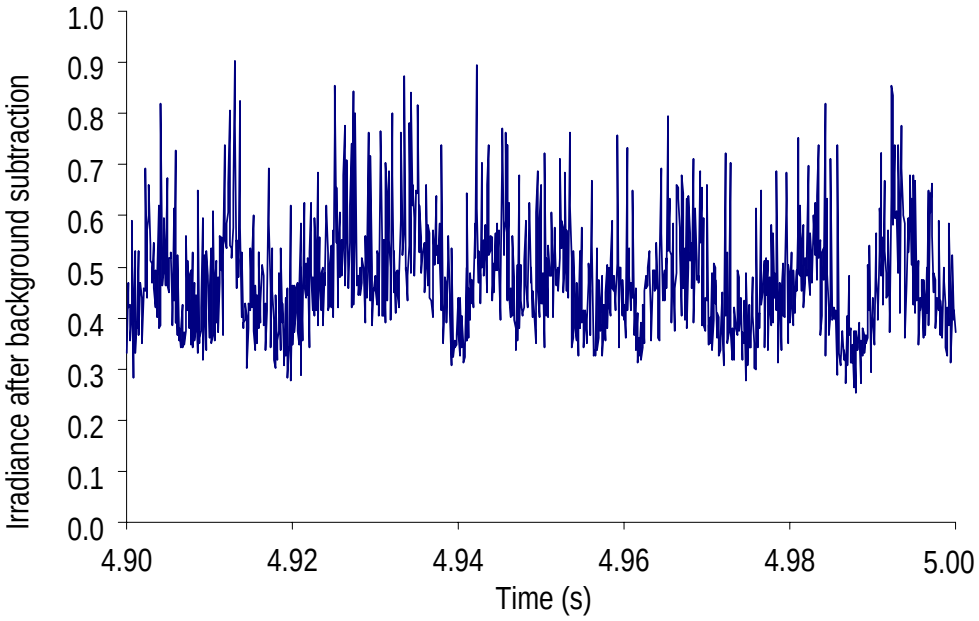

Figure 3.17: Variation in pulse-to-pulse irradiance measured by the InSb radiometer for the engine off.

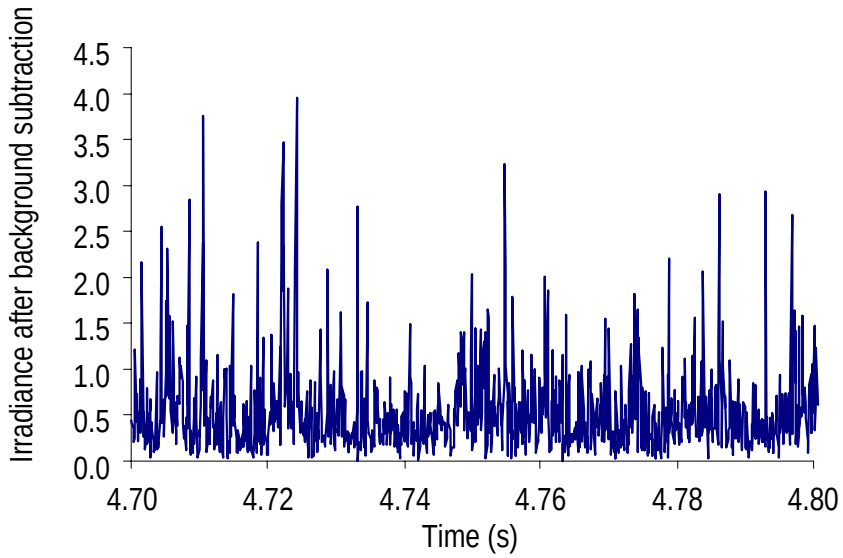

Figure 3.18: Variation in pulse-to-pulse irradiance measured by the InSb radiometer for the engine at maximum power.

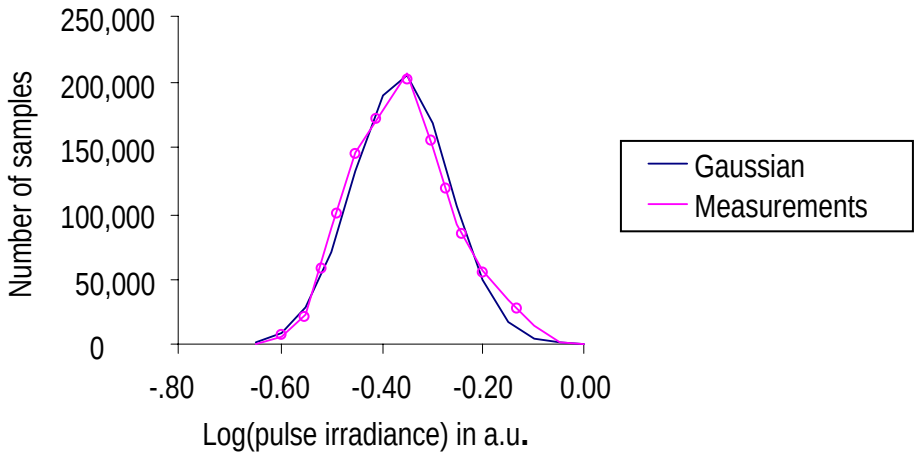

Figure 3.19: Distribution of log(pulse irradiance) for the engine off condition calculated from radiometer data.

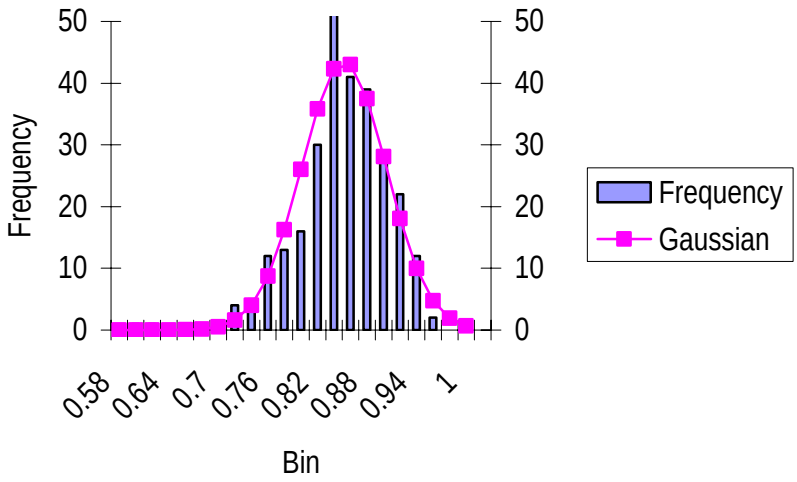

Figure 3.20: Engine off log(pulse irradiance) calculated from camera data using 13x13 pixels.

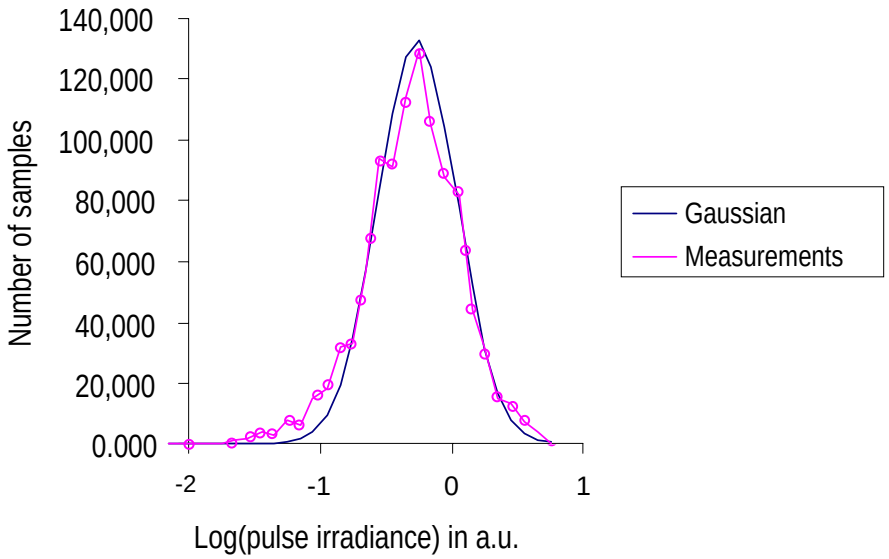

Figure 3.21: Distribution of log(pulse irradiance) for the engine at maximum power calculated from radiometer data.

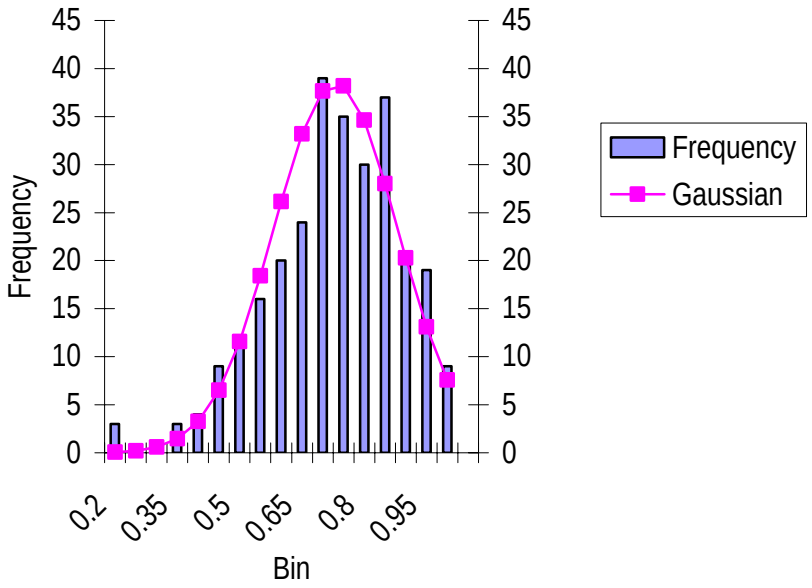

Figure 3.22: Engine maximum log(pulse irradiance) calculated from camera data using 13x13 pixels.

Notable is the super-Gaussian 'tail' on the left-hand side of Figure 3.21 suggesting there is a greater than expected probability of very low irradiances. However, the result is uncertain as the standard deviation of the baseline level is significant; being a third that of the case where the engine is running at maximum continuous RPM (refer to Table 3.2). The parameters of the Gaussian distributions in Figure 3.19 to Figure 3.22 are given in Table 3.2.

Table 3.2: Mean and standard deviation for the four Gaussian distributions.

	Radiometer		13x13 pixel area in camera	
	Mean (log)	Standard deviation (log)	Mean (log)	Standard Deviation (log)
Engine off	-0.36	0.095	0.842	0.051
Engine at maximum	-0.26	0.300	0.707	0.149

The data in Table 3.2 shows that both the radiometer and camera method give a factor of ~3 increase between the jet off and jet at maximum cases for approximately equal areas.

The reason for the approximate factor of 2 difference in the standard deviations between the radiometer and the camera is not clear. Because the distribution is log-normal, differences in gain will just shift the mean and not affect the standard deviation. The only factor that could affect the standard deviation is the different bandwidths of the two instruments. The radiometer is designed to sample up to 50 kHz, so its 3 dB bandwidth is not less than about 100 kHz. For comparison, the camera has an effective integration time of 56 μs (337 laser pulses at 10 kHz detected in 600 frames). Certainly, if the laser pulses have fine structure that is in the 10 – 100 kHz range, this will be detected by the radiometer and (as the peak radiometer values are used) contribute to its standard deviation, while the camera will almost entirely average it out.

3.4 Discussion

It is expected that the primary cause of the change in refractive index, which changes the centroid of the energy of the laser beam, is the temperature of the gas because the refractive index of the gas varies approximately inversely with its absolute temperature. The change in mean centroid position would then be dependent on the difference between the refractive index at the core temperature and that at ambient temperature as the plume acts like a weak cylindrical lens, whilst the degree of centroid motion would also depend on the length of the laser path through the mixing zone.

The turbulent mixing needs to be also considered as it affects the refractive indices within the plume. The energy required to drive the turbulent mixing comes from the difference in the flow velocities between the jet and the ambient air. For the turbofan case, the core jet plume is encased in a slower-moving (relatively) cool plume of air from the compressor so there are two mixing zones: the hot and cool plumes and the cool plume to the ambient air. The cool plume has a temperature 10ºC above ambient at idle and 68ºC above ambient at maximum power, and it will have a different refractive index to the ambient air (refer to Figure 3.23).

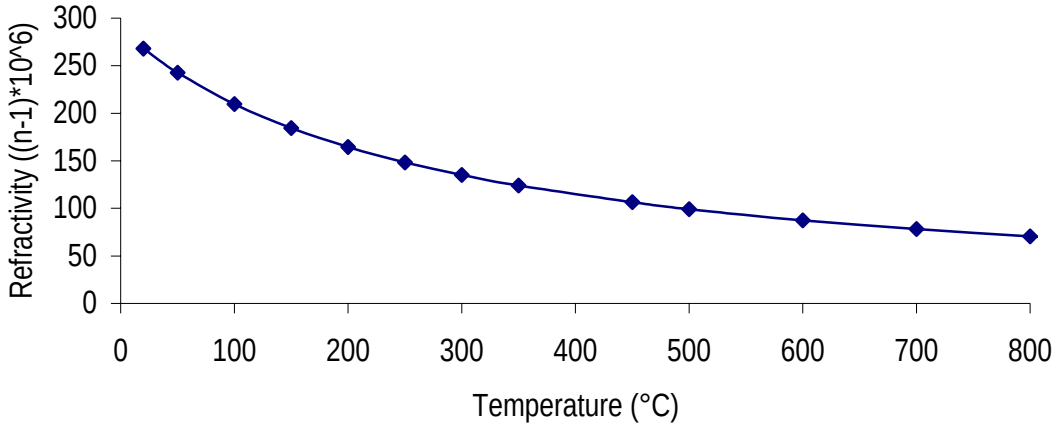

Figure 3.23: Calculated refractivity of dry air as a function of temperature at 4.67 µm.

The other factor affecting the plume refractive index is that the concentrations of both CO_2 and H_2O are dependent on engine-setting. The maximum temperature that the gas reaches will depend on the ratio of fuel to air. The mixture is always lean, having an equivalence ratio < 1.0. A typical level of CO_2 in the plume core is 3% by volume at idle; this may reach 5% at the maximum engine setting [136]. In Figure 3.24 the effect of 3% CO_2 at 0ºC on the refractive index is plotted. At a higher temperature the effect will be proportionately less. Comparing this with Figure 3.23 it is clear that the impact of CO_2 concentration on the refractive index is much smaller than the effect of temperature.

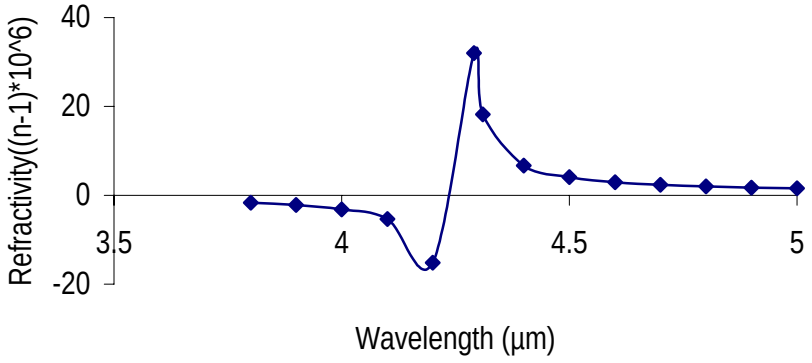

Figure 3.24: Refractivity of dry air with 3% CO_2 at STP near the 4.3 µm absorption band.

3.4.1 Refractive Index Structure Size in the Plume

Measurements of centroid motion as a function of frequency show that at 'audio' frequencies (up to 1 kHz) the level of centroid motion in the direction along the plume (x) is fairly flat, whilst in the cross-plume direction (y) it falls steeply from low frequencies until it reaches a plateau at about the same level as the x-direction motion. Measurements using different integration times (and therefore different numbers of laser pulses in the integration 'window') indicate that the centroid motion is approximately constant up to about 100 – 150 microseconds integration time (*t*) and then falls off proportional to $t^{0.5}$. This is consistent with the positions of the laser centroids being correlated up to periods of about 100 - 150 microseconds and uncorrelated for longer periods. As the laser beam is approximately 20 mm wide ($1/e^2$ points) at the plume axis; 150 microseconds at the engine idle setting corresponds to about 2 beam widths, so it is difficult to measure much shorter correlation times.

The far-field measurements also give an insight into the size structures of refractive index in the plume. Because the intensity distribution in the far-field is the Fourier transform of the refractive index structure in the plume, small-scale effects in the plume produce large-scale changes in the far-field. The images of the laser beam with the engine setting at maximum show little variation on scales larger than about 100 - 150 mm, significantly smaller than the 600 mm size of the beam at 150 metres range. This suggests that there is little effect from structures smaller than 5 - 7 mm, even though the inner scale is calculated to be of the order of a few hundred μm.

A beam that is less than the size of a turbulence cell will be deviated by the cell but will not break up; a beam that is much larger than a turbulence cell will break up, but its deviation will be reduced.

Measurements of intensity in the far-field, using both a radiometer and an IR camera, show that the distribution is close to a log Gaussian for both jet off and jet maximum conditions. This is predicted for atmospheric turbulence when the Rytov approximation is valid (the scintillation is not saturated). This suggests that the effect of the plume can be treated as a single phase plate. This suggests the phase changes, caused by the refractive index structure of the plume, may be less than or of the order of one wavelength. Alternatively, if the phase changes are greater, this could be because the distance

over which the plume modifies the phase of the laser beam is so short that it does not significantly modify the spatial intensity distribution of the laser beam while the laser beam is still within the plume.

3.5 Closing Remarks

The results for one wavelength only, 4.67 µm, provided data that could be analysed for the jet engine study. The study showed the standard deviation of the beam movement in a single direction (x or y) at the 4.67 µm wavelength to be in the order of 100 to 200 microradians for the engine conditions and propagation paths tested.

One of the more interesting results was seen when propagating the laser beam at 0.5 m from the nozzle. A dip in the centroid motion was noted as the engine power was increased from idle to maximum power. This was unexpected because at the engine setting at which the dip occurred there was not a corresponding change in either the nozzle exit temperature or the thrust.

A laboratory study where parameters are controlled and the conditions of the flow is better characterised will give a greater insight into the significance of the flow and laser characteristics that affect beam propagation through hot turbulent gases such as those found in the jet engine exhaust. The experimental details of a laboratory study are outlined in the Chapter 4.

Chapter 4

Simple Jet Parametric Study

4.1 Introduction

Systems level studies, including that outlined in Chapter 3, have been conducted to quantify the effect of a jet engine's exhaust gases on laser beam propagation, dispersion and divergence, for various conditions. In order to better predict the degree of divergence and dispersion of the laser beam, an understanding of the exhaust gas structure and its influence is required. Specifically, it is beneficial to understand the effect of each parameter separately; such as temperature, carbon dioxide concentration, turbulence intensity and length scales as well as the laser beam wavelength and beam diameter. A study of laser beam propagation through a well characterised environment provides new insight and much needed data in this field.

Chapter 4 outlines the experimental set-up and methodology for a parametric study under laboratory controlled conditions that was undertaken to examine the individual effects of various laser and flow parameters on laser beam propagation. The characterisation of the flow field encountered by the laser beam for the experimental conditions is also documented.

4.2 Parametric Study Objectives

The objective of the experiments was to understand the effects of a number of parameters associated with the laser and the propagation path. Key parameters include:

- Turbulence intensity
- Turbulence length scales
- Gas composition (eg: CO_2 or H_2O)
- Temperature of the gas
- Laser beam diameter
- Laser beam wavelength

The experiments were conducted in such a way to isolate the effect of a number of these parameters on the angular divergence, beam wander and beam break-up of various laser beams.

4.3 Experimental Apparatus and Setup

The apparatus used to produce hot turbulent flow is depicted in Figure 4.1. The apparatus consisted of a 290 mm long steel tube with an internal nozzle cross section of 21 mm x 21 mm. Compressed air, CO_2 and H_2 were used in the experiment and were introduced at the bottom of the tube. The gases were controlled by pressure regulators, with the flow condition monitored using flow meters, and were pre-mixed before entering the nozzle. Velocity uniformity of the flow at the nozzle was confirmed using a pitot-static tube and visually by burning a methane-air fuel mixture.

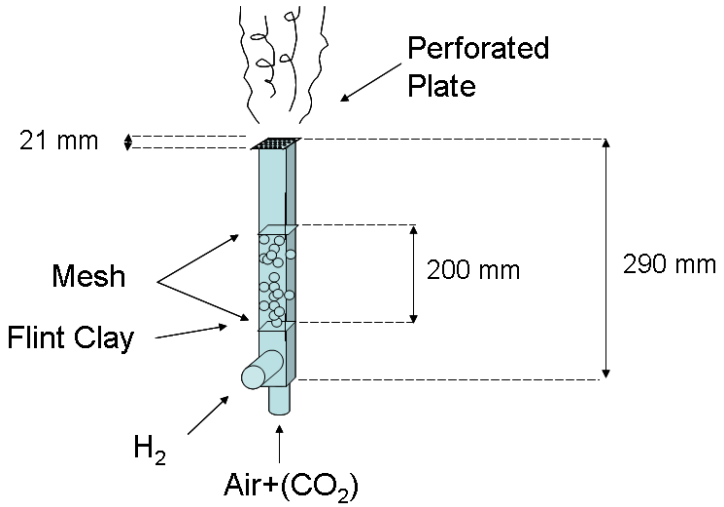

Figure 4.1: Schematic of apparatus used to produce the high temperature turbulent flow.

To produce the high temperature turbulent flow a lean mix of hydrogen and air was combusted. The reacting mixture of hydrogen and air generated temperatures up to 1500°C at the nozzle exit. The nozzle dimension was chosen to allow a tube Reynolds number above 10,000 to be obtained considering the constraints of the laboratory air supply and the high temperatures required. The apparatus was packed with fine flint clay particles to prevent the hydrogen mixture from flashing back down the tube. The particles were irregularly sized. They were all ~1 mm thick and were no more than 5 mm across at the longest diameter.

Maintaining the reacting flow at temperatures below 400°C was problematic. Consequently, lower temperatures were achieved with a non-reacting flow, using an on-line electric heater to regulate the temperature of the compressed air from ambient to 320°C.

Perforated plates of various diameter holes and blockage ratios were used throughout the experiment to condition the flow at the nozzle exit. These perforated plates were chosen to allow the effect of turbulent intensity and turbulent cell size (or length scale) on the propagating beam to be studied. Varying the hole diameters and blockage ratios of the plates altered the turbulence intensity and turbulence eddy scales. The various plate sizes that were available for use are shown in Table 4.1.

Table 4.1: Perforated plate specifications.

Plate Number	Hole Diameter (mm)	Dist between holes (mm)	Thickness (mm)	Open Area (%)	Blockage Ratio
1	3	1	1	50	50
2	6	2.5	1	45	55
3	8	3	1	47	53
4	5	1	1	63	37
5	5	2	1.5	45	55
6	5	3	1	35	65

Three perforated plates were also used with almost the same blockage ratio but with varied diameter holes to allow the turbulence intensity to remain constant while the turbulence cell distribution was changed. The plates used were plate numbers 1, 2 and 3 (shaded green in Table 4.1).

Three perforated plates were used with the same diameter holes but varied blockage ratios to maintain the turbulence cell size distribution while changing the turbulence intensity. The plates used were plate numbers 4, 5 and 6 (shaded orange in Table 4.1).

Figure 4.2 depicts the optical set-up of the experiment. Two collimated laser beams were introduced at 85 mm above the nozzle exit. That distance guaranteed a coherent flow structure for all perforated plates. The 4.67 μm laser beam was generated using a CO_2 doubled gas laser pulsed at 10 kHz. The 632.8 nm laser beam was generated using a HeNe (Continuous Wave) CW laser. The visible, 632.8 nm, laser beam was expanded 10 times to produce a collimated beam of 8 mm diameter to closely match the diameter of the infrared laser beam. The beam diameters were then controlled using an adjustable iris placed 450 mm from the burner. The beams were passed through the flow and were steered with mirrors to obtain sufficient path length and hence displacement, before striking a screen at 16 meters from the burner.

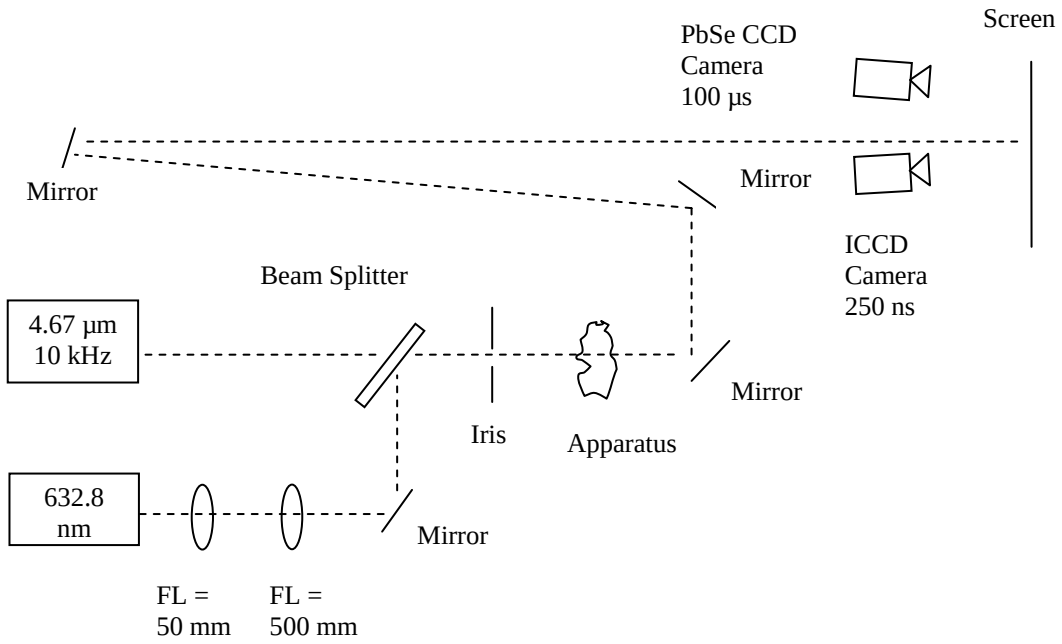

Figure 4.2: Sketch of optical setup.

Two cameras were used to monitor the beams' displacements. To image the visible spot an intensified CCD camera, Princeton Instruments ICCD-576-R-1, was used. A collection array of 166 by 111 pixels or

266 by 111 pixels was used with a rate of 10 frames-per-second (fps). The integration time was set at 250 nanoseconds, effectively setting the pulse length at 250 nanoseconds and ensuring “frozen” flow.

A PbSe FPA camera, the Radiance HS, was used to image the infrared laser spot. The array size was 256 by 256 pixels with a frame rate of 50 fps. The integration time was set at 100 microseconds while the laser was pulsed at 10 kHz to ensure only one laser pulse per integration period. The laser pulse length was 15 ns.

A PC was used to collect images and the data capture was triggered off the lasers which were not synchronised.

4.4 Methodology

The Reynolds number, based on hydraulic diameter, was kept constant at 10,000 for all cases, with flow rates adjusted to account for increased viscosity with increased temperature.

Temperatures in the flow were recorded by logging the reading from the thermocouple. The thermocouple was placed at the height of the laser beam and positioned in the middle of the flow to record the temperature before a run. At the end of the data collection the probe was re-positioned and confirmed to be in position by reading the same initially recorded temperature. A K-type thermocouple was used to measure the electrically heated air and an N-Type for the higher temperature combusted cases. Thermocouples and meters were accurate to better than 2%.

Carbon dioxide was added to the flow to simulate the exhaust from the back of a jet engine.

Turbulence intensity and length scales were varied using a set of perforated plates.

A summary of the experimental runs and the different parameters is listed in Table 4.2.

Table 4.2: List of experimental runs and their parameters.

Beam Diameter (mm)	Carbon Dioxide Volume (%)	Perforated Plate Hole Diameter (mm)	Perforated Plate Blockage Ratio (%)	Beam Crossing Height Above Nozzle (mm)	Temperature at Crossing Height (°C)*
3	0 to 10	N/A	N/A	85	320
3,6,8	0	5	37	85	500
3,6,8	0	5	55	85	500
3,6,8	0	5	65	85	500
3,6,8	0	3	50	85	500
3,6,8	0	6	55	85	500
3,6,8	0	8	53	85	500
3	0	N/A	N/A	85	50 to 1200
3	0	8	53	40 to 200	300
3	0	8	53	40 to 240	760 to 240
2,3,4,5,6,8	0	N/A	N/A	85	700
2,3,4,5,6,8	0	5	55	85	700
2,3,4,5,6,8	0	5	37	85	280

*All temperatures below 320°C achieved using an on-line electric heater. Other temperatures achieved by a reacting H_2/air mixture at different equivalence ratios.

4.4.1 Beam Spot Samples

The cameras were configured, using position and optics, to record an image of the moving laser spot that covered as much of the pixel space as possible in order to achieve the best spatial resolution. The spatial resolution is resolved to better than 2% of the variance of the centroid displacement for both the 4.67 μm and 632.8 nm experiments at the standard operating temperature of 700°C. Examples of the recorded images are shown in Figure 4.3 and Figure 4.4. More images are recorded in Appendix G.

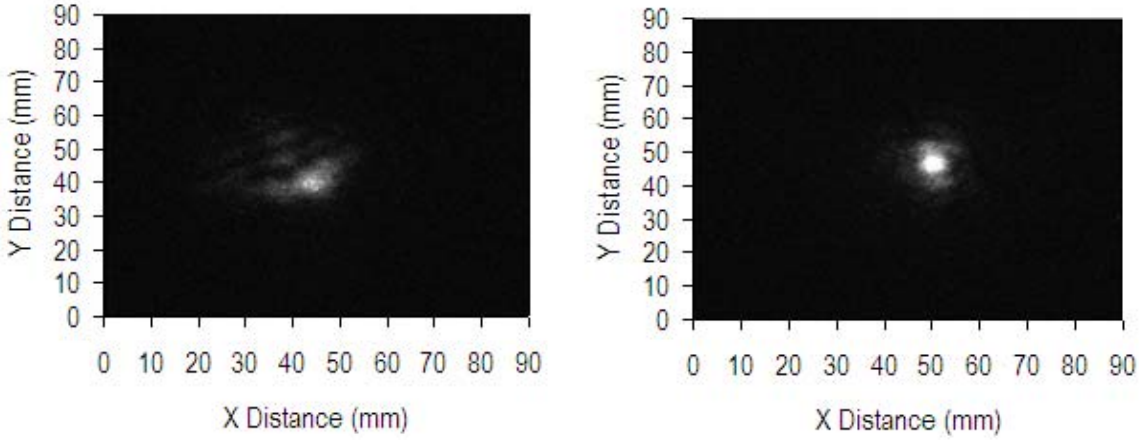

Figure 4.3: Two consecutive images of the 632.8 nm beam after propagating through a 3 mm iris and a turbulent zone at 800°C.

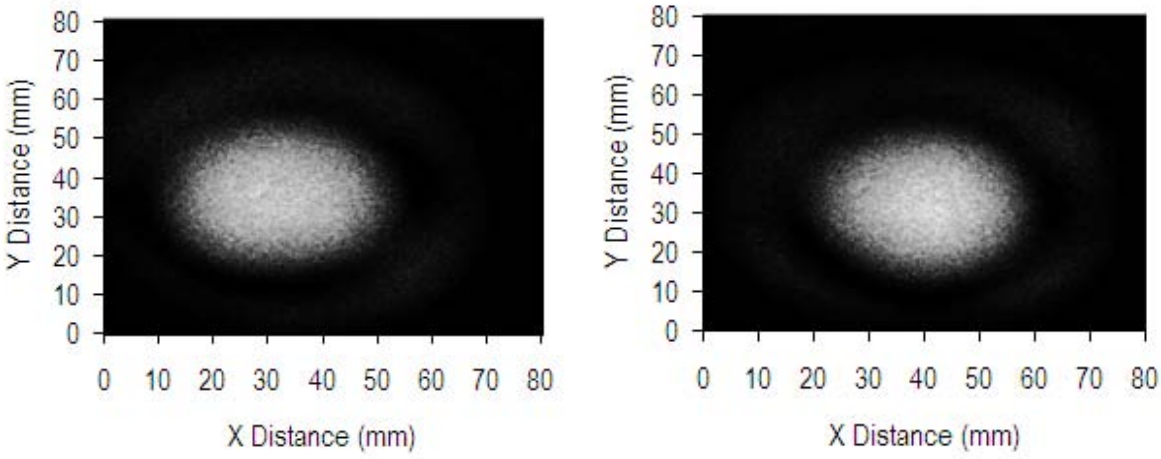

Figure 4.4: Two consecutive images of the 4.67 µm beam after propagating through a 3 mm iris and a turbulent zone at 800°C.

The images were both captured with a 12 bit resolution and saved to a hard disk. In all experimental conditions the worse case signal-to-noise ratio (SNR) was 50, calculated as signal rms divided by dark-cell noise rms. The images were processed by first performing pixel-to-pixel averaging across frames in a background file (a sequence of frames where the laser beam was blocked). The averaged background file was subtracted, per pixel, frame by frame from the laser image sequence. The remaining noise floor was further reduced by zeroing all pixel values less than $1/e^2$ times the value of the maximum pixel in the frame. Figure 4.5 shows a raw image of the infrared beam spot and the image after processing, or "correction".

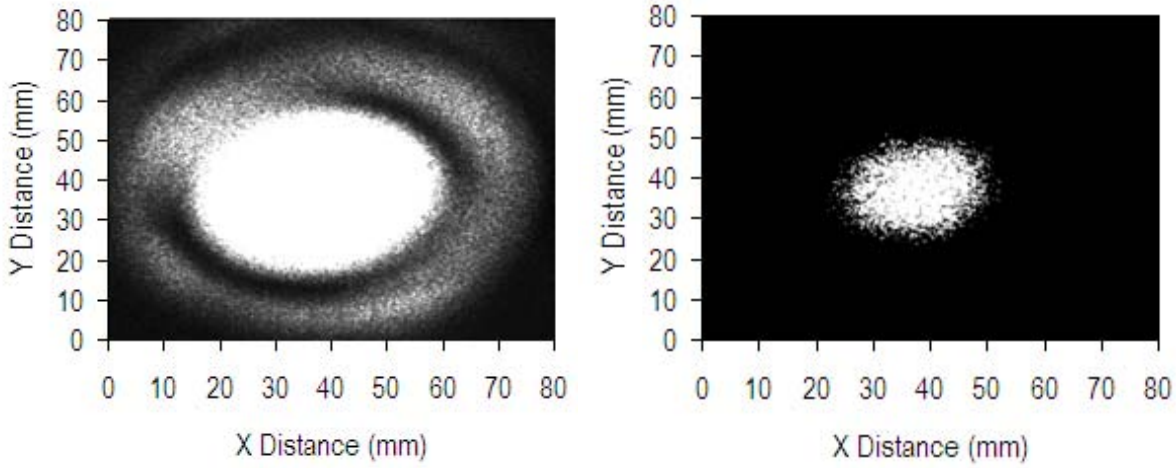

Figure 4.5: The left hand image depicts the raw image of the 4.67 µm beam captured after propagating through a 800°C flow. The right hand image is a corrected version of the left hand image; background subtraction and the $1/e^2$ threshold has been applied.

It is significant to note that Miller and Friedman [139] reported that the location of a blur spot on a focal plane can be determined to an accuracy that equals the optical resolution divided by approximately the signal-to-noise ratio (SNR) up to a SNR of around 100 and greater than 5. In our case the centroid position can be reported to a sub-pixel resolution equivalent to around one pixel divided by the SNR, or 0.02 of a pixel.

Increasing the number of samples can increase the statistical confidence of the measurement when reporting the centroid angular movement produced by the turbulent hot gases. The number of samples needed to obtain statistically independent measurements was tested experimentally. The graph in Figure 4.6 shows that the standard deviation does not converge to a constant for less than 1000 samples. Consequently, the number of frames sampled was set at 2000.

In order to place confidence intervals on the data, the beam realizations were treated as a random variable following a normal distribution by application of the central limit theorem. To within a 95% confidence interval, the single sided error, when reporting the centroid position was evaluated using, $E = \sqrt{\frac{(1.96)^2 \sigma^2}{n}}$, where n is the number of frames and σ^2 the sample variance. The 4.67 µm beam had a variance that ranged from 65 to 205 microradians whilst the 632.8 nm beam had a measured

variance from between 68 to 220 microradians. The error bounds on the centroid position for n = 2000 was then determined to be better than ±10 microradians for all runs.

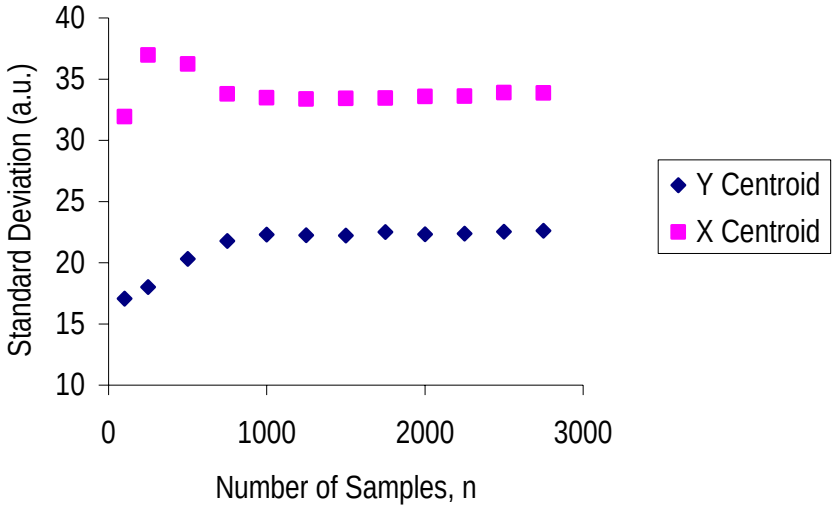

Figure 4.6: Typical file showing standard deviation of centroid position as a function of the number of samples.

Inherent long-term drift of the centroid position made the comparison of parameter change effects using a centroid position metric difficult. Instead, the second-moment of beam displacement, the variance, was used to quantify parametric change effects.

Discussed further in Appendix D, the lower, $L_1 = (n-1)S^2 / \chi^2_{\alpha/2}$, and upper, $L_2 = (n-1)S^2 / \chi^2_{1-\alpha/2}$, bounds for a chi-squared distribution having *n* = ~2000 degrees of freedom shows that the variance can be reported with a confidence of better than 95% within these bounds. That is for a sample size of 2000, the variance can be reported with 95% confidence to within 5% of its measured value.

In order to determine whether a parameter change produced a significant change in the variance of the beam displacement the statistical variance test, known as the F-test [140], was considered as a guide. The sample size of 2000 frames in each run provided a fixed value of F critical at 1.075 that enables a 95% confidence statement in declaring runs significantly different. The larger ratio of the variance of two runs must exceed the F critical value for the effect of the parameter change to be declared significant. That is, approximately a 7.5% change in variance between runs.

4.4.2 Temperature and Water

To achieve temperatures greater than 400°C a reacting flow was used. The equivalence ratio of combusting lean mixture of H_2 and air was adjusted to allow the temperature to be regulated from 400°C to 1200°C.

The combustion of hydrogen and air resulted in water, oxygen and nitrogen as products. The addition of water was a factor that needed to be taken into account when considering the laser beam propagation. The program Gaseq [141] was used to determine the amount of water generated as a by-product of the combustion and to determine the mean equilibrium temperature of a given air-hydrogen mixture. These calculations assume the H_2/air mixture has reacted to an equilibrium condition. Table 4.3 shows the volume fraction of water produced at various temperatures. Note that the air from the air-compressor passes through a water trap and is assumed to be "dry air". Under our normal laboratory conditions (25ºC, 30% humidity) the air contains ~1% volume fraction of H_2O in the air.

Table 4.3: Showing volume fraction of water present in the flow at various temperatures for an equivalence ratio less than 1.

Temperature (°C)	Dry Air Volume Fraction (%)	H_2O Volume Fraction (%)
100	100	<1
200	100	<1
300	100	<1
500	95.4	4.6
700	91.2	8.8
900	88.4	11.6
1200	84.3	15.7

The displacement of the laser beam, after having interacted with the hot gases, is mainly due to the change in the local refractive index. There are two main factors that may change the refractive index; the local gas temperature and molecular absorption. These two effects are wavelength dependent.

Knowing the gas mixture allowed a theoretical calculation of the refractive index to be determined. This was done using equations recommended by Ciddor [43, 142, 143]. The calculated refractive index difference between the surrounding ambient air and the turbulent flow is plotted in Figure 4.7.

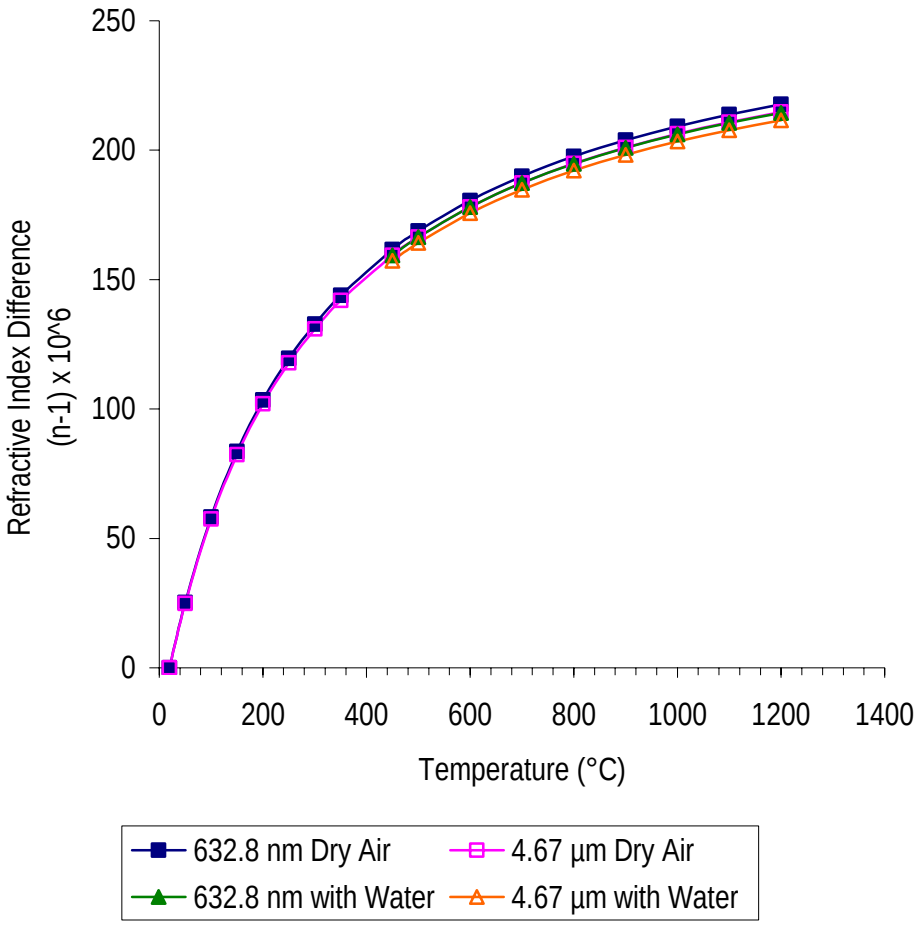

Figure 4.7: Calculated refractive index gradient at 632.8 nm and 4.67 µm over a range of temperatures and for the experimental conditions at the higher temperatures.

The refractive index difference between the two wavelengths is less than 2% with the 4.67 µm beam refracted slightly less than the 632.8 nm. The inclusion of water into the dry air also produces less than 5% decrease in the refractive index. The plots show that the effect of wavelength and water inclusion can be expected to be minor compared to the influence of temperature.

4.4.3 Carbon Dioxide

Carbon dioxide levels in the flow could be altered by introducing carbon dioxide with the air at the inlet port. The volume of air was reduced as the carbon dioxide volume was increased, in order to maintain a constant Reynolds number. Calculations found the change in viscosity as air is replaced by carbon dioxide is only a minor consideration. In the experiment the carbon dioxide levels were adjusted, replacing the air mixture with the addition of up to 10% (by volume) of carbon dioxide.

4.4.4 Turbulent Intensity and Eddy Size

Laser beam displacement is related to turbulence scales. In the atmosphere the time-scales are long and the eddy scales are large compared to the gases emitted from a jet engine. In the plume of an engine the temperature variability is great as the shear layer of the plume mixes the high temperature exhaust gases with the surrounding air. The result is high turbulence intensity and the generation of eddy scales, or length scales, smaller than those found in the normal atmosphere.

Consider a laser beam propagating through a turbulent gaseous flow. A large eddy, greater than the beam diameter, might be expected to steer, by application of Snell's law, the entire beam front uniformly. A smaller eddy could result in the beam front splitting. The beam would be seen as bright and dim patches of light on a target board as the beam was broken-up to produce regions of destructive and constructive phase interference.

Previous work at high temperatures [108, 132, 144-146] has been performed with limited control over the beam influencing parameters. Often only the net effect of a combination of parameters on the beam displacement is observed. The experimental-setup employed in this work allowed the scale size and turbulence intensity to be controlled. This allowed the effects of beam size, eddy-scale and turbulence intensity to be tested at high temperatures in a controlled manner.

One means of controlling the turbulence is by using a perforated plate attached to the nozzle outlet. Gas flow passing through a perforated plate is broken-up by the holes to produce wakes that merge together and then continue to become nearly homogenous and isotropic. The region in which this occurs is called

the power-law region [76]. The turbulence scales within the resulting flow can be controlled by using different hole-diameters (*D*) in the perforated plates. The turbulence length scale is generally limited to the size of the hole-diameter, though the length scale does increase with distance downstream [79].

Liu et al. [73, 75] reported on ambient temperature air passing through various perforated plate dimensions at different Reynolds numbers and distances downstream of the exit plane for wind tunnel conditions. They found that the length scale of turbulence depends on plate solidity (σ) and distance downstream (X) but is independent of Reynolds number.

The introduction of a perforated plate at the nozzle outlet also provides a means of increasing, or controlling, the turbulence intensity. The turbulence intensity was found [73] to decrease with distance down-stream from the hole diameter (X/D) following a power law relationship;

$$\left(\frac{u'}{U}\right)^2 = A\left(\frac{X}{D} - \frac{X_0}{D}\right)^{-n} \tag{4-1}$$

where A is universal or decay coefficient (~0.01 to 0.04) and the exponent, n is ~ 1 to 1.4.

Furthermore, Liu et al. [73] found the turbulence intensity to increase in an exponential fashion as the plate solidity increased. It is noted that the conditions under which the tests were performed were for a wind tunnel, with perforated plates reported to have hole diameters in the order of centimeters.

4.4.5 Path Length

To obtain path length information propagation tests were performed at different heights above the nozzle under various conditions. The expanding jet would produce a different cross section, increasing with distance from the nozzle outlet. However, other parameters such as temperature, length scale and turbulence intensity are also changing and need to be considered. Further data were obtained by maintaining the same temperature at the different propagation heights, although length scale and turbulence intensity were not necessarily fixed. To determine the impact of the path length, the flow was

characterized at these points; in terms of length scale, turbulence intensity and temperature profile. The effect of path length was then obtained by combining these flow characterization results, the beam propagation results and the knowledge gained from length scale and turbulence intensity propagation tests.

4.5 Flow Characterisation Study

To characterize the spatial and temporal eddy cell fluctuations in the flow a range of flow visualization techniques discussed in Chapter 2 were considered. Availability of equipment and conceptual ease of implementation were factors that decided that Particle Image Velocimetry (PIV) would be used to characterize the flow under the conditions of interest.

A schematic of the experimental layout is shown in Figure 4.8. The two illumination pulses at 532 nm were generated as the 2nd harmonic from two Quantel Nd:YAG lasers; one pulse per laser. Two laser heads were used as the time between pulses was too fast to enable sufficient power to be produced from the charge/discharge of the laser in the time period. The maximum pulse energy was 450 mJ and the pulse duration was 5 ns. The timing and power of the laser beam pulses was controlled by the laser switching unit and using an external delay box. The laser beams were conditioned by optics to be co-linear and to produce a 1 mm thin vertical optical sheet of light at the flow. Particle movement in the flow could then be traced in the vertical plane using the scattered light from the optical sheets.

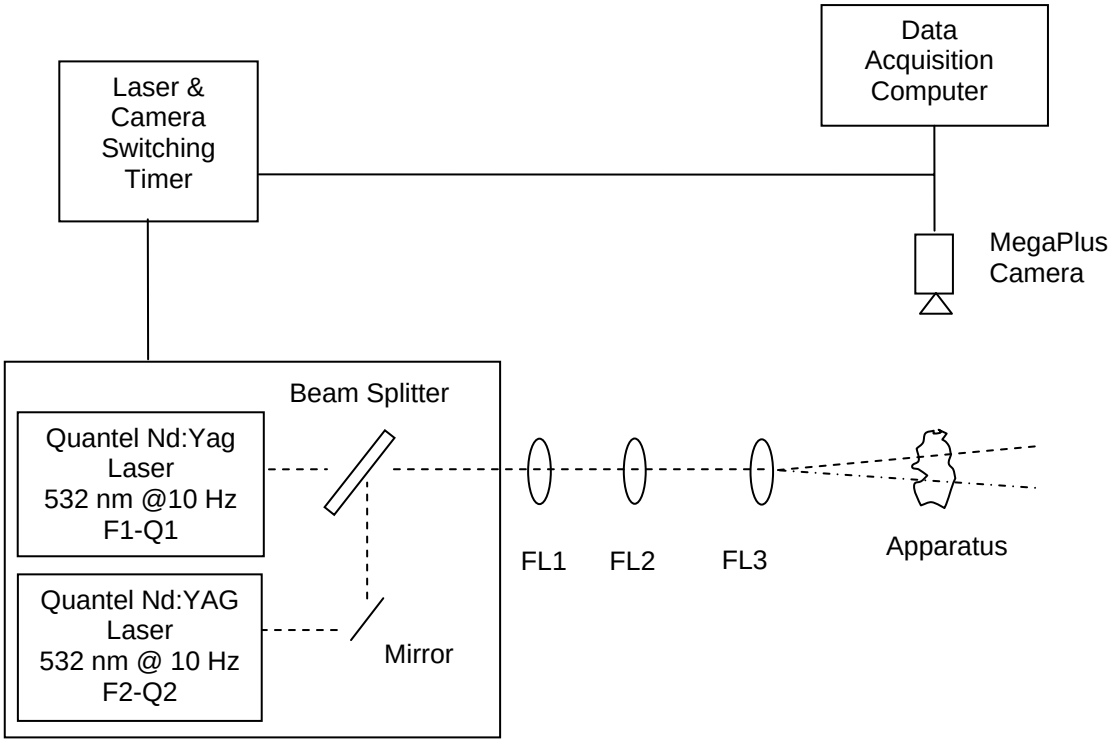

Figure 4.8: Schematic of the experimental layout used for Particle Image Velocimetry (PIV).

The flow was seeded with 0.5 micron aluminum oxide (Al_2O_3) particles that followed the flow and provided sufficient light scatter at a direction 90 degrees to the sheet. The scattered light from the two light sheets was imaged and recorded by a high speed CCD camera. Over 700 image images were collected, the limit of the acquisition memory, for each experimental configuration studied. This enabled over 350 frames of the velocity in the flow to be calculated using image pair correlations over the region recorded by the camera. The 350 frames proved sufficient to produce reliable correlations, a sample size comparable to Chen et al. [147] who found 300 PIV frames provided enough data for equivalent flows. Further post-processing of the velocity fields enabled the integral length scale to be determined and the fluctuations of the velocity to be quantified.

4.5.1 Seeding the Flow

A number of factors were considered when choosing the seeding material. The material needed to be non-corrosive, non-toxic and chemically inert at the temperatures within the flow. The particle size had to be sufficiently large to scatter enough light but not too large that they did not follow the flow [86].

Furthermore, the particle size distribution needed to be tight to avoid unwanted pixel saturation in the camera. Cost and availability was also a consideration.

Given the constraints on the seed type, Aluminum oxide (Al_2O_3) with a nominal particle size of 0.5 µm was chosen as the seed.

The introduction of the seed into the flow was achieved by using an aerosol generator, or seeder. The design was simple. The seed, in powder form, was contained on the floor of a vessel. Air was introduced to the vessel through a small diameter tube which entered the vessel at the top and continued down to almost the floor of the vessel. A number of very small (< 0.5 mm) diameter holes were placed at intervals around and along the small tube. Air entering the vessel then caused the powder to dislodge and mix in the vessel before being carried out an exit tube at the top of the vessel.

Two seeders were used in the set-up, as shown in Figure 4.9. One seeder is for seeding the core-flow while the other is for the co-flow. Co-flow was needed to enable the velocity points at the edge of the flow to be measured accurately using the cross-correlation function when processing the images pairs. The best dispersion of the co-flow seed, while maintaining low velocity, was found to be obtained by piping the seeded air into a funnel that was covered by a mesh with 5 mm diameter holes and blockage ratio 50%. A separate air supply was used for the co-flow.

The air for the primary flow could be diverted through the seeder by means of a valve. This ensured that the net volume of air was maintained for a given experimental condition.

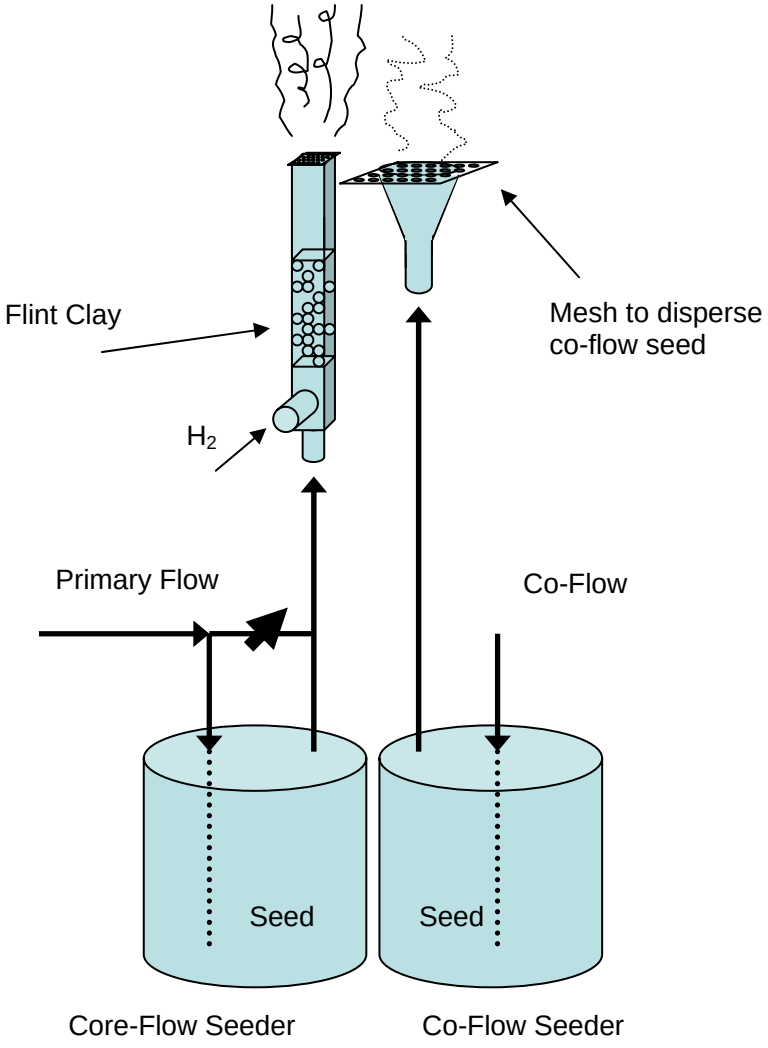

Figure 4.9: Diagram of the Seeder configuration.

4.5.2 Camera and Timing

The velocity of the flow, the number of pixels of the camera and the desired spatial resolution determined the separation time between laser pulses. The camera has a CCD array of size 1008 x 1023 pixels. Only one side of the flow was imaged as the flow was considered symmetrical about the centre-line, temperature profiling provided confirmation of flow symmetry. The field of view that was used to image one side of the flow was set to a minimum size of 30 mm by 30 mm. The minimum was determined by the extent of the sheer layer in the flow. These dimensions equated to 1 mm of the lateral displacement of the flow corresponding to roughly 35 pixels. Performing a correlation using a correlation

box window size of 32 x 32 pixels was found to be a suitable setting for these flows [85]. Note also that the correlation box window sets the minimum spatial resolution so that a window of 32 x 32 pixels therefore equated to 1 square millimetre in this instance.

The flow velocity determined the spatial movement of the Al_2O_3 particles. The scattering of each laser sheet is recorded as an image on the camera. Consecutive illuminations of the flow by two closely separated, in time, laser pulses produces two images known as an image pair. In order to achieve any true correlation between image pairs the particle movement between images must not exceed the correlation window. Better correlations are obtained when the movement is less than half a correlation window and hence 50% overlap of correlation windows were used when processing the image pairs.

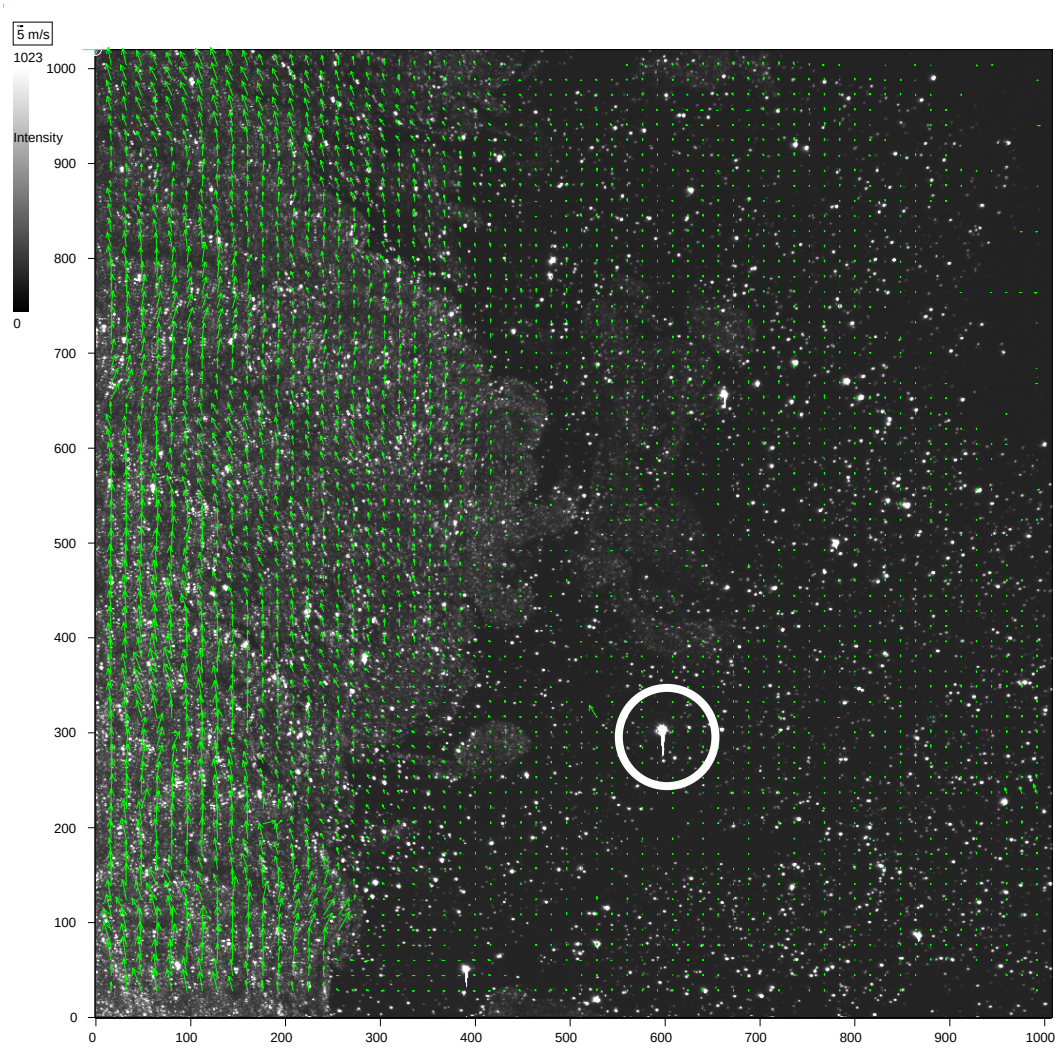

Figure 4.10: A processed image, showing some saturation (inside white ring).

For most runs the delay between the Flash and the Q-Switch activation was set at 300 μs, with the delay between pulses at 10 μs. Some pixel saturation did occur at the power level chosen but there was a trade off between removing saturation and having sufficient particles detected to allow full analysis of the flow. The saturation was possibly due to particle clumping as the saturation, when it did occur, was usually seen in the co-flow. Figure 4.10 shows an example of the saturation. The saturation, highlighted by the circled white ring, covers multiple pixels and results in energy 'bleeding' between pixels in the vertical direction. The saturation events were few and normally only occurred in the co-flow. The corrupted data normally affected less than 0.01% of the pixels and as a result they were not considered to cause any significant corruption of the data.

4.5.3 Temperature Profiling

A K-type and N-type thermo-couple, each having a diameter of 1 mm, were used to measure the temperature at points of interest in the flow. The temperature along a single line was recorded at various heights and flow conditions. These gave temperature profiles for the experimental conditions of interest. The temperature readings were made at 2 mm intervals and initially were done entirely across the flow. These results showed strong symmetry and subsequent readings were only performed from the centre line along a radial direction, to a position outside the shear layer.

4.6 Data Reduction

The temperature profile readings were manually recorded and plotted. The thermocouple data are not corrected for radiation losses as the thermocouple was shielded. The PIV analysis was more involved. Each image was recorded from the camera on to the computer in TIFF format. To produce the velocity vectors of the particles an image pair needed to be processed. The processing was done using a program called PIVview [148]. Each image pair was cross-correlated to produce a displacement vector for each correlation window position. The displacement vector was translated to a velocity vector by dividing by the pulse separation time. The correlation window was 32 x 32 pixels and stepped across the image with a 50% overlap with the previously calculated correlation. The result was an array of ~60 x 60

velocity vectors representing the 30 mm by 30 mm field-of-view captured by the camera. Over 350 image pairs were recorded and processed in this way for each experimental condition. Further post-processing was required to extract length scale and velocity fluctuation information.

4.6.1 Data Error Analysis

Broadly, the simple jet experiment involves the establishment and measurement of flow and temperature conditions, the setup up a laser beam and propagation of that beam through the flow, and the measurement of the resultant laser beam spot. There are a number of sources of error that may be attributed to each of these processes. A discussion on the error sources in these experimental processes is given in the proceeding sections. Following these sections the PIV experiment and results are further described and discussed.

4.6.1.1 Flow and Temperature

Gas mixtures and flow rates are controlled and measured using pressure regulators and tube and float type flowmeters. Inaccuracies in the flowmeters will introduce errors in the gas velocity and compositions, affecting the overall accuracy and repeatability of the flow conditions. The minimum flow error is obtained when the flowmeters are operated at full-scale. At full scale reading the flowmeters are specified to be accurate to 2% with a repeatability of 0.5%, while the pressure gauges were also expected to have errors of the same order [149]. Operation near full-scale was not always possible, though every attempt was made to operate in this region.

Temperature readings were made using a thermocouple that was accurate to within 2%. Positioning of the probe within the flow had inherent errors. Measurement of the vertical position was undertaken by referencing to the visible laser beam. The thermocouple tip was positioned to intersect at 90° the visible laser beam that was set to have a 1 mm diameter. The horizontal measurement of the temperature was performed by traversing the probe across the flow with a minimum possible position measurement of 1 mm, although data was recorded at 2 mm steps.

The accuracy of the velocity, using PIV, is dependent on the time delay and spatial resolution. Time measurements were assessed to be accurate to less than 0.1 μs, or better than 1%. The measurement of particle displacement was performed by the imaging camera where 1 mm displacement equated to 35 pixels. Not considering sub-pixel resolution, the displacement can be resolved to better than 0.03 mm. For the experimental settings the velocity could therefore be resolved to better than 0.03 m/s accuracy.

4.6.1.2 Laser Beam and Propagation

Vernier calipers were used to set the iris diameter and consequently the beam diameter. Accuracy was expected to be better than 0.1 mm, although there was an inherent risk of altering the iris diameter as the calipers were removed from the iris. To minimize this risk, the aperture opening and closing mechanism was held as the calipers were removed.

The beam was propagated over the centre axis of the burner. In order to ensure repeatability between experiments a board with 5 mm grid squares was positioned atop the burner. The position of the impingement of the laser on this board was checked and adjustments made to the positioning were made if required. Given the laser beam diameter and the alignment method, it is assessed that the laser beam could be up to 2 mm from the centre line of the burner. However this error was somewhat mitigated by using the temperature probe to confirm the laser beam was passing the hottest region of the flow, which lay at the centre axis of the burner.

Height adjustments to the laser beam crossing position above the burner nozzle were made by adjusting the height of the burner. This was achieved by moving the burner up or down on a tripod. The height was determined by measuring the distance from the burner to the floor using a tape measure with minimum scale of 1 mm. The height of the laser above the floor was fixed.

4.6.1.3 Laser Beam Spot

The laser beam impinged on the target board and the resulting beam spot was imaged. The angular displacement was determined by considering the distance moved across the board and the path length of the propagating beam. The beam path length was determined by using a tape measure, measuring the length of the path from the burner to the target board. Given the number of separate measurements along the path length and the minimum scale of the tape measure, it was assessed that the path length measurement was accurate to better than 0.1%, or 20 mm. The displacement across the board was measured using the imaging camera. The image size captured by the cameras and the pixel count of the cameras allowed the spatial resolution to be determined. For both cameras the position could be resolved to better than 0.05 mm. Angular displacement is therefore reportable to ± 3 microradians for the given path length and beam displacement errors.

4.6.2 Length Scale

The PIV experiment allows a measurement of the length scales within the flow. An autocorrelation of the velocities at a horizontal line passing across the flow reveals the spatial distance at which the velocity fluctuations are not correlated. Determining the length scale using the autocorrelation function has been used by others [147, 150, 151]. The length scale of the velocity fluctuations was calculated as an integral length scale using a discrete version of the autocorrelation function as outlined by Chen et al. [147] and shown in Equation (4-2).

$$f(\Delta r) = \frac{\overline{v'(r,x)v'(r+\Delta r,x)}}{\overline{v'(r,x)^2}} \qquad (4\text{-}2)$$

where r is the radial displacement, x is the axial position, Δr is the radial distance between two velocity vectors and v' is the instantaneous velocity fluctuation defined as;

$$v' = v - \overline{U} \qquad (4\text{-}3)$$

where *v* is the instantaneous velocity and $\overline{U}$ is the mean velocity.

Chen et al. found that Equation (4-4) was a good fit to the resulting autocorrelation function curve.

$$f(\Delta r) = a\left(1-\frac{b\Delta r}{2}\right)e^{-b\Delta r} + c\left(1-\frac{d\Delta r}{2}\right)e^{-d\Delta r} \tag{4-4}$$

The integral under the curve, calculated for *r* = 0 to ∞, represented the integral length scale and is evaluated from Equation (4-4) as;

$$l_f = \frac{a}{2b} + \frac{c}{2d} \tag{4-5}$$

An example taken from the processed data of the plotted autocorrelation and its curve fit is presented in Figure 4.11.

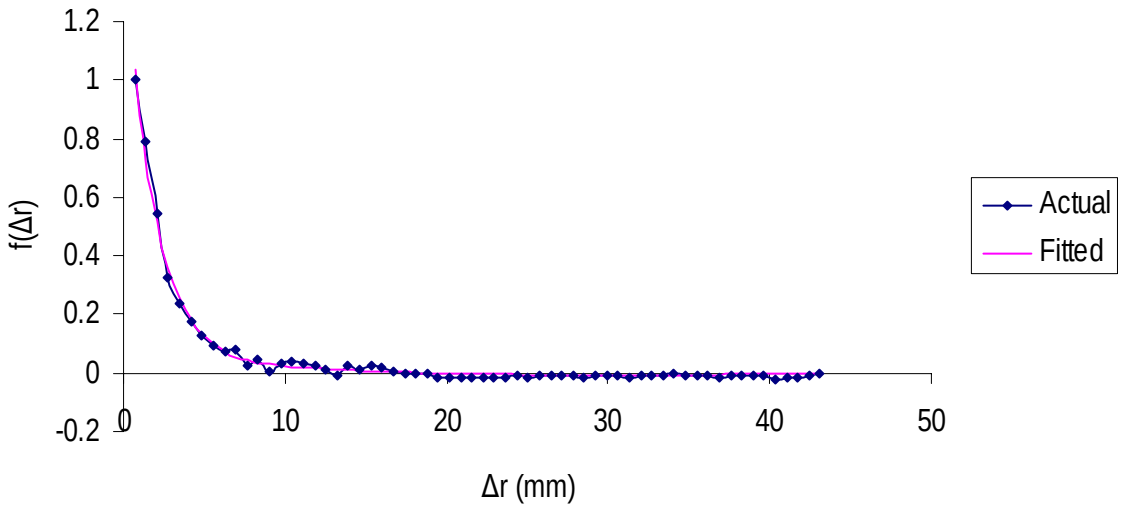

Figure 4.11: Graphical presentation of the calculated integral length scale. In this case the integral length scale was calculated from the curve fit to be 2.86 mm, being the area under the curve.

Note that the integral length scale represents the range of length scales within the flow, and the integral length scale could be considered as an approximate average of all the length scales.

4.6.3 Turbulence Intensity

The level of fluctuation in the flow was determined by computing the degree of variability of the instantaneous velocity at a point of interest. The turbulence intensity at a point is the standard deviation of these fluctuations divided by the average velocity at that point. That is;

$$I = \frac{\sigma(v)}{\overline{U}} = \frac{u'}{\overline{U}} \tag{4-6}$$

Or,

$$I = \frac{\sqrt{\frac{1}{N}\sum_{i=1}^{N}(r_i - v)^2}}{\overline{U}} \tag{4-7}$$

where v is the instantaneous velocity, u' is the standard deviation of the instantaneous velocity, $\overline{U}$ is the mean velocity and r is the radial position in the flow.

4.7 Results

The cross-correlation data was computed using a program called PIVview [148]. The output from this program was processed using a custom made National Instruments LabVIEW program which implemented the functions to calculate the standard deviation of the velocities and the average velocities at user input crossing lines. The program also executed the autocorrelation function and curve fitted to Equation (4-4) by iterating to find the coefficients. The program then calculated the integral length scale from the coefficients using Equation (4-5). The data was collected for all experimental conditions that were encountered by the laser beams in the parametric study. The temperature and flow field results are presented in the following sections.

4.7.1 Effect of Blockage Ratio

A number of setups were used in the parametric experiment where the blockage ratio was varied while all other experimental parameters remained unchanged. Blockage ratio was changed from 37%, 55% and 65% while keeping the other values constant. The perforated plate hole diameters was fixed at 5 mm, peak temperature at the laser beam crossing height of 85 mm above the nozzle was fixed at 500°C and Reynolds number at the nozzle fixed at 10,000.

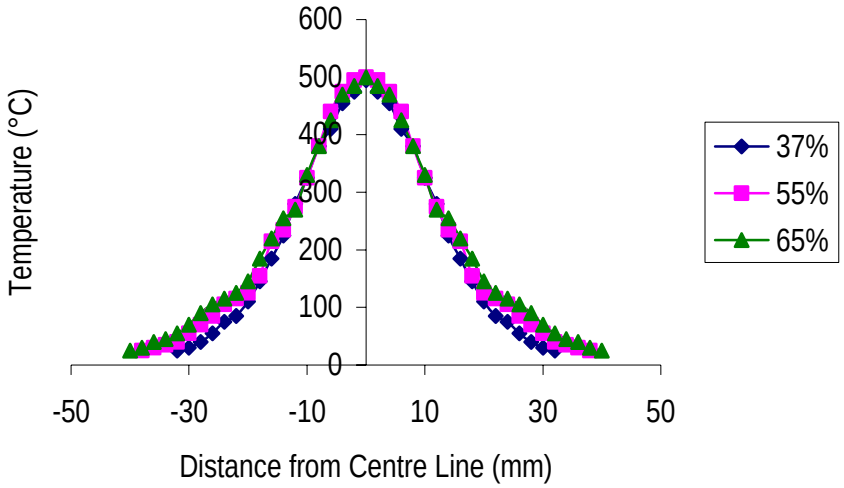

Figure 4.12: Temperature profile for blockage ratios 37%, 55% and 65% at a distance of 85 mm and Re = 10,000.

Figure 4.12 shows the temperature profiles that were measured for the three blockage ratios; 37%, 55% and 65%. It is clear that there is a minor change in the path length of the heated flow at the laser beam crossing height.

PIV characterisation was also performed on the three cases. The integral length scale calculated from the autocorrelation function is shown for each case in Figure 4.13. There is a slight increase in integral length scale with increased blockage ratio for the conditions tested.

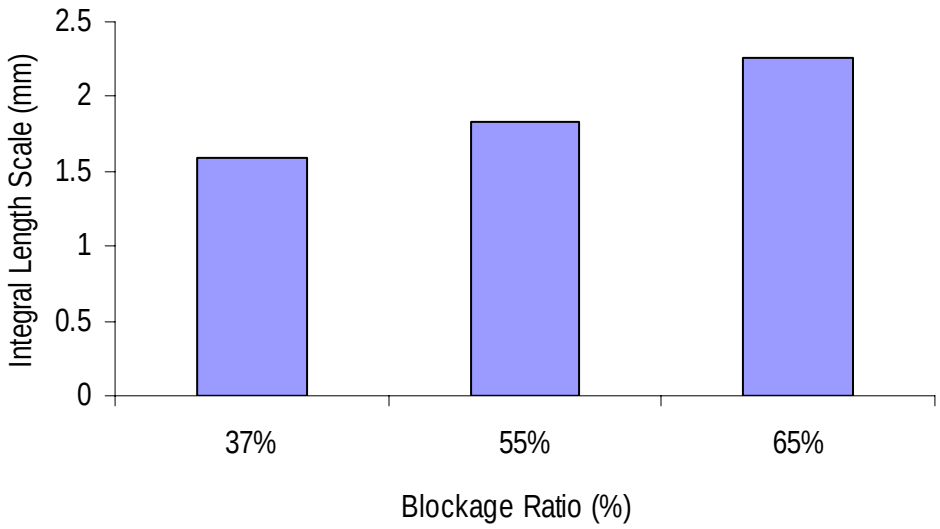

Figure 4.13: Integral length scales calculated for blockage ratios 37%, 55% and 65%.

At the laser beam crossing height the average velocity profile across the flow for the three blockage ratio conditions is shown in Figure 4.14 while the standard deviation of the instantaneous velocity fluctuations is shown in Figure 4.15. Turbulence intensity is derived from dividing the standard deviation of the instantaneous velocity fluctuations by the average velocity at each point. The average velocity decreases with distance from the centre line and eventually becomes the velocity of the co-flow.

The velocity fluctuation profiles (Figure 4.15) exhibit a plateau which increased in width with the increase in blockage ratio before decreasing to co-flow conditions away from the centre.

The radial profiles of the turbulence intensity are shown in Figure 4.16. The profiles show an increase in turbulence intensity with radial distance before a drop and a plateau towards co-flow conditions. Higher blockage ratios show higher turbulence intensity at this axial location. The peak values occur at 10 mm, 15 mm and 22 mm for the 37%, 55% and 65% blockage ratios, respectively. The locations of the different peaks are not well understood and can be related to the location of the shear layer between the jet flow and the surrounding air. The key issue however, is the capturing of the total width of the flow, as seen visually in Figure 4.12 and Figure 4.14.

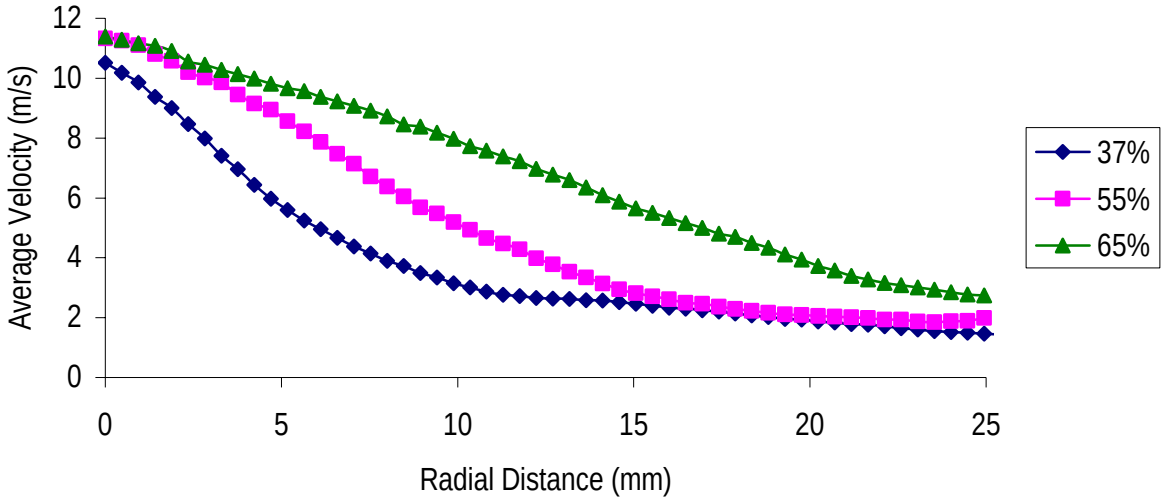

Figure 4.14: The average velocity measured along a radial outwards from the axial core for the 37%, 55% and 65% blockage ratio cases at 500°C with 5 mm diameter holes.

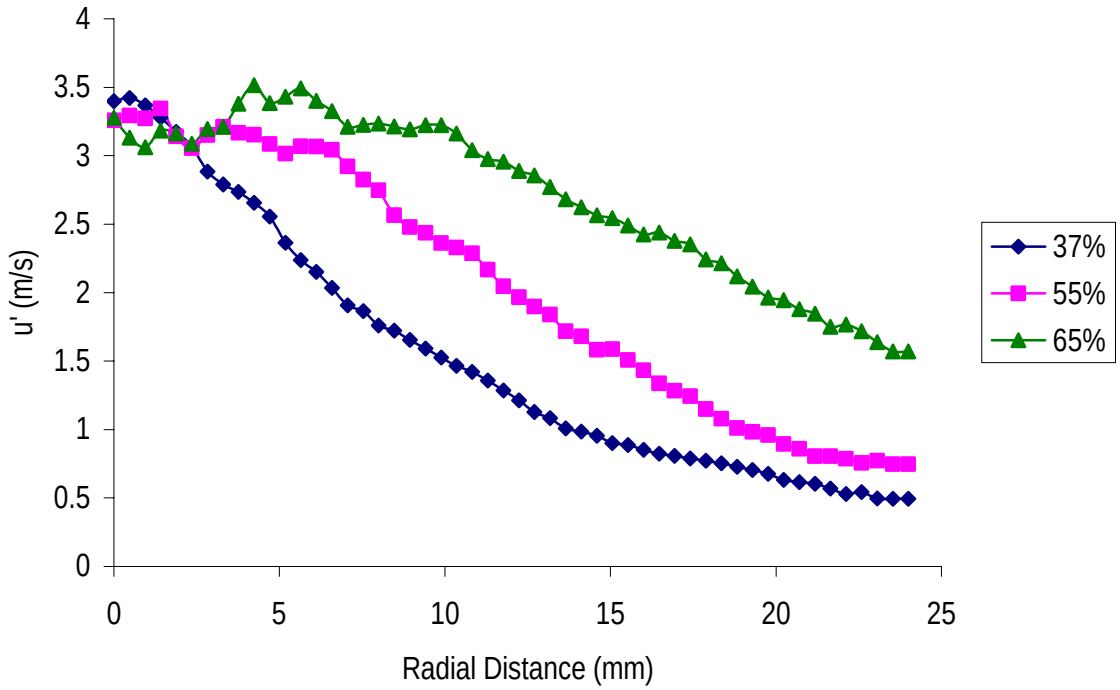

Figure 4.15: The standard deviation of the instantaneous velocity plotted against radial distance for the 37%, 55% and 65% blockage ratio cases at 500°C with 5 mm diameter holes.

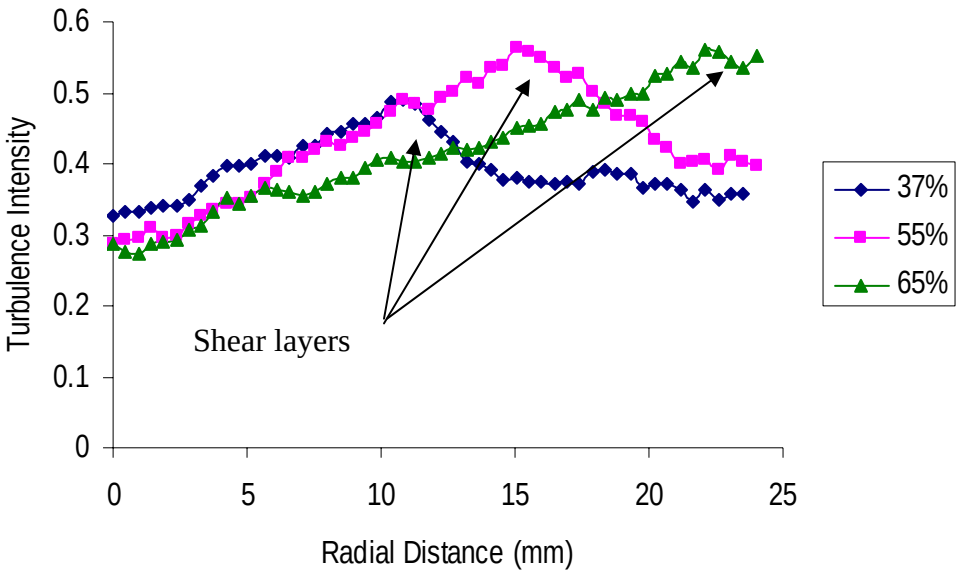

Figure 4.16: Turbulence intensity for blockage ratio cases 37%, 55% and 65% at 500°C with 5 mm diameter holes.

4.7.2 Effect of Hole Diameter

The hole diameter in the perforated plates was changed in three cases whilst all other experimental parameters were left unchanged. These three setups, in which the flow was characterized, were those used for the simple jet parametric study where the laser beam was propagated through the flow and the resulting beam image recorded. In these setups the hole diameter was changed from 3 mm to 6 mm and 8 mm and the blockage ratio was maintained at ~50%, with the temperature's peak value being 500°C at the laser beam crossing height and the Reynolds number at the tube exit fixed at 10,000.

The measured temperature profiles for the three hole diameters; 3 mm, 6 mm and 8 mm is shown in Figure 4.17. It is clear that there is little difference between the temperature profiles for the three cases.

The integral length scale calculated from the autocorrelation function is shown for each case in Figure 4.18. There is a notable increase in integral length scale with the increase in hole diameter. For plates with a 3 mm hole diameter the integral length scale was found to be 2.09 mm, for a 6 mm hole diameter it was 2.91 mm and for a 8 mm diameter, 5.01 mm.

Velocity data is plotted in Figure 4.19 and Figure 4.20. Velocity variance and average velocity decreased as the hole diameter decreased. This is because the jets from the perforated plates combine to form a single jet at different heights above the plate. For the same blockage ratio, smaller diameter jets will combine earlier and have a lower momentum; hence a larger centerline velocity decay. Turbulence intensity is plotted in Figure 4.21. Turbulence intensity values were similar in all cases, except for the 8 mm hole diameter case where the turbulence intensity values were higher at the flow edge than the turbulence intensity values produced by the 3 mm and 6 mm plates.

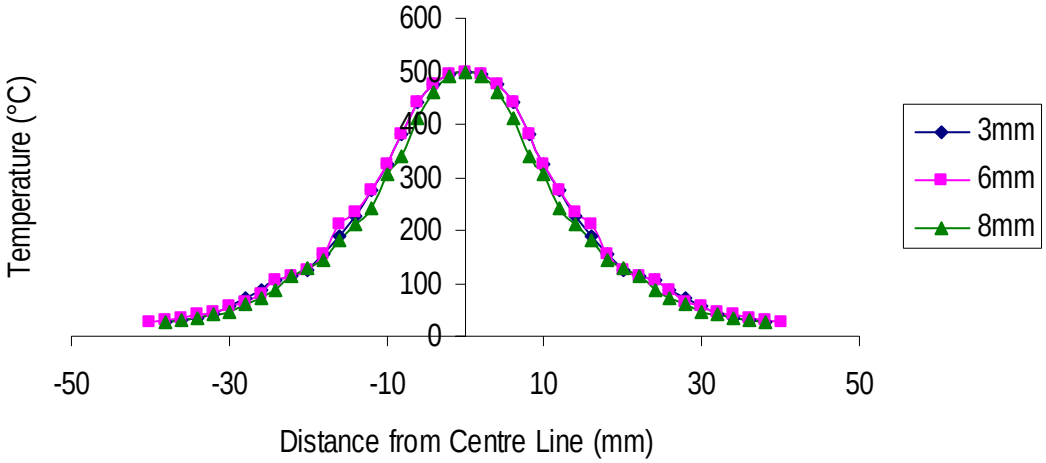

Figure 4.17: Temperature profile for hole diameters 3 mm, 6 mm and 8 mm at 500°C with ~50% blockage ratio.

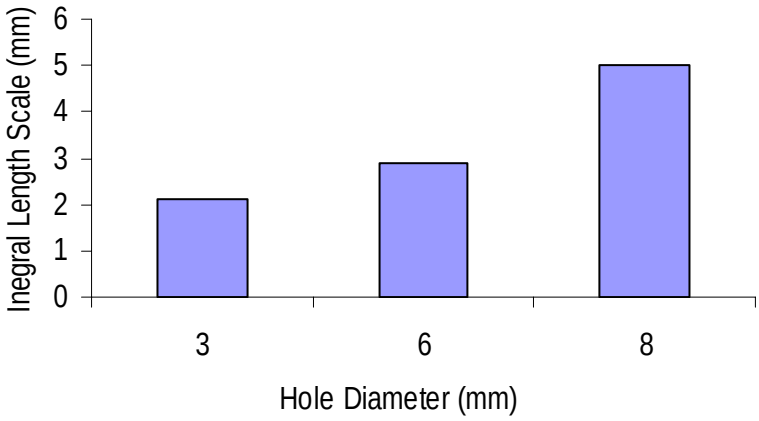

Figure 4.18: Integral length scales calculated hole diameters 3 mm, 6 mm and 8 mm at 500°C with ~50% blockage ratio.

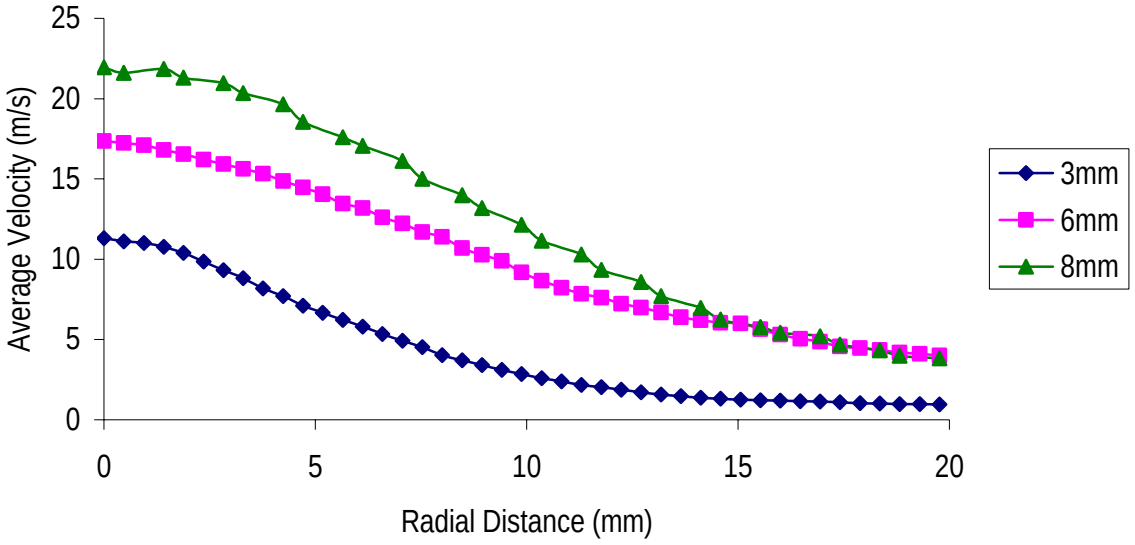

Figure 4.19: The average velocity measured along a radial outwards from the axial core for the 3 mm, 6 mm and 8 mm hole diameter cases at 500°C with ~50% blockage ratio.

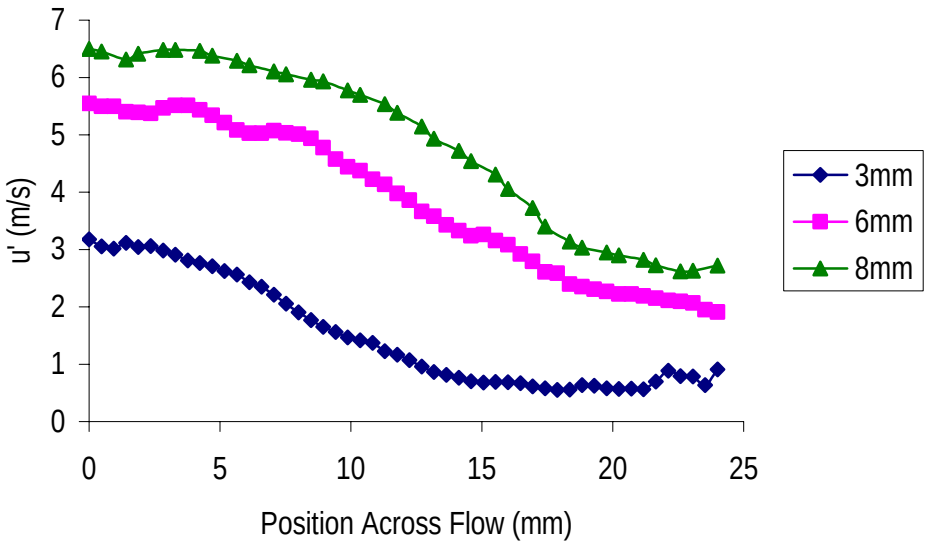

Figure 4.20: The standard deviation of the instantaneous velocity plotted against radial distance for the 3 mm, 6 mm and 8 mm hole diameter cases at 500°C with ~50% blockage ratio.

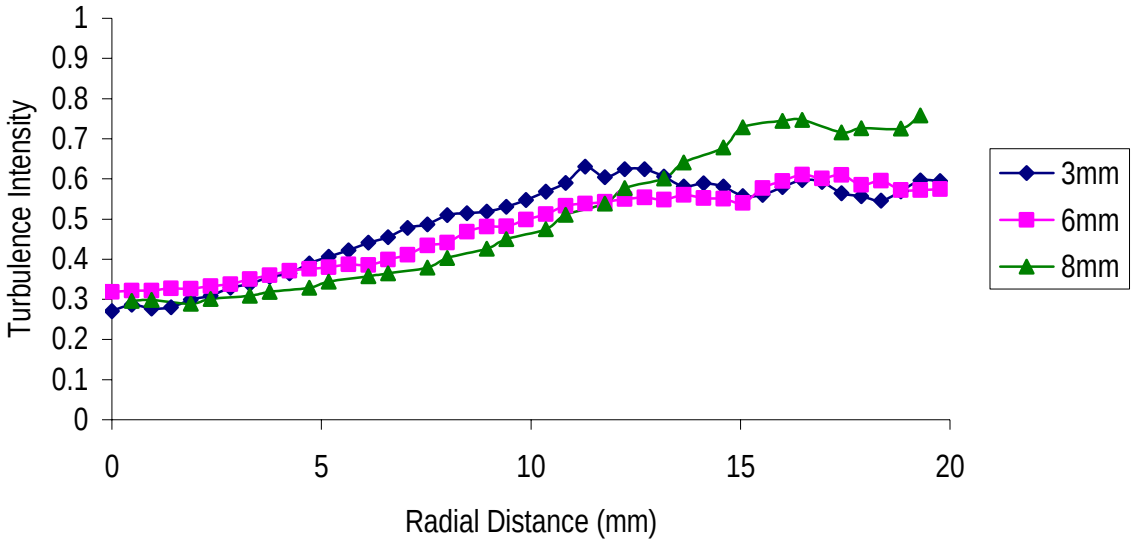

Figure 4.21: Turbulence intensity for hole diameter cases 3 mm, 6 mm and 8 mm at 500°C with ~50% blockage ratio.

4.7.3 Effect of Path Length and Temperature

This experiment was aimed at characterizing the interaction of the beam and the heated flow under conditions where the temperature path through the heated flow was changing. The temperature at different heights above the nozzle exit was manipulated via a combination of the gas volume and the mixture equivalence ratio. A perforated plate with a 8 mm hole diameter was used. The Reynolds number at the exit plane was kept constant in all cases. The experiment consisted of two parts.

In one part of the experiment the temperature was set to 300°C at different heights above the nozzle. In the other part of experiment the temperature was preset at the nozzle exit. The temperature was measured at different heights above the nozzle for the burner operating conditions described above. The difference between the two experiments was that in the second experiment the temperature was allowed to decay and was not adjusted.

4.7.3.1 Fixed Temperature at the Nozzle

In the case where the temperature was kept fixed at the nozzle, the temperature profiles were measured at different heights downstream (X/D). The temperature profile is shown in Figure 4.22. The path length through the flow was defined as the distance between the 13.5% ($1/e^2$) of maximum temperature points and is shown in Figure 4.23 to be increasing with distance downstream. A plot of the average temperature gradient at each height tested is shown in Figure 4.24 and clearly shows the gradient is greatest close to the nozzle.

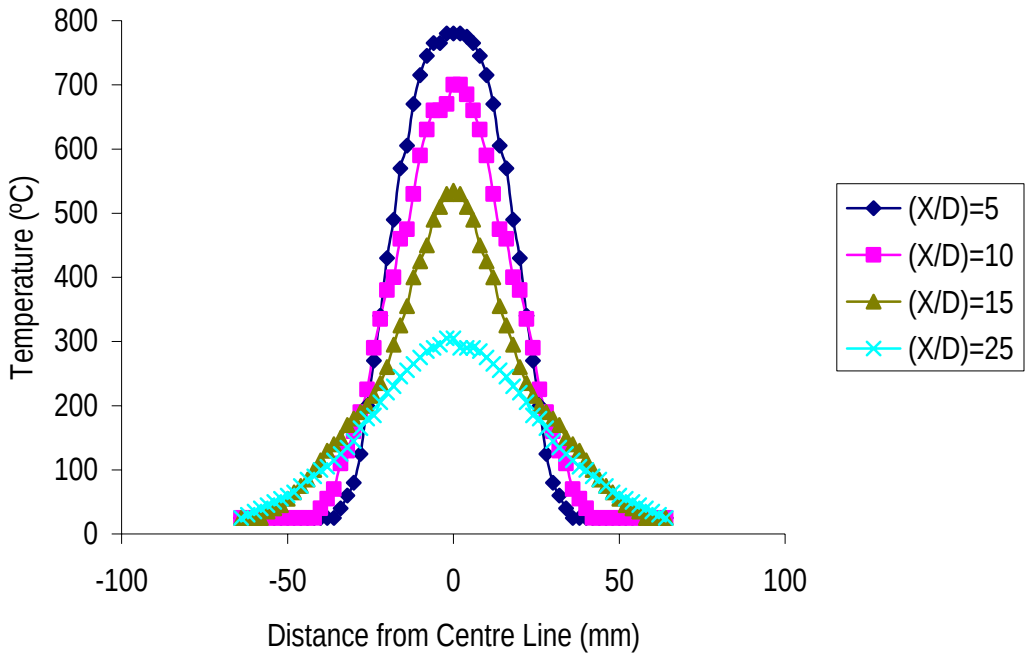

Figure 4.22: Temperature profiles at various heights above the nozzle for the same conditions.

The autocorrelation function was applied to produce the integral length scale at the various heights. Figure 4.25 shows the integral length increasing with height above the nozzle. The increase in length-scale is, in this case, related to the decrease in average velocity and turbulence intensity. The velocity is shown in Figure 4.26 to decrease with distance form the nozzle.

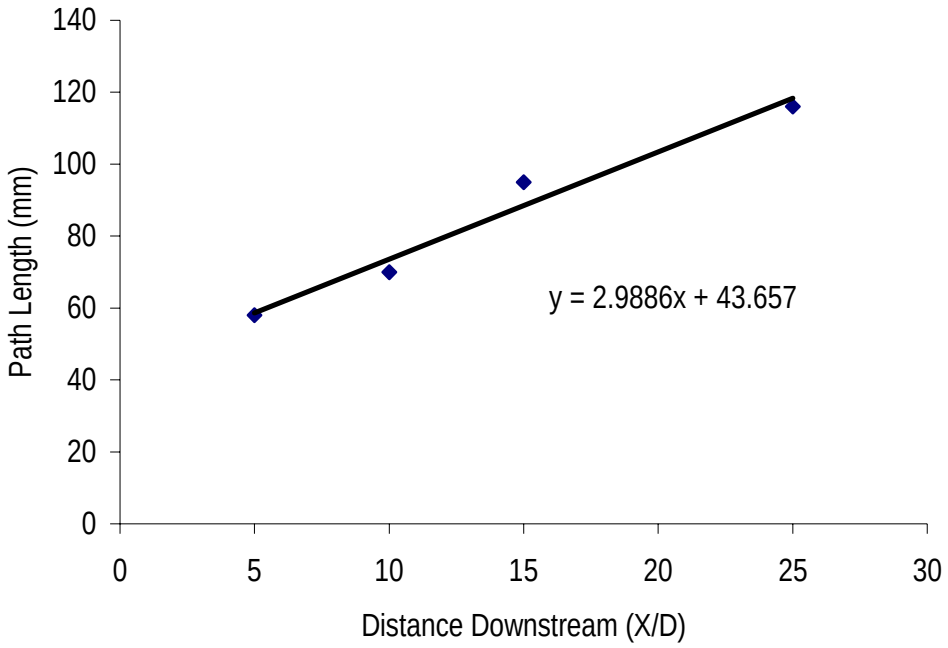

Figure 4.23: Path length through the hot gases at various heights with the conditions fixed at the nozzle.

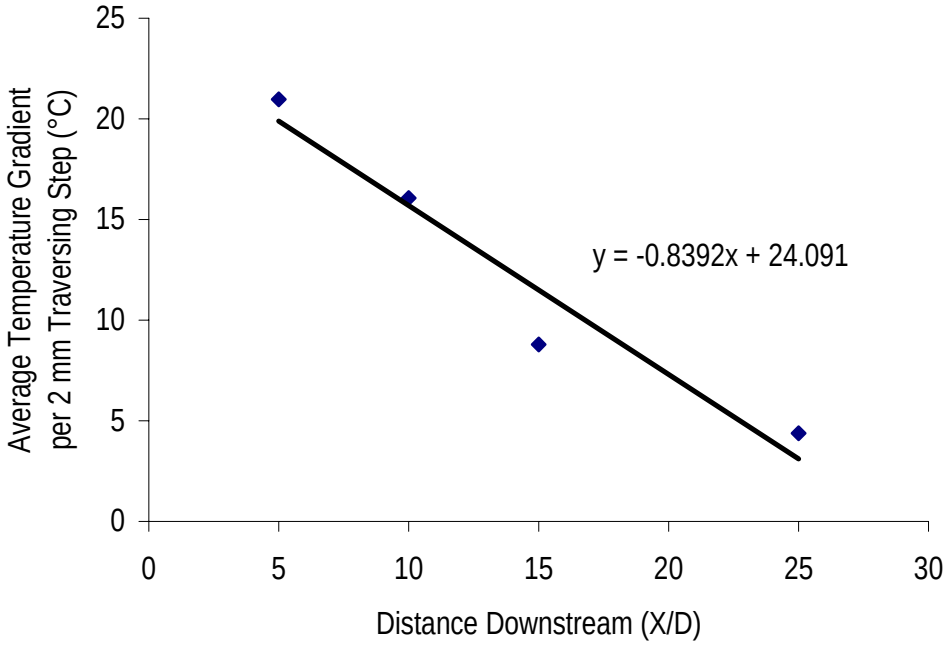

Figure 4.24: Average temperature gradient each 2 mm path length step shown for various heights with the conditions fixed at the nozzle.

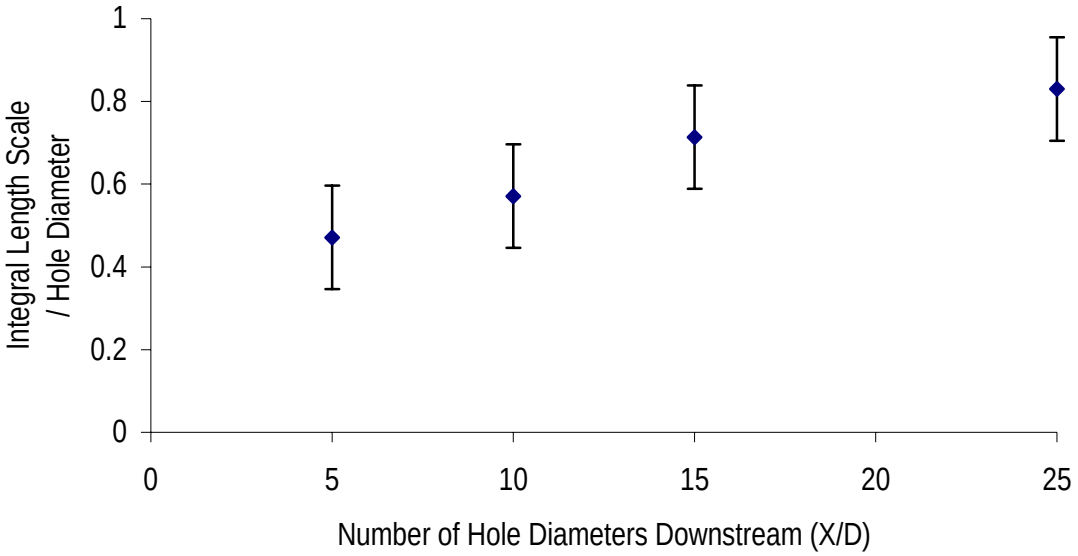

Figure 4.25: Integral length scale as a function of propagation height above the nozzle with the flow conditions at the nozzle the same for each case.

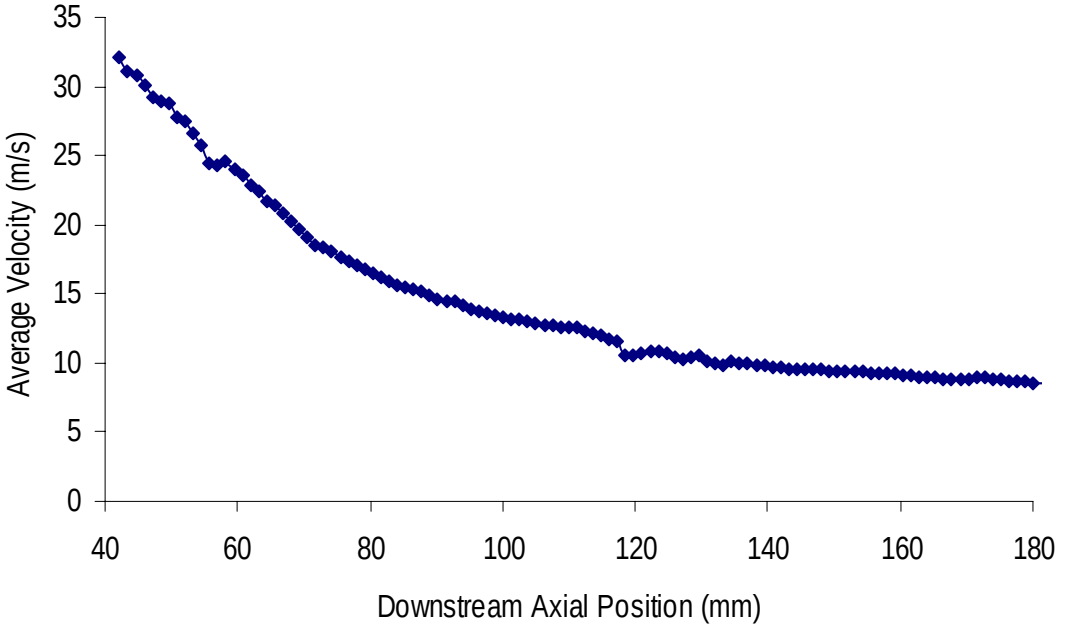

Figure 4.26: The average velocity measured along the flow axis with the flow conditions fixed at the nozzle.

The velocity data for the propagation paths across the flow at various distances above a nozzle with fixed flow conditions is shown in Figure 4.27, Figure 4.28 and Figure 4.29. Mean velocity and velocity fluctuations are greatest at lower heights, closer to the nozzle. The turbulence intensity is similar at all heights near the axial core but increases near the shear layer which is seen to increase radially with distance downstream. The greatest turbulence intensity is in the shear layer closest to the nozzle outlet.

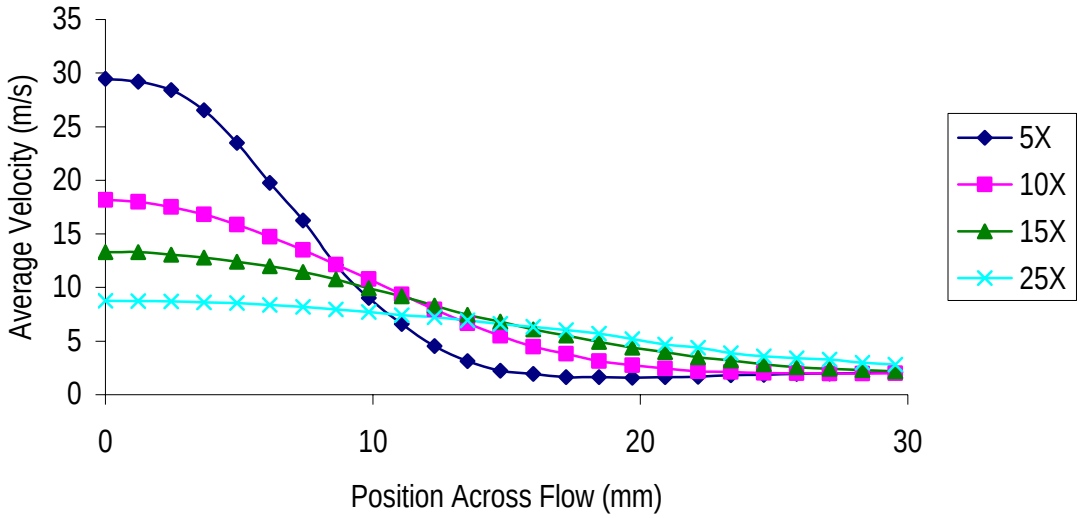

Figure 4.27: The average velocity measured along a radial outwards from the centre axis at heights above the nozzle of 5, 10, 15 and 25 times the 8 mm perforated plate hole diameter.

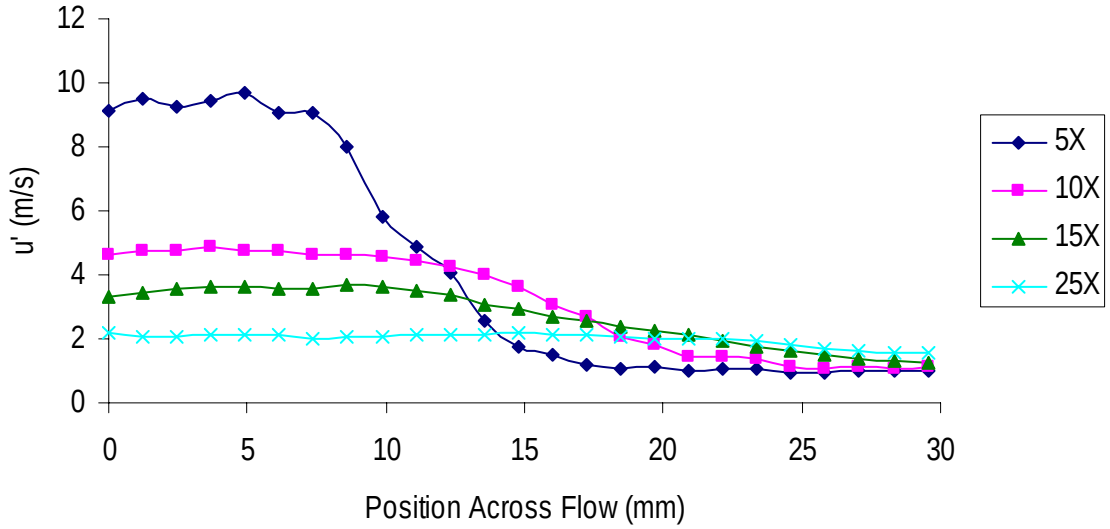

Figure 4.28: The standard deviation of the instantaneous velocity plotted against radial distance for heights above the nozzle of 5, 10, 15 and 25 times the 8 mm perforated plate hole diameter.

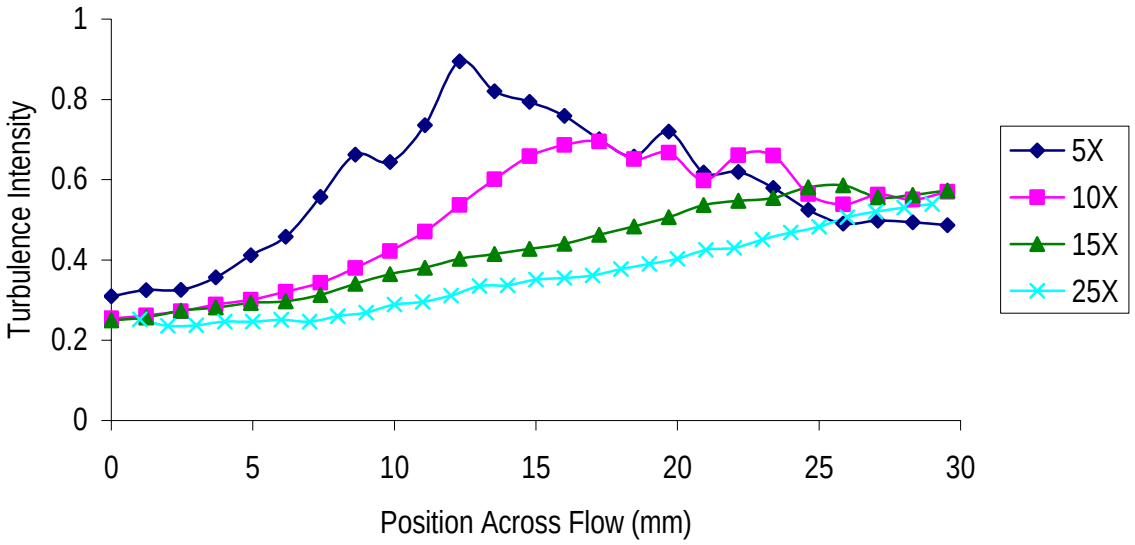

Figure 4.29: Turbulence intensity for heights above the nozzle of 5, 10, 15 and 25 times the 8 mm perforated plate hole diameter.

4.7.3.2 Variable Temperature at the Nozzle

The flow characterization was performed for the simple jet parametric experiment runs where the laser beam was propagated across the flow at different heights where the peak temperature was set to 300°C. In these runs the temperature at the nozzle was varied, while maintaining a constant Reynolds number of 10,000 at the tube exit, to obtain 300°C at the various heights above the nozzle. Measurements were taken up to 15 hole diameters downstream, beyond which the temperature was hard to maintain at the required 300°C.

The temperature profiles were successfully measured for a number of heights, including 20 hole diameters above the burner. The temperature profiles are shown in Figure 4.30. The path length was determined from these profiles. Shown in Figure 4.31 is a plot of the path length for the various heights with the path length through the flow defined as the distance between the 13.5% ($1/e^2$) of maximum temperature points. A plot of the average temperature gradient at each height tested is shown in Figure 4.32. The figures show the path length increasing as the height increases, though offset by a decrease in the temperature gradient per path length step.

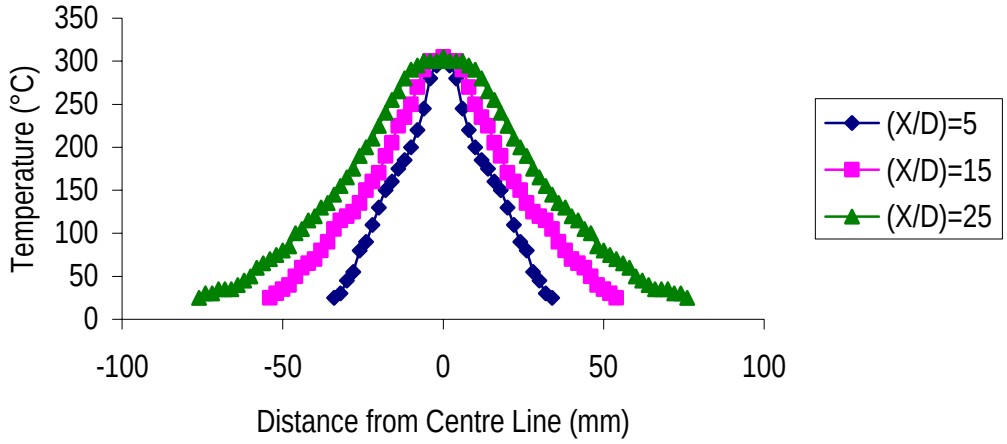

Figure 4.30: Temperature profiles at various heights with the peak temperature fixed at 300°C.

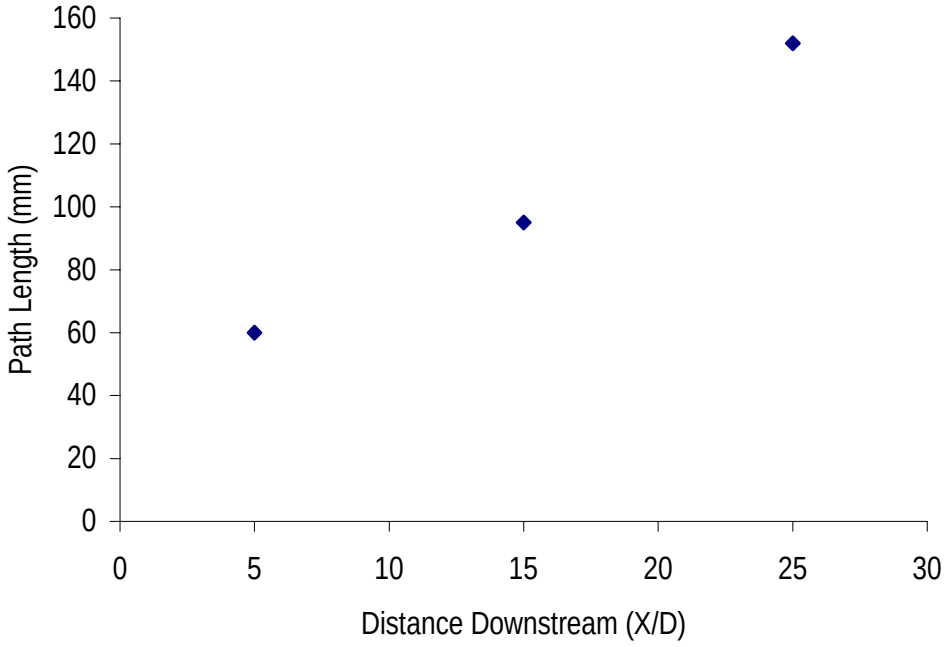

Figure 4.31: Path length through the hot gases at various heights with the peak temperature fixed at 300°C.

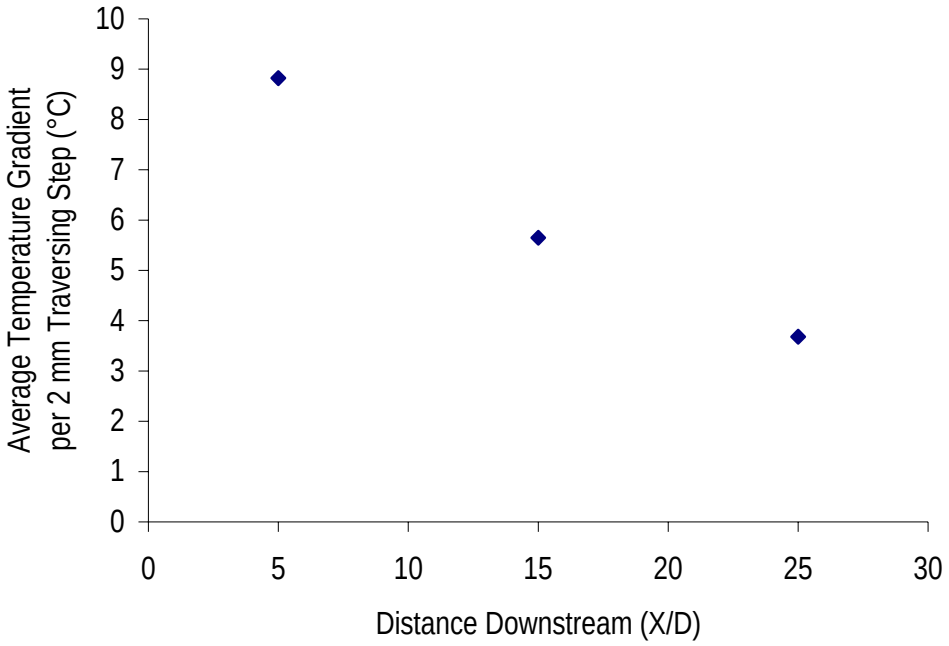

Figure 4.32: Average temperature gradient each 2 mm path length step shown for various heights with the peak temperature fixed at 300°C.

The integral length scales were determined at the various heights by application of the autocorrelation function to the PIV determined velocity vectors. The integral length scales were calculated at the various heights for the case where the peak temperature in the crossing path was always fixed at 300°C. Figure 4.33 shows the integral length scales increasing with height above the burner.

The velocity data for the propagation paths across the flow at various distances above the nozzle with the temperature fixed at 300°C at the various heights is shown in Figure 4.34, Figure 4.35 and Figure 4.36. The mean velocity and velocity fluctuations are similar for all runs with, in each case, the values greatest closer to the core. The turbulence intensity is similar at all heights and is always seen to increase near the shear layer.

The notable changes with increased height for the 300°C cases are therefore the increase in path length, accompanied by a decrease in the piece-wise temperature gradient, and the increase in integral length scale.

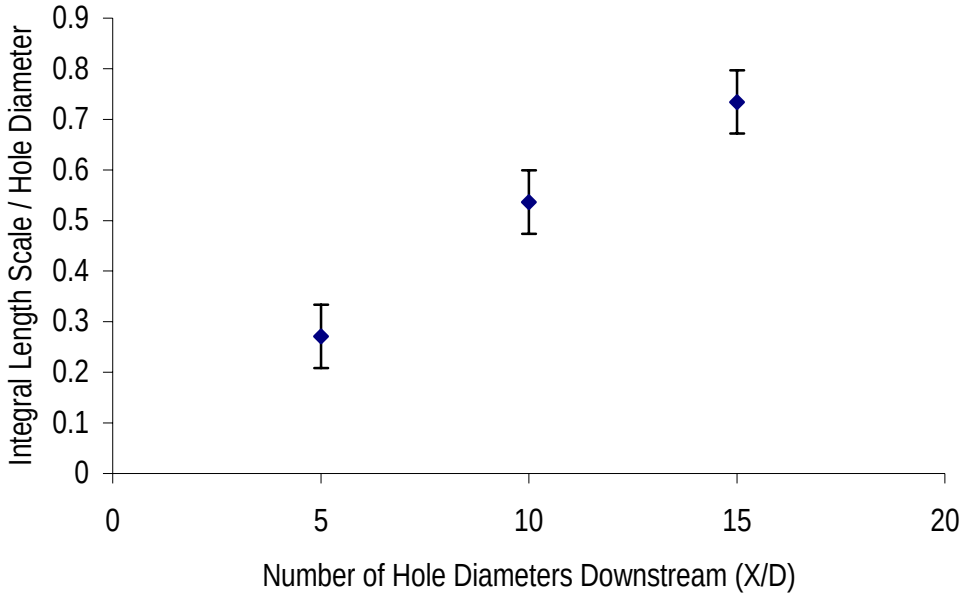

Figure 4.33: Integral length scale as a function of propagation height above the nozzle with the peak flow temperature fixed at 300°C at the various propagation heights.

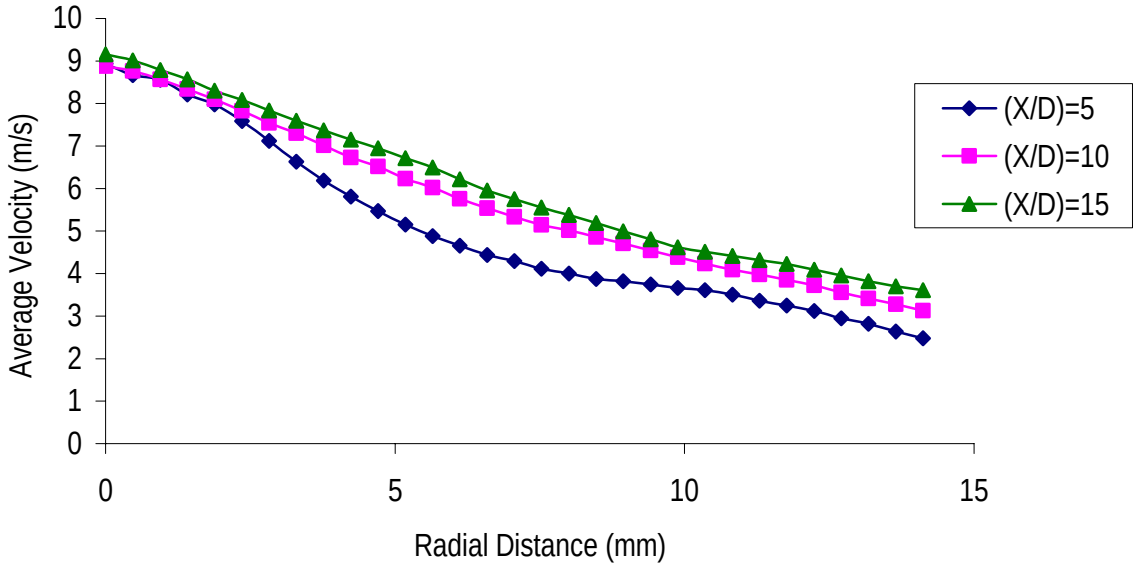

Figure 4.34: The average velocity measured along a radial outwards from the centre axis at heights above the nozzle of 5, 10, 15 times the 8 mm perforated plate hole diameter with the temperature fixed at 300°C at the various heights.

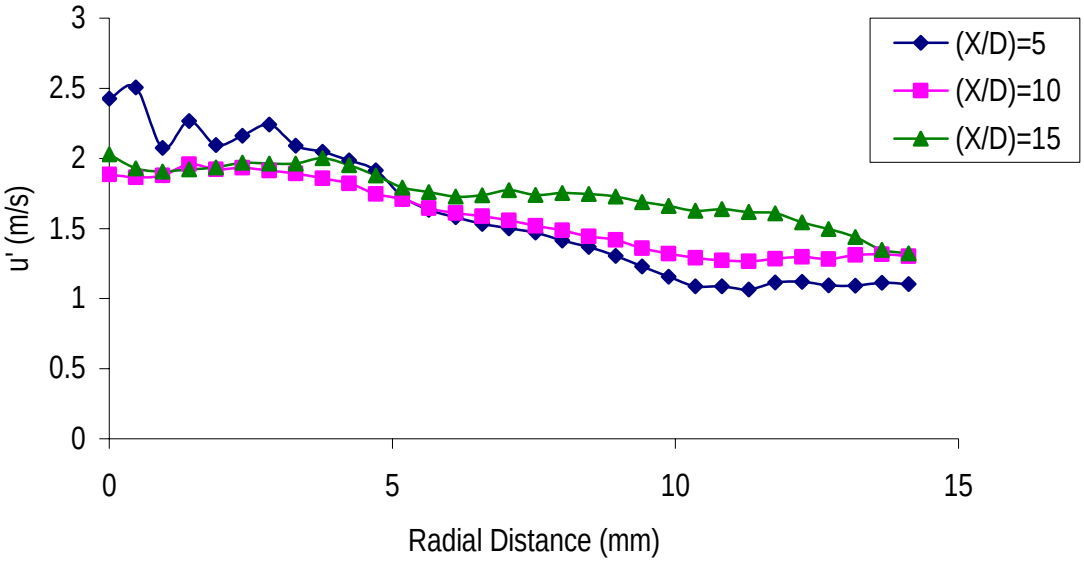

Figure 4.35: The standard deviation of the instantaneous velocity plotted against radial distance for heights above the nozzle of 5, 10 and 15 times the 8 mm perforated plate hole diameter with the temperature fixed at 300°C at the various heights.

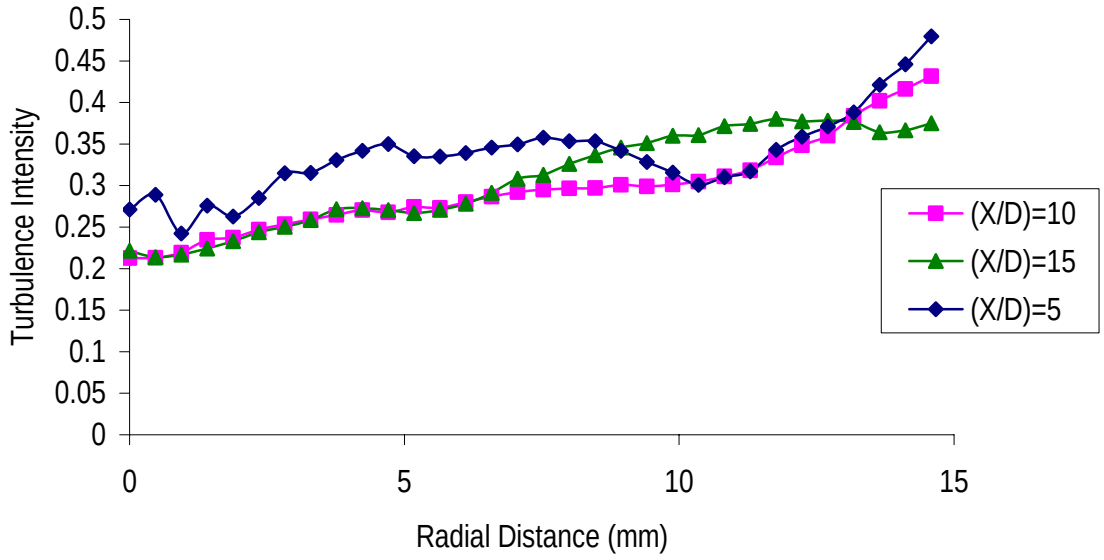

Figure 4.36: Turbulence intensity for heights above the nozzle of 5, 10 and 15 times the 8 mm perforated plate hole diameter with the temperature fixed at 300°C at the various heights.

4.8 Summary

The simple jet parametric experiment allowed the measurement of laser beam movement under a variety of turbulent flow conditions. The turbulence conditions were altered in a number of ways. The addition of perforated plates of various hole diameters and blockage ratio to the nozzle allowed the flow's length scale and turbulence intensity to be altered.

Temperature of the gas flow was also varied, while maintaining a constant Reynolds number, by controlling the hydrogen-air combustion mixture. Further, controlling the laser beam parameters, including the crossing heights, provided information on the beam effects due to path length, beam diameter and wavelength at elevated temperatures of interest.

Temperature and velocity characterisation of the flow was undertaken for a number of cases identified in the simple jet parametric experiment, including; changing blockage ratio, changing perforated plate hole diameter, height and path-length tests. A thermocouple was used to measure the temperature at 2 mm steps across regions of the flow that matched the path the laser beam traversed in the parametric experiments. Estimations of the path length and path length piece-wise gradient were made form these measurements. Particle Image Velocimetry (PIV) was successfully used to determine the velocity characteristics of the flow, including measuring the integral length scale by using the autocorrelation function.

The flow characterisation tests performed with various blockage ratios showed there was a slight increase in integral length scale with increase in blockage ratio. There is a greater horizontal expansion of the flow at the measurement height as the blockage ratio increased, resulting in a slightly increased path length through the hot gases. The turbulence intensity is marginally increased in the shear layer as the blockage ratio increased.

Hole diameter changes in the perforated plate resulted in an increase in integral length scale with increase in hole diameter. There was no notable difference in the path length and the turbulent intensities were similar.

The path length was seen to increase with distance down-stream in the case where the flow conditions were maintained at the nozzle and flow characterisation was performed at various heights above the nozzle. The temperature gradients were greatest close to the nozzle. The integral length scale was seen to increase with distance downstream while the average velocity and velocity fluctuations decreased. The turbulence intensity was similar at all heights near the centre of the flow. The turbulence intensity increased near the shear layer, increasing in this region with distance downstream.

In the case where the temperature was maintained at 300°C at various heights, the path length increased with height, accompanied by a decrease in the piece-wise temperature gradient, and an increase in integral length scale. Turbulence intensity values were similar.

Chapter 5

Beam Propagation: Results and Analysis

5.1 Introduction

In this chapter the results of the beam propagation study and the impact of the flow characteristics on the beam quality are presented. The flow characterization work presented in Chapter 4 provided detailed knowledge of various flow conditions that were present during the parametric study. The effect on the beam, resulting from the propagation through the flow, is linked to the flow characteristics in this chapter.

5.2 Gas Temperature and Laser Wavelength

In this section, the impact of the flow field temperature on the beam energy distribution for both the visible (632.8 nm) and infrared beams (4.67 μm) is presented and discussed. The experimental conditions are listed in Table 4.2. To recap, in the simple jet parametric experiment the temperature of the turbulent flow was increased from ambient to 320°C using the electric heater and from 400°C to 1200°C using the combustion of hydrogen in air. The Reynolds number was kept at a constant value at the nozzle exit by increasing the air volume to counteract the decrease in viscosity as the temperature of the gas flow increased. The visible and infrared laser beams were propagated across the flow at various temperatures and the resulting beam spot movements imaged from a screen were recorded.

5.2.1 Comparison of Spot Images

In Figure 5.1 sample images of the spot image for the visible and infrared beams for a gas temperature of 700°C are presented. The spot images of the visible and infrared beams imaged from the screen were notably different for all cases. The visible spot is seen to be considerably broken-up in comparison to the infrared spot. The reason for the different spot structures is partly related to the diffraction limits of the wavelengths. The smallest spot size achievable for the 632.8 nm beam is more than 7 times smaller than the 4.67 µm beam, as the spot size doubles when the wavelength of the laser beam doubles. Further discussion on the difference in spot shapes is given in Section 6.3.3.

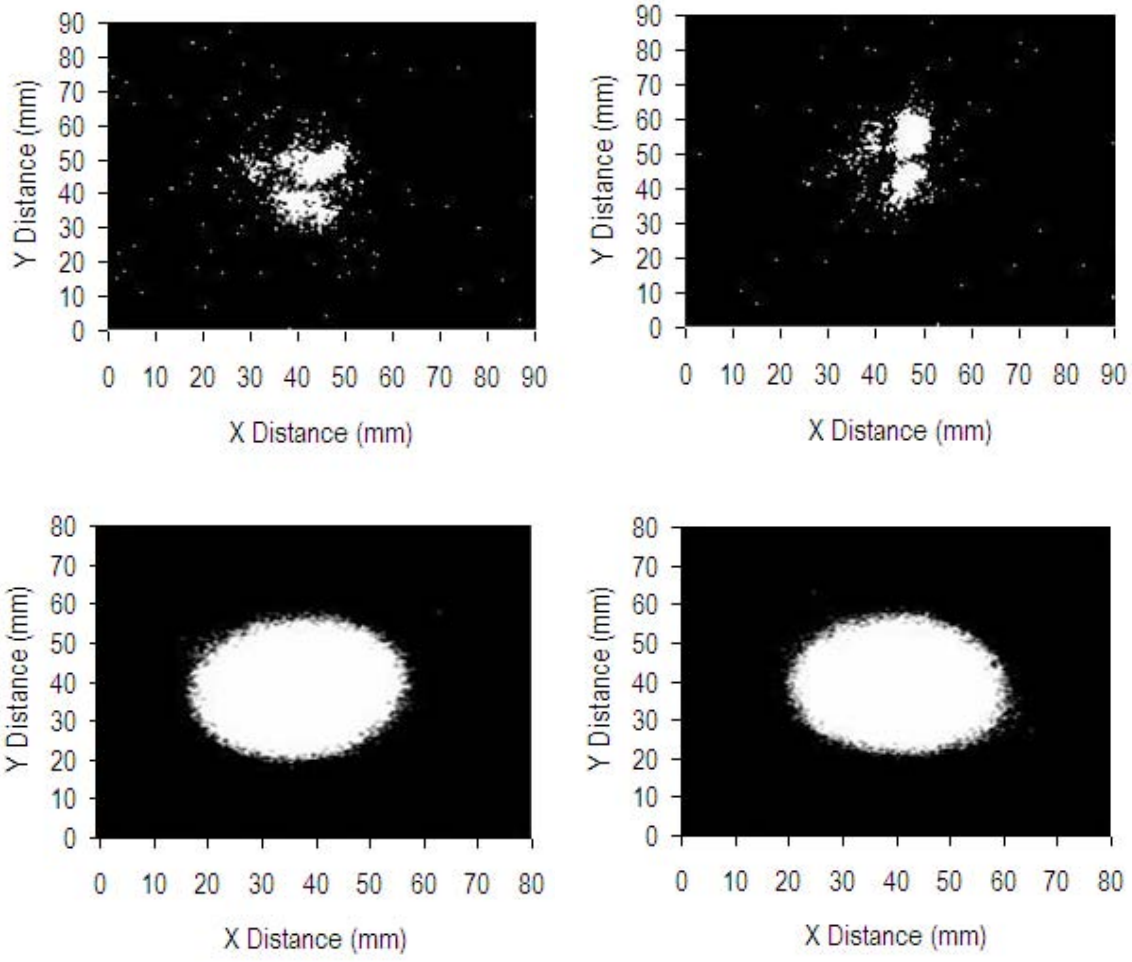

Figure 5.1: Two consecutive images of the 632.8 nm beam (top) and 4.67 µm beam (bottom) having propagated through a 3 mm iris and a turbulent zone at 700°C. The contrast has been set to show any pixels with a value not zero as white. A threshold of 13.5% has been applied.

5.2.2 Analysis of the Beam Image

Analysis of the frame-to-frame beam movement and spatial distribution was also performed. This involved post-processing of the recorded images. In all cases the average background image was removed from the captured image to improve the contrast and the signal-to-noise ratio. Background images were obtained by recording the screen image with no laser beam spot present. Processing techniques to determine the beam movement and spatial distribution of the propagated beams are discussed with reference to the results.

5.2.2.1 Centroid Displacement

To quantify the beam movement the centroid of the beam spot was first determined in the x and y directions. The centroid was defined by using the “centre of mass”, which considers the positions of the illuminated pixels and their values. The position of the centroid was calculated using Equations (5-1) and (5-2).

$$X = \frac{\sum_x \sum_y I(x,y)x}{\sum_x \sum_y I(x,y)} \tag{5-1}$$

$$Y = \frac{\sum_x \sum_y I(x,y)y}{\sum_x \sum_y I(x,y)} \tag{5-2}$$

where $I(x,y)$ is the intensity at position (*x,y*) in the pixel array.

The resultant centroid standard deviation is calculated using Equation (5-3), used by Chiba [87].

$$\sigma_R = \sqrt{\sigma_X{}^2 + \sigma_Y{}^2} \tag{5-3}$$

where σ_X is the standard deviation of the centroid X position and σ_Y is the standard deviation of the centroid Y position.

The standard deviation of the centroid position for the visible 632.8 nm and infrared 4.67 µm beam are plotted in Figure 5.2.

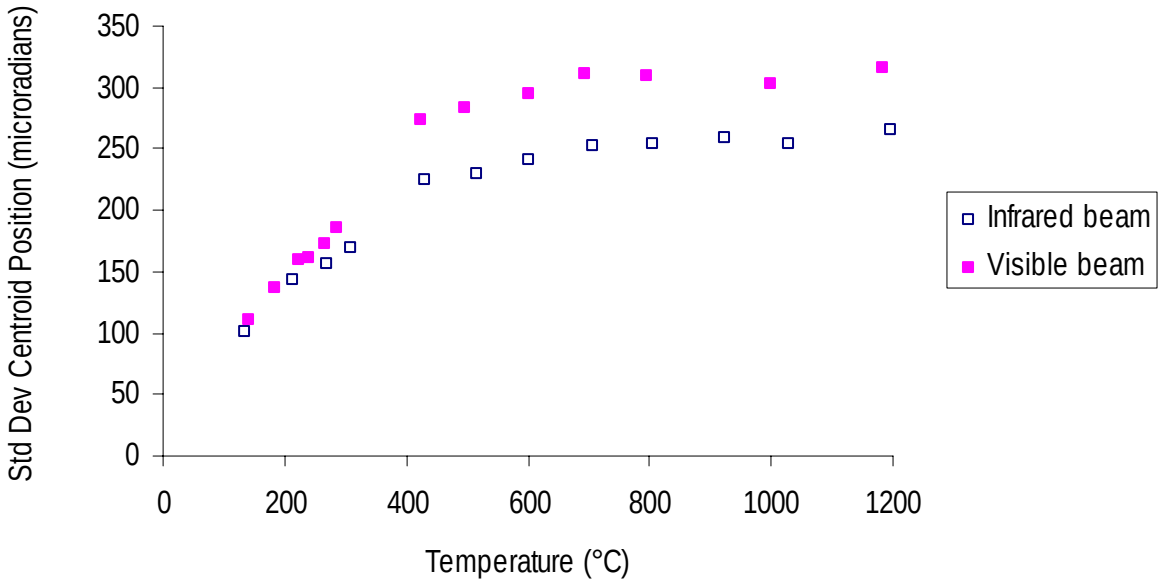

Figure 5.2: Measured standard deviation of centroid position for 632.8 nm and 4.67 µm beams, with beam diameter 3 mm, over a range of temperatures.

It is clear from Figure 5.2 that there is a strong roll-off of the measured standard-deviation of beam displacement as the temperature increases above 400ºC. Notably the departure of the visible from the infrared becomes more pronounced at higher temperatures. The departure is, as a percentage difference, 5% at low temperatures and up to 20% at high temperatures, though there are few points taken at lower temperatures with which to make the comparison.

Existing theory, discussed in Chapter 2, predicts that the refractive index changes with the inverse of temperature. Equation (2-7) is repeated as Equation (5-4) for clarity.

$$n_1 = n - 1 = \frac{77.6P}{T} \times 10^{-6} \quad (5\text{-}4)$$

where T is the temperature of the air in Kelvin and P the pressure of the air in millibars.

A curve was derived when the refractive index gradient between the ambient air and the hot flow at various temperatures is plotted for both wavelengths, as seen in Figure 5.3. The refractive index of the hot gas includes the effects of water introduced as a result of the combustion at high temperatures. It is notable that the refractive index difference at the visible and infrared wavelengths does not produce a significant separation in the refractivity graphs unlike the difference in standard deviation of the centroid movement measured at the two wavelengths.

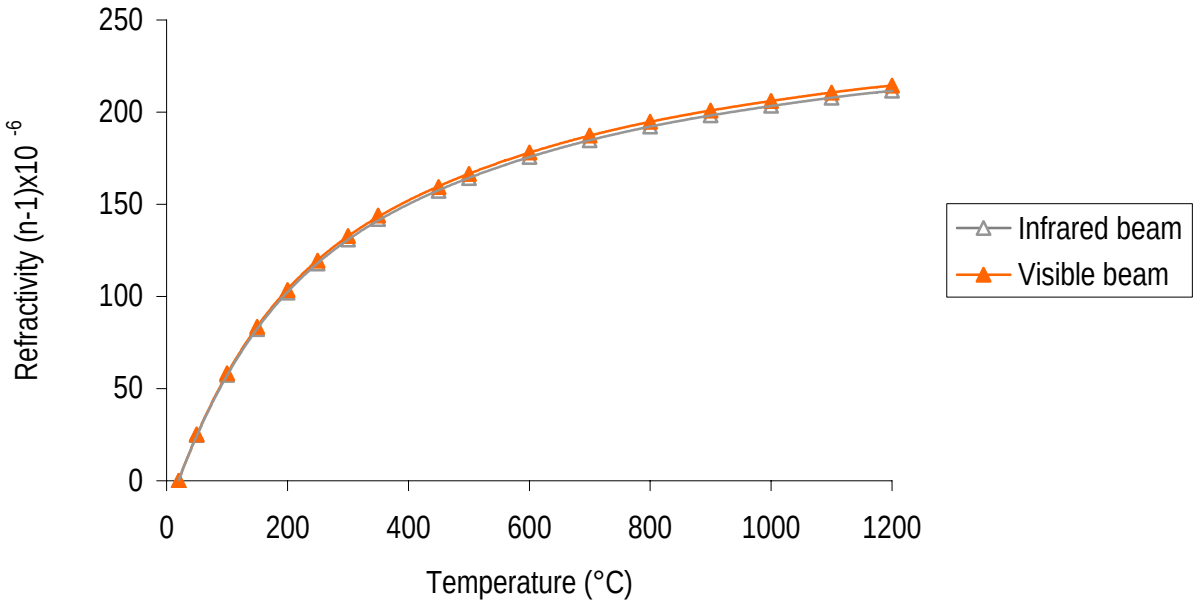

Figure 5.3: Theoretical refractive index calculated using Ciddor's equations for the gas conditions at each experimental point for the 632.8 nm and 4.67 µm beams.

Chiba [87] found that the standard deviation of the beam displacement could be linked to refractive index but changed with the inverse of temperature squared. Chiba's findings are discussed in Chapter 2, Section 2.5.5. Applying an inverse temperature squared function to the data shown in Figure 5.2 produces functions that provide excellent correlations. Figure 5.4 and Figure 5.5 show the curve fits to

the visible and infrared beams respectively. The function used to fit the standard deviation of beam displacement to temperature was;

$$\sigma^2 = \frac{a}{b + \left(1/T\right)^2} \tag{5-5}$$

where the coefficients are given in table for the two wavelengths studied.

Table 5.1: Coefficients for the beam displacement fitting function.

	a	b	Correlation (R)
Visible	0.00620025 ± 0.000469	1.8579 e-5 ± 0.2268 e-5	0.9860
IR	0.00622200 ± 0.000536	2.3115 e-5 ± 0.1686 e-5	0.9866

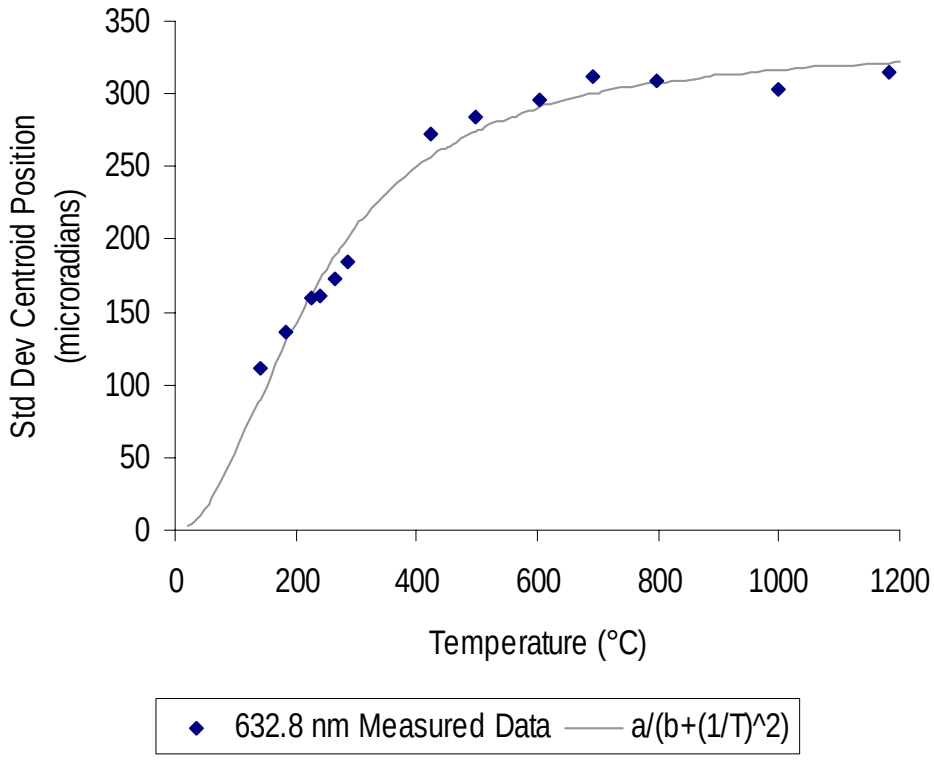

Figure 5.4: Curve fit to measured standard deviation of centroid position for the 632.8 nm beam over a range of temperatures.

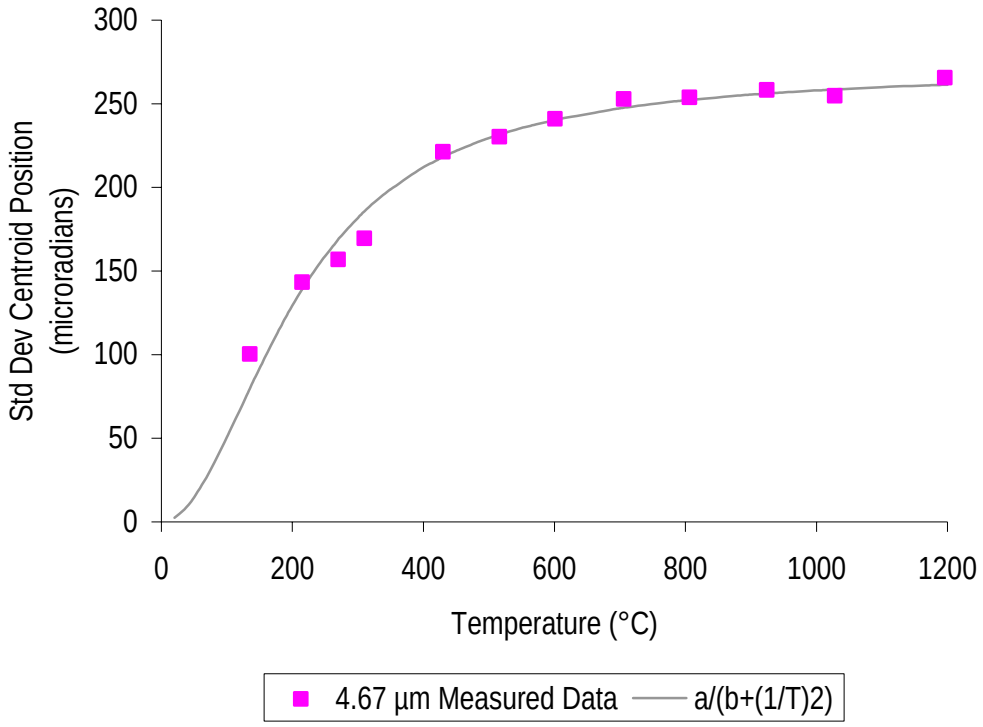

Figure 5.5: Curve fit to measured standard deviation of centroid position for the 4.67 µm beam over a range of temperatures.

It was hypothesized that the strong departure of the visible beam from the infrared beam, noted at higher temperatures (Figure 5.2), could be due to spurious energy detected by the pixels, seen in Figure 5.1 as isolated white pixels. These apparently spurious signals appeared to become more prominent as the temperature of the gas increases. Software windowing was performed in order to determine the effect of these pixels on the calculation of the standard deviation of the centroid position. Frame by frame the centroid was calculated using energy from the entire array. In each frame various sized windows, or "boxes", where placed around the calculated centroid position, for that frame, and a new centroid position was calculated using only the energy contained within the box. In this way a change in the centroid position due to changing array size, and hence inclusion of "spurious" signals was assessed. Figure 5.6 shows the result of these investigations. The calculation of the standard deviation of centroid position appears to be fairly independent of the "spurious" signals, with the centroid movement closely reflecting the movement shown in Figure 5.2 that was calculated using the full array for all window sizes used. This independence of centroid position standard deviation with collection area is a notable result.

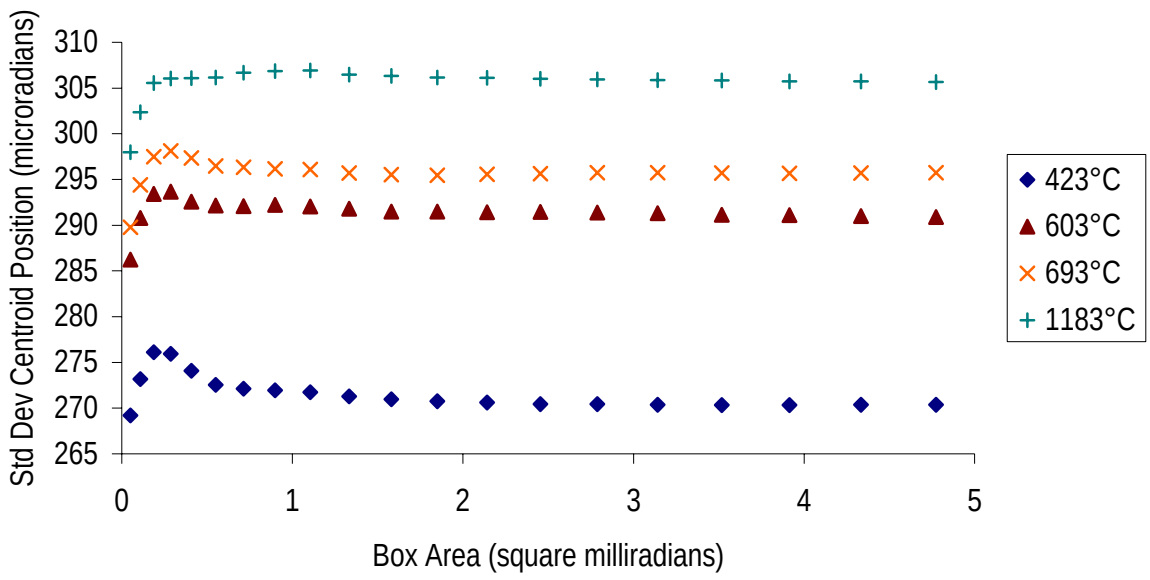

Figure 5.6: Standard deviation of the visible beam's centroid position calculated for various box areas placed each frame around that frames un-windowed calculated centroid position.

The reason for the difference between the 632.8 nm and 4.67 µm beams in the standard deviation of the centroid position, if not the spurious signals, could then only be linked to the difference in refraction of the beams. The actual propagation path would consist of the laser beam crossing multiple refractive index gradients at various angles. The initially small differences in angular deviation of the wavefront between the two wavelengths can be amplified as multiple refractive index gradients of various curvatures, or cell size, are encountered. Sirazetdinov et al. [109, 111] have noted the same difference in standard deviation of position for the various wavelengths when propagating through a jet engine exhaust, but offered no explanation.

5.2.2.2 Spot Area

To determine the spatial effects of the temperature on the beams a spot "area" calculation was used. The spot area was calculated by summing all the pixels containing counts above the threshold level; in this case 13.5% ($1/e^2$) of the maximum count of any pixel in the frame. Figure 5.7 and Figure 5.8 show the standard deviation of the spot area over the experimental temperature range for both the 632.8 nm and the 4.67 µm beams normalized by the standard deviation of the spot area of the beam when not

passing through the gas. It was observed that compared to the infrared laser beam the visible laser beam has ten times the standard deviation of the frame-to-frame spot area value. This order of magnitude increase in variability is related to break-up, seen as focusing and defocusing parts of the beam. The increase in break-up is due to the increased refraction of the visible beam compared to the infrared beam, and to the smaller diffraction limited spot size of the visible beam. That is, the visible beam is able to be focused to a spot that is smaller than the infrared beam.

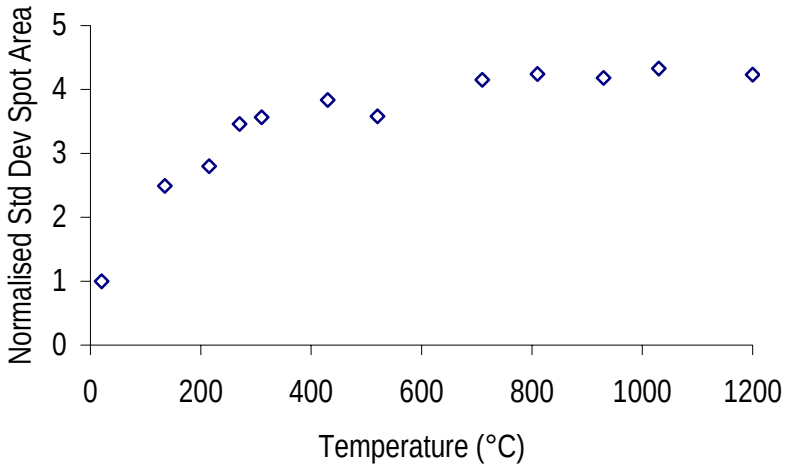

Figure 5.7: Normalized standard deviation of spot area for the 4.67 µm beam.

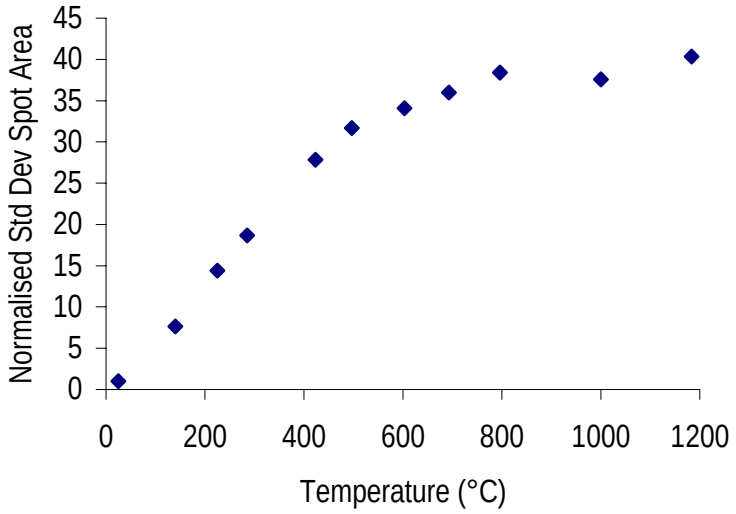

Figure 5.8: Normalized standard deviation of spot area for the 632.8 nm beam.

The spot area and its standard deviation increases with temperature, and tends to reach a plateau at high temperatures. Figure 5.9 and Figure 5.10 show plots of the ratio of the spot area to the standard deviation of the spot area over the experimental temperature range for both the 632.8 nm and the 4.67 µm beams. The results show the increase in standard deviation of the spot area matches the increase in spot area at the high temperatures as the ratio remains constant.

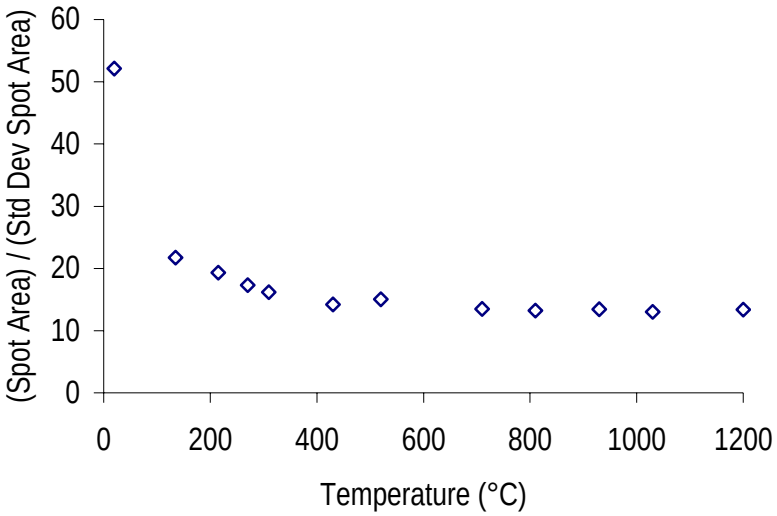

Figure 5.9: Spot area divided by standard deviation of spot area for the 4.67 µm beam.

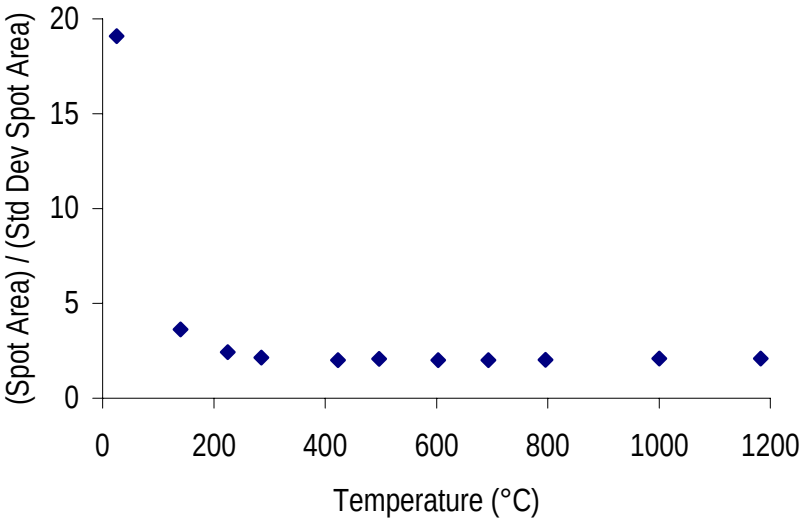

Figure 5.10: Spot area divided by standard deviation of spot area for the 632.8 nm beam.

It was observed that for both beams a definite asymptote is reached for temperatures larger than 400ºC. For the 4.67 µm beam the normalized value reached a level of 14 while for the 632.8 nm beam the value was only 2. These results highlight the spatial stability of the energy distribution of the infrared beam compared to the visible beam. Reaching an asymptote is not surprising if the phenomena of scintillation saturation is considered, in which the variance of the amplitude of a received signal saturates. This saturation effect has previously been linked to turbulence strength and path length in atmospheric conditions [92].

An alternative way to determine the effect of temperature on the spatial distribution of the perturbed beam for the two wavelength beams was to perform the same pixel count measurements over a range of viewing areas. This enabled the effect of viewing aperture sizes to be assessed and the spatial distribution of the beams to be better measured. Figure 5.11 and Figure 5.12 show plots of the mean pixel count at various window sizes for the infrared and visible laser beams, respectively. The plots have been normalized with reference to the beam passing through room temperature gas. This was done to enable the differences due to the effects of temperature to be better visualized. The plot of the mean pixel count for the 4.67 µm beam suggests there is only a few percent points difference in between the pixel counts when passing through unheated gas compared to the heated gas, indicating the spatial spread at 4.67 µm is not significant.

The plot of pixel count for the 632.8 nm beam (Figure 5.12) shows a significant difference in the pixel counts when passing through unheated gas compared to the heated gas. There is notable difference in the mean count as the temperature increases and the interrogation window increases. The increase in this difference as the interrogation window increased is quite apparent. The spatial area that the unperturbed 632.8 nm beam takes up is around 0.3 square milliradians, while for the 4.67 µm the area is seven times the size, 2.1 square milliradians. It is notable that the effect of the temperature on the pixel count is most pronounced at window sizes larger than the area of the unperturbed beam.

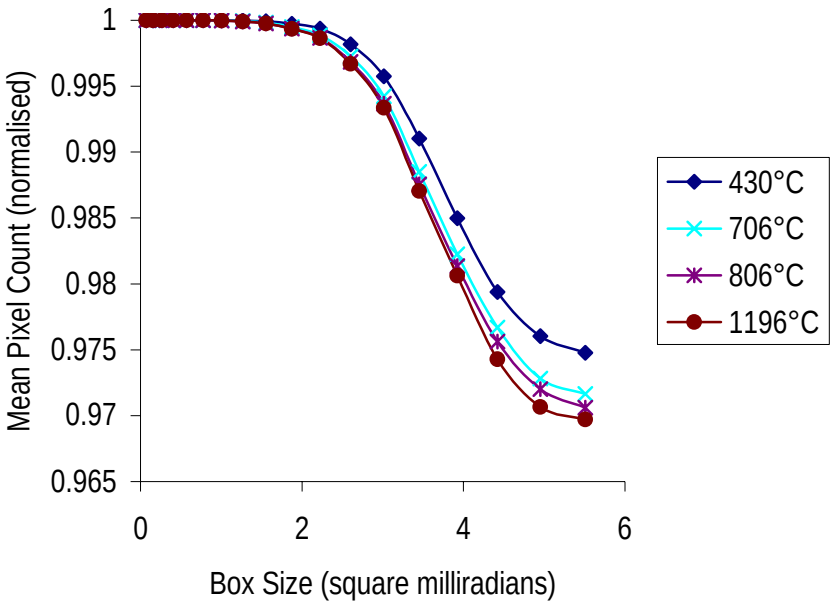

Figure 5.11: The average number of pixels containing counts that are over the $1/e^2$ threshold plotted against the interrogation window size for the 4.67 µm beam. Normalisation is done by dividing the data for each temperature by the data obtained when traversing the beam through ambient room conditions with the gas flow off.

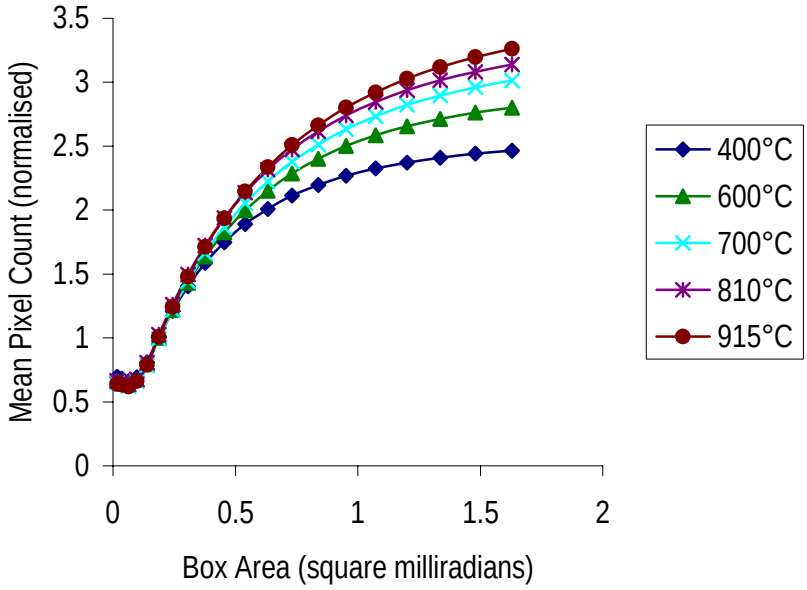

Figure 5.12: The average number of pixels containing counts that are over the $1/e^2$ threshold plotted against the interrogation window size for the 632.8 nm beam. Normalisation is done by dividing the data for each temperature by the data obtained when traversing the beam through ambient room conditions with the gas flow off.

The standard deviation of the beam count was also determined and is shown for the two beams in Figure 5.13 and Figure 5.14:. The infrared beam has no variation of pixel count in the area less than the unperturbed beam size, consequently the normalized standard deviation goes to infinity at small box windows. The visible and the infrared beam both show the standard deviation of pixel count increased as the temperature increased. The increase in count variance, with respect to the unperturbed beam, was greater for the visible beam than the infrared beam as the window sizes were increased. However when not normalized the standard deviation increases as the window size increases for both beams.

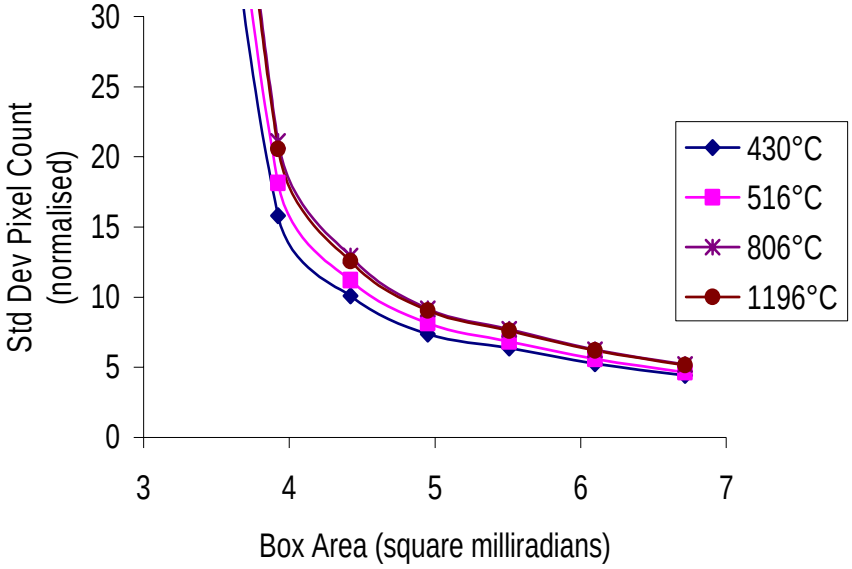

Figure 5.13: The standard deviation of the number of pixels containing counts that are over $1/e^2$ threshold plotted against interrogation window size for the 4.67 µm beam. Normalisation is done by dividing the data for each temperature by the data obtained when traversing the beam through ambient room conditions with the gas flow off.

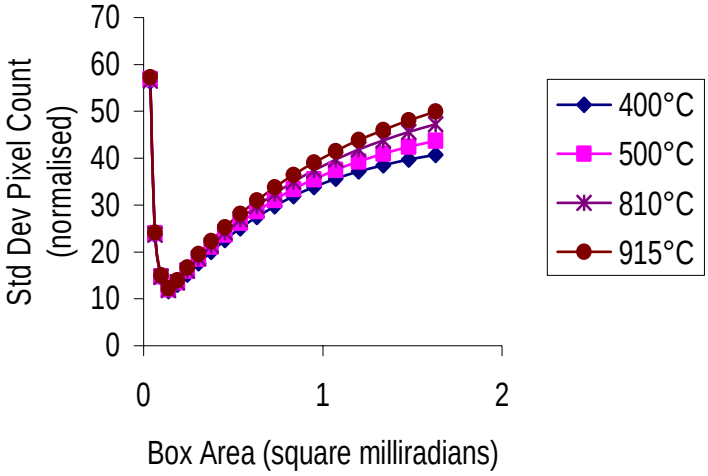

Figure 5.14: The standard deviation of the number of pixels containing counts over the $1/e^2$ threshold plotted against interrogation window size for the 632.8 nm beam. Normalisation is done by dividing the data for each temperature by the data obtained when traversing the beam through ambient room conditions with the gas flow off.

Figure 5.15 and Figure 5.16 show the non-normalised plots of the variation in pixel count for both the visible and infrared beams for different temperatures over the range of window areas. It is clear that there was an increase in the variation in the spread of the laser energy as the temperature was increased for a given aperture size.

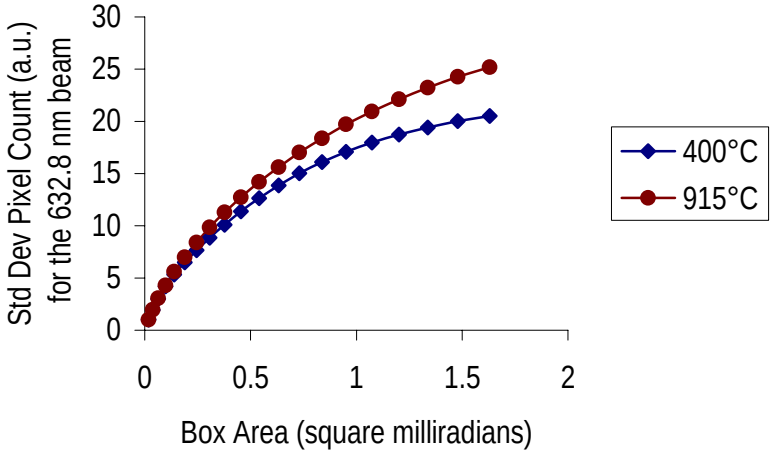

Figure 5.15: The standard deviation of pixel count at various integration window sizes for the 632.8 nm beam propagating through various turbulent gas temperatures.

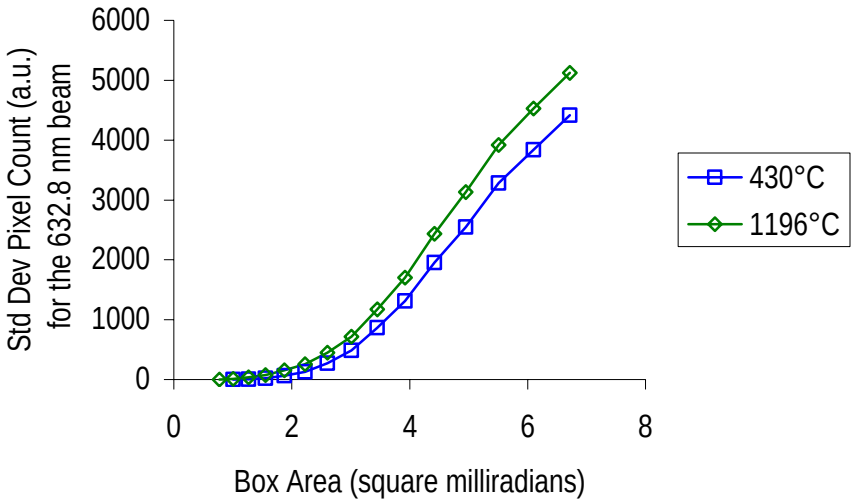

Figure 5.16: The standard deviation of pixel count at various integration window sizes for the 4.67 µm beam propagating through various turbulent gas temperatures.

Further analysis was performed to link not only the beam spread, but the energy distribution, to various sized software implemented windows and is discussed in the following section.

5.2.2.3 Distribution of Received Energy

The interrogation windows, or "boxes", of various sizes were placed around the average centroid position of the beam spot, calculated over the 2000 frames captured in each run. In the interrogation windows the number of pixels and counts per pixel where used to determine the energy distribution of the resultant beam. To measure the frame-to-frame fluctuation of the received energy, the pixel values were summed within these boxes and the standard deviation of the total count was calculated across the frames. The scintillation was referenced to the inherent scintillation due to the atmospheric path without the heated turbulent gas flow. This was done by "normalizing" the scintillation. The scintillation calculated when the beam passes through the heated gas was divided by the case when the heated gas flow is off.

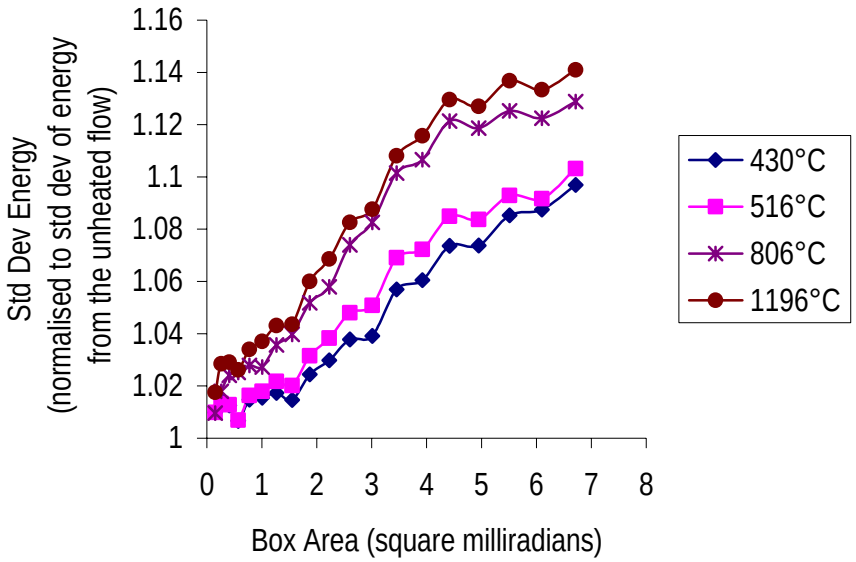

Figure 5.17: Measured standard deviation of energy determined at various integration window sizes for the 4.67 µm laser beam propagating through various turbulent gas temperatures, normalized by the standard deviation of energy in the corresponding window sizes when the laser propagates through an ambient temperature gas.

Figure 5.17 and Figure 5.18 show the result obtained for the 4.67 µm beam. Figure 5.17 clearly shows the received energy variance increases in all window sizes as the temperature of the gas flow increases, while in Figure 5.18 the increase in the standard deviation of the received energy as the size of the window is increased is most apparent.

It was calculated that the spot area (the number of pixels illuminated with a value greater than $1/e^2$ the maximum pixel value) for the unperturbed 4.67 µm beam equates to a square box of area 2.1 square milliradians. It is notable that the received energy variance does not roll-off until after this dimension and soon saturates as the window size increases. Figure 5.18 clearly shows the affect on the 4.67 µm beam.

The visible beam produced a result that was significantly different to the infrared beam. Figure 5.19 and Figure 5.20 show the result obtained for the visible beam. The greatest variation in received energy is at the smaller window sizes, though notably not the smallest. At large window sizes the variation in received energy, or “scintillation”, tails down to an asymptote.

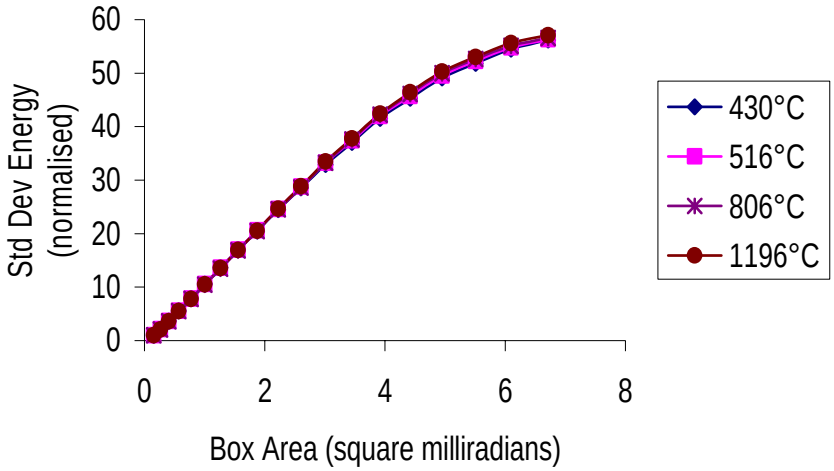

Figure 5.18: Measured standard deviation of energy determined at various integration windows sizes normalized to the standard deviation of energy in the smallest window size, for the 4.67 µm beam propagating through various turbulent gas temperatures.

It is significant that the average spot area for an undisturbed visible beam, which equates to a square box of dimension 0.3 square milliradians, coincides with the window size where the peak standard deviation of energy value occurs in both Figure 5.19 and Figure 5.20.

It is also worth noting that the shape of the function in Figure 5.19 appears to resemble an inverse chi-squared probability distribution. That is, there is a cross-over of the various temperatures curves such that at small box sizes the highest temperature has produced the least scintillation while at higher box sizes the highest temperature has resulted in the greatest scintillation. This cross-over occurs whether normalizing against an ambient temperature gas flow, as in Figure 5.19, or not normalizing. However, when normalizing against the standard deviation of energy in the smallest window size, at the temperature of interest, the standard deviation curves of Figure 5.20 do not cross-over as they decrease to a horizontal asymptote. This is because the standard deviation of received energy in the smaller apertures was measured as greatest at the lower gas temperatures. This appears counterintuitive as the higher temperature flow would be expected to produce the stronger refractive index gradients and greater energy variation in the imaged spot. However, at the lower temperatures the beam structure is less dispersed (as discussed in Section 5.2.2.2) such that the effects of beam wander more significantly affect the received energy count on a frame to frame basis. This explains why an increase in standard deviation of the received energy at lower temperatures and aperture size was measured.

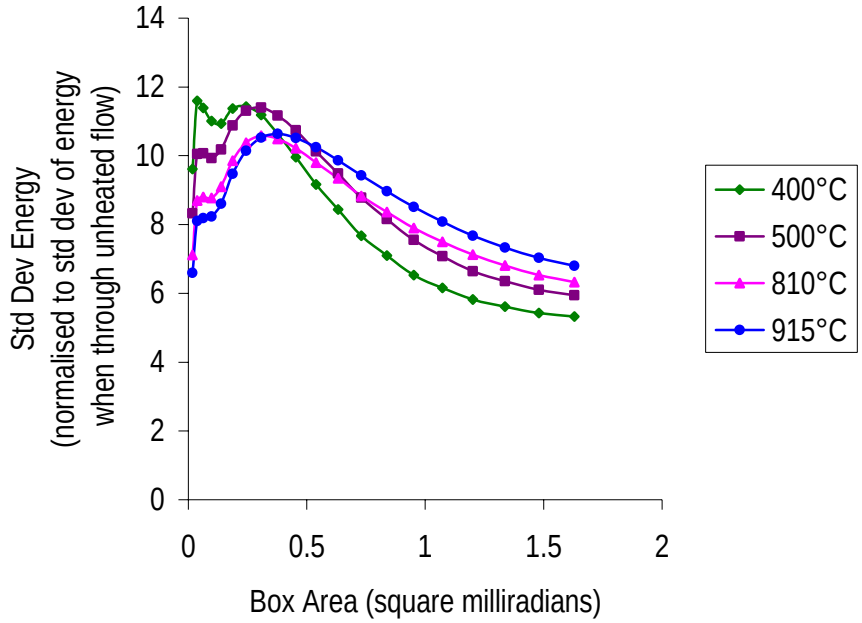

Figure 5.19: Measured standard deviation of energy determined at various integration window sizes for the 632.8 nm beam propagating through various turbulent gas temperatures, normalized by the standard deviation of energy in the corresponding window sizes when the laser propagates through an ambient temperature gas.

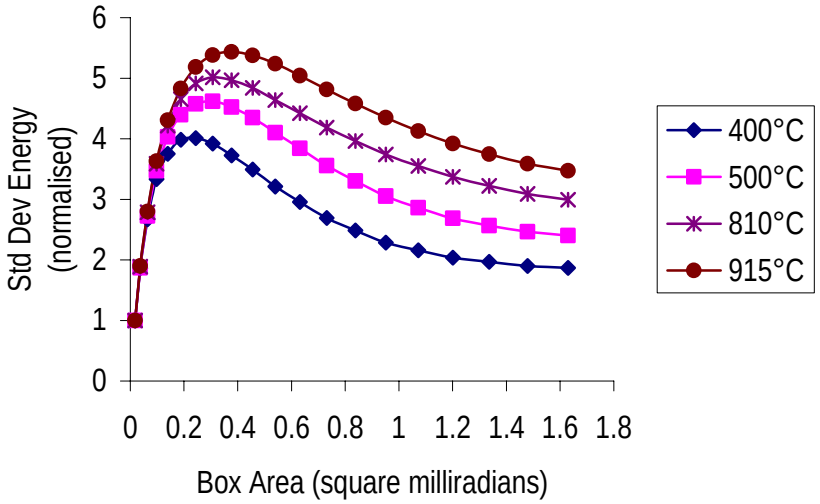

Figure 5.20: Measured standard deviation of energy determined at various integration windows sizes normalized to the standard deviation of energy in the smallest window size, for the 632.8 nm beam propagating through various turbulent gas temperatures.

Another measure of the beam disturbance is the average count per frame, or average 'energy', contained in an interrogation window. The average count per frame is determined by summing the values in all pixels having values above the 13.5% threshold in each frame and then averaging them over the 2000 frames. Figure 5.21 shows the result for the 632.8 nm and 4.67 µm beams. As expected the average count per frame tends towards 1 as the window size increases. Not all the energy is accounted for as pixels with values less than the 13.5% threshold are not included and consequently it is possible for the asymptotes to be less than 1 as the light is diffracted to be recorded over more pixels. The greater spatial spread of energy for the 632.8 nm beam is suggested as the graph is reaching an asymptote with a value less than that of the 4.67 µm beam asymptote. Furthermore it suggests the higher temperatures are causing greater beam break-up of the 632.8 nm beam than the 4.67 µm beam.

The increased break-up of the beams with temperature can also be seen in Figure 5.22 and Figure 5.23. In the figures the average count per pixel is derived from the total counts per frame divided by the number of illuminated pixels in the frames, averaged over all the frames. It is clear that as the temperature is increased, the beam is further dispersed, spreading the energy over more pixels and lowering the average count per pixel value.

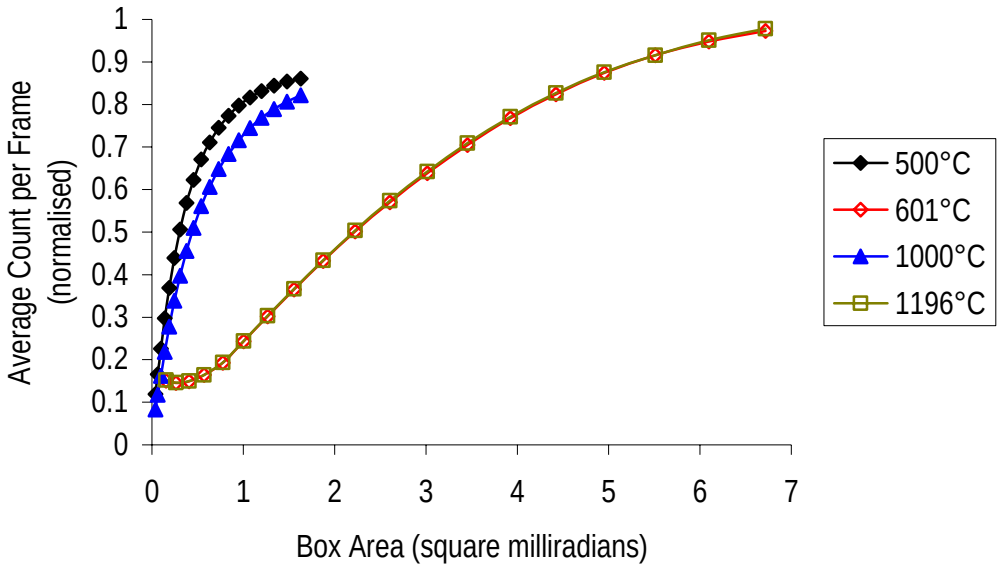

Figure 5.21: Average count per frame determined at various integration window sizes for the 632.8 nm (closed symbols) and 4.67 µm (open symbols) beams propagating through various turbulent gas temperatures, normalized by the average count per pixel in the corresponding window sizes when the laser propagates through an ambient temperature gas.

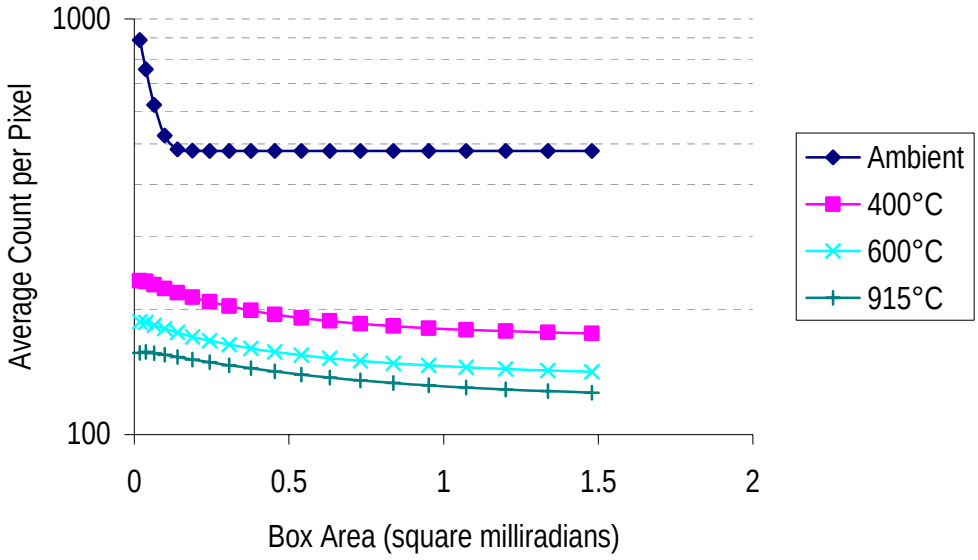

Figure 5.22: Average count per illuminated pixel calculated over a range of interrogation windows from a number of temperature measurements for the 632.8 nm beam.

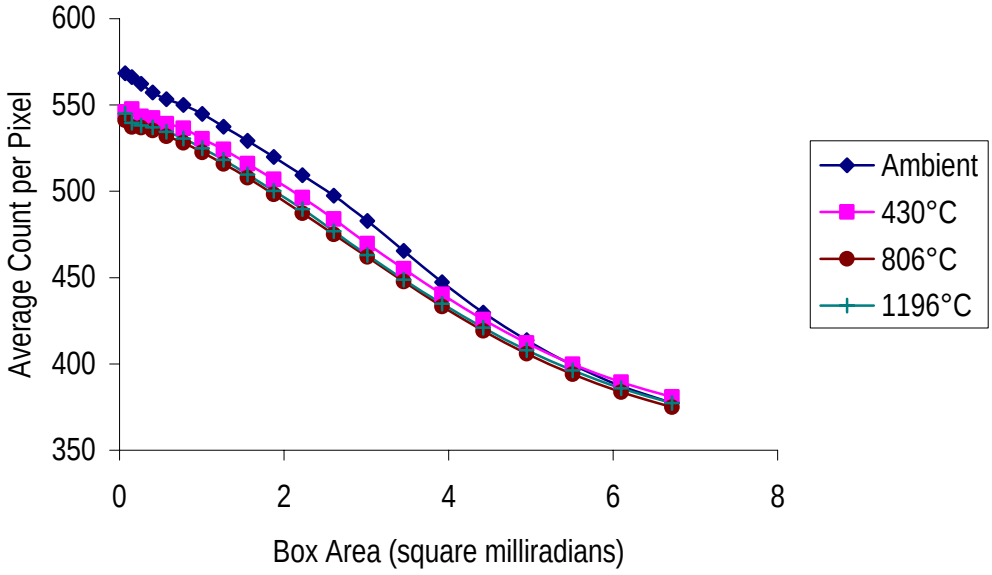

Figure 5.23: Average count per illuminated pixel calculated over a range of interrogation windows from a number of temperature measurement for the 4.67 µm beam.

5.3 Effect of Carbon Dioxide on Beam Propagation

The laser beams were propagated through a 700°C turbulent flow and the volume fraction of carbon dioxide varied up to a maximum of 10% to replicate conditions in a jet engine exhaust. The standard deviation of the resulting laser beam centroid displacement was calculated from the imaged data for both beams. The standard deviations of the centroid displacements are shown in Figure 5.24. The experimental results, shown in Figure 5.24, indicate that the standard deviation of the centroid displacement of the 4.67 µm beam is spread over a range of 10 microradians while the 632.8 nm wavelength is spread over 5 microradians. The statistical confidence levels determined in Section 4.4.1 are shown as confidence bars applied to the data (see Figure 5.24). The figure shows there is not sufficient resolution to determine a trend. It is clear the effect of CO_2 concentrations did not produce significant beam displacement at both 632.8 nm and 4.67 µm. The conclusion that can be drawn is that the variation in the beam centroid displacement, as a result of introducing CO_2 for both the visible and infrared laser beams, is non-existent; the differences being within the experimental uncertainty across the range of conditions measured.

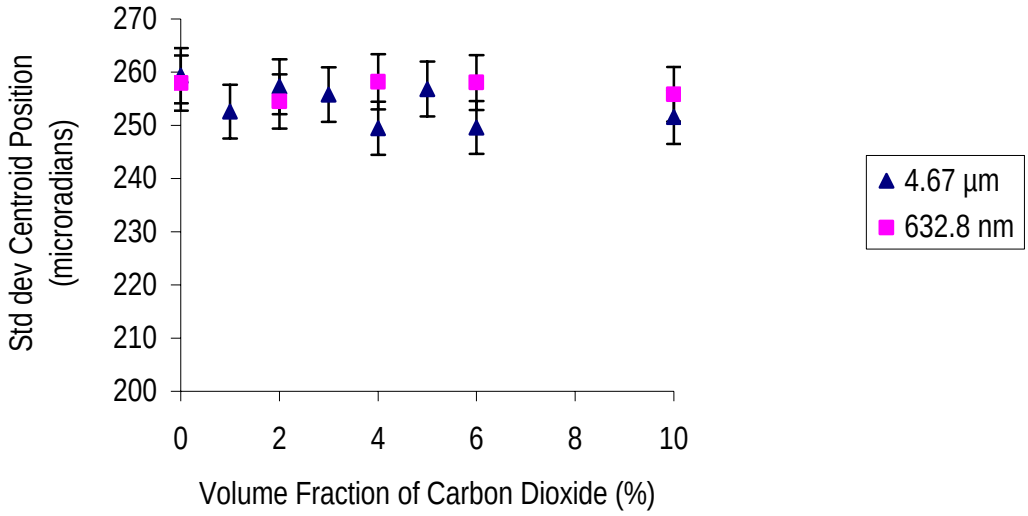

Figure 5.24: Standard deviation of centroid position for 4.67 µm and 632.8 nm beams versus carbon dioxide percentage by volume in H_2 flame at constant temperature of 700°C.

The effect of carbon dioxide and water in the gas mixture was expected to alter the dispersive properties of the mixture. The refractive index of the medium is a summation of the effects due to density, the continuous refractive index, and molecular absorption properties, i.e. the "anomalous" component of the refractive index for a given propagation wavelength. The refractive index is proportional to the gas density. As the air temperature increases the molecules are spaced further apart, reducing the density of the gas, which decreases the refractive index. In the hot gas flow the refractive index is lower than the surrounding air. Introduction of a volume of CO_2 in place of a volume of air results in an increase in density and refractive index for a given temperature. In the case of heated gas flow, the refractive index gradient between the surrounding air and the gas jet would be decreased and the laser beam displacement could be expected to be reduced.

Water is added into the experiment as a by-product of burning hydrogen in the H_2/air mixture. The gas mixture density is altered as a 9% volume fraction of H_2 replaces air when setting the flow temperature to 700°C at the laser propagation height. In this case there may be expected to be a small increase in the laser beam displacement, contrary to the effect described for carbon dioxide.

The effect of anomalous dispersion was considered for the 632.8 nm and 4.67 μm wavelengths. Water has dominant absorption lines at 0.94, 1.13, 1.37, 1.87, 2.7, 3.2 and 6.3 μm, while carbon dioxide absorbs at 2.0, 4.3 and 15 μm [152]. Note that the effect of the 0.94 μm band on 632.8 nm laser is accounted for in the "continuous" refractive index formulation for water (Section 2.2.2.1.1). For carbon dioxide the 4.3 μm band is the strongest and nearest of the lines. Calculation of the effect of the absorption lines on the refractive index was done using the Kronig-Kramer equation [7];

$$n^2 - 1 = \frac{Ne^2}{\varepsilon_0 m} \sum_s \frac{f_s}{\omega_s^2 - \omega^2} \tag{5-6}$$

where s is the number of molecular oscillators, represented as a weighting factor known as oscillator strength, f, in which $\sum_s f_s = 1$, ω_s is the absorption frequency, or natural frequency, and N is the number of molecules per unit volume that will oscillate.

Figure 5.25 shows that this band has only a minor influence on the 4.67 µm beam encountering a CO_2 molecule.

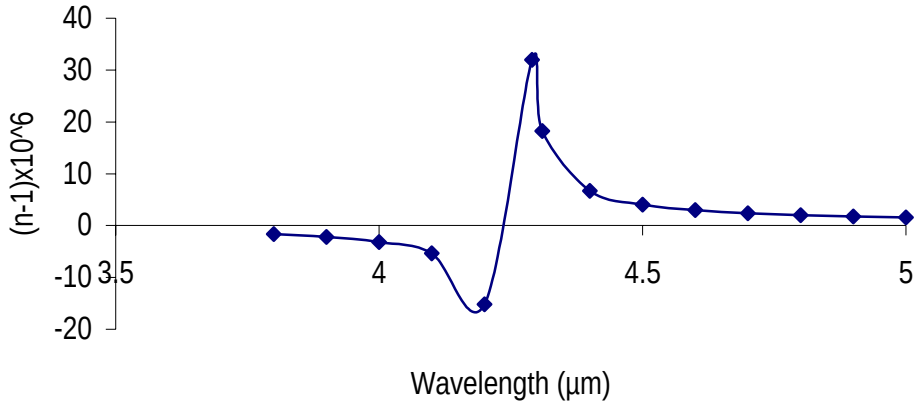

Figure 5.25: Calculated refractivity change due to 4.25686 and 4.27965 µm absorption lines in a 3% CO_2 per volume in air.

At 4.67 µm there is only ~2% increase in refractive index compared to standard air. The effect of increased temperature is not considered when using this equation. An increase in temperature can also change the magnitude of the anomalous absorption effect. Simeckova [49] used the HITRAN database to determine the oscillator strength for a given species and temperature. Her formulations include the effect of temperature on the statistical weight of the number of molecules in the different energy levels. The molecular distribution follows a Boltzmann distribution in the upper and lower energy states and the temperature increase affects both the emission line intensity and width [19, 153]. The effect of this on CO_2 refractivity is not calculated as it is a secondary effect with the nearest significant absorption line at 4.3 µm. Furthermore, increasing temperature will only decrease further the effect of anomalous absorption as the available vibration states of the molecules are more populated. Popov & Shvartsblat [154] and Penner [155] showed results that have the line width and strength decreasing with increasing temperature.

The calculations using Ciddor's recommended equations (Section 2.2.2.1.1) show that the inclusion of carbon dioxide into the flow, in place of air, does produce a slight change in the refractive index gradient for a fixed temperature as seen in Figure 5.26. The 4.67 µm is affected more than the 632.8 nm line which suggests the effect of anomalous absorption of the 4.3 µm band is represented by Old's equation

[38]. The net change in refractive index is minor as it corresponds to a temperature change effect of less than 25°C.

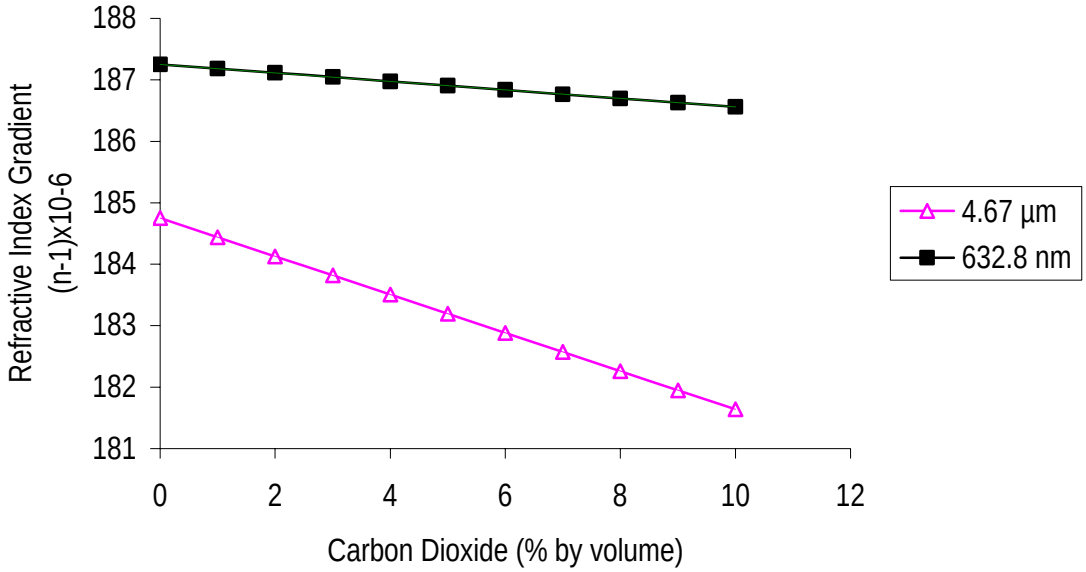

Figure 5.26: The calculated effect of changing carbon dioxide levels in the gas on the refractive index gradient between dry air at 20ºC and 700ºC produced from combusting H_2 at 4.67 µm and 632.8 nm.

The laser beam displacement measurements were therefore consistent with the existing theory, in that no significant effect on the beam propagation due to the inclusion of carbon dioxide was measured for the conditions studied.

5.4 Turbulence Intensity and Eddy Size

The turbulence intensity and eddy sizes within the flow were altered by placing perforated plates over the nozzle outlet. Fixing the hole diameters of the plates and varying the blockage ratio, or fixing the blockage ratio and varying the hole diameters provided control over the mixing dynamics. Measurements were taken at a fixed height of 85 mm above the nozzle with various plates solidities and hole diameters. The temperature at this location was maintained at 500°C for all runs. The resulting laser beam displacements are shown in Figure 5.27 for the cases where the hole diameters were fixed and the blockage ratio was altered.

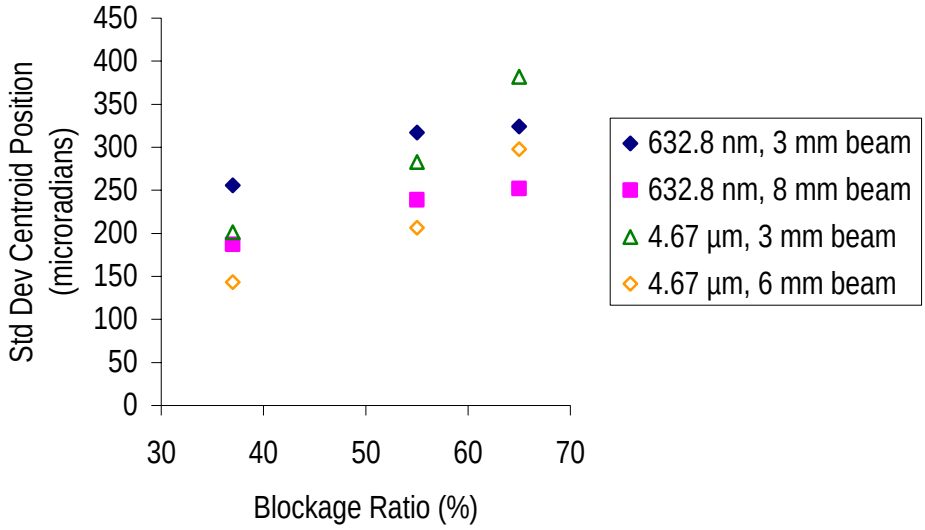

Figure 5.27: Beam displacements of the 632.8 nm and 4.67 µm laser beams with diameters of 3 mm, 6 mm and 8 mm traversing the 500°C turbulent flow at a height of 85 mm above the 5 mm perforated plate at various plate solidities.

Noteworthy is that the 632.8 nm beam displacement appears to be flattening at high blockage ratios while the 4.67 µm beam displacement is growing in an exponential manner. For the high blockage ratios the 4.67 µm beam moves further than the 632.8 nm beam. In fact the 4.67 µm beam moved beyond the apparent variance limit that was previously seen (Section 5.2) at temperatures above 600°C. Furthermore, refractive index effects alone were previously found to move the 632.8 nm beam further than the 4.67 µm beam.

Flow characterization results presented in Chapter 4 indicate that there is a minor increase in the integral length scale with increased blockage ratio (Figure 4.13). More significant were the increase in magnitude of the standard deviation of the velocity fluctuations over the flow path with increased blockage ratio and the increase in the width from the core centre to the sheer layer (Figure 4.15). These results suggest the increased path length through an extended turbulent region has resulted in the increased beam displacement. It is not understood why there is a cross-over of the visible and infrared beams for the high blockage ratio case, although it is noted the displacement trend is the same as the displacements have still increased for both beams with the increased blockage ratio.

The second test results, shown in Figure 5.28, are cases where perforated plates of different hole diameter but similar (~50%) blockage ratio were used to generate the "grid" turbulence. The results show that the 8 mm hole produced 1.1 times more beam displacement than the 6 mm hole and 1.3 times that of the 3 mm hole. Changing the hole diameters was expected to scale the eddy current sizes in the flow, however, turbulence intensity needed also to be considered because measuring at a fixed height meant turbulence intensity became a variable too. Applying the power-law relationship for turbulence;

$$\left(\frac{u'}{U}\right)^2 = A\left(\frac{X}{D}\right)^n \tag{5-7}$$

where *n* is -1.3, it was predicted that the 8 mm hole plate will generate 1.5 times the turbulence as the 6 mm hole and 3.5 times that of the 3 mm hole at this distance.

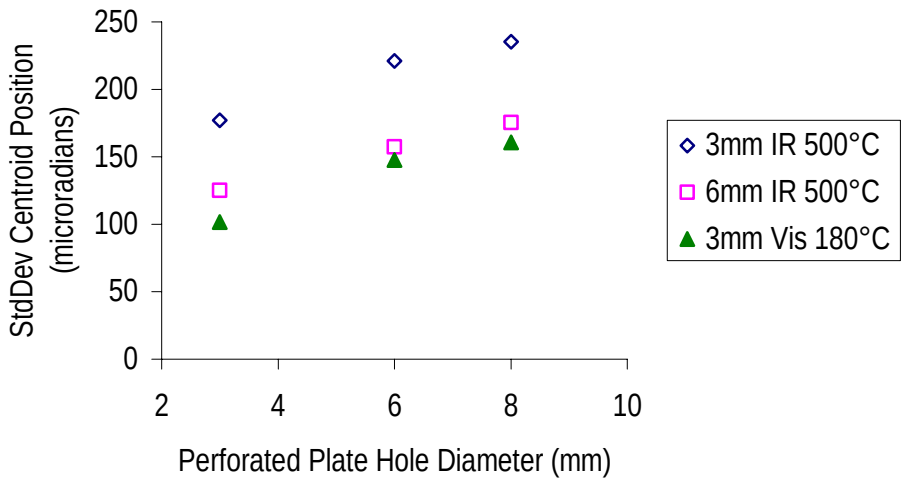

Figure 5.28: Standard deviation of beam displacement versus perforated plate hole diameter for perforated plates with a blockage ratio ~50% with the 4.67 µm infrared and 632.8 nm visible laser beams and traversing the flow at a height of 85 mm above the nozzle and through a temperature of 500°C and 180°C respectively.

The flow characterization results showed that the standard deviation of the velocity fluctuations increased with increasing hole diameter, although the turbulence intensities remained similar as the bulk velocities also increased with hole diameter. However the gas velocities differences are assessed as not being significant. In the cases studied the velocity of the gas is fast enough to provide a new gas volume

for the beam front to propagate across each frame. The image frames were collected at a rate of 10 Hz for the visible beam and 100 Hz for the infrared beam. Even at the lowest gas flow velocities, considering the average velocity and the standard deviation of the velocity fluctuation, the beam front for both lasers will intersect a new region of gas for each image instance. There should be no correlation between frames in all cases. Also the pulse length for the infrared beam and the "effective" pulse length of the visible beam are temporally short enough to ensure the flow is temporally frozen while the beams traverse the gas flow. ("Effective" because the pulse length of the visible beam, although the beam is continuous, is set by the integration time of the intensified CCD camera.) This meant that one pulse only was captured per image so that correlation effects did not need to be considered within the frames.

The flow characterisation results revealed a strong increase in turbulence length scale with increased hole diameter (Figure 4.18). The path lengths across the flow appeared very similar (Figure 4.17) and suggest path length differences were not a strong contributor to the propagation results for the changing-hole-diameter cases. These results indicate that integral length scale is a principal factor, besides wavelength and beam diameter, that affects the beam displacement given temperature and path lengths are similar.

Further analysis determined that the average standard deviation of displacement per mm hole diameter change in the perforated plate was 11.36 microradians, using a linear fit to the points in Figure 5.28. An exponential best fit was also applied and the average standard deviation of displacement was determined to increase as $e^{0.074X}$ where X is the hole diameter size. Over these hole diameter sizes the integral length scale was also measured to be changing. A linear-fit calculated a rate of change of the integral length scale as 0.558 mm per mm hole diameter or applying an exponential fit was determined to increase as $e^{0.169X}$ where X is the hole diameter size.

To view the relationship between integral length scale and beam displacement the movements shown in Figure 5.28 where averaged and plotted against the integral length scale calculated (Figure 4.18) for the hole diameters being tested. The graph is shown in Figure 5.29. The displacements increase with integral length scale. There is a notable roll-off of the displacement but more integral length scale data points, obtained using perforated plates of other hole diameters, would be needed to confidently quantify the trend.

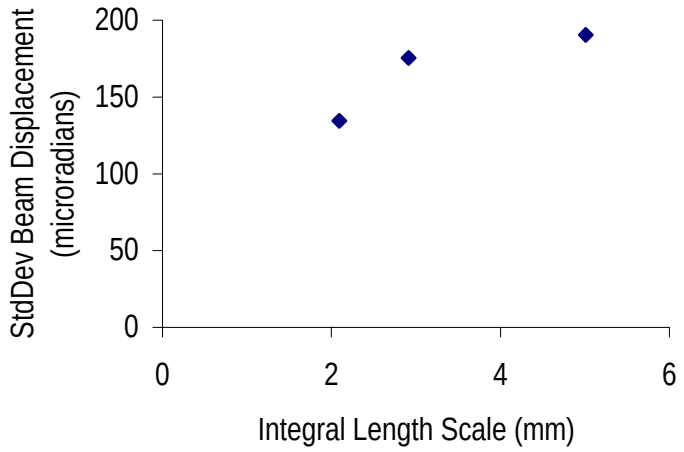

Figure 5.29: The average standard deviation of beam displacement for the cases measured in Figure 5.28 plotted against the integral length scale determined for the flow conditions.

5.5 Laser Beam Diameter

The propagation of beams has been described mathematically for uniform spherical and plane waves with assumptions made on the scales of turbulence. In the parametric experiment the laser beam is in fact a truncated Gaussian spherical wave so the mathematical predictions may not be precise. However, the theoretical and practical work of others [88, 94, 97, 107] tend to show that in general the beam displacement is related to the beam diameter. Most expressions describe beam displacement as being a product of the structure constant, the path length cubed and the inverse of the third root of the beam diameter. This considered, the standard deviation of the beam displacement for a collimated spherical beam passing through an iris and then propagating through a turbulent flow was expected to produce a beam displacement related to the iris size, the turbulence scales and the path length.

Measurements of the standard deviation of centroid motion for the two wavelengths are shown in Figure 5.30. The beam displacement in Figure 5.30 decreased with increasing beam diameter for a given wavelength and turbulence condition. Measurements were performed at the same temperature and beam conditions for the 632.8 nm and 4.67 µm beams with and without Perforated Plates (PP holes diameters 5 mm and solidity 55%). Experiments were also conducted with the 632.8 nm beam traversing

the open jet at 315°C and with a perforated plate with 5 mm diameters holes, 55% blockage ratio, at 280°C.

Best-fit power curves were added to the measurements as shown in Figure 5.30. The results show the beam displacement to be closely proportional to the inverse third root of the beam diameter as predicted theoretically [88] in turbulent atmospheric conditions.

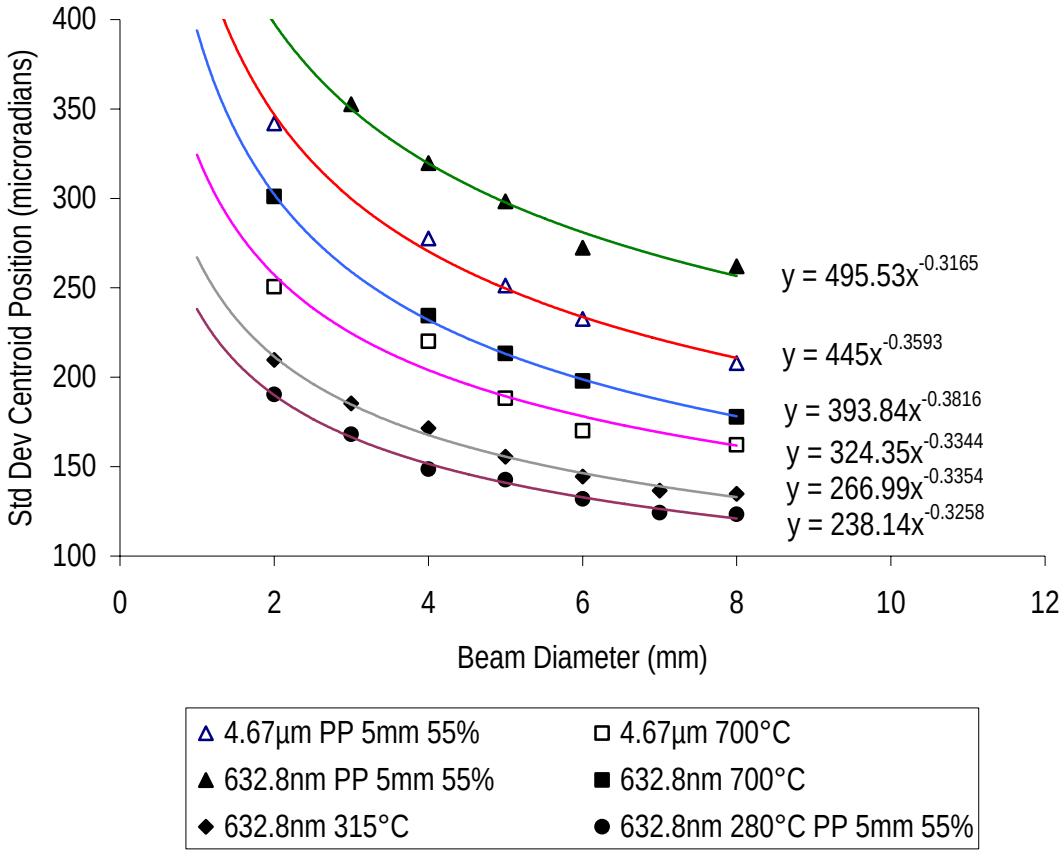

Figure 5.30: Beam displacement versus beam diameter for 632.8 nm and 4.67 µm beams with and without a 5 mm diameter perforated plate over the nozzle with a 55% blockage ratio.

From the data points in Figure 5.30 the effect of adding the perforated plate was quantified. The 632.8 nm beam displacement was increased by 36% while the 4.67 µm beam displacement was increased by 32%, a similar amount. The insertion of the perforated plate, with the resultant changes in the turbulence eddy scales and intensity, has not produced any significant difference in propagation effects when comparing the two wavelengths. However, the results, for the given experimental confidence levels,

show there is a significant difference in beam displacement between wavelengths for a given aperture, or beam size. The visible beam on average moved 14% or 8/7ths more than the infrared beam. A corollary would be that the 4.67 μm wavelength beam passing through a certain size iris will produce approximately the same beam displacement as a 632.8 nm wavelength beam passing through an iris 8/7ths times larger.

5.6 Path Length

A path length experiment was performed with the 8 mm diameter perforated plate with blockage ratio 53% using two tests (see Section 4.4.5). In the first test the laser beams were propagated at various heights (X) above the nozzle. The temperature was adjusted to 300°C for each (X/D) distance tested. The results showing the standard deviation of beam displacement are plotted in Figure 5.31. The beam displacement standard deviation is seen to increase with increased height above the nozzle despite the peak temperature being maintained at 300°C at all heights. Flow characterization revealed in these cases (Figure 4.25) that the integral length scale increased with height above the nozzle and so too the path length increased (Figure 4.23 and Figure 4.24). The results analyzed in Section 5.4 revealed the beam displacement standard deviation increased with increasing integral length scale. The impact of path length on the beam displacement, although expected to play a role [122], was not clear in this test. Comparisons with the integral length scale test (Section 5.4) show the movement is more than expected, if considering the effect of integral length scale alone. Further data was obtained in a second test.

In the second test data were collected by keeping the temperature constant at the nozzle exit and varying the height of propagation. This meant the temperature was different at each propagation height, with the temperature decreasing as height increased. The peak temperature measured at each distance downstream was 765°C, 571°C, 408°C and 238°C. The beam displacement was expected to decrease as the temperature decreased down-stream. Figure 5.32 shows this was not the case. The expected trend was being counter-acted as the beam displacement remained almost constant with distance down-stream. The reason for the increase in beam movement variation is thought to be due to the increased path length of the hot turbulent region resulting from the gas jet expanding downstream.

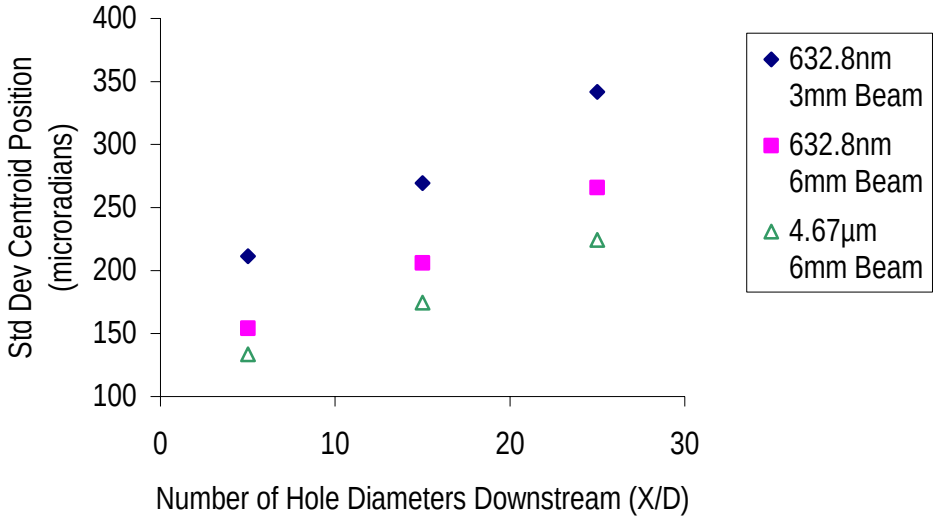

Figure 5.31: Standard deviation of centroid displacement of the 632.8 nm and 4.67 µm beam Three series of runs with temperature fixed at each position at 300°C, Perforated Plate 8mm at 53%.

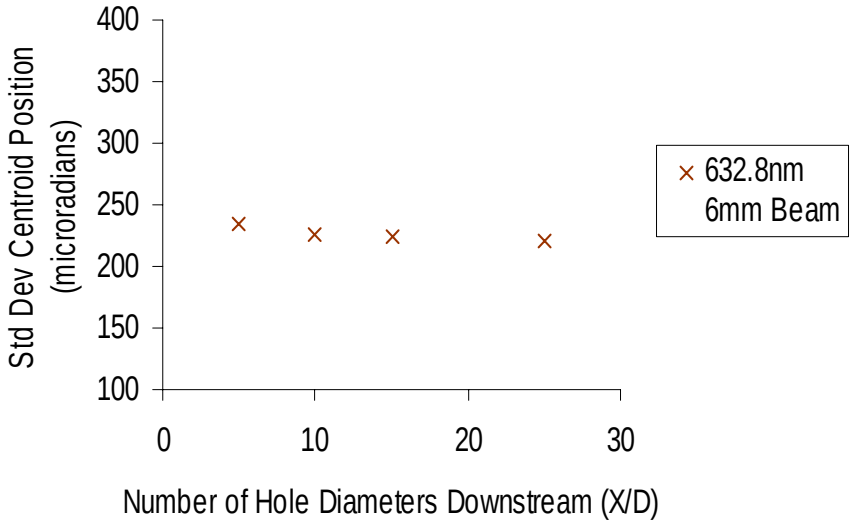

Figure 5.32: Standard deviation of centroid displacement of the 632.8 nm beam when traversing the flow at different heights above the nozzle with temperature decreasing with distance downstream. The nozzle exit temperature and flow conditions were fixed.

The flow characterization experiments performed on this set-up revealed the integral length scale, as well as the path length, were both again increasing with increasing height above the nozzle (Figure 4.31, Figure 4.32 and Figure 4.33). It is noted that the turbulence intensity in the shear layer decreased as the

height above the nozzle increased. Turbulence intensity was determined not to be a significant factor in these experiments (Section 5.4). However, the effect of path length can not be easily decoupled from the other parameters. Certainly in both cases, fixed and varied temperature down-stream, there were factors other than temperature, such as turbulence eddy size and path length involved, in the displacement of the beam.

5.7 Summary

Laboratory based parametric experiments were conducted to study the propagation of both 632.8 nm and 4.67 μm laser beams through various hot turbulent flow conditions. Beam displacement and energy distribution was seen to depend strongly on wavelength as expected. Beam displacement for both wavelengths was measured for a temperature range from ambient to 1200°C. The displacements were closely matched until above 400°C, at which point a greater increase in displacement of the visible beam was observed. The displacement of both beams was seen to be asymptotic above 600°C. This effect is similar to the phenomena of scintillation variance saturation that has been described in atmospheric laser beam propagation scenarios.

An analysis of the beam break-up was undertaken at high temperatures for both the 632.8 nm and 4.67 μm beams. The variance of the received energy was seen to increase with increasing receiver aperture size until the aperture size reached the dimension of an unperturbed beam. For the 632.8 nm beam this was clearly seen, with the energy variance increasing to a peak around the dimension of the unperturbed beam and then decreasing towards an asymptote for larger aperture sizes. In the case of the 4.67 μm beam the saturation of variance appeared to occur near the unperturbed beam diameter with no subsequent decrease in variance noted as the aperture size further increased.

The effect of temperature on the energy variance was also measured to be different for both the 632.8 nm and 4.67 μm beams and receiver aperture sizes. In both cases the temperature affected the variance. An increase in gas temperature was generally associated with an increase in the variance of the received energy in a given aperture size. The exception being in the case of the 632.8 nm beam at aperture sizes less than the unperturbed beam diameter, where higher temperature caused less energy variance.

A measurement of the spatial distribution of the energy showed that increasing the gas temperature produced an increase in spatial variance for both beams with a subsequent decrease in the average energy per illuminated pixel across all receiver aperture sizes.

The effect of increasing the volume fraction of carbon dioxide on the refractive index was also determined. The CO_2 levels and the temperature were adjusted to represent the exhaust plume of a jet engine. For CO_2 levels up to 10% and a temperature of 700°C it was found that the effect of CO_2 on the refractive index and beam displacement at the wavelengths studied was so small as to be within the experimental uncertainty of the experiment.

A lean mix of hydrogen and air was combusted to produce the high temperature flow. The resulting H_2O by-product was calculated to have minimal effect on the refractive index, especially when compared to the effect of temperature.

Beam displacement was found to be closely related to the inverse of the beam diameter cubed for the truncated Gaussian spherical beam. This result matched theoretical and experimental works of others. The dependence of beam displacement on wavelength was noted, with the 632.8 nm beam displacement standard deviation approximately 8/7ths times more than the 4.67 μm beam for the case studied.

A number of additional experiments were conducted under various flow conditions. Parameters such as turbulence intensity, length scales and path length were altered. An analysis of the results showed that length scale and path length were significant parameters. An increase in the integral length scale resulted in an increase in the standard deviation of the beam displacement. Similarly, an increase in the path length through the hot flow produced an increase in beam displacement.

Chapter 6

General Discussion

6.1 Introduction

In Chapter 5 data were presented on the laser beam propagation effects due to changes in flow temperature and composition, laser beam wavelength and diameter, path length, and turbulence intensity and eddy size. In this chapter the results of the simple jet parametric study are further discussed with reference to the work of others.

The jet engine study documented in Chapter 3 provided data on laser beam propagation through the exhaust of a jet engine. The analysed data from this study is also discussed in this chapter with reference to available literature, in particular the previously reported studies of laser beam propagation through jet engine exhausts.

6.2 Propagation through a Jet Engine Exhaust

The jet engine study, presented in Chapter 3, not only allowed the effect of the laser beam propagation to be studied through an engine exhaust but also the parameters of the flow field to be determined indirectly using the laser beam. A number of key findings from the jet engine study are discussed in this section and related to, or compared with, the work of other authors where relevant.

6.2.1 Turbofan vs Turbojet

The difference in the effect of turbofan and turbojet engines on laser beam propagation was not found to be reported elsewhere. The nearest similarity is that reported by Sjöqvist et al. [112] in which a jet engine's combustion product is mixed with free-streaming air to simulate flight conditions. The temperature of the free-streaming air is not reported. They report an increase in the standard deviation of the centroid of the beam (around 30%) when the free-streaming air was applied at the two positions measured. The laser beam was propagated parallel to the exhaust direction and at two positions offset to the centre-axis of the flow.

In the system level study the by-pass air was heated from 10°C to 68°C above ambient as the engine changes from idle to full power. The air was used to produce a by-pass ratio of 1:1 (turbofan). The by-pass air was derived from a second engine. The application of the by-pass air did not produce a significant change in the laser beam centroid for most laser beam crossing aspects. An effect on the beam was noted when the laser beam crossed close (0.5 m) to the 0.16 m diameter nozzle. At this point the turbofan engine caused a slight increase in the centroid variance when compared to the turbojet engine. More notable at this crossing point was the transition in beam movement that occurred when the laser beam propagation path was directed at different heights through the plume. A notable increase in beam movement occurred as the beam crossed the core air / by-pass air mixing layer and when the engine thrust was increased. However, the turbojet engine produced more change in beam movement than the turbofan engine (see Section 3.3.4) suggesting there is a more distinct 'edge' to the turbulent region close to the nozzle outlet for the turbojet engine. A DIRCM should avoid directing a laser beam through this region.

6.2.2 Turbulence Spectrum – Integration Time and Frame Rate

A novelty of the jet engine study was the use of variable integration times and frame rates to deduce the turbulence spectrum characteristics of the jet engine flow. Lower frequency gas fluctuations were studied by varying the frame rate of the imaging camera, while higher frequency effects were studied by varying the integration time of the camera to alter the number of pulses collected in the sampling frame.

Changing the frame rate of the camera and measuring the beam centroid movement showed there was a difference in the *x* and *y* range of beam centroid movement rates. The *x*-direction centroid power spectrum was seen to be reasonably flat across the frequency range while the *y*-direction centroid was measured to have more power in the low frequencies. Simply expressed, in the *y*-direction (across the plume) the greatest variation in movement was at the lower frequencies, or greatest time separation between frames. The distribution in the power spectrum of the centroid motion remained reasonably constant for time separations greater than 5 milliseconds.

The difference between the *x* and *y* centroid motions would be linked to the greater change in velocity and temperature gradients in the vertical direction across the beam front. The temperature gradient in the y-direction would tend to increase the beam steering in the vertical, or *y*, direction. In Section 3.2.3 it was shown that a parcel of gas from the jet engine will traverse the laser beam front in 40 – 80 µs. A low frequency movement in the *y* direction at less than 200 Hz (5000 µs) indicates the presence of large and slow moving temperature gradients across the vertical direction of the beam. The engine thrust is in the *x* direction which would impart greater velocity in the *x* direction than the *y* direction.

Changing the integration time of the camera showed that the centroid motion decreased with increasing integration time. This effect was linked (Section 3.3.5) to Einstein's random walk [137], where the variance of uncorrelated events decreases by the square root of the number of samples. However, it was noted that the decrease in centroid variance was not strong until the integration time reached ~100 µs. This suggested that there was reasonable correlation between centroid movements until this time. Notable is that the correlation time decreased as the engine thrust increased (refer to Figure 3.13 and Figure 3.14). The result is not surprising, if the velocity of the gas and the laser beam front diameter is considered. As mentioned, a parcel of gas from the jet engine was determined to traverse the laser beam front in 40 – 80 µs. The slower moving parcel of gas will remain in the path of the beam front for longer, so that more pulses will traverse the same, or very similar, gas field in a given time. In the same way, the collection time can be increased so that eventually pulses will traverse a new gas field, or scene.

Above it was stated that the centroid correlation decreased for integration times above ~100 µs. This means that if a sensor, or target in the case of a missile, were to be sampling slower than 10 kHz (100

μs) the pulse to pulse correlations may not be strong. For a missile tracking a target, the target's position is commonly updated in the missile's tracking loop at a continuous rate [156] so the poor correlations may not cause a problem. However, the DIRCM track loop may be affected if the DIRCM track loop samples discretely. If the centroid position correlations are decreasing at rates slower than 10 kHz, the centroid position in a sensors field-of-view will be shifted to a new location, uncorrelated with past centroid positions. It is not possible to determine the degree of the effect, either positively or negatively, on the missile and DIRCM tracking performance without a detailed analysis that includes details of the missile and DIRCM tracking and guidance loops. However, this result does suggest the DIRCM jamming performance may be altered.

6.2.3 Refractive Index Structures in the Plume

The size of the refractive index structures in the plume were deduced from the structure seen in the camera image of the target board (refer to Section 3.3.6). However, the technique was rather coarse as it required a visual assessment of the structure size. Structures of size down to 7 mm definitely existed in the plume, determined from the size of the speckle on the image board, the lasers inherent divergence and the path length from the plume to the screen. The smallest structure sizes are hard to determine by visual means. Tatarski's theory (Section 3.3.6) predicted the inner scale to be smaller, ~200 μm, which was however too small for the visual assessment to estimate.

Sirazetdinov et al. [66, 106-109, 111, 157] predicted the structure by estimating the average refractive index structure constant from beam wander equations and assigning values of inner and outer scale to match-up theoretical power spectrums with measured results. An inner scale in the order of 1 mm was deduced, with the outer scale in the order of 0.5 m. Sjöqvist et al. [112, 131, 132] then assumed an inner scale of 1 mm and an outer scale of 0.5 m in their work.

6.2.4 Irradiance at the Target

The irradiance was measured using both the radiometer and the camera. The spatial variation of the irradiance was determined using the camera to measure the irradiance at a number of window sizes. The spatial variation of the irradiance was determined to mainly occur at window sizes less than the 20 x

20 pixels. This confirmed that most of the variation was in structures less than 20 pixels (~7 mm at the plume).

The radiometer was used to determine the temporal irradiance profile. The distribution of the logarithm of the laser irradiance was found to follow a Gaussian profile. This log-normal distribution is typical of atmospheric propagation and can be representative of strong turbulence, though other statistical distributions may be better fits [97]. The measurements determined from the camera data showed a distinct skewing of the Gaussian profile, favouring low irradiances. The standard deviation of the log irradiance was also measured and the radiometer and camera measurements gave different results. The reason for the differences between the two measurements results was not readily apparent. The only conceived reason related to the difference in bandwidth of the two instruments (refer to 3.3.7). Sirazetdinov et al. [66, 106-109, 111, 157] and Sjöqvist et al. [112, 131, 132] have not presented the log-irradiance profiles for their studies of laser beam propagation through jet engines, so no insight could be gained. However, Fante [97] discussed other workers findings related to probability density of the received laser beam intensity after propagation through various turbulence regimes. Fante states that by the central limit theorem the field must be a complex Gaussian random variable and the intensity must satisfy an exponential probability density function. However Fante further states that because of skewness, the sum of N log-normal random-variables approaches Gaussian statistics much more slowly than for variables without skewness. Barakat [158] shows that the intensity variance, and consequently the number of independent ray paths, must be very large before purely Gaussian statistics will be observed. These statements support the view that sampling rate differences between the camera and the radiometer may have affected the measured distribution.

The temporal intensity variations measured at the target for engine off and engine on conditions can be viewed in Figure 3.17 and Figure 3.18. The plots show that a DIRCM system firing a mid-IR laser beam through a jet engine exhaust plume can produce peak powers at the missile that are 5 times that produced when the laser beam does not pass through the jet engine's exhaust. Furthermore, there are equivalent occurrences of low irradiances when propagating through the hot exhaust gases. Obviously 5 times more jamming power is advantageous, while the lower jamming power is not. A further consideration is that the power fluctuations are very short lived and dynamic. Consequently, a more

detailed assessment of these effects on a missile's guidance track loop would be required to better determine the effect on jamming performance.

6.2.5 Beam Movement

Beam movement was measured by determining the standard deviation of the beam displacement. The jet engine study suggested the beam movement was linked to the temperature of the exhaust gases. For example (refer to Figure 3.4 and Figure 3.7), single axis centroid displacement standard deviation ranged from 350 to 550 microradians as the Turbine Exit Temperature (TET) varied from 380 – 580°C. The increase in thrust as the engine changed from 14,000 RPM to 20,000 RPM, while the TET remained constant, did not indicate any significant variation in the beam displacement. Only qualitative comparison with other jet engine studies is possible as the parametric study showed that the beam displacement depended on other factors such as beam diameter, wavelength, path length and length scale. Full characterisation of the experimental setups ought to be known to allow meaningful quantitative comparisons.

Table 6.1 summarises the beam displacements reported in a number of laser beam propagation experiments involving various jet engine types and conditions. The table shows the beam displacement tends to be in the order of hundreds of microradians. In general the shorter wavelength beams and the smaller diameter beams appear to have the most displacement. The results of the jet engine study presented in Chapter 3 follow these trends. It is apparent the results are reasonably qualitative. An example is taken from Sirazetdinov et al. [107-111]. Their study was undertaken to consider the effects of the path length through the plume and the position of the intersection with the plume on the spatial characteristics of the beam. Qualitative analysis of the results from the study indicated that the angular divergence of the propagating laser beam increased by about an order of magnitude. A greater value occurred for the longer laser beam paths through the plume, and could be up to 35 times greater than the natural divergence of the source. For shorter path lengths and particularly those close to the edge of a well-developed plume the value was of the order of a factor of six. It was observed that the greatest impact occurred with the shortest wavelength laser light, as anticipated from the Kolmogorov theory. These results allow only qualitative comparison as the characteristics of the hot turbulent flow through

which the laser beam is traversing are not known. Consequently, the parametric experiment was undertaken, in which the gas medium was well characterized, to provide robust quantitative results.

Table 6.1: Laser beam movements reported in various jet engine beam propagation studies.

λ (μm)	Beam Diameter (mm)	Movement	Conditions	References
0.53 1.06 0.53 1.06	10 10 30 30	10 mm beam is ~ 2x 30 mm beam 0.53 μm is ~ 2x 1.06 μm Ranged from 50 – 300 μradians over range experimental conditions	10, 45 and 90° crossing angles Various engine settings	[106, 108, 109, 130]
0.53 1.06 0.53 1.06	10 10 30 30	10 mm beam is ~ 2x 30 mm beam 0.53 μm is ~ 2x 1.06 μm 20% increase at plume boundary compared with plume center	Side boundary experiment, propagating at various heights	[110]
0.488 3.39	0.8 1.55	0.488 μm 430 μradians and 1.55 μm 100 μradians	Angled across plume	[146]
0.904	40	500 μradians	Angled across plume	[105]
0.632	30	Not reported	90° crossing angle	[129]
1.57 3.5	Not reported	Ranged from 50 – 150 μradians over range experimental conditions	Along and across plume	[132]
1.55	45	Ranged from 65 – 200 μradians over range experimental conditions	Along plume and with Mach 0.6 co-flow	[112]
0.532 1.52 3.56	10-15	Ranged from 50 – 120 μradians across plume and 75 – 230 μradians along plume. Minimal difference between 1.52 μm and 3.56 μm displacements	Across and along plume	[131]
4.6	10	Ranged from 200 to 500 μradians	Various engine settings	[144, 145]

Own jet engine study

6.3 Parametric Study of Propagation through a Simple Jet Flow

The simple jet parametric study, outlined in Chapter 4, provided data on beam effects due to various flow parameters. The effect on the laser beam propagation due to these parameters is further discussed in the sections below.

6.3.1 Effect of Refractive Index

The displacements of the laser beam, after having interacted with the hot gases, are mainly due to the change in the local refractive index and the path length over which the refractive index has been changed. Refractive index effects are related to wavelength, temperature and flow composition. The literature review revealed that most current research on refractive indices has been done with geodesy and using the 632.8 nm wavelength [32, 40, 159]. In geodesy the representations of the refractive index are generally considered only over a short wavelength range and with the effect of a few associated absorption lines incorporated into the formulation.

Ciddor [43, 142, 143, 160] had extensively reviewed the work on refractive index and outlined an approach to determine the refractive index that accounts for the effect of wavelength by providing an estimate for the refractive index of air containing known volume fractions of water and/or carbon dioxide. The formulations (see Section 2.2.2.1.1) allowed for the determination of the refractive index for various gas compositions that had been validated over the wavelength range of interest, and for temperatures less than 100°C. It is noteworthy that the refractive index formulations were also developed from experimental data with temperatures less than 100°C. In our study these formulations were tested for a much wider temperature range and for two wavelengths (632.8 nm and 4.67 μm). The following sections discuss the experimental results.

6.3.2 Effect of Temperature

Reported studies of laser beam propagation through high temperatures were found to be scarce in the literature. Not including jet engine system level studies, only recently a few publications related to

propagation of short wavelength light through plasmas have been published [161-163]. No previous study of the propagation of 632.8 nm and 4.67 μm laser beams through high temperatures, as used in the parametric study, were found in the literature.

As the temperature of a gas mixture increases, the refractive index of the mixture decreases. This inverse relationship was given in Equation (2-7). An increase in temperature can also change the magnitude of the anomalous absorption effect. However, as discussed in Section 4.4.2, the equations outlined by Simeckova [49] and the results of Popov & Shvartsblat [154] and Penner [155] showed that the strength of the anomalous absorption effect was minor and decreased with the increase in temperature. This meant that the equations published by Ciddor [43, 142, 143, 160], validated for temperatures less than 100°C, would be expected to reasonably represent the refractive index at high temperatures. Consequently Ciddor's formulations were used to predict the refractive index change over the range of our experimental temperatures and gas compositions.

The expectation was that the variance of the laser beam centroid displacement would be related to the temperature of the flow, and consequently the refractive index. The refractive index gradient between ambient air and hot flow at various temperatures was calculated using Ciddor's formulations (see Figure 5.3). The laser beams' standard deviation of centroid displacement were measured and displayed in Figure 5.2. The plot showed the laser beam displacement tended to follow the change in refractive index resulting from the increase in temperature. However, at higher temperatures (>400°C) the roll-off was sharper than predicted by Ciddor's equation. The beam displacement variance was found to be related to the inverse of the temperature squared as described by Chiba [87], with good correlations of the data with a temperature squared function.

Interestingly, saturation of the beam wander was also identified by Fante [96], though not related to high temperature effects. Fante identified that increasing the path length, or turbulence strength (C_n^2), will eventually result in the mean square beam centroid position no-longer increasing as the beam wander saturates. The effect of high temperature, and its strong refractive index changes, produces effects comparable to those produced by increased path length or turbulence strength. The effect of temperature on the refractive index structure constant, or turbulence strength, is discussed in the next section.

6.3.2.1 Effect of Temperature on Refractive Index Structure Constant

The effect of temperature on the refractive index structure constant (C_n^2) can be determined by measuring the resultant spot sizes. Hogge and Vivinsky [129] used the work of Gebhardt and Collins [99] (refer to 2.5.3 on Spot Size) and that of Fried and Seidman [89] to calculate C_n^2. The same process was applied here to determine the value of C_n^2 for a number of temperature settings used in the parametric experiment. The value of C_n^2 (see Equation (6-1)) was derived from the expression for the log amplitude variance of a spherical wave given by Hogge and Vivinsky [129].

$$C_n^{\ 2} = \left(\frac{C_l^{\ 8}(0)}{0.124 k^{7/6} z^{11/6}} \right)^{1/2} \tag{6-1}$$

where $k = 2\pi / \lambda$, z is the range from the source to the receiver, and $C_l^8(0)$ is the log amplitude variance of a spherical wave.

The value of $C_l^8(0)$ is determined from rearranging the expression for the ratio of the spot radii, $\left(\frac{\omega_t}{\omega} \right)$, presented by Hogge and Vivinsky [129] to the form;

$$C_l^{\ 8}(0) = -\ln\left(\frac{\omega_t}{\omega} \right) \Big/ \left[\left[\langle l(0) \rangle / C_l^{\ 8}(0) \right] + \left[C_l(0) / C_l^{\ 8}(0) \right] \right] \tag{6-2}$$

where ω_t is the radius at which the intensity drops to $1/e^2$ of the beam spot in the receiver plane after passing through hot turbulent region, ω is the unperturbed collimated beam radius in the receiver plane, $\langle l(0) \rangle$ is the mean of the log amplitude (normally distributed) energy in the receiver plane of a finite diameter Gaussian beam (the laser beam), $C_l(0)$ is the log amplitude variance of the finite diameter Gaussian beam and $C_l^8(0)$ is the log amplitude variance of a spherical wave.

The values of the intensity fluctuations depend on the beam diameter, in particular the dimensionless beam-size parameter;

$$\Omega = k\alpha_0^{\,2} / z \tag{6-3}$$

where α_0 is the beam radius at the source.

The values of $\langle I(0)\rangle / C_l^{\,8}(0)$ for various beam-size parameters are tabulated in Gebhardt and Collins [99], while the values of $C_l(0) / C_l^{\,8}(0)$ are tabulated in Fried and Seidman [89].

This approach was adopted to calculate the values of C_n^2 for the range of tested temperatures. The radii of the spot sizes at the receiver plane were determined using the data used to generate Figure 5.21, using the $1/e^2$ of the energy. Noteworthy is that a slight inaccuracy in the total energy is expected as the energy summed on a pixel-by-pixel basis does not include energy in a pixel where the energy was less than $1/e^2$ the maximum pixel energy in the frame. However, the ratios would be expected to be similar which is important for the relative computed change in C_n^2 with temperature.

Calculated C_n^2 values are shown in Table 6.2. The calculations from measurements taken by Hogge and Vivinsky [129] on a jet engine at temperatures ranging from 293°C to 615°C using a 632.8 nm beam are also included. It is clear that the C_n^2 values are lower in the simple jet parametric experiment than in the jet engine study conducted by Hogges and Vivinsky [129]. This is not surprising as the Reynolds number would be higher in the jet engine plume. It is notable that there was a significant variation in the values determined by Hogges and Vivinsky across the temperature range without showing any strong trend. In the well controlled parametric experiment there is a definite non-linear increase in C_n^2 value with increasing temperature, in-line with the increase in spot size.

Translating the temperature changes into C_n^2 value changes allows formulations to be used that relate beam effects to C_n^2, such as Equation (2-81) which describes the beam displacement standard deviation as being directly proportional to the refractive index structure constant.

Table 6.2: C_n^2 values computed from measured spot areas.

Temperature (°C)	C_n^2 using 632.8 nm beam (x10^{10}) for this work.	C_n^2 using 632.8 nm beam (x10^{10}) - measured by Hogges and Vivinsky on a jet engine exhaust.
332		15.68
400		
430	1.75	
540		7.18
600		
606		11.76 and 18.66*
615		24.40
700		
706	2.60	
806	2.73	
810		
915		
1196	2.87	

*Measured on different days

6.3.2.2 Effect of Temperature on the Beam's Spatial Energy Distribution

To further study the effects of temperature, the spatial energy distribution was compared for both beams over the range of temperatures at various interrogation window sizes, or aperture sizes. For both beams the variance of the energy received in a given aperture size increased as the temperature increased. This effect would be linked to the decrease in refractive index resulting from the increased temperature. The subsequently increased refractive index gradient would act to increase the spatial spread of the energy. This is seen in plots showing spot area standard deviation increasing with temperature, Figure 5.7 and Figure 5.8, and also in plots of the average energy per pixel, Figure 5.22 and Figure 5.23, which indicate the average energy per pixel decreases with increased temperature.

The increased spatial spread results from the path the light makes through the flow. At high temperatures the refractive index differences encountered by the beam as it crosses the flow are greater. This results in increased deviation of the beam. The spatial spread of the beam is due to the various angles of intersection that the beam wavefront makes with the pockets of gas in the turbulent flow. In some instances, considering Snell's law, there may be minimal deviation of the wavefront and even focusing in the case when the wavefront propagates through a concave pocket of gas. Pockets of gas smaller than the beam wavefront will also break-up the beam. The atmospheric scenario that might replicate these effects would be an increase in propagation path length, such that the beam intersects more refractive index gradients and eddies as the beam propagates further. The result being more beam break-up and spread at long distances than short distances. This would translate to increased variance of received energy at longer path lengths. Indeed the variance of energy, or scintillation, has been linked to path length, wavelength and turbulence strength (C_T^2) in the atmosphere [164].

It is notable that the intensity decreased with increasing temperature over the range of aperture sizes. This is seen in Figure 5.22 and Figure 5.23, with the effect pronounced at the shorter wavelength. The apparent energy loss is due to pixels with counts less than $1/e^2$ the maximum pixel value in the frame being discarded from the calculations as part of the image processing procedure. The decrease in the average count per pixel indicates the energy of the beam is being spatially spread as the temperature increases.

The data were further analyzed by plotting a histogram of the total number of counts across all pixels in each frame. The data revealed the frame values of the visible beam tended to decrease as the temperature increased (shown in Figure 6.1 and Figure 6.2). That is, the distribution shifts to the left, indicating lower frame irradiance values, as the temperature increases.

The infrared beam does not exhibit a significant distribution shift with temperature. There is minimal change in the infrared beam irradiance as shown in Figure 6.3 and Figure 6.4. Notable is the increase in the probability of high energy pulses for the IR laser beam, seen by the tail on the right side of the distribution. However, the distribution maintained the same shape when the beam was imaged after

passing only through ambient air. This indicates the irradiance distribution was a temporal feature of the laser and not a phenomenon of the propagation of the beam through the hot gas flow.

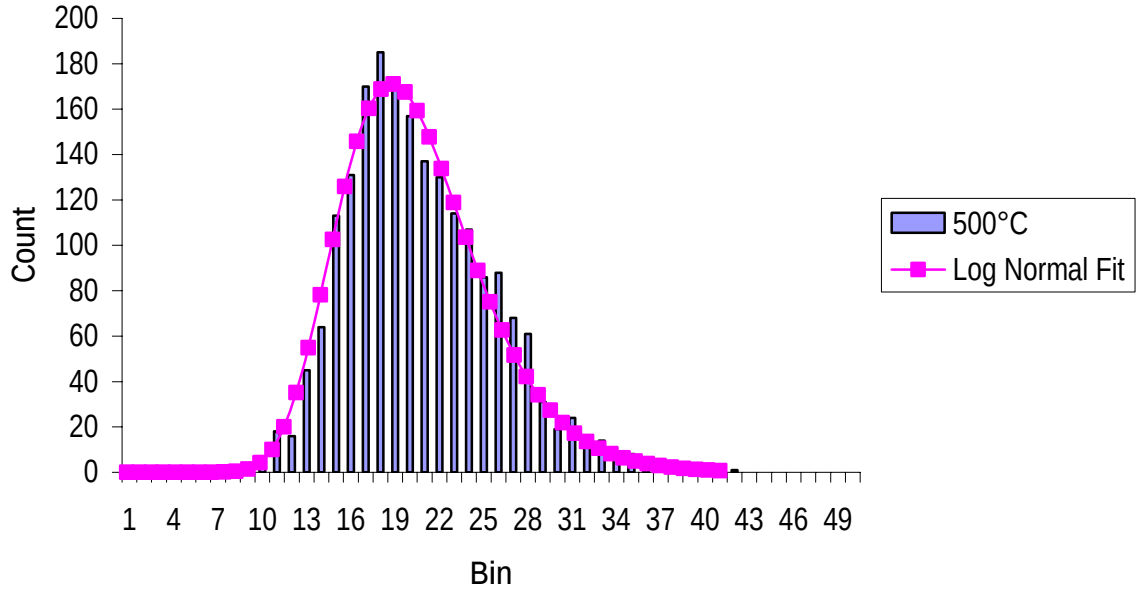

Figure 6.1: A histogram of frame-to-frame irradiance (total count) distribution for the 632.8 nm beam propagating through low temperature gas.

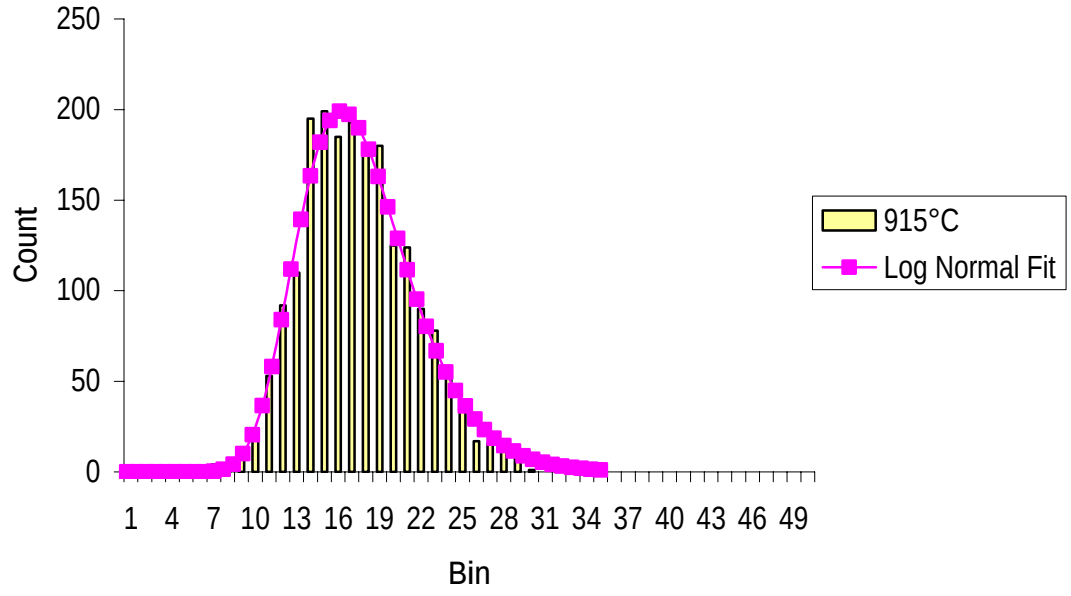

Figure 6.2: A histogram of frame-to-frame irradiance (total count) distribution for the 632.8 nm beam propagating through high temperature gas.

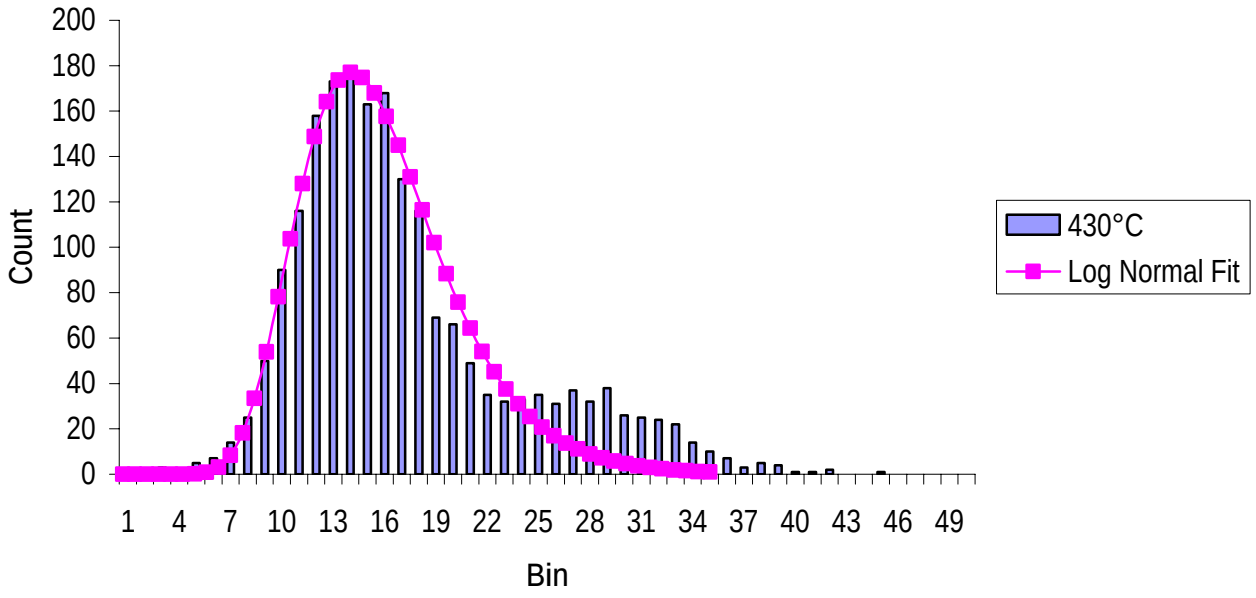

Figure 6.3: A histogram of frame-to-frame irradiance (total count) distribution for the 4.67 μm beam propagating through low temperature gas.

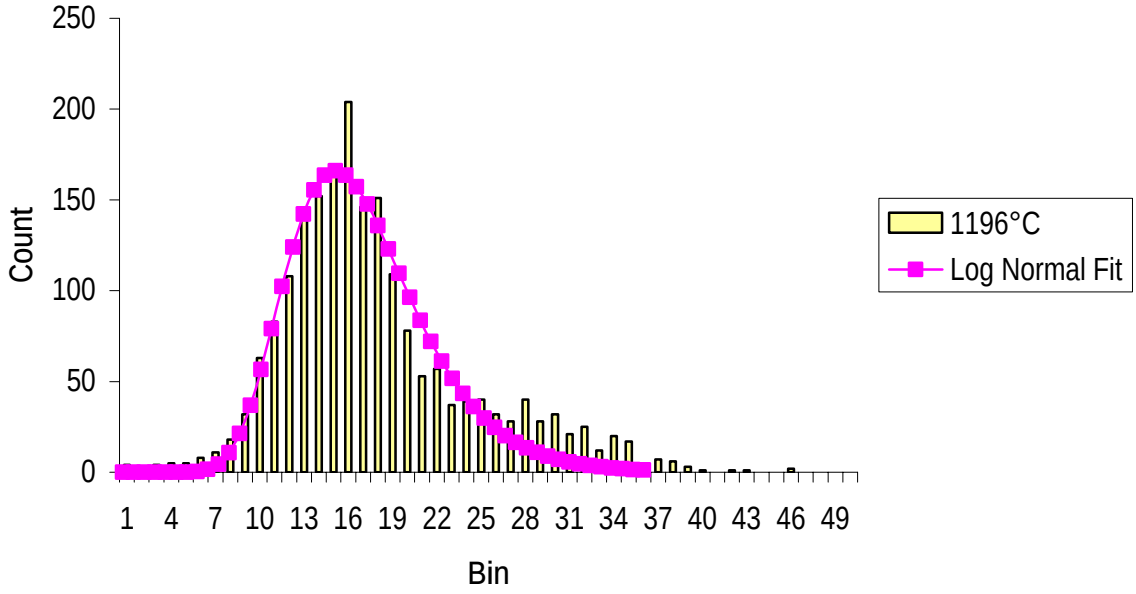

Figure 6.4: A histogram of frame-to-frame irradiance (total count) distribution for the 4.67 μm beam propagating through high temperature gas.

The data suggest that in the case of a DIRCM, particularly if operating at shorter wavelengths, the average received energy on the target is reduced if the beam has propagated through high temperatures. This is due to the spatial spreading of the beams energy. This is despite the increase in standard deviation of pixel count (number of pixels containing energy, see Figure 5.20) which shows the irradiance variation on a frame to frame basis increasing with temperature.

6.3.3 Effect of Wavelength

The refractive index calculations plotted in Figure 5.3 (Section 5.2.2.1) showed minimal difference between the visible and infrared beams. However, the beam centroid displacement variance, shown in Figure 5.2, differed noticeably between the two wavelengths. It was postulated that the actual propagation path would consist of the laser beam crossing multiple refractive index gradients at various angles and so that the angular difference between the two wavelengths is expected to increase. The initially small differences in angular deviation of the wavefront between the two wavelengths would increase as multiple refractive index gradients of various curvatures, or cell size, are encountered. The path length differences through the various cells will also affect the final direction of the beams. Sirazetdinov et al. [109, 111] noted the same notable difference in standard deviation of position for the various wavelengths when propagating through a jet engine exhaust. The variance of the beam displacement has been related to the wavelength by the factor $\lambda^{-1/6}$ [139]. The standard deviation is then related by $\lambda^{-1/12}$. Using the same approach it is found that for the 632.8 nm case the beam's centroid standard deviation was predicted to be 18% higher than the 4.67 µm beam. The results reported in this thesis showed ~14% change in the beam centroid standard deviation as the wavelength increased from 632.8 nm to 4.67 µm. It appears the effect of wavelength on beam displacement at high temperatures is closely matched to existing formulations derived and validated at lower temperatures.

In the simple jet parametric study, Chapter 4 and 5, other differences between the 632.8 nm and 4.67 µm beams, besides centroid displacement variance, were noted. The differences between the spot structure imaged on the screen for the visible and infrared beams were significant. There was a noticeable break-up of the visible beam into multiple spots. Results are shown for the two beams in Figure 6.5. The reasons behind this are attributed to a number of different factors and will be discussed here below.

Firstly, both beams have spherical wave-fronts that have approximately the same transverse beam size as the distance from the iris to the flow is short (450 mm). In this region Fresnel diffraction theory applies to both beams as $\sqrt{\lambda L}$ << *a*, where *a* is the iris size and *L* is the path length. As the beams propagate further they enter the Fraunhofer region where they diverge at a rate related to the wavelength and iris size, approximately λ/*a*. The diffraction effects start to significantly increase the minimum spot size.

Secondly, the lateral phase coherence length of the turbulence needs to be considered. For turbulence scales with lateral coherence length larger than the beam diameter, a wave is steered, undistorted, through the medium. However, as the turbulence eddy size is reduced to a size less than the beam diameter the wave-front is distorted and the beam is broken-up [165]. In this study, the beam diameter for the 632.8 nm and the 4.67 µm wavelength beams were the same, as the iris was placed close to the burner, so the turbulence scales acting across the beam-front at each wavelength ought to be the same.

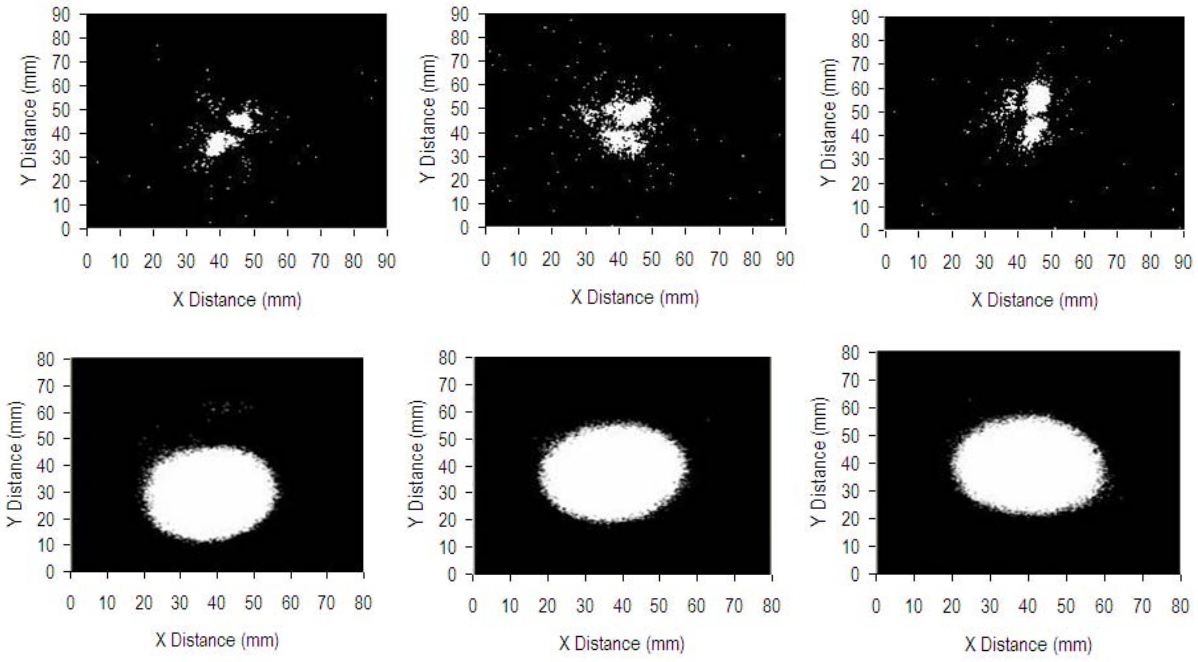

Figure 6.5: Three consecutive images of the 632.8 nm beam (top) and 4.67 µm beam (bottom), both having propagated through a 3 mm iris and a turbulent zone at 700°C. The contrast has been set to show any pixels with a value not zero as white. A threshold of 13.5% has been applied.

Lastly, in the hot turbulent gas there are a variety of refractive index changes due to the changes in temperature and hence density through the flow. These refractive index changes can cause the gas to act as a "thermal" lens. These changes produce multiple thermal lensing conditions across the beam front and act to focus and defocus parts of the beam. The effect on the spot size is wavelength dependent. That is, if both beams pass through the same thermal lens, the spot of the visible beam will be much smaller than the IR spot. The spot size doubles when the wavelength of the laser beam doubles, as given by [166];

$$\varpi(z) = \frac{\lambda z}{\pi \varpi_0} \tag{6-4}$$

where $\omega(z)$ is the beam radius at propagation distance z, ω_0 is the beam radius at the beam waist and λ is the wavelength.

The spot size for the 632.8 nm beam is more than 7 times smaller than the 4.67 µm beam. The thermal lensing effect, combined with the diffraction limit of the wavelength, have resulted in the visible beam seen as a broken-up spot while the 4.67 µm beam is contained within the same spot. This result is similar to that noted by Raidt and Höhn [167] who discuss the result for 632.8 nm and 10.6 µm beams propagating in the atmosphere.

The scintillation, or variance in the received irradiance, has been related to the wavelength by $\lambda^{-7/6}$ as seen in Equation (2-48). The standard deviation is then related by $\lambda^{-7/12}$. Comparing the two wavelengths, the 632.8 nm beam would have a standard deviation that is 3.2 times that of the 4.67 µm beam. The measured results shown in Figure 5.17 and Figure 5.19 indicate the standard deviation of the visible beam is 5 times greater than the infrared beam. Differences may either arise because not all energy was accounted for as the threshold was set to $1/e^2$ or, more probably, the aperture sizes are different. The variance would be expected to further reduce due to aperture averaging as the collection area of the visible beam increased to match that of the infrared beam. The results appear in-line with expected wavelength effects though notably they appear not to remain in scale with increasing temperature. An increase in temperature increases the variance of the visible beam to a greater degree than the infrared beam. Considering a receiver aperture size of 1.5 square milliradians, the infrared

beam has an increase in scintillation standard deviation of 3% over a 500 degree temperature range compared with 30% for the visible beam over the same temperature range. To the author's knowledge, this is the first time this temperature comparison result has been recorded.

6.3.4 Effect of Composition (CO_2 and H_2O)

The deflection of light in a homogenous medium arises due to refractive index gradients which are related to the density changes across the medium. Besides temperature and pressure, the molecular mass of the gas composition in the medium affects the density. The molecular polarizability and the sum of atomic polarizability are secondary effects that may also change the refractive index [18]. During the parametric experiment the gas composition, and hence the refractive index, was changed in two ways. The first was as a result of combusting air and hydrogen to achieve the high temperatures. The combustion by-product was water. The second was the deliberate inclusion of carbon dioxide by replacing a known volume of air by the equivalent volume of carbon dioxide (refer to Section 5.3).

The effect of the varying percentage of water was estimated by calculating the refractive index using Ciddor's formulations (refer to Section 4.4.2). The inclusion of water (up to 15% volume fraction) produced a less than 5% decrease in the theoretically determined refractive index. It was expected that the beam movement would then also exhibit a 5% decrease at high temperatures. However, to make this comparison a high temperature condition without the presence of water was required, which was not possible. A slight decrease in the magnitude of beam displacement and spread would need to be considered if comparing with any future work at high temperatures that did not include water.

The substitution of a volume of carbon dioxide into the flow in place of a volume of air will result in an increase in density and hence refractive index of the gas mixture (Section 5.3). The increase in refractive index would result in a decrease in the refractive index gradient between the surrounding air and the gas jet, hence decreasing the laser beam displacement.

The effect of the anomalous absorption due to carbon dioxide at various temperatures on the refractive index, and hence beam displacement, was also considered. It was shown to be a secondary effect (Section 5.3), and furthermore its effect decreases with increasing temperature.

The impact of carbon dioxide on beam displacement is documented in Section 5.3 with the experimental results given in Figure 5.24. The measured beam displacement changed only a few percent as the carbon dioxide levels were increased to 10% flow volume. These changes were within the experimental uncertainty of the experiment for the range of conditions studied. The beam degradation as a result of inclusions of carbon dioxide was assessed to be minor compared to the effects of other parameters such as temperature. A 20°C temperature change has the same impact as increasing the carbon dioxide levels to 10% of the flow volume. For this reason, the impact of carbon dioxide need not be considered as a significant factor when assessing the impact of the flow on the beam displacement of a DIRCM system.

6.3.5 Effect of Beam Diameter

The propagation of beams has been described mathematically for uniform spherical and plane waves with assumptions made on the scales of turbulence. The laser beam is in fact a truncated Gaussian spherical wave so the mathematical predictions may not be precise. However, the theoretical and practical work of others [88, 94, 97, 107] show that the beam displacement fluctuations are related to the beam diameter.

The results from the parametric experiment showed (Figure 5.30) that for both the 632.8 nm and 4.67 µm beams the beam wander was linked to the beam diameter under the range of temperature and turbulence conditions tested. For all cases the displacements were linked to the beam diameter by the factor; D^y where D is the beam diameter at the iris and y ranged from -0.3165 to -0.3816. The almost cubed root relationship agrees closely with the work of others. For example, recently Andrews et al. [113, 122] found that for a collimated beam, propagating through the atmosphere, the root mean square of the beam displacement was;

$$\left\langle r_c^{\,2} \right\rangle = 2.42 C_n^{\,2} L^3 D^{\,-1/3} \left[1 - \left(\frac{0.25 \kappa_0^{\,2} D^{\,2}}{1 + 0.25 \kappa_0^{\,2} D^{\,2}} \right)^{1/6} \right] \tag{6-5}$$

where κ_0 is the outer scale, D is the beam diameter, L is the propagation path length and C_n^2 the structure constant.

Other atmospheric beam wander formulations, presented in Section 2.5.5, all show the dependency on beam diameter to the cubed root.

The measured results at high temperatures supports the practical work of others [88, 94, 97, 107] primarily performed at atmospheric temperatures. It was found that the beam wander closely depends on the beam diameter to the root cubed. The implication for a DIRCM system is that beam displacement variance through the engine exhaust can be mitigated by increasing the laser beam diameter. Increasing beam diameter will improve pointing accuracy but will also reduce the radiance ($Wm^{-2}sr^{-1}$). However, advances in laser technologies will produce increased laser power allowing the beam diameter to increase without a reduction in jamming effectiveness.

6.3.6 Effect of Turbulence Intensity

The turbulence intensity is a measure of the magnitude of the temporal velocity fluctuations in the flow (refer to Section 2.3.1). The parametric experiment was conducted using perforated plates of various blockage ratios to alter the turbulence intensity of the flow at the laser beam propagation height. Characterization of the flow for the various run set-ups allowed for quantification of the velocity fluctuations. It was revealed that the velocity fluctuation changes were predominately altered by changing the blockage ratios. Increasing the blockage ratio was found to expand the flow at the measurement height while also increasing the velocity fluctuations across the flow, although the turbulence intensities (the ratio of the velocity fluctuations to the average velocities) remained similar (Figure 4.15 and Figure 4.16).

The strongest turbulence intensity is found in the shear layer (apparent in Figure 4.16). It was anticipated that the beam displacement variance may increase in-line with the turbulence intensity in the shear layer. This is because the greatest mixing of the ambient air with the hot gas jet is occurring in this region. The beam displacement variance was seen to increase with blockage ratio but there was not a strong connection with the shear layer turbulence.

Further analysis of the turbulence intensity plots (Figure 4.16) with respect to the beam displacement plots (Figure 5.27) did however reveal a definite relationship between beam displacement variance and the turbulence intensity along the path of the beam. That is, not only was the turbulence intensity at the shear layer considered, but also the turbulence intensity across the rest of the flow. The evidence is presented in Figure 6.6 where the average beam displacement variance for all measurements, taken at the same flow conditions, is plotted against the sum of the turbulence intensities across the flow at the propagation height. In this case, the beam displacement variance increases as the turbulence intensity summation increases. This is, however, really an effect of path length and shows the pointing accuracy of a DIRCM laser system would be further degraded as the path length through the hot turbulent exhaust is increased.

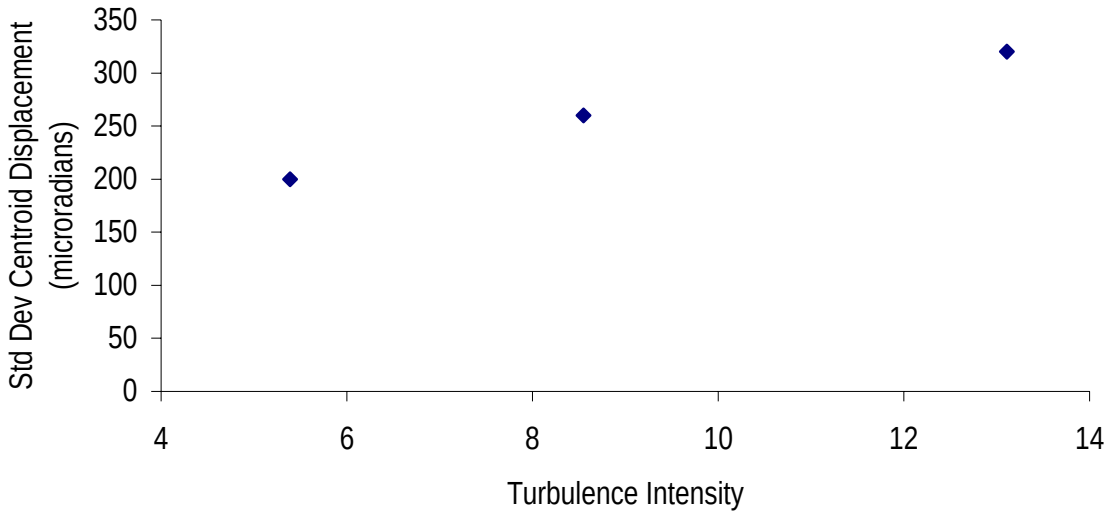

Figure 6.6: The beam displacement standard deviation averaged over all runs plotted against the turbulence intensity calculated as an integral of the turbulence intensity between the jet's centre axis and the centre of the shear layer.

It is noted that the structure constant is often used as a measure of turbulence strength, the greater the value of the structure constant, the greater the turbulence strength. In particular the refractive index structure constant, C_n^2, is used in formulations that describe beam wander in turbulence. The refractive index structure constant is linked to the temperature structure parameter, C_T^2, (see Section 2.3.1.1) which is calculated from an ensemble of temperature differences between points in the flow. The definition is spatial in its construction but if the flow is considered frozen then the spatial properties can

be translated into temporal properties. The outcome is that measurements of the structure parameter are usually carried out by averaging over time [138]. The calculation of the structure constant involves scaling the ensemble of the magnitude differences by the spatial or temporal separation over which the measurements are made. Depending on the scaling, an increase in the magnitude of the temperature differences measured either spatially or temporally, can result in an increase in the value of the structure constant.

In the simple jet parametric study, velocity fluctuations, measured temporally, were used to determine the turbulence intensity. The turbulence intensity is a measure of changing velocity while the structure parameter used in laser beam formulations that describe beam wander is a measure of changing refractive index, or temperature. The beam can only be displaced by a change in refractive index and therefore the turbulence intensity is linked to the fluctuations in temperature resulting from the turbulent mixing of the hot jet gases with the ambient air.

6.3.7 Effect of Length Scale

The spatial size of the various air pockets in the flow can influence the propagating laser beam. The term length scale refers to the size of these air pockets, measured either spatially or temporally (refer to Section 2.3.2). These air pockets can cause beam break-up, or when larger than the beam diameter, beam steering. The resulting intensity fluctuations at the receiving plane are referred to as scintillation. The temporal and spatial amplitude variations of the scintillation are related to the characteristics of the gas medium through which the beam has propagated (refer to Section 2.5.2). In the parametric experiment the flow characteristics were altered by introducing perforated plates of various hole diameter over the outlet nozzle. These plates were introduced to change the length scales in the flow (refer to Section 2.3.3). Measurements of the flow presented in Chapter 4 showed the introduction of perforated plates of increasing hole diameter altered the flow by increasing the length scales in the flow. The standard deviation of the laser beam displacement was seen to increase with increasing hole diameter (Figure 5.25). Path lengths were identical (Figure 4.17) and the turbulence intensity across the path similar (Figure 4.21). The magnitude of temperature fluctuations would be similar for each of the various hole diameter runs. This is because the various flow characteristic curves (mean temperature

and turbulence intensity) were similar for each hole diameter test. The laser beam displacement was therefore primarily due to increased integral length scale.

In Section 2.5.5 the effects of beam wander were presented. In particular, Andrews et al. [68, 113, 122, 168] show that as the laser beam diameter approaches the outer scale of turbulence the large scale effects of beam wander tend to vanish. The simple jet parametric experiment showed, Figure 5.28, that the beam wander increased as perforated hole size, and as discussed and shown (Figure 5.29), integral scale, increased. The increase in beam wander closely matches the increase in hole diameter, with a slight roll-off in wander when using the 8 mm hole diameter perforated plate, which produced flow with the largest integral length scale. This trend follows from the corollary generated from Andrews et al. [68, 113, 122, 168]. That is, for a fixed diameter beam the beam wander increases to a limit as the turbulence scale increases. In our case, the beam diameter was 3 mm, and the roll-off in beam-movement appears to have occurred between the integral length scale of 2.91 mm and 5.01 mm (Figure 5.29). Therefore, we have determined that at the high (500°C) temperature studied beam wander is increasing with integral length until the interal length scale is matching the beam diameter. At which point roll-off of beam wander is occurring.

6.3.8 Effect of Path Length

The path length through which the beam travels is known to be linked to the displacement of the beam. For example, Chiba [87] derived an expression for beam displacement which assumes a Kolmogorov turbulence function between the inner and outer turbulence scales where the laser beam diameter is larger than the inner scale. The case derived is applicable when the beam waist is in the centre of the propagation path. The resulting expression for radial variance was;

$$\sigma_r^{\,2} = 1.83 C_n^{\,2} \lambda^{-1/6} L^{17/6} \qquad (6\text{-}6)$$

where $\sigma_x = \sigma_y = \sqrt{\sigma_r^{\,2}/2}$ and $\sigma_x = 3.14 C_n L^{17/12}$ where L is the path length.

Later work has produced a variety of expressions based on mathematical derivations and experimental observations. To describe the variance of single-axis beam wander where *D* is the beam diameter, for a collimated beam Churnside and Lataits [88] derived the expression;

$$\sigma_{COL}{}^{2} = 0.97 C_n^2 D^{-1/3} L^3 \tag{6-7}$$

Also Andrews et al. [113, 122] recently found that for a collimated beam, propagating through the atmosphere, the root mean square of the beam displacement was related to the cubed root of the path length (refer to Equation (6-5)).

It is notable that a L^3 dependency is present in all these equations, with the C_n^2 value assumed constant along the path length. However, other authors use only an *L* dependency. Andreev and Gel'fer [119] showed the mean square of the angular displacement of the light centre of gravity of the diverging beam as;

$$\left\langle \beta^2 \right\rangle = 0.48 \alpha C_n{}^2 L (2\rho_e)^{-1/3} \tag{6-8}$$

where: β is the angular displacement; Cn^2 is the structure constant; *L* is the path length; the coefficient $\alpha = 1$ for $\lambda L/\pi\rho_e^2 >> 1$ and $\alpha = 2$ for $\lambda L/\pi\rho_e^2 << 1$, and ρ_e is the effective beam radius.

In our parametric experiment the beam propagates through a very short but highly turbulent gas flow with steep temperature gradients. This scenario more closely resembles a jet engine scenario than a long path through the atmosphere. It was expected that the beam movement might be directly related to path length as represented by Sirazetdinov et al. [109] and shown in Equation (6-9), where the variance of the beam displacement is given as;

$$\sigma_{c,x(y)}^2 = 2.84 C_n^2 L D^{-1/3} \left\{ 1 - 0.1 \left(\frac{D^2}{L_{0,x(y)} L_{0,y(x)}} \right)^{1/6} \left(3 \left[\frac{L_{0,x(y)}}{L_{0,y(x)}} \right]^2 + 1 \right) \right\} \tag{6-9}$$

where $L_{0,x(y)}$ denotes the outer scale length in the x and y directions, respectively.

Experiments were devised to determine the effect of the path length on the laser beam propagating through the hot turbulent flow. The results and analysis were presented in Section 5.6. Flow characterization revealed that not only path length but other parameters such as the integral length scale were changing in the tests. For example, Figure 4.25 shows the integral length scale increasing with distance downstream while Figure 4.23 shows path length also increasing with distance downstream in the same experiment.

The effect of integral length scale on the laser beam was determined to be linked to the beam displacement standard deviation (Section 5.5). Not withstanding the absence of data points, if a linear relationship is assumed between integral length scale and beam displacement, a change in integral length scale of 1 mm results in a change in beam standard deviation of 17 microradians (applying a line between the lower and upper integral length scales in Figure 5.29).

Figure 4.25 showed there was a change in integral length scale of 0.4 x Hole Diameter = 3.2 mm as the distance downstream changed from 5 to 25 hole diameters from the nozzle. Applying the results from Figure 5.29, the beam displacement standard deviation would be expected to increase by 3.2 x 17 = 55 microradians if the effect of integral length scale alone is considered. However, the beam wander decreased by only ~10 microradians as the distance downstream increased (Figure 5.32). Other factors besides integral length are effecting the beam displacement in this case and are discussed below.

As already stated, the path length was increasing and hence the movement was expected to increase. Temperature was however decreasing, from 770 to 240°C. The beam wander, considering peak temperature alone (Figure 5.2), would result in the beam displacement standard deviation decreasing from 300 microradians to 160 microradians, a drop of 140 microradians, as the temperature decreased with height. Therefore, considering the expected increase of 55 microradians due to the increase in integral length scale, and the expected decrease of 140 microradians due to the decrease in peak temperature, there is a net 85 microradians decrease in beam wander anticipated as a result of temperature and integral length scale changes. The actual measured beam displacement standard deviation showed only a 10 microradian decrease, resulting in a 75 microradian discrepancy. This suggests the increase in path length with distance downstream has resulted in a beam wander standard deviation increase of 75 microradians. This is 20% of the final measured movement. This effect of path

length is not surprising but the analysis of the results hinged on the accuracy of a number of trends, particularly beam wander versus integral length scale.

Further, consider the path length was measured as increasing by 90 mm (60 to 150 mm, that is 2.5 times) as the distance downstream increased from 5 to 25 beam diameters. However, over the same downstream range the temperature gradient was decreased by 5.5°C per 2 mm step (9 to 3.5°C per 2 mm step; that is ~2.5 times). This shows that although the path length is longer, the magnitude of the temperature fluctuations along the path are less. The net result may be that the “effective” (temperature weighted) path lengths are similar.

The second path length experiment measured the beam displacement at a different distance downstream but with the temperature adjusted to 300°C at each measurement position. The beam standard deviation was measured as increasing by 140 microradians as the distance downstream changed from 5 to 25 hole diameters from the nozzle. The integral length scale changed at a rate of 0.44 x Hole Diameter = 3.52 mm as the distance downstream changed from 5 to 15 hole diameters from the nozzle. Therefore measuring from 5 to 25 hole diameters downstream would result in an integral length change of 7.04 mm assuming a linear increase. Again, applying the results from Figure 5.29, the beam displacement standard deviation would be expected to increase by 7.04 x 17 = 120 microradians if the effect of integral length scale alone is considered.

The peak temperature was the same at each height which meant the extra 140 - 120 = 20 microradians of beam movement could not be attributed to temperature and could be attributed to the increased path length through the heated turbulent gas. However, again the analysis of the results hinged on the accuracy of a number of trends, particularly beam wander versus integral length scale. Furthermore, the path lengths and the steepness of the temperature gradients along the paths were again different in each case. This time, the path length was measured as increasing by 60 mm (60 to 120 mm, that is 2 times) as the distance downstream increased from 5 to 25 beam diameters. Over the same downstream range the temperature gradient was decreased by 20°C per 2 mm step (~20 to 5°C per 2 mm step; that is ~4 times).

It is clear from the data from these experiments that although some effect of the path length is evident, the true effect of path length was hard to quantify. This is because the effect of path length is a combination of length through the flow and the temperature fluctuations along that path. It was hoped that the two experiments would provide enough data to draw definitive conclusions. However the flow characterization analysis has revealed that the experimental arrangements were not suitable to isolate the effects of path length from other parameters, in particular temperature gradient.

Chapter 7

Summary and Conclusions

The emerging threat of advanced infrared guided missiles to both military and civilian authorities requires a robust countermeasure system. Advances in laser technology have allowed the development of a portable, aircraft carried, laser beam based countermeasure system (DIRCM). The DIRCM detects, tracks and then directs modulated IR energy in the form of a laser beam on to the missile's IR seeker to disrupt the missile's guidance. An identified deficiency is the DIRCM performance when tracking and targeting a missile through the hot turbulent region of the aircraft exhaust. It is known that the laser beam will be significantly degraded over this propagation path.

The degradation of the propagated laser beam has been examined at a system level, using a ground-jet engine, and in a controlled experimental laboratory setting where individual parameters of the flow and laser beam parameters, such as laser wavelength, beam diameter and flow temperature, were varied.

7.1 Jet Engine Study

In the jet engine study the extent of the beam break-up as the laser beam passed through a ground-based jet engine's efflux was examined for various engine settings, geometries and engine types (turbofan and turbojet).

It was found that the beam displacement generally increased with engine RPM as the turbine exit temperature increased. A decrease in the beam displacement was noted with an increase in thrust, and

was thought to be due to increased mixing (and cooling) of the plume. Propagating at increasing height above the core centre was linked to a decrease in the standard deviation of the beam centroid.

Minimal difference in the laser beam degradation was noted for the turbojet and turbofan (1:1 bypass) cases. The beam displacement was slightly lower at idle (14,000 RPM) for the turbofan compared with the turbojet. However, higher values were noted as the laser beam propagated through at the mixing layer of the turbofan engine.

The temporal energy distribution of the laser beam, once propagated through the plume, closely resembled a log Gaussian distribution; similar to non-saturated scintillation in atmospheric turbulence where the Rytov approximation is valid. The result suggested that the plume can be modelled by a single phase screen, as described in Section 2.7.1.

Radiometer and camera measurements of the propagated beam suggested that refractive index structures of less than 5 mm in the plume appeared to have minimal impact of the resulting structure, or energy distribution, of the beam.

7.2 Simple Jet Parametric Study

A significant contribution of the thesis has been the development and use of a laboratory-based high temperature turbulent flow with controllable parameters for the study of laser beam propagation. The combustion of hydrogen was used to generate high temperatures, while the application of perforated plates of various hole dimension and blockage ratio allowed the turbulent flow characteristics to be altered. Until now there had not been a controlled laboratory-based experiment at high temperatures and turbulence conditions to study the effects of various parameters on the propagated laser beam energy. Laser propagation studies in the past had been limited to atmospheric studies and a few jet-engine system level studies [102, 105-112, 131, 132, 169].

The 632.8 nm and 4.67 μm beams produced significantly different beam patterns once propagated through the turbulent flow. The difference was found to be primarily due to the physics of diffraction. The propagation of two lasers of different wavelength through various high temperatures revealed a slight

difference in the displacement variance of the calculated centroids. Refractive index calculations predicted the longer (4.67 µm) wavelength beam would be refracted the least, by less than five percent. The effect of the increased quantity of water in the flow as a product of hydrogen-air combustion were theoretically considered and determined to have less impact than the wavelength differences. Over the hot turbulent path the 632.8 nm beam centroid standard deviation was measured to deviate by up to 18% more than the 4.67 µm beam, fitting the $\lambda^{-1/12}$ dependence on centroid standard deviation cited by Miller [139]. The displacement difference was expected if the two beams were to propagate between two different refractive index mediums. This is because the increased displacement, and difference, is due to the initially small difference in angular deviation of the wavefront between the two wavelengths being amplified as multiple refractive index gradients of various curvatures, or cell size, are encountered. The beam displacement, resulting from the difference in refractive index at the two wavelengths, was however found to be less significant than variations in the gas temperature. This was indicated by a comparison of beam displacement through various temperature gases compared to the calculated refractive index. It was also noted that the beam displacement variance due to temperature tended to head towards an asymptote above 400°C, with the change in the increase in beam displacement variance being related to the inverse square of temperature.

Other degradation effects on the beam due to temperature changes, besides centroid displacement variance, were also measured. As temperature increased a number of degradation effects were noted. The trends for both the 632.8 nm and 4.67 µm beams were similar, although the 632.8 nm beam exhibited greater beam degradation with temperature. For both beams, as temperature increased;

- Structure constant increased non-linearly (see Table 6.2)
- Spot size variance increased non-linearly above 400°C (see Figure 5.7 and Figure 5.8)
- Spot size increased, at the same rate as spot size variance above 400°C (see Figure 5.9 and Figure 5.10)
- Beam displacement variance increased non-linearly (see Figure 5.5)
- Irradiance variance increased non-linearly (see Figure 5.18 and Figure 5.20)
- Average irradiance slightly decreased (see Figure 5.21)
- Average count per pixel decreased non-linearly (see Figure 5.22 and Figure 5.23)

where;

- Structure constant was determined from spot size
- Spot size was defined as number of pixels in a frame with counts over $1/e^2$ the maximum pixel value in the frame
- Irradiance (or total counts per frame) was defined as the sum of all pixel values for pixels with counts over $1/e^2$ the maximum pixel value in the frame
- Count per pixel was defined as the pixel value for a pixel with a count over $1/e^2$ the maximum pixel value in the frame

Further, the 632.8 nm beam was observed to have an order of magnitude greater energy fluctuation than the 4.67 µm beam over the range of temperatures measured. Fresnel diffraction effects are wavelength dependent and were used to explain the difference in beam break-up between the two wavelengths as the beams propagate through the same turbulence zone.

The values measured for these beam parameters (viz: spot size, irradiance and energy per pixel) were affected by the measurement area, or aperture size. For example, there was an increase in the variation of the spread of the laser energy as the temperature increased for a given aperture size. The results can be applied to a missile engagement, showing, for example, as the incoming missile approaches the laser beam source the variation in spatial illumination is reduced while the irradiance variation is increased.

The effect of carbon dioxide concentration on beam degradation was also studied. The introduction of increased levels of carbon dioxide into the flow demonstrated that the effect of carbon dioxide on the displacement of the 632.8 nm and 4.67 µm beams was not significant. At levels found in the jet engine exhaust the effect of carbon dioxide can be ignored as other influences, such as temperature variations in the flow, have far greater effect on the beam degradation.

The beam displacement for both wavelengths was found to increase as the beam diameter decreased, closely following the inverse third root of the beam diameter. It was found the 632.8 nm beam would need to be 8/7ths times greater in diameter than the 4.67 µm beam to produce the same beam displacement variance. Increases in beam diameter can result in significant minimization of beam

displacement. The beam displacement was more sensitive to changes in beam diameter than temperature at the high temperatures found in a jet engine exhaust.

The simple jet parametric study also showed turbulence intensity was linked to laser beam degradation. Increased beam degradation with increasing turbulence intensity is understood to be due to the increased mixing of the hot jet gases with the surrounding air.

The beam displacement was seen to be significantly increased as the integral length scale of the turbulence increased. The displacement was also found to be tending towards an asymptote as the integral length scale of the flow exceeded the laser beam diameter. This is an important finding as a measurement of the integral length scale of the flow would be required before an estimate of the beam displacement could be provided.

Path length, although known to be a significant parameter, could not be quantitatively studied with the experimental set-up, although attempts were made. The results did indicate that path length was a parameter that ought to be considered. However, in the region of the plume the refractive index gradients are severe compared to atmospheric conditions. The refractive index variations, in the form of the refractive index structure constant, need to be integrated along the path length and averaged in order for the path length to be used. Existing derivations for the impact of path length, using an averaged C_n^2 value, are too approximate for use with large temperature variation, short path length scenarios.

Overall, the jet engine and simple jet parametric study results can be used to estimate the temporal and spatial characteristics of the energy received by the collection optics of the incoming missile for various laser beam and path conditions through hot turbulent flows. The propagation of the 632.8 nm and 4.67 µm laser beams through hot turbulent flow in a controlled laboratory experiment appears to be a world first and has provided valuable insight into the influence of beam and flow parameters on the beam degradation as the electro-optic wavefront propagates through the highly aberrant media.

7.3 DIRCM Implications

A number of findings were made through-out the studies that were considered directly applicable to DIRCM design and operation. These are summarized in the following paragraphs.

In the jet engine study, Chapter 3, the turbojet engine produced more change in beam movement than the turbofan engine (see Section 3.3.4). The results suggested there was a more distinct 'edge' to the turbulent region close to the nozzle outlet for the turbojet engine. Furthermore, there was an increase in beam movement as the beam crossed the core air / by-pass air mixing layer. A DIRCM should avoid directing a laser beam through these regions.

The analysis of the jet engine study also found that centroid frame-to-frame correlations measured for the propagated beam decreased for integration times above ~100 μs. For a missile tracking a target, the target's position is commonly updated at a continuous rate [156] so the poor correlations may not be a problem. However, for a DIRCM tracking a missile the effect may be significant if the DIRCM track loop is updated discretely. If the DIRCM tracker was following a missile using a track loop with a sampling rate slower than 10 kHz (100 μs) the pulse to pulse correlations may not be strong. A poor correlation means that the centroid position in the sensors field-of-view will be shifted to a new location, uncorrelated with past centroid positions. This result suggests the DIRCM jamming performance may be altered. Further study would be needed to determine the effect, whether is it either negative or positive, on the missile and DIRCM tracking and guidance loops.

A further notable finding was the temporal variations in intensity resulting from the laser beam propagating through the jet engine exhaust. Plots (Figure 3.17 and Figure 3.18) show that a DIRCM system firing a mid-IR laser beam through a jet engine exhaust plume can produce peak powers at the missile that are five times that produced when the laser beam does not pass through the jet engine's exhaust. Furthermore, there are equivalent occurrences of low irradiances when propagating through the hot exhaust gases. These effects on a missile's guidance track loop need to be studied to determine the effect on jamming performance.

The simple jet parametric study demonstrated that the propagation of longer wavelength laser radiation through the hot turbulent gases will produce an increase in the average received energy on the target when compared to the shorter wavelengths. This has implications when choosing an operating frequency; in consideration with the target detectors response characteristics and atmospheric absorption bands.

An assessment of the effect of CO_2 on the propagating beam was made as part of the parametric study. The beam degradation as a result of inclusions of carbon dioxide was assessed to be minor compared to the effects of other parameters such as temperature. It was found a 20°C temperature change has the same impact as increasing the carbon dioxide levels to 10% of the flow volume. For this reason, the impact of carbon dioxide need not be considered as a significant factor when assessing the impact of the flow on the beam displacement of a DIRCM system propagating a laser beam through the jet engine exhaust.

The effect of beam diameter was studied and the results are relevant to DIRCM system design. The data from the simple jet study confirmed that beam wander closely depends on the beam diameter. The implication for a DIRCM system is that beam displacement variance through the engine exhaust can be mitigated by increasing the laser beam diameter. Increasing beam diameter will improve pointing accuracy but however will also reduce the radiance ($Wm^{-2}sr^{-1}$). This is a trade-off the DIRCM designer must consider.

With regards turbulence intensity, the simple jet parametric study revealed a definite relationship between beam displacement variance and the turbulence intensity along the path of the beam. In the study the beam displacement variance increased as the turbulence intensity summation increased. This means the pointing accuracy of a DIRCM laser system would be degraded as the path length through the hot turbulent exhaust is increased.

7.4 Recommendations

There are a number of avenues for further research that were noted during the study. Firstly, an experimental rig could be set-up to better investigate the role of path length in the turbulent flow region. It

would be interesting to note whether the beam displacement saturates as the path length increases, much the same as increasing the peak temperature beyond 400°C tends to see a rapid roll-off towards a displacement variance asymptote.

Secondly, further high temperature studies with different wavelengths could be performed to provide a greater data set on the effects of the high temperature turbulent region on the displacement of the various wavelength laser beams.

Seeding the flow to allow the particle image velocimetry to be performed was problematic. The use of an already well characterized nozzle could help affirm the results if the test was to be re-performed.

Presently, schemes are being developed that remove phase front aberrations by comparing a modulated wave with a CW wave that is close in wavelength to the modulated wave, to remove scintillation effects [170]. However these appear to have not yet been studied when the lasers are fired through extreme environmental conditions, as in the case of a jet engine exhaust.

Further research may involve comparing the effects of different mid-IR wavelengths over a propagation path that could include a simulated engine exhaust, with co-flow, and about one kilometre of nominal atmosphere, to simulate a realistic operational optical path.

Bibliography

1. Craig, B. *Presentation on Commerical Aircraft Signatures (unclassified)*. 2004, DSTO: Edinburgh, Australia.

2. Titterton, D.H., *Requirement for laser devices used in countermeasure applications.* Proceedings - SPIE The International Society for Optical Engineering, 2005. 5989(07).

3. Coulman, C.E., *Atmospheric "seeing": a review of fundamental and applied aspects.* Am. Rev. Astr. Ap., 1985. 23.

4. Beland, R.R., *Propagation through Atmospheric Optical Turbulence*, in *The Infrared and Electro-Optical Systems Handbook*. 1993, SPIE: Bellingham, WA.

5. Andrews, L.C., Phillips, R.L. and Hopen, C.Y., *Laser Beam Scintillation with Applications*. 2001, Washington: SPIE Press.

6. Guenther, R., *Modern Optics*. 1990: John Wiley & Sons. 720.

7. Born, M. and E. Wolf, *Principles of optics - electromagnetic theory of propagation interference and diffraction of light*. sixth ed. 1980, New York: Pergamon Press.

8. Britannica, E. *"Cauchy, Augustin-Louis, Baron." Encyclopædia Britannica Online. 3 Sept. 2008* <*http://original.britannica.com/eb/article-9021867>*. 2008.

9. Wikipedia. *http://en.wikipedia.org/wiki/Cauchy's_equation*. 2008.

10. Wikipedia. *http://en.wikipedia.org/wiki/Sellmeier_equation*. 2008.

11. Dale, T.P. and J.H. Gladstone, *The influence of temperature on the refraction of light.* Philosophical Transactions - Royal Society, 1858. 148: p. 887-894.

12. Powell, B., *Comparison of some recently determined refractive indices with theory.* Proceedings of the Royal Society of London, 1859. 10: p. 199-204.

13. Birch, K.P. and M.J. Downs, *An updated Edlen equation for the refractive index of air.* Metrologia, 1993. 30: p. 155-162.

14. Davis, R.S., *Equation for the determination of the density of moist air (1981/91).* Metrologia, 1992. 29: p. 67-70.

15. Edlen, B., *The dispersion of air.* J. Opt. Soc. Am., 1953. 43(5): p. 339-344.

16. Erickson, K.E., J. Opt. Soc. Am., 1962. 52: p. 781.

17. Galkin, Y.S. and R.A. Tatevian, *Influence of resonances on the phase and the group refractive indices of air.* Journal of Geodesy, 1997. 71: p. 690-684.

18. Gardiner, W.C., Jr., Y. Hidakea, and T. Tanzawa, *Refractivity of combustion gases.* Combustion and Flame, 1981. 40: p. 213-219.

19. Hill, R.J., S.F. Clifford, and R.S. Lawrence, *Refractive-index and absorption fluctuations in the infrared caused by temperature, humidity, and pressure fluctuations.* J. Opt. Soc. Am., 1980. 70(10): p. 1192-1205.

20. Kerr, D.E., ed. *Propagation of Short Radio Waves* 1951, McGraw-Hill Book Co., Inc.: New York.

21. Kestin, J., S.T. Ro, and W.A. Wakeham, *Viscosity of carbon dioxide in the temperature range 25-700 degC.* J. Chem. Phys., 1972. 56(8): p. 4114-4118.

22. Koch, J., Nov. Act. Sov. Ups., 1909. 4(2): p. 61.

23. Kosters, W. and P. Lampe, Phys. Z., 1934. 35(223).

24. Matsumoto, H., *The refractive index of moist air in the 3-um region.* Metrologia, 1982: p. 49-52.

25. Meggers, W.F. and C.G. Peters, *Index of refraction of air for wavelengths from lamda2218 to lambda9000.* Bulletin of the Bureau of Standards, 1918. 14(327): p. 697-740.

26. Peck, E.R. and B.N. Khanna, *Dispersion of air in the near-infrared.* J. Opt. Soc. Am., 1962. 52(4): p. 416-419.

27. Penndorf, R., *Tables of the refractive index for standard air and the Rayleigh scattering coefficient for the spectral region between 0.2 and 20u and their application to atmospheric optics.* Journal of the Optical Society of America, 1955. 47(2): p. 176-182.

28. Schlueter, D.J. and E.R. Peck, *Refractivity of air in the near infrared.* Journal of the Optical Society of America, 1958. 48(5): p. 313-315.

29. Smith, E.K. and S. Weintraub, *The constants in the equation for atmospheric refractive index at radio frequencies.* Proceedings of the I.R.E., 1952. 41(8): p. 1035-1037.

30. Svensson, K.F., *Measurements of the dispersion of air for wavelengths from 2302 to 6907 Aring.* Arkiv for Matematik, Astonomi och Fysik, 1960. 16(35): p. 361-384.

31. Traub, W., *Dispersion of air in ultra-violet.* Annalen der Physik, 1920. 61(6): p. 533-548.

32. Edlen, B., *The refractive index of air.* Metrologia, 1966. 2(2): p. 12-80.

33. Ishimaru, A., *Wave propagation and Scattering in Random Media - vol 2*. 1978, New York: Academic Press.

34. Koch, J., *Dispersion of light in gases in ultra-violet region.* Arkiv for Matematik, Astonomi och Fysik, 1913. 9(6): p. 1-11.

35. Koch, J., *Dispersion of light in gases in ultra-violet region.* Arkiv for Matematik, Astonomi och Fysik, 1913. 8(20): p. 1-25.

36. Koch, J., *The dispersion of light in gaseous bodies with the ultra-violet spectrum. IV.* Arkiv for Matematik, Astonomi och Fysik, 1924. 18(3): p. 1-15.

37. Owens, J.C., *Optical refractive index of air: dependence on pressure, temperature and composition.* Applied Optics, 1967. 6(1): p. 51-59.

38. Old, J.H., L. Gentili, and E.R. Peck, *Dispersion of carbon dioxide.* J. Opt. Soc. Am., 1971. 61(1): p. 89-90.

39. Peck, E.R. and K. Reeder, *Dispersion of air.* J. Opt. Soc. Am., 1972. 62(8): p. 958-962.

40. Birch, J.P., *Precise determination of refracometric parameters for atmospheric gases.* J. Opt. Soc. Am. A, 1991. 8(4): p. 647-651.

41. Birch, K.P. and M.J. Downs, *The precise determination of the refractive index of air*. 1988, National Physical Laboratory.

42. *International Association of Geodesy Report of the Ad-Hoc Working Party on Refractive Indices of Light, Infrared and Radio Waves in the Atmosphere of the IAG Special Commission SC3 - Fundamental Constants (SCFC)*. 2000; Available from: http://www.gfy.ku.dk/~iag/Travaux_99/wp51.htm.

43. Ciddor, P.E., *Refractive index of air: new equations for the visible and near infrared.* Applied Optics, 1996. 35(9): p. 1566-1573.

44. Birch, K.P. and M.J. Downs, *Correction to the updated Edlen equations for the refractive index of air.* Metrologia, 1994. 31: p. 315-316.

45. Barrell, H. and J.E.J. Sears, *Refraction and dispersion of air for visible spectrum.* Philosophical Transactions of the Royal Society of London, 1939. 238A(786): p. 1-62.

46. Hill, R.J., S.F. Clifford, and R.S. Lawrence, *Computed refraction and absorption fluctuations caused by temperature, humidity, and pressure fluctuations - radio waves to 5um.* NOAA Technical Memorandum, 1980.

47. Goody, R.M., *Atmospheric Radiation*. 1964: Oxford University Press.

48. Hill, R.J. and R.S. Lawrence, *Refractive index of water vapor in infrared windows.* Infrared Phys., 1986. 26(6): p. 371-377.

49. Simeckova, M., D. Jacquemart, L.S. Rothman, R.R. Gamache, and A. Goldman, *Einstein A-coefficients and statistical weights for molecular absorption transitions in the HITRAN database.* Journal of Quantitative Spectroscopy & Radiative Transfer, 2006: p. 130-155.

50. Tihov, M., *Chemical sensors based on distributed feedback quantum cascade laser for environmental monitors*. 2003, Ecole Polytechnique, Fedeale de Laussane. p. 112.

51. Cox, L., M. Dubovinsky, D.H. Titterton, T. Porter, and E. Mancini, *Portreath Plume Trial (CLASSIFED REPORT)*. 2003.

52. Wey, C.C., et al,, *Engine gaseous, aerosol precursor and particulate at simulated flight altitude conditions*. 1998.

53. Allen, C.W., *Astrophysical Quantities*. Third ed. 1973, London: The Athlone Press.

54. Cox, A.N., *Allen's Astrophysical Quantities*, ed. A.N. Cox. 2000, New York: Springer-Verlag.

55. Birch, K.P. and M.J. Downs, *The results of a comparison between calculated and measured values of the refractive index of air.* J. Phys. E: Sci. Instrum., 1988. 21: p. 694-695.

56. Goody, R.M. and Y.L. Yung, *Absorption by atmospheric gases*, in *Atmospheric Radiation*. 1989, Oxford University Press. p. 189-215.

57. Hill, R.J., Clifford, S.F. and Lawrence, R.S., *Computed refraction and absorption fluctuations caused by temperature, humidity, and pressure fluctuations - radio waves to 5um*. 1980, Wave Propagation Laboratory: Boulder, California. p. 25.

58. Pope, S.B., *Turbulent Flows*. First ed. 2000: Cambridge University Press.

59. Williams, F.A., *Combustion Theory*. Second ed. 1985: The Benjamin/Cummings Publishing Company, Inc.

60. Turns, S., *An Introduction to Combustion: Concepts and Applications*. Second ed. 2000: McGraw-Hill Publishing Company Limited.

61. Chigier, N., *Energy, Combustion, and Environment*. 1981: McGraw-Hill Book Company.

62. Lane, R.G., A. Glindemann, and J.C. Dainty, *Simulation of a Kolmogorov phase screen.* Waves in Random Media, 1992. 2: p. 209-224.

63. Roddier, F., ed. *The effect of atmospheric turbulence in optical astronomy*. Progress in Optics, ed. E. Wolf. Vol. 19. 1981. 282-376.

64. Smith, F.G., *Atmospheric Propagation of Radiation*. The Infrared and Electro-Optical Systems Handbook, ed. F.G. Smith. Vol. 2. 1993, USA: Infrared Information Analysis Center and SPIE Optical Engineering Press.

65. University of Berkeley. *Turbulence*. 2005; Available from: http://astron.berkeley.edu/~jrg/ay202/node166.html.

66. Sheremet'eva, T.A.a.F., G.N. *Estimation of a spectrum of fluctuations of a refractive index of turbulent medium.* in *SPIE* 2004.

67. Hill, R.J. and S.F. Clifford, *Modified spectrum of atmospheric temperature fluctuations and its application to optical propagation.* J. Opt. Soc. Am., 1978. 68(7): p. 892-899.

68. Andrews, L.C., *An analytical model for the refractive index power spectrum and its application to optical scintillations in the atmosphere.* J. Mod. Opt., 1992. 39: p. 1849-1853.

69. AMS. *Glossary of Meterology* 2009.

70. Tennekes, H. and J.L. Lumley, *A first course in turbulence*. 1972, Massachusetts: The MIT press.

71. Townsend, A.A., *The Structure of Turbulent Shear Flow*. Second ed. 1976: Cambridge University Press.

72. Hinze, J.O., *Turbulence*. Second ed. 1975: McGraw-Hill.

73. Liu, R., Ting, D, S-K. and Checkel, M.D., *Constant Reynolds number turbulence downstream of an orificed perforated plate.* Experimental Thermal and Fluid Science, 2006. 31: p. 897-908.

74. Baines, W.D., Peterson, E.G., *An investigation of flow through screens.* Journal of Applied Mechanics, 1951. 73: p. 467-478.

75. Liu, R., Ting, D, S-K. and Rankin, G.W., *On the generation of turbulence with a perforated plate.* Experimental Thermal and Fluid Science, 2002. 28: p. 307-316.

76. Mohamad, M.S. and J.C. LaRue, *The decay power law in grid-generated turbulence.* J. Fluid Mech., 1990. 219: p. 195-214.

77. Warhaft, Z. and J.L. Lumley, *An experimental study of the decay of temperature fluctuations in grid-generated turbulence.* Journal of Fluid Mechanics, 1978. 88(4): p. 659-684.

78. Berkritskaya, S.I. and A.A. Pavel'ev, *On the power law of decay of grid turbulence.* Fluid Dynamics, 1983. 18(4): p. 640-642.

79. Checkel, M.D. *Measurements of turbulence generated by 60% solid perforated plates*. in *The Winter Annual Meeting of ASME*. 1985. Miami Beach, Florida.

80. Cox, A.J., DeWeerd, A.J. and Linden, J., *An experiment to measure Mie and Rayleigh total scattering cross sections.* American Journal of Physics, 2002. 70(6): p. 620-625.

81. Miles, R.B., W.R. Lempert, and J.N. Forkey, *Laser Rayleigh scattering.* Meas. Sci. Technol., 2001. 12: p. R33-R51.

82. Masri, A.R., Dibble, R.W. and Barlow, R.S., *The structure of turbulent nonpremixed flames revealed by Raman-Rayleigh-LIF measurements.* Progress in Energy and Combustion Science, 1996. 22: p. 307-362.

83. Miles, R., Lempert, W., *Two-dimensional measurement in turbulent high-speed air flows by UV Rayleigh scattering.* Applied Physics B, 1990. 51: p. 1-7.

84. Jensen, K.D., *Flow Measurements.* J. of the Braz. Soc. of Mech. Sci. & Eng. 2004. 26(4): p. 400-419.

85. Raffel, M., Willert, C., Wereley, S. and Kompenhans, J., *Particle Image Velocimetry - a practical guide*. Second ed. 2007: Springer.

86. Melling, A., *Tracer particles and seeding for particle image velocimetry.* Measurement Science and Technology, 1997. 8: p. 1406-1416.

87. Chiba, T., *Spot dancing of the laser beam propagated through the turbulent atmosphere.* Applied Optics, 1971. 10(11): p. 2456-2461.

88. Churnside, J.H. and R.J. Lataitis, *Wander of an optical beam in the turbulent atmosphere.* Applied Optics, 1990. 29(7): p. 926-930.

89. Fried, D.L. and J.B. Seidman, *Laser-beam scintillation in the atmosphere.* Journal of the Optical Society of America, 1967. 57(2): p. 181-185.

90. Hill, R.J. and G.R. Ochs, *Optical-scintillation method of measuring turbulence inner scale.* Applied Optics, 1985. 24: p. 2430-2432.

91. Hogelnik, H., *Propagation of laser beams*, in *Applied optics and engineering*, R.R. Shannon and J.C. Wyant, Editors. 1979, Academic Press, Inc.: London. p. 155-190.

92. Sancer, M.I. and A.D. Varvatsis, *Saturation calculation for light propagation in the turbulent atmosphere.* J. Opt. Soc. Am., 1970. 60(5): p. 654-659.

93. Sutton, G.W., *Effect of turbulent fluctuations in an optically active fluid medium.* AIAA Journal, 1969. 7(9): p. 1737-1743.

94. Tartaskii, V.I., *The Effects of the Turbulent Atmosphere on Wave Propagation*. 1971, National Technical Information Service.

95. Tatarski, V.I., *Wave propagation in a turbulent medium*. 1961, Dover Publications, Inc.: New York.

96. Fante, R.L., *Electromagnetic beam propagation in turbulent media.* Proceedings of the IEEE, 1975. 63(12): p. 1669-1692.

97. Fante, R.L., *Electromagnetic beam propagation in turbulent media: an update.* Proceedings of the IEEE, 1980. 68(11): p. 1424-1443.

98. Frehlich, R., *Simulation of laser propagation in a turbulent atmosphere.* Applied Optics, 2000. 39(3): p. 393-398.

99. Gebhardt, F.G. and A.A. Collins, Jr., *Log-amplitude mean for laser-beam propagation in the atmosphere.* Journal of the Optical Society of America, 1969. 39(9): p. 1139-1148.

100. Roggemann, M.C. and C.L. Matson, *Power spectrum and Fourier phase spectrum estimation by using fully and partially compensating adaptive optics and bispectrum postprocessing.* J. Opt. Soc. Am. A, 1992. 9(9): p. 1525-1535.

101. Roggemann, M.C. and B. Welsh, *Imaging through turbulence*. 1996, New York: CRC Press.

102. Sjoqvist, L., M. Henriksson, and O. Steinvall. *Simulation of laser beam propagation over land and sea using phase screens - a comparison with experimental data*. in *Technologies for Optical Countermeasures II*. 2005: SPIE.

103. Stromqvist Vetelino, F., Clare, B., Corbett, K., Young, C., Grant, K. and Andrews, L., *Characterizing the propagation path in moderate to strong optical turbulence.* Applied Optics 2006. 45: p. 3534-3543.

104. Terentiev, E.N., F.V. Shugaev, L.S. Shtemenko, O.I. Dokukina, and O.A. Ignateva, *Modeling of laser beam propagation through turbulent medium.* Atmospheric Propagation II, Proceedings of SPIE, 2005. 5793: p. 56-67.

105. Barrett, J.L. and P.A. Budni, *Laser beam propagation through strong turbulence.* J. Appl. Phys., 1992. 71(3): p. 1124-1127.

106. Borisova, N.F., I.V. Ivanova, and V.S. Sirazetdinov. *Distortions of laser beams by turbulent aero-engine jet: experiment and numerical modeling*. 2004: SPIE.

107. Sirazetdinov, V.S., D.I. Dmitriev, I.V. Ivanova, and D.H. Titterton, *Effect of turbo-engine jet on laser radiation. Part 2. Random wandering of disturbed beam.* Atmos. Oceanic Opt., 2001. 14(10): p. 830-834.

108. Sirazetdinov, V.S., D.I. Dmitriev, I.V. Ivanova, and D.H. Titterton. *Angular divergence of laser beams disturbed by an aero-engine exhaust jet*. in *Eight International Symposium on Atmospheric and Ocean Optics*. 2002: SPIE.

109. Sirazetdinov, V.S., D.I. Dmitriev, I.V. Ivanova, and D.H. Titterton. *Random wanderings of laser beams under the effect of a turbulent jet of an aero-engine*. in *Eighth International Symposium on Atmospheric and Ocean Optics*. 2002: SPIE.

110. Sirazetdinov, V.S., D.I. Dmitriev, I.V. Ivanova, and D.H. Titterton. *Effect of turbulence intermittence on the structure of laser beams intersecting an aero-engine jet exhaust*. in *Ninth Joint International Symposium on Atmospheric and Ocean Optics/Atmospheric Physics. Part 1: Radiation Propagation in the Atmosphere and Ocean.* 2003: Proceedings of SPIE.

111. Sirazetdinov, V.S., I.V. Ivanova, A.D. Starikov, D.H. Titterton, T.A. Sheremet'eva, G.N. Filippov, and Y. Y.N. *Experimental study of the structure of laser beams disturbed by turbulent stream of aircraft engine*. in *Optical Pulse and Beam Propagation II*. 2000: SPIE.

112. Sjoqvist, L., O. Gustafsson, and M. Henriksson. *Laser beam propagation in close vicinity to a downscaled jet engine exhaust*. in *Technologies for optical countermeasures*. 2004: SPIE.

113. Andrews, L.C. and R.L. Phillips, *Laser beam propagation through random media*. Second ed. 2005, Bellingham, Washington: SPIE - The International Society for Optical Engineering.

114. Fried, D.L., *Propagation of a spherical wave in a turbulent medium.* J. Opt. Soc. Am., 1967. 57(2): p. 175-180.

115. Schmeltzer, R.A., *Means, variances, and covariances for laser beam propagation through a random medium.* Quart. Applied Math., 1966. 24(4): p. 339-354.

116. Banish, M.R., R.L. Clark, and A.D. Kathman, *Wavelength dependence of blur circle size through turbulent flow.* Window and Dome Technologies and Materials II, Proceedings of SPIE, 1990. 1326: p. 196-206.

117. Andrews, L.C., *Field Guide to Atmospheric Optics*. SPIE Field Guides, ed. J.E. Greivenkamp. 2004, Bellingham, Washington: SPIE Press.

118. Perlot, N. and D. Fritzsche, *Aperture-Averaging - Theory and Measurements*. 2004, SPIE.

119. Andreev, G.A. and E.I. Gel'fer, *Angular random wakes of the center of gravity of the cross section of a diverging light beam.* Radiophysics and Quantum Electronics, 1971. 14: p. 1145-1147.

120. Kuriger, W.L., *Technique for measuring laser beam propagation direction fluctuations.* Applied Optics, 1971. 10(11): p. 2462-2467.

121. Cook, R.J., *Beam wander in a turbulent medium: an application of Ehrenfest's theorem.* J. Opt. Soc. Am., 1975. 65(8): p. 942-948.

122. Andrews, L.C., R.L. Phillips, R.J. Sasiela, and R. Parenti, *Beam wander effects on the scintillation index of a focused beam.* Atmospheric Propagation II, Proceedings of SPIE, 2005. 5793: p. 28-37.

123. Livingston, P.M., *Proposed method of inner scale measurement in a turbulent atmosphere.* Applied Optics, 1972. 11(3): p. 684-687.

124. Consortini, A. and K.A. O'Donnell, *Measuring the inner scale of atmospheric turbulence by correlation of lateral displacements of thin parallel laser beams.* Waves in Random Media, 1993. 3: p. 85-92.

125. Hill, R.J., *Comparison of scintillation methods for measuring the inner scale of turbulence.* Applied Optics, 1988. 27(11): p. 2187-2193.

126. Wheelon, A.D., *Electromagnetic Scintillation II: Weak Scattering*. 2008, London: Cambridge University Press.

127. Consortini, A., S.Y. Yi, L.Z. Ping, and G. Conforti, *A mixed method for measuring the inner scale of atmospheric turbulence.* Journal of Modern Optics, 1990. 37(10): p. 1555-1560.

128. Yi, S.Y., L.Z. Ping, A. Consortini, and C. Innocenti. *A new method for measuring inner scale of atmospheric turbulence*. in *19th Congress on the International Commission for Optics: Optics for the Quality of Life*. 2003: SPIE.

129. Hogge, C.B. and W.L. Visinsky, *Laser beam probing of jet exhaust turbulence.* Applied Optics, 1971. 10(4): p. 889-892.

130. Dmitriev, D.I., I.V. Ivanova, V.S. Sirazetdinov, and D.H. Titterton, *Statistics of structural state fluctuations of a laser beam disturbed by a jet of aircraft engine.* Atmos. Oceanic Opt., 2004. 17(1): p. 39-45.

131. Henrikkson, M., L. Sjoqvist, D. Seiffer, N. Wendelstein, and E. Sucher. *Laser beam propagation experiments along and across a jet engine plume*. in *Technologies for Optical Countermeasures V*. 2008: SPIE.

132. Henriksson, M., L. Sjoqvist, and O. Gustafsson. *Experimental study of mid-IR laser beam wander close to a jet engine exhaust*. in *Technologies for Optical Countermeasures III*. 2006. Stockholm, Sweden: SPIE.

133. Joia, I.A., R.J. Perkins, B.J. Uscinski, G. Balmer, D. Jordan, and E. Jakeman, *Optical properties of a planar turbulent jet.* Applied Optics, 1995. 34(30): p. 7039-7050.

134. Joia, I.A., B.J. Uscinski, R.J. Perkins, G. Balmer, D. Jordan, and E. Jakeman, *Intensity fluctuations in a laser beam due to propagation through a plane turbulent jet.* Waves in Random Media, 1997. 7: p. 169-181.

135. Shapiro, A.R., *Laser propagation in aircraft wakes.* SPIE, 1973. 2005: p. 139-154.

136. Cox, L.J., *Personal communication "Data from Gnome engine operators Thermofluids Pty. Ltd."*. 2005.

137. Haw, M. *Einsteins Random Walk*. 2005; Available from: http://physics.sjtu.edu.cn/archive/EinsteinSRandomWalk.pdf.

138. Smith, F.G., *The infrared & electro-optical systems handbook*. Atmospheric propagation of radiation. Vol. 2. 1993, Washington: SPIE optical engineering press.

139. Miller, J.L. and E. Friedman, *Photonics rules of thumb* 2nd ed. 2004, Bellingham, Washington USA: SPIE.

140. Ross, S.M., *Introduction to Probability and Statistics for Engineers and Scientists*. 1987, New York: John Wiley.

141. Morley, C. *Gaseq - A Chemical Equilibrium Program for Windows*. 2006; Available from: http://www.arcl02.dsl.pipex.com/.

142. Ciddor, P.E., *Refractive index of air: 3. The roles of CO2, H2O, and refractivity virials.* Applied Optics, 2002. 41(12): p. 2292-2298.

143. Ciddor, P.E. and R.J. Hill, *Refractive index of air. 2. Group index.* Applied Optics, 2000. 38(9): p. 1663-1667.

144. Isterling, W.M., L.J. Cox, M. Dubovinsky, D.H. Titterton, and T. Porter. *Laser interaction with jet engine induced turbulence*. in *4th Australian Conf. on Laser Diagnostics in Fluid Mechanics and Combustion*. 2005. Adelaide.

145. Isterling, W.M., L.J. Cox, M. Dubovinsky, D.H. Titterton, and T. Porter, *Laser Beam Propagation through a Jet Engine Exhaust*, in *AOC International Symposium and Exhibition 2006*. 2006: Adelaide.

146. Titterton, D.H. *Measurement of the distortion generated in a laser beam's characteristics resulting from passage through an engine's wake*; in *RTO SET Symposium on "E-O propagation, signature and system performance under adverse meteorological conditions considering out-of-area operations"*. 1998. Naples, Italy: IAFA.

147. Chen, Y.-C., P.A.M. Kalt, A.R. Masri, and R.W. Bilger, *Feasibility study of integral length scale measurements in turbulent jet flows using DPIV*, in *2nd Australian Conference on Laser Diagnostics in Fluid Mechanics and Combustion*. 1999: Monash University, Melbourne, Australia. p. 1-5.

148. PIVTEC GmbH - Particles, I.a.V. *www.pictec.com*. 2009 [cited 2009].

149. *ABB Automation, Specification: Variable Area Flowmeters – Series 10A6100.* 2000.

150. Barrett, M.J. and D.K. Hollingsworth, *On the calculation of length scales for turbulent heat transfer correlation.* Transactions of the ASME, 2001. 123: p. 878-883.

151. Yamamoto, K., S. Inoue, H. Yamashita, D. Shimokuri, S. Ishizuka, and Y. Onuma, *PIV measurement and turbulence scale in turbulent combustion.* Heat Transfer - Asian Research, 2006. 35(7): p. 501-512.

152. Allen, C.W., *Allen's Astrophysical Quantities*. Fourth ed, ed. A.N. Cox. 2000, New York: Springer-Verlag.

153. Rothman, L.S., C.P. Rinsland, A. Goldman, S.T. Massie, D.P. Edwards, J.-M. Flaud, a. Perrin, C. Camy-Peyret, V. Dana, J.-Y. Mandin, J. Schroeder, A. McCann, R.R. Gamache, R.B.

Wattson, K. Yoshino, K.V. Chance, K.W. Jucks, L.R. Brown, V. Nemtchinov, and p. Varanisi, *The Hitran Molecular Spectroscopic Database and Hawks (HITRAN Atmospheric Workstation): 1996 Edition.* Journal of Quantitative Spectroscopy & Radiative Transfer, 1998. 60(5): p. 665-710.

154. Popov, Y.A. and R.L. Shvartsblat, *IR absorption coefficients and refractive indices of CO2 and steam.* Consultants Bureau, 1974. 12(6): p. 1047-1050.

155. Penner, S.S., *Quantitative Molecular Spectroscopy and Gas Emissivities*. 1959, MA: Addison-Wesley Publishing Company, INC.

156. Allan, S.L.R.I., *A Study of Infrared Missile Seekers and the Countermeasure Techniques Employed to Defeat Them*, in *Aerosystems Engineering*. 1987, Loughborough University of Technology and Royal Air Force College Cranwell.

157. Sheremet'eva, T.A. and G.N. Filippov, *Method for simulating random perturbations of the wave front within a wide range of fluctuation scales.* Atmos. Oceanic Opt., 2000. 13(5): p. 492-496.

158. Barakat, R., *Sums of independently lognormally distributed random variables.* J. Opt. Soc. Am., 1976. 66(March): p. 211-216.

159. Galkin, Y.S. and R.A. Tatevian, *The problem of obtaining formulae for the refractive index of air for high-precision EDM.* Journal of Geodesy, 1997. 71: p. 483-485.

160. Ciddor, P.E., *Refractive index of air: 3. The roles of CO2, H2O, and refractivity virials: erratum.* Applied Optics, 2002. 41(33): p. 7036.

161. Neimann, C., R.L. Berger, L. Divol, D.H. Froula, O. Jones, R.K. Kirkwood, N. Meezan, J.D. Moody, J. Ross, C. Sorce, L.J. Suter, and S.H. Glenzer, *Green frequency-doubled laser-beam propagation in high-temperature hohlraum plasmas.* Phys Rev Lett., 2008. 100(4).

162. Froula, D.H., L. Divol, N. Meezan, S. Dixit, J.D. Moody, P. Neumayer, B.B. Pollock, J. Ross, and S.H. Glenzer, *Ideal laser-beam propagation through high-temperature ignition Hohlraum plasmas.* Phys Rev Lett., 2007. 98(8).

163. Niemann, C., L. Divol, D.H. Forula, G. Gregori, O. Jones, R.K. Kirkwood, A.J. Makinnon, N.B. Meezan, J.D. Moody, C. Sorce, L.J. Suter, R. Bahr, W. Seka, and S.H. Glenzer, *Intensity limits for propagation of 0.527 micron laser beams through large-scale-length plasmas for intertial confinement fusion.* Phys Rev Lett., 2005. 94(8).

164. Weichel, H., *Laser beam propagation in the atmosphere*, ed. R.F. Potter. 1990, Washington: SPIE - The International Society for Optical Engineering. 98.

165. Davis, J.I., *Consideration of atmospheric turbulence in laser systems design.* Applied Optics, 1966. 5(1): p. 139-147.

166. Griot, C.M. *http://www.cvimellesgriot.com/Products/Documents/TechnicalGuide/Gaussian-Beam-Optics.pdf*. 2009.

167. Raidt, H. and D.H. Höhn, *Instantaneous intensity distribution in a focused laser beam at 0.63 μm and 10.6 μm propagating through the atmosphere.* Applied Optics, 1975. 14(11): p. 2747-2749.

168. Andrews, L.C., *Laser beam propagation through random media*. 1998: SPIE.

169. Henriksson, M. and C. Breitholtz. *Estimation of thrust and mass flow in a jet engine*. in *International conference on control applications*. 2004. Taipei, Taiwan: IEEE.

170. Davies, J.E., B.D. Nener, K.J. Grant, K. Corbett, and B. Clare. *Numerical experiments in atmospheric scintillation correlation for applications in dual channel optical communications*. in *Atmospheric Propagation II*. 2005. Florida: SPIE.

171. Breck, W.G., R.J.C. Brown, and J.D. McCowan, *Chemistry For Science and Engineering*. 2nd ed. 1988, Kingston, Ontario: McGraw-Hill Ryerson Limited.

172. Merzkirch, W., *Flow Visualization*. Second ed. 1987: Academic Press, INC.

173. Montgomery-jr, G.P. and D.L. Reuss, *Effects of refraction on axisymmetric flame temperatures measured by holographic interferometry.* Applied Optics, 1982. 21(8): p. 8.

174. Wilke, C.R., Journal of Chemical Physics, 1950. 18: p. 517.

175. Bird, R.B., W.E. Stewart, and E.N. Lightfoot, *Transport Phenomena*. 1960, New York: John Wiley and Sons.

176. Zhilkin, B.P., Larionov, I.D. and Shuba, A.N., *Applications of an infrared imager for determining temperature fields in gas flows.* Instruments and Experimental Techniques, 2004. 47(4): p. 136-147.

Appendix A

Laser Beam Calculations

This appendix describes in greater detail the laser calculations referred to throughout the thesis.

A.1 Detailed calculation of scaling factor for measurements of centroid motion

The experiment consisted of a laser, the beam of which was directed on to a reflecting mirror and then through the plume of a jet engine and onto a screen. This is shown in Diagram 1 below.

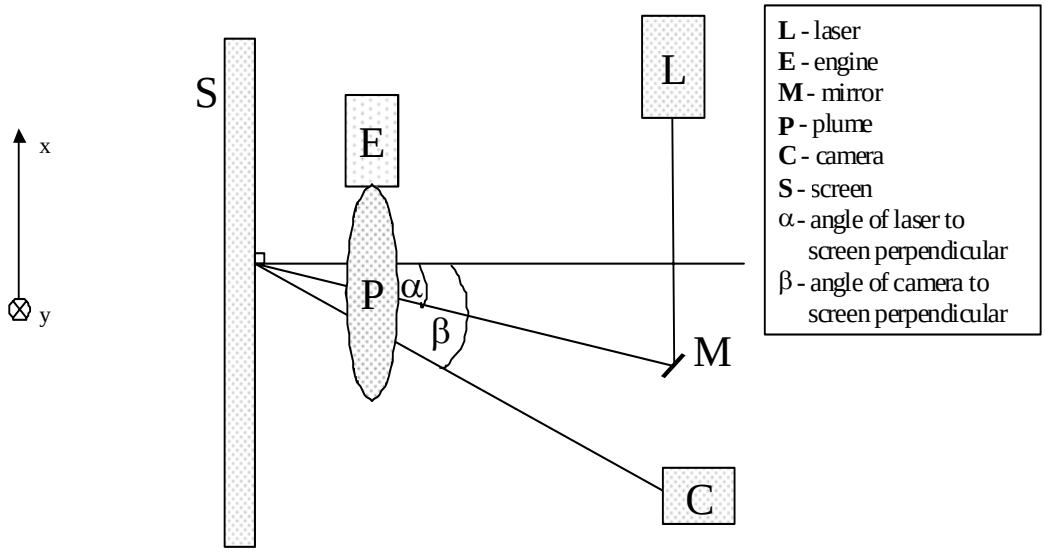

Diagram 1: View from above of experimental set-up, detailing relative positions of laser, camera, plume and screen.

The angle α is defined as the angle the laser beam makes with the normal to the screen, as viewed from above. Similarly, β is the angle that the camera makes with the normal to the screen as viewed from above. Diagram 2 shows the same experimental set-up viewed from a side position.

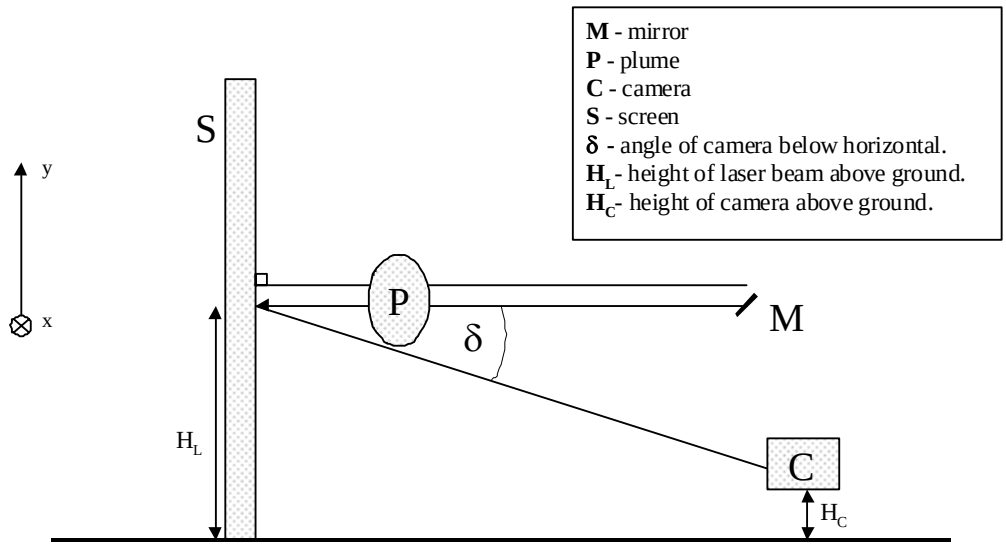

Diagram 2: Side on view of experimental set-up showing camera position relative to laser beam and plume.

The camera was positioned such that it had a clear view of the region where the laser beam illuminated the screen. This was done by positioning the camera below the laser plume and tilting it upwards to view the desired region. The plume of the jet engine was not in the field of view of the camera.

The angle δ is defined as the angle the camera makes with the laser beam.

The angle δ can be calculated using trigonometry;

$$\sin(\delta) = (H_L - H_C) / Dc\text{-}s \qquad (1)$$

where HL =1.22 m, HC = 0.98 m and Dc-s is the distance from the camera to the screen.

The smallest value for Dc-s used in the experiment was 5.91 m. This corresponds to the largest value of δ which was calculated using the above formula to be approximately 2.33 degrees. As the distance between the camera and the screen was increased, δ decreased.

For a distance D_A on the screen, the camera will record a distance D_O at an angle δ given by;

$D_O = D_A \cos(\delta)$

$D_A = D_O / \cos(\delta)$ and for $\delta = 2.33$ degrees

$D_A = 1.00083\, D_O$

As the effect of the angle δ on our calculations is negligible, it has been ignored and the distance of the camera to the screen is taken to be perpendicular to the screen.

Diagram 3 shows a basic camera geometry consisting of a lens of focal length *f*, detector of width *D* and a detector element of length *d*.

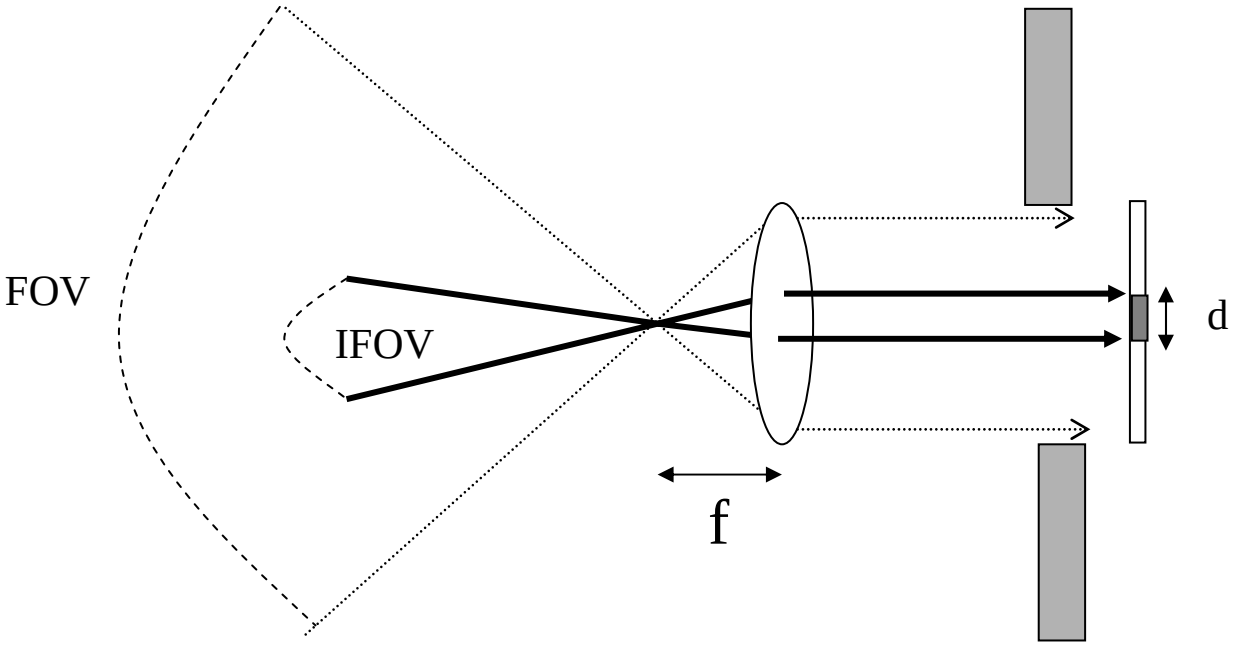

Diagram 3: Geometry of a basic detector.

For example, the dimensions for the Jade camera used in the UK plume trial are given as;

Each pixel is square with a side length, d = 30E-06 m.
Resolution: 320 x 240 pixels (x and y directions respectively)
Focal length, f = 5E-02 m.

The instantaneous field of view (IFOV) is given by;

$$IFOV = 2\tan^{-1}(d/2f) \quad (2)$$

= 6E-04 radians
= 600 micro radians

Now the angular movement of the laser beam in the y direction as observed from the camera can be given by;

Angular Movement Y(at camera)
= Centroid Y (Std Dev) x IFOV (radians) (3)

(this is the standard deviation of the laser centroid in the y-direction in pixels multiplied by field of view per pixel in radians)

However we wish to calculate the angular movement not from the camera but rather from the plume as this is where the deviation in the laser beam occurs (due to turbulence). To find this we must consider Diagram 4 below.

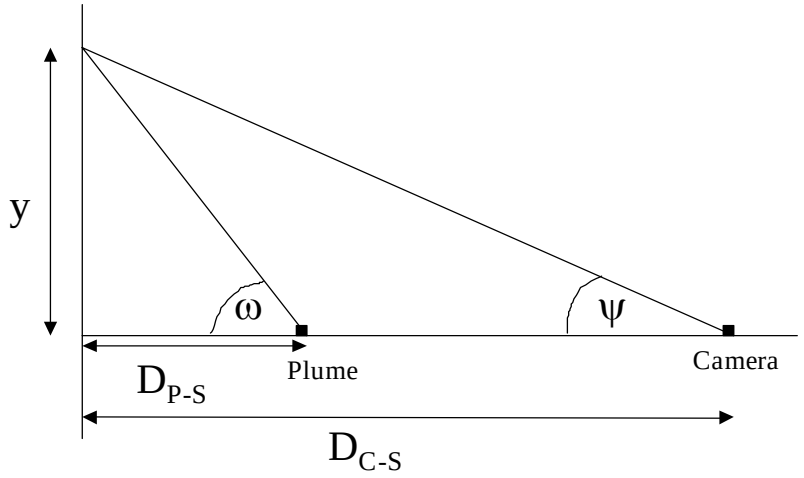

Diagram 4: Geometry of angles and distance for both camera and engine plume.

The above diagram shows that for a given height *y*, the angular movement from the camera is ψ and from the plume is ω. Diagram 4 gives;

$\text{Tan}(\omega) = y/D_{P\text{-}S}$

$\text{Tan}(\psi) = y/D_{C\text{-}S}$

For small angles $\tan(\alpha)$ is approximately equal to α so rearranging we get;

$\omega D_{P\text{-}S} = \psi D_{C\text{-}S}$ or

$$\omega = (D_{C\text{-}S} / D_{P\text{-}S})\ \psi \qquad (4)$$

This tells us that the angular movement at the plume is equal to the angular movement at the camera multiplied by the distance from the camera to the screen ($D_{C\text{-}S}$), divided by the distance from the plume to the screen ($D_{P\text{-}S}$).

Combining this with Equation (1) we now have;

Angular Movement Y(at plume) = (5)
Centroid Y (Std Dev) x IFOV x ($D_{C\text{-}S}$ / $D_{P\text{-}S}$) (radians)

The angular movement of the laser beam at the plume (in the *x*-direction) would also be given by Equation (5 for when both the laser beam and camera are perpendicular to the screen. However for the more general case when the camera makes an angle β to the normal of the screen, and the laser beam itself makes an angle α to the normal of the screen, we must consider Diagram 5 below.

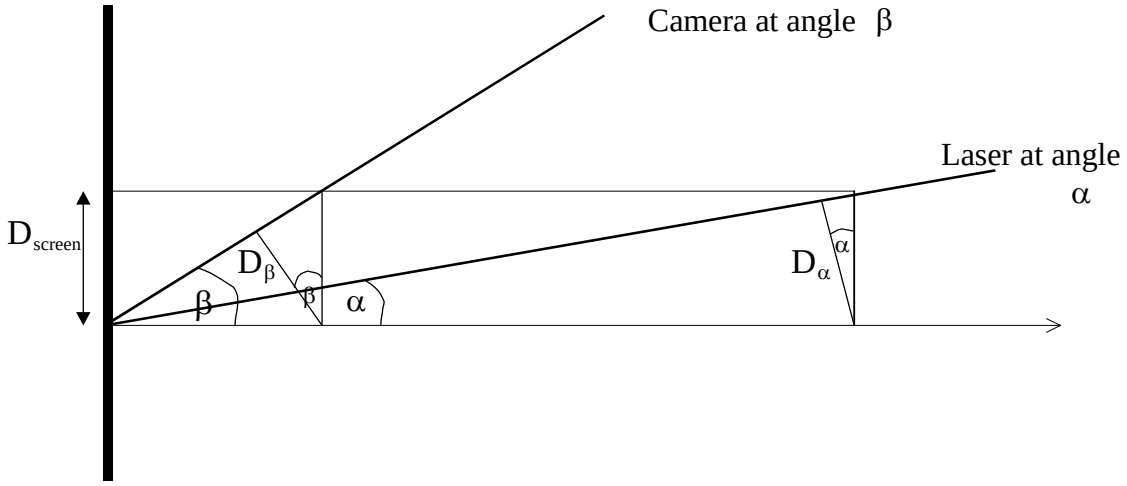

Diagram 5: Geometry of respective angles and distances as view from above.

A laser beam strikes a screen at an angle α. The spatial component of the beam, perpendicular to its direction of travel, given as D_α in Diagram 5, creates an image of length $D_{screen,}$ at the screen. Using geometry we can relate these two distances as follows;

$$D_{screen} = D_\alpha / \cos(\alpha)$$

A camera at angle β to the same screen will record the distance D_{screen} as D_β. We can relate these two distances by the following equation;

$D_{screen} = D_{\beta} / \cos(\beta)$

Now equating these two formulas gives;

$$\boldsymbol{D_{\beta} = [\cos(\beta)/\cos(\alpha)]\, D_{\alpha}} \qquad (6)$$

This shows that the camera records an image the length of which is a factor $[\cos(\beta)/\cos(\alpha)]$ times that of the original.

Using both Equations (5) and (6) we can now define the angular movement in the *x*-direction as;

Angular Movement X(at plume)

$$= \text{Centroid X (Std Dev)} \times \text{IFOV} \times \boldsymbol{(D_{C\text{-}S} / D_{P\text{-}S})} \times [\cos(\beta)/\cos(\alpha)] \text{ (radians)} \qquad (7)$$

where $D_{C\text{-}S}$ is the distance from the camera to the screen, $D_{P\text{-}S}$ is the distance from the plume to the screen, α is the angle of the laser beam to the normal of the screen and similarly β is the angle of the camera to the normal of the screen.

To calculate the area of the laser spot at the screen we multiply the area of the laser spot as recorded by the camera (the Effective Area in pixels) by the IFOV in the *x* and *y* directions, and the square of the distance of the camera to the screen. Using Equations (5), (6) and (7) we then have;

$$\text{Area (at screen)} = \text{Effective Area} \times (\text{IFOV} \times D_{C\text{-}S})^2 \times [\cos(\beta)/\cos(\alpha)] \text{ (m}^2\text{)} \qquad (8)$$

The angular area (measured in steradians) of the laser spot from the plume is then given by;

Angular Area (9)

$$= \text{Effective Area} \times (\text{IFOV} \times D_{C\text{-}S}/D_{P\text{-}S})^2 \times [\cos(\beta)/\cos(\alpha)] \text{ (steradians)}$$

Similarly the Angular area standard deviation is then given by;

Ang Area Std Dev (10)

= Eff Area Std Dev x (IFOV x $D_{C\text{-}S}/D_{P\text{-}S}$)^2 **x [**cos($\beta$)/cos($\alpha$)**]** (steradians)

Table A 1 lists the positions of the screen and camera in a reference frame where the axis of the plume is at (0, 0, 0), the plume velocity is along the +ve *x* axis, the +ve *y* axis is vertically upwards and the +ve *z* axis is towards the screen. All the distances in Table A 1 are in metres.

Table A 1: Calculated positions in Cartesian co-ordinates relative to point where laser beam crosses axis of plume.

Position	Angle to	Height	Screen spot			Phoenix camera		
along plume	plume axis	above plume	X	Y	Z	X	Y	Z
0.5	90	0	0.00	-0.53	4.86	0.35	-0.50	2.52
0.5	90	4	0.00	-0.41	4.86	0.35	-0.50	2.52
0.5	90	8	0.00	-0.28	4.86	0.35	-0.50	2.52
0.5	90	12	0.00	-0.16	4.86	0.35	-0.50	2.52
0.5	90	16	0.00	-0.03	4.86	0.35	-0.50	2.52
0.5	90	20	0.00	0.09	4.86	0.35	-0.50	2.52
0.5	90	24	0.00	0.21	4.86	0.35	-0.50	2.52
1.0	90	0	0.00	-0.55	4.90	-0.15	-0.50	2.54
1.0	90	4	0.00	-0.42	4.90	-0.15	-0.50	2.54
1.0	90	8	0.00	-0.30	4.90	-0.15	-0.50	2.54
1.0	90	12	0.00	-0.17	4.90	-0.15	-0.50	2.54
1.0	90	16	0.00	-0.04	4.90	-0.15	-0.50	2.54
1.0	90	20	0.00	0.09	4.90	-0.15	-0.50	2.54
1.0	90	24	0.00	0.21	4.90	-0.15	-0.50	2.54
1.5	90	0	0.00	-0.44	5.13	-1.60	-0.51	2.51
1.5	90	4	0.00	-0.32	5.13	-1.60	-0.51	2.51
1.5	90	8	0.00	-0.19	5.13	-1.60	-0.51	2.51
1.5	90	12	0.00	-0.07	5.13	-1.60	-0.51	2.51
1.5	90	16	0.00	0.06	5.13	-1.60	-0.51	2.51
1.5	90	20	0.00	0.19	5.13	-1.60	-0.51	2.51
1.5	90	24	0.00	0.31	5.13	-1.60	-0.51	2.51
0.5	65	0	-2.28	-0.49	4.89	-1.47	-0.50	2.70
0.5	65	4	-2.28	-0.37	4.89	-1.47	-0.50	2.70
0.5	65	8	-2.28	-0.24	4.89	-1.47	-0.50	2.70
0.5	65	12	-2.28	-0.12	4.89	-1.47	-0.50	2.70
0.5	65	16	-2.28	0.00	4.89	-1.47	-0.50	2.70
0.5	65	20	-2.28	0.13	4.89	-1.47	-0.50	2.70
0.5	65	24	-2.28	0.25	4.89	-1.47	-0.50	2.70

Using the data in Table A 1, the angle at the plume corresponding to 1 pixel at the camera can be calculated as follows:

Scale (mrad) = detector pitch (in mm) * (distance from screen to camera – camera focal length)/(camera focal length * distance from plume axis to screen).

Because camera focal lengths are not usually manufactured with tolerances better than about 1% of the focal length, an error of at least ± 1% in the scale should be assumed. All the distance measurements were made to a precision of 10 mm.

The *X* and *Y* factors multiply the scale in the *x* and *y* directions to take account of the camera not being exactly in line with the laser beam, so observing the spot on the screen from an angle. The scale and *X* and *Y* factors the Phoenix IR FPA camera are listed in Table A 2.

Table A 2: Calculated scale factors (mrad) and multiplication factors for both measurement directions.

Position along plume	Angle to plume axis	Height above plume	Phoenix Scale	Phoenix X factor	Y factor
0.5	90	0	0.285	1.011	1.000
0.5	90	4	0.286	1.011	1.001
0.5	90	8	0.287	1.011	1.004
0.5	90	12	0.289	1.011	1.010
0.5	90	16	0.292	1.011	1.019
0.5	90	20	0.295	1.010	1.031
0.5	90	24	0.299	1.010	1.044
1.0	90	0	0.281	1.002	1.000
1.0	90	4	0.282	1.002	1.001
1.0	90	8	0.283	1.002	1.004
1.0	90	12	0.286	1.002	1.010
1.0	90	16	0.288	1.002	1.019
1.0	90	20	0.292	1.002	1.030
1.0	90	24	0.295	1.002	1.045
1.5	90	0	0.352	1.172	1.000
1.5	90	4	0.353	1.171	1.002
1.5	90	8	0.355	1.169	1.005
1.5	90	12	0.357	1.167	1.010
1.5	90	16	0.359	1.164	1.017
1.5	90	20	0.362	1.161	1.025
1.5	90	24	0.365	1.157	1.035
0.5	65	0	0.254	1.008	1.000
0.5	65	4	0.255	1.008	1.002
0.5	65	8	0.256	1.008	1.006
0.5	65	12	0.258	1.008	1.013
0.5	65	16	0.261	1.008	1.023
0.5	65	20	0.264	1.008	1.035
0.5	65	24	0.268	1.008	1.050

Appendix B

Determining Anomalous Dispersion Effects

Alternative Refractive Index Calculation

B.1 Determining Anomalous Dispersion

The effects of anomalous dispersion can be modelled with an equation given by Hill et. al. [19] is dependant on the gas concentration and the wavelength (through the wavenumber ν).

$$n_{ai} = \frac{S_i Q f x 10^6}{4\pi^2 \upsilon_i} \tag{1}$$

Where *S* is the line intensity, *Q* is the concentration of the gas in units molecule/cm^3, *f* is the line shape factor and ν is the wavenumber of the line in the spectra.

This equation is only valid for one line in the molecules spectra. To find the total influence of the anomalous dispersion, these effects must be summed over all lines in the spectra yielding,

$$n_a = \sum_i n_{ai} \tag{2}$$

The intensity and the wavenumber are obtained using the HITRAN database (2004). To find the line shape several different model can be applied (Gaussian , Lorentzian, etc). The Lorentzian as described in Table 1 of Hill et al. [19] is;

$$f = \frac{\upsilon_i - \upsilon}{(\upsilon_i - \upsilon)^2 + \alpha_i^2} \tag{3}$$

where α is the line width which can be found using HITRAN.

The anomalous dispersion relation is dependant on all important factors except temperature. This dependence can be introduced via a temperature correction of the line width and the line intensity. These corrections are described by Rothman et. al. [153] as;

$$S_i(T) = S_i(T_{ref})\frac{Q(T_{ref})}{Q(T)}\frac{\exp(\frac{-c_2 E_i}{T})\left[1-\exp(\frac{-c_2 \upsilon_i}{T})\right]}{\exp(\frac{-c_2 E_i}{T_{ref}})\left[1-\exp(\frac{-c_2 \upsilon_i}{T_{ref}})\right]} \quad (4)$$

where Q is the total internal partial sum of the molecule, E is the lower energy state of the transition and c_2 is the second radiation constant = hc/k. And,

$$\gamma(p,T) = (\frac{T_{ref}}{T})^n(\gamma_{air}(p_{ref},T_{ref})(p-p_s) + \gamma_{self}(p_{ref},T_{ref})p_s) \quad (5)$$

where, γ is the half width with γ_{air} and γ_{self} available for look up in the HITRAN database along with n, the coefficient of temperature dependence of the air-broadened half width. P is the pressure and p_s is the partial pressure which is found using the relation, $p_s = (mf)p$, where mf is the mole fraction of the molecule in the mixture of gases [171].

Combining all of these equations gives the final relation for the anomalous dispersion through a gas.

B.2 Alternative Refractive Index Calculation

Using a Gladstone-Dale equation the refractive index can be found in terms of the density [172];

$$n-1=K\rho \tag{1}$$

where *n* is the refractive index, *K* is the Gladstone-Dale constant, *ρ* is the density.

The Gladstone-Dale constant has the form;

$$K=\frac{Le^2}{2\pi m_e M}\sum\frac{f_i}{\nu_i^2-\nu^2} \tag{2}$$

where *e* is the charge, *L* is the Loschmidt Number, m_e is the mass of an electron, *M* is the molar mass of the gas, *f* is the oscillator strength, ν_i is a resonant frequency and ν is the frequency of interest.

Therefore from equations (1) and (2) the following relation can be found.

$$n-1=\frac{\rho Le^2}{2\pi m_e M}\sum\frac{f_i}{\nu_i^2-\nu^2} \tag{3}$$

The temperature of the gas mixture can be incorporated into the refractive index model by using the ideal gas law [173];

$$\rho(\vec{r})=p\left[RT(\vec{r})\sum_j(m_f)_j(\vec{r})M_j^{-1}\right]^{-1} \tag{4}$$

$$n(\vec{r})-1=\rho(\vec{r})\sum_j k_j(m_f)_j(\vec{r}) \tag{5}$$

$$n(\vec{r})-1=p\left[RT(\vec{r})\sum_i(m_f)_i(\vec{r})M_i^{-1}\right]^{-1}\sum_j k_j f_j(\vec{r}) \tag{6}$$

$$n(\vec{r})-1=p\left[RT(\vec{r})\sum_i(m_f)_i(\vec{r})M_i^{-1}\right]^{-1}\sum_j\left[\frac{Le^2(m_f)_j(\vec{r})}{2\pi m_e M_j}\sum_k\frac{f_k}{\nu_k^2-\nu^2}\right] \tag{7}$$

To find the oscillator strength a relation given by Simeckova et. al. [49] can be used;

$$f=\frac{g_2}{g_1}\frac{\varepsilon_0 mc}{2\pi e^2\upsilon_0^2}A \tag{8}$$

where g_2, g_1 are statistical weights corresponding to the upper and lower states for a transition of a molecule. ε_0 is the permittivity of a vacuum = 8.854187817x10^{-12} (Fm^{-1}), m is the mass of an electron , c is the speed of light through a vacuum = 2.997x10^8 ms^{-1}, e is the charge of an electron and ν_0 is the wavenumber of the spectral line and A is the Einstein-A coefficient.

To obtain the temperature dependence for the refractive index the Einstein coefficient can be written in terms of the line intensity [49], which as seen previously can be associated with a temperature correction factor;

$$A=\frac{8\pi c\upsilon_0^2 Q_{tot}(T)S(T)}{\exp(\frac{-c_2E}{T})(1-\exp(\frac{-c_2\upsilon_0}{T}))I_a g_2} \tag{9}$$

where I_a is the isotropic abundance, which can be found through HITRAN also.

Appendix C

Reynolds Number Calculation

Reynolds Number, which relates the inertial and viscous forces within a flow, can be used to determine whether a flow is turbulent or not. Reynolds number is defined as;

$$\mathrm{Re} = \frac{V.l.\rho}{\mu} = \frac{V.l}{\nu} \tag{1}$$

where V is the velocity, l is the characteristic length, ρ is the fluid density, μ is the dynamic viscosity, ν is the kinematic viscosity ($\nu = \mu/\rho$).

Viscosity, based on the Wilke [174] formula, modified by Bird et al. [175] can be calculated for a mixture by;

$$\mu = \sum_{k=1}^{K} \frac{X_k \mu_k}{\sum_{j=1}^{K} X_j \phi_{kj}} \tag{2}$$

where μ =dynamic viscosity (g / cm sec), X = mole fraction of the species and

$$\phi_{kj} = \frac{1}{\sqrt{8}} \left(1 + \frac{W_k}{W_j}\right)^{\frac{-1}{2}} \left(1 + \left(\frac{\mu_k}{\mu_j}\right)^{\frac{1}{2}} \left(\frac{W_j}{W_k}\right)^{\frac{1}{4}}\right)^2 \tag{3}$$

where W = molecular weight (grams / mole).

Appendix D

Statistical Considerations

How many laser spot samples are required?

Empirical studies show a minimum of 30 samples is needed to produce a Normal statistical distribution [140].

Confidence interval for mean

For a Normal (Gaussian) distribution (Central Limit Theorem) with 95% confidence level;

$$E = \sqrt{\frac{(1.96)^2 \sigma^2}{n}}$$

where *n* is the number of samples, σ^2 is the variance and *E* is the error margin about the mean, μ. The level of confidence that the samples from this sample space with a mean of $\mu \pm E$ is 95%. I.e.: $P(\mu - E < \mu < \mu + E) = 0.95$

For example, if we consider a 1000 samples, which produced a (sample) variance of 10 pixels.

I.e.: $1000 = \frac{(1.96)^2 10}{E^2}$

and therefore E = 0.196 pixels.

The sample mean can be reported, once calculated, to be at a position of $\mu \pm 0.196$ pixels with a 95% confidence.

In general the mean is plus or minus 0.5 pixel for a standard deviation of 5 pixels for the IR runs with 400 samples and plus or minus 0.15 pixel for a standard deviation of 5 pixels for the IR runs with 4000 samples.

Confidence interval for variance

To calculate the upper and lower bounds, L_1 and L_2 respectively, for a 100(1-α) % confidence interval on the variance, σ^2 for a random sample of size n we use:

$$L_1 = (n-1)S^2 \Big/ \chi^2_{\alpha/2} \qquad \text{and} \qquad L_2 = (n-1)S^2 \Big/ \chi^2_{1-\alpha/2}$$

For a 95% confidence interval the chi-squared values for the various sample sizes used in the parametric experiments are:

For 800 samples; using CHIINV function in EXCEL, $\chi^2_{.025}$ = 879 and $\chi^2_{.975}$ = 722.

For 1200 samples, $\chi^2_{.025}$ = ~1280 and $\chi^2_{.975}$ = 1005.

Example: Consider two runs; one with a standard deviation of 42 and the other 40. These equate to a variance of 1764 and 1600 respectively.

If 800 samples were used, then the confidence limits on the variance for the first run are:

L_1 = 799 * 1764 / 879 and L_2 = 799 * 1764 / 722

That is, L_1 = 1603 and L_2 = 1952

Square-rooting these limits, the confidence limits on the standard deviation are obtained.

L_1 = 40 and L_2 = 44.18

For the second run:

L_1 = 799 * 1600 / 879 and L_2 = 799 * 1600 / 722

That is, L_1 = 1454 and L_2 = 1770

Square-rooting these limits, the confidence limits on the standard deviation are obtained.

L_1 = 38.1 and L_2 = 42.07

The runs results appear too close to separate based on variance.

Computation for a standard deviation of 100, using 800 samples, produces limits of 100 ± 5 on the standard deviation. Increasing the number of samples to 1200 produces a lower limit of 96.8 and an upper limit of 109.3. Yet, 400 samples produce a lower limit of 93.5 and an upper limit of 107.45. It appears the calculation is failing at the upper limit for sample values greater than around 1000. Overall, it appears that a statistical error margin of around ± 5 % appears to apply for the data collected.

Are two runs significantly different to show a parameter change has affected the movement?

In a set of runs the number-of-samples were kept constant. Sample sizes used to calculate the variance estimates were either 800, 1200 or 4000.

Comparisons of variance will be done between equal size samples such that F-obtained is calculated by dividing the larger variance by the smaller variance.

The F TEST can be used to determine if the variances differ sufficiently to allow the effect of a parameter change to be declared significant.

F-obtained is compared to F-critical, found from the F distribution. If F-obtained is less than F-critical the variances are considered to be the same for a given confidence level.

Ross [140] states that the F TEST is not particularly powerful, with the null hypothesis; equal variances, being rejected often when in fact the variances are different. Employing the F distribution with an alpha of 0.2 is considered satisfactory. Thus, for an alpha of 0.2, F-critical is determined for the various sample sizes.

For 800 samples F-critical is 1.0949

For 1200 samples F-critical is 1.0768

For 4000 samples F-critical is 1.0413

Thus, for the 800 sample results we can say a parameter change has resulted in a significant variance change when there has been a change in variance of 9.5%. Similarly; for 1200 samples, a variance change of 7.7% and for 4000 samples 4.1%.

Appendix E

Characterizing the Flow

Imaging using a FPA camera

Imaging the flow in the IR (3-5 micron region) gave a sense of the structure of the flow. A K-type thermocouple probe was introduced into the flow and the recorded temperature matched to the counts seen by the camera to enable the counts to be translated to a temperature. However, because the camera was recording a 2D average of a 3D space the results were not helpful in precisely determining the refractive index gradients. Others have used this technique [176] but invasive thermally reactive materials were needed.

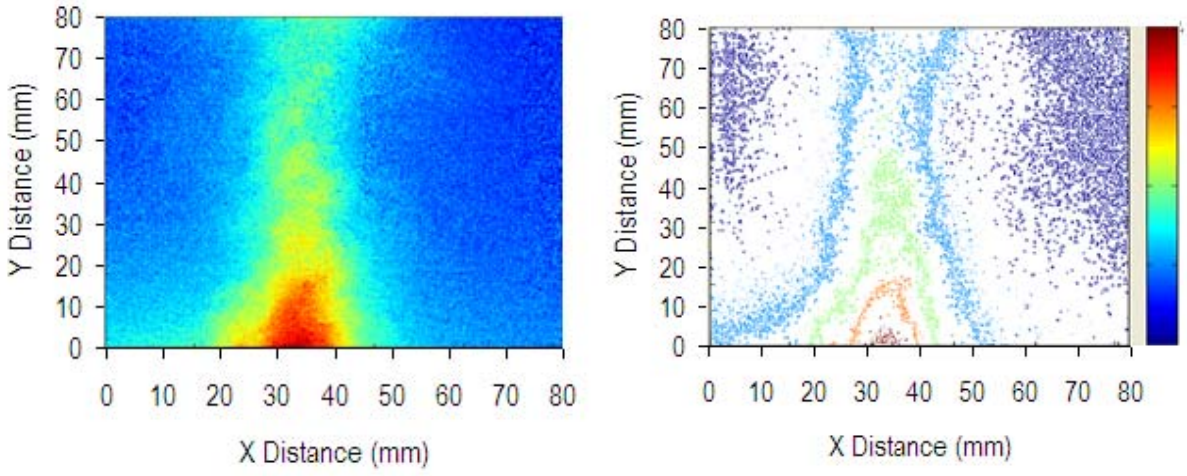

Figure E - 1: Image taken of electrically heated flow with an infrared camera using a 100 µs integration time. Image processing has removed the background. Red indicates high temperature and the right hand side plot shows temperature contour lines.

Appendix F

HITRAN: CO_2 and H_2O Spectral Line Intensities

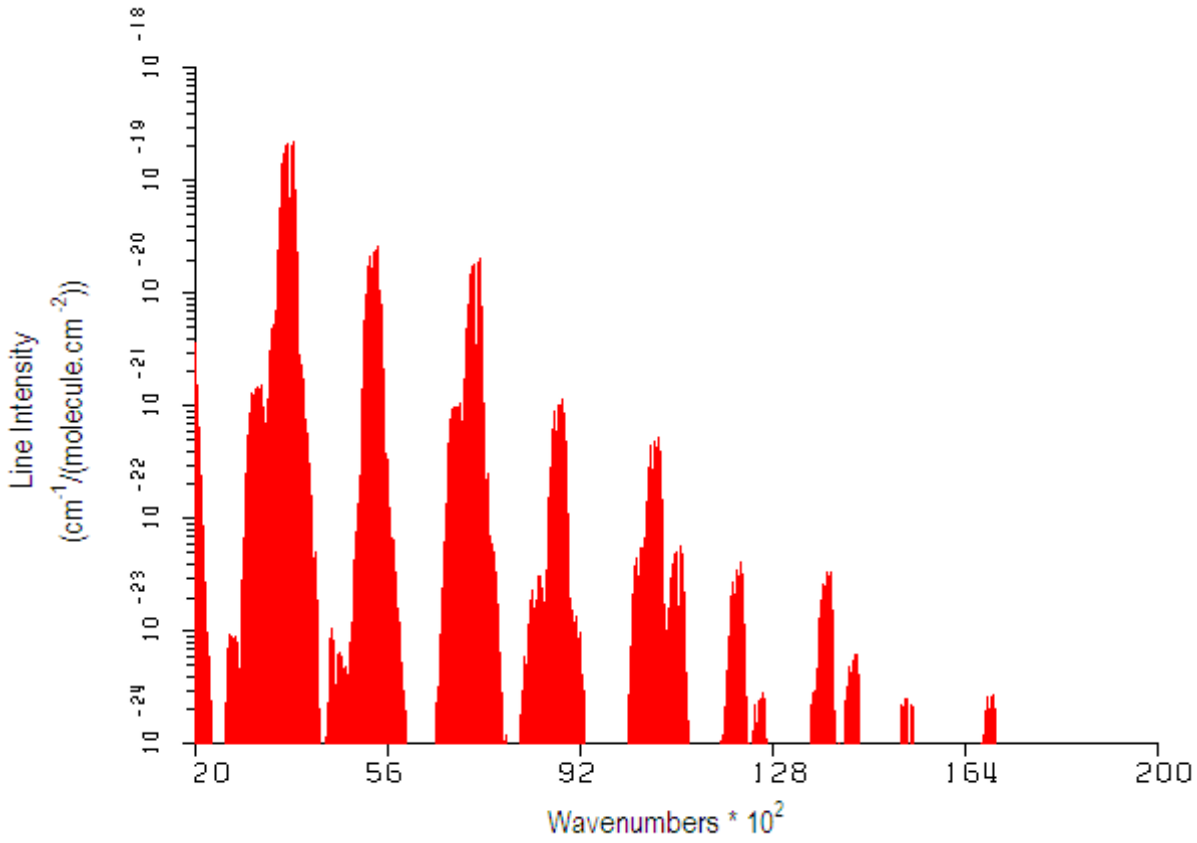

Figure F - 1: Spectral line intensity of Carbon Dioxide. IR laser radiation is at wavenumber $21.41*10^2$ cm^{-1} and visible laser radiation is at wavenumber $158.00 *10^2$ cm^{-1}.

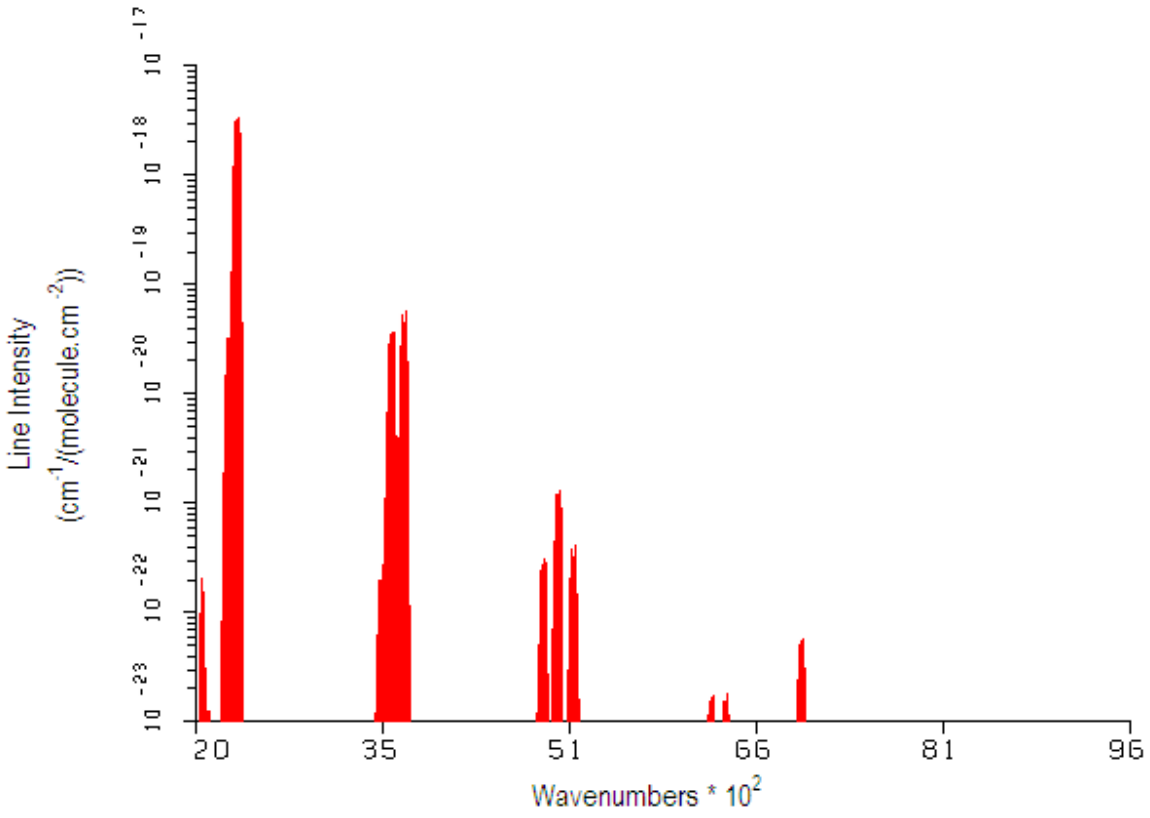

Figure F - 2: Spectral line intensity of Water. IR laser radiation is at wavenumber $21.41*10^2$ cm^{-1} and visible laser radiation is at wavenumber $158.00*10^2$ cm^{-1}.

Appendix G

Examples of Spot Images

632.8 nm Radiation Laser Beam

The following figures document example images of the the 632.8 nm radiation laser beam. Three consecutive images are shown in each figure. The temperature of the turbulent flow is increased with each subsequent figure. The effect of the increased temperature of the turbulent flow on the propagating beam can be visually seen in the images.

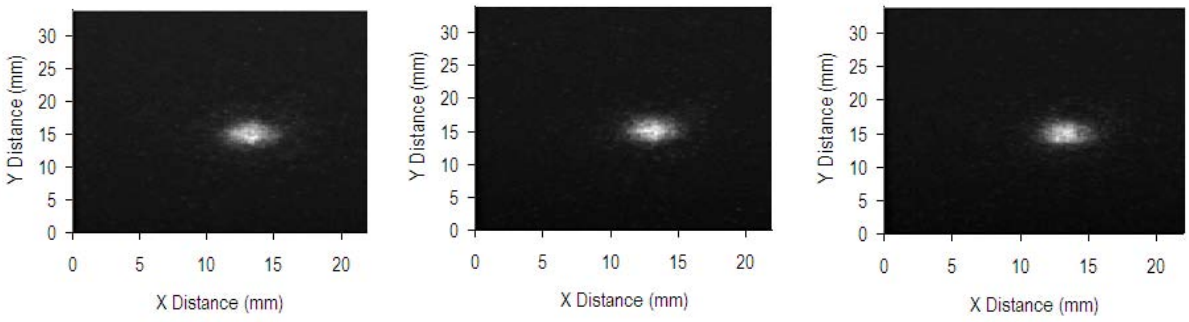

Figure G - 1: Three consecutive images of the 632.8 nm beam recorded after propagating through ambient temperature turbulent flow (Re=10,000).

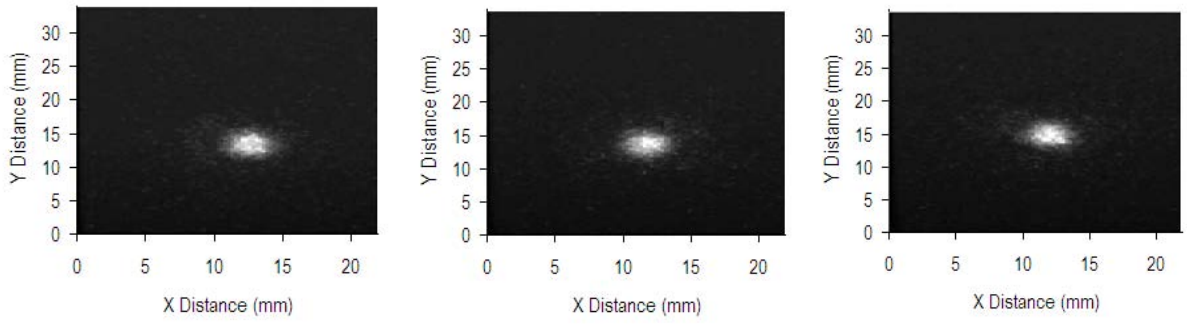

Figure G - 2: Three consecutive images of the 632.8 nm beam recorded after propagating through turbulent flow (Re=10,000) with peak temperature 110°C.

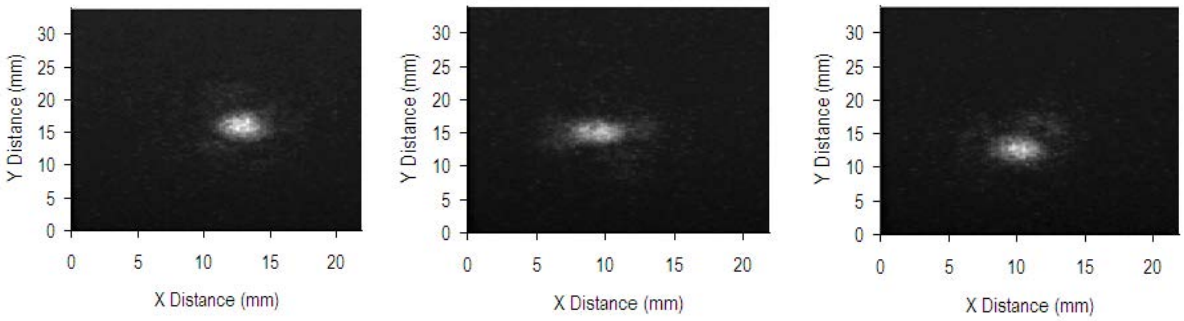

Figure G - 3: Three consecutive images of the 632.8 nm beam recorded after propagating through turbulent flow (Re=10,000) with peak temperature 210°C.

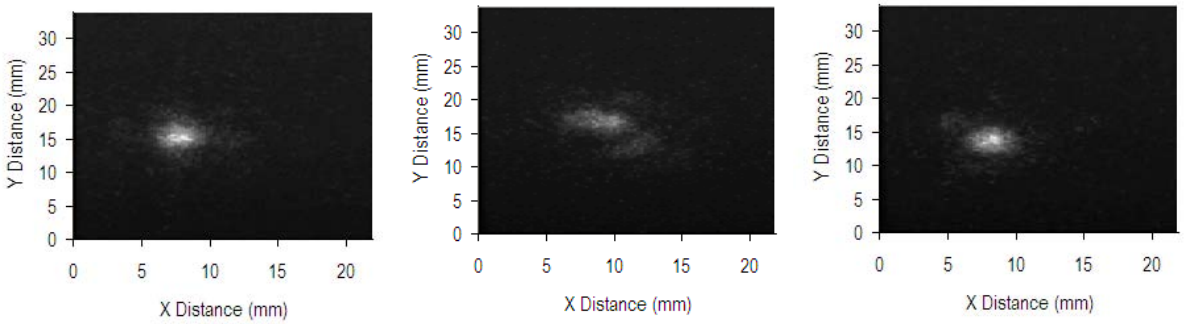

Figure G - 4: Three consecutive images of the 632.8 nm beam recorded after propagating through turbulent flow (Re=10,000) with peak temperature 300°C.

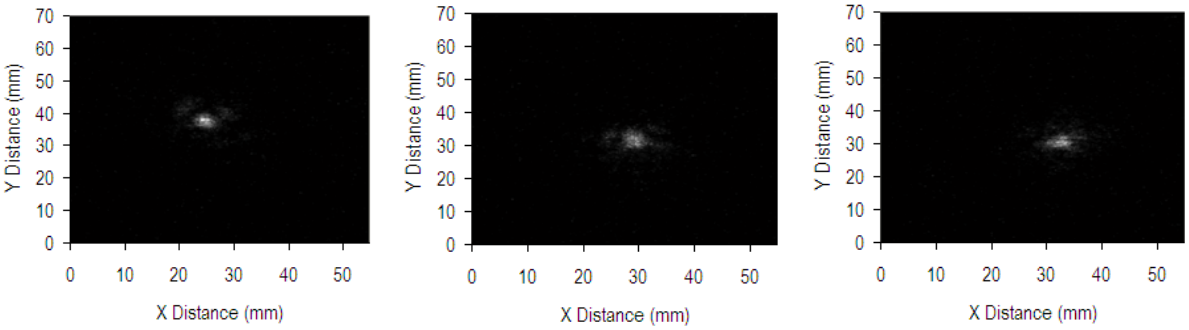

Figure G - 5: Three consecutive images of the 632.8 nm beam recorded after propagating through turbulent flow (Re=10,000) with peak temperature 430°C.

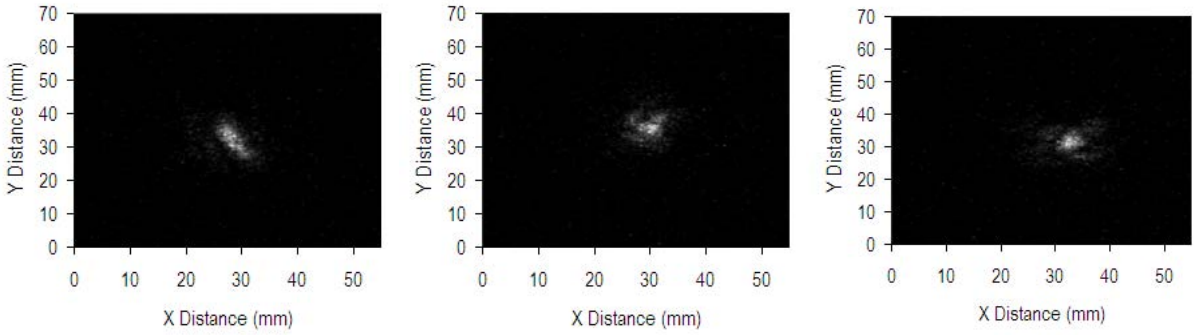

Figure G - 6: Three consecutive images of the 632.8 nm beam recorded after propagating through turbulent flow (Re=10,000) with peak temperature 500°C.

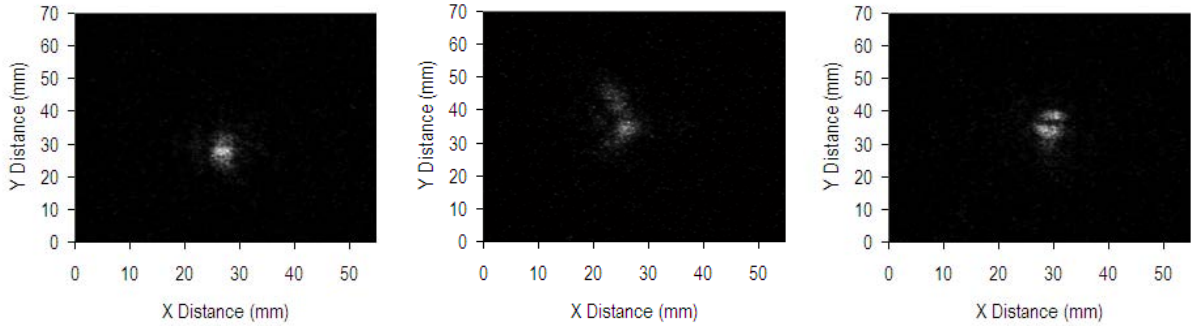

Figure G - 7: Three consecutive images of the 632.8 nm beam recorded after propagating through turbulent flow (Re=10,000) with peak temperature 600°C.

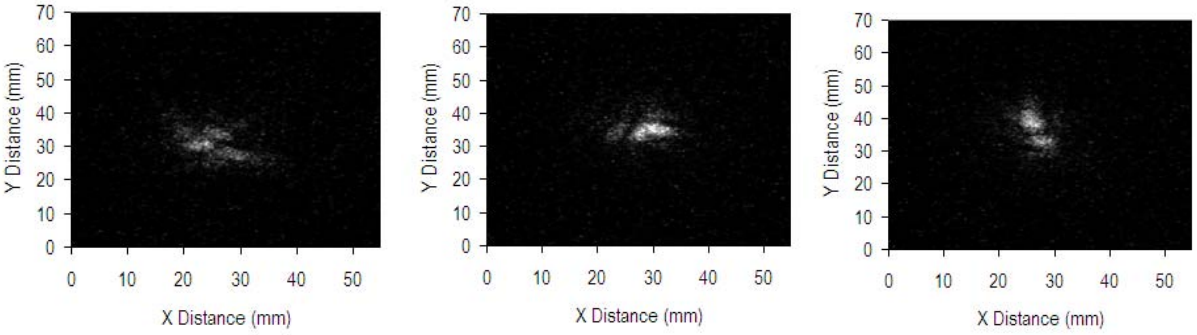

Figure G - 8: Three consecutive images of the 632.8 nm beam recorded after propagating through turbulent flow (Re=10,000) with peak temperature 700°C.

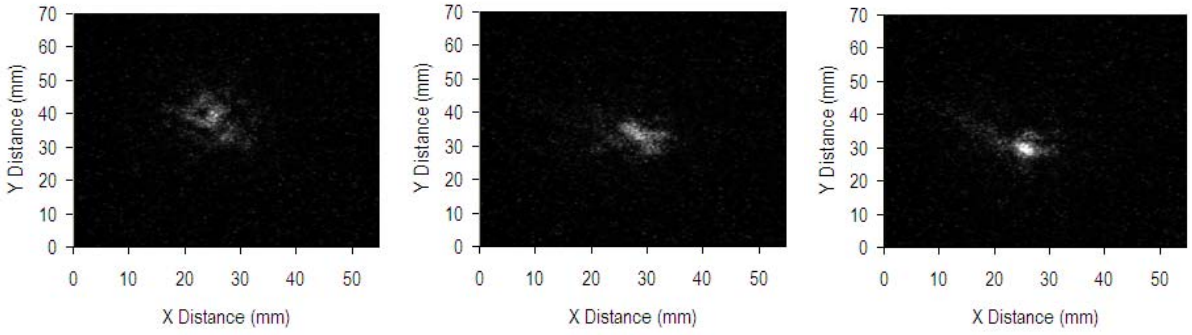

Figure G - 9: Three consecutive images of the 632.8 nm beam recorded after propagating through turbulent flow (Re=10,000) with peak temperature 800°C.

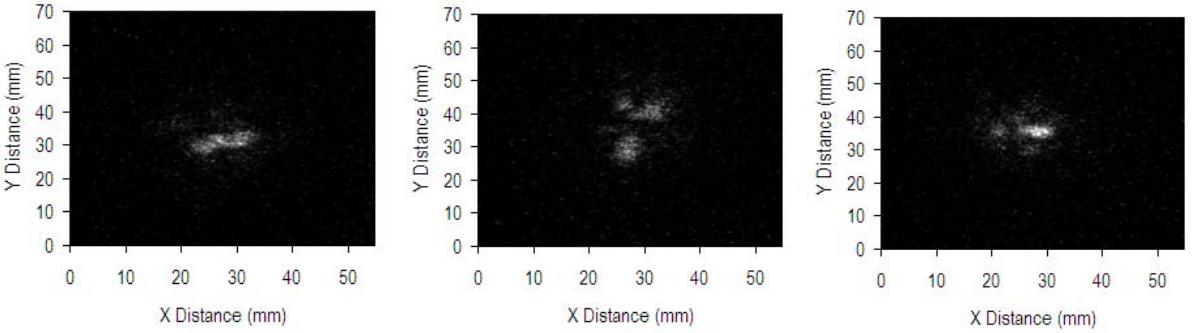

Figure G - 10: Three consecutive images of the 632.8 nm beam recorded after propagating through turbulent flow (Re=10,000) with peak temperature 1000°C.

4.67 µm Radiation Laser Beam

The following figures document example images of the 4.67 µm radiation laser beam. Three consecutive images are shown in each figure. The temperature of the turbulent flow is increased with each subsequent figure. The effect of the temperature of the turbulent flow on the propagating beam can be visually seen in the images. However, the effect on the beam due to increasing temperature is not as visually apparent as seen with the 632.8 nm radiation beam.

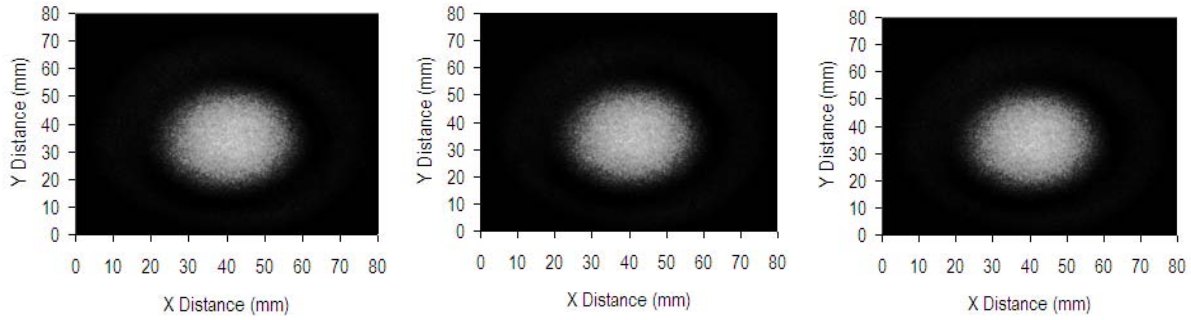

Figure G - 11: Three consecutive images of the 4.67 µm beam recorded after propagating through ambient temperature turbulent flow (Re=10,000).

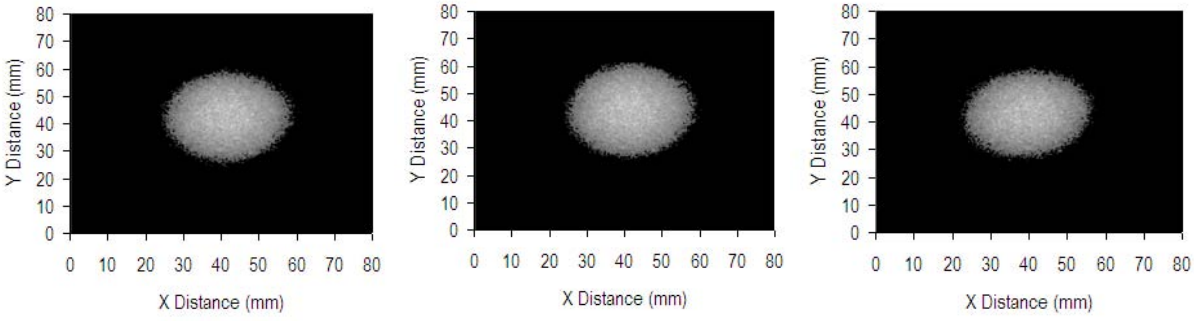

Figure G - 12: Three consecutive images of the 4.67 µm beam recorded after propagating through turbulent flow (Re=10,000) with peak temperature 130°C.

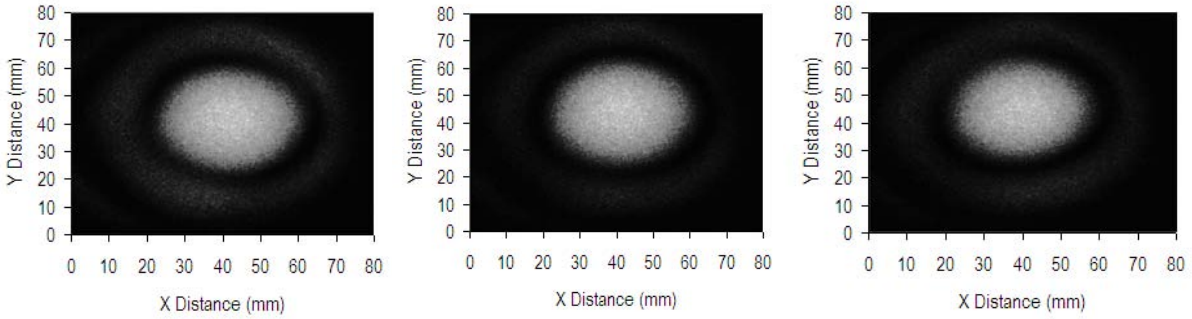

Figure G - 13: Three consecutive images of the 4.67 µm beam recorded after propagating through turbulent flow (Re=10,000) with peak temperature 215°C.

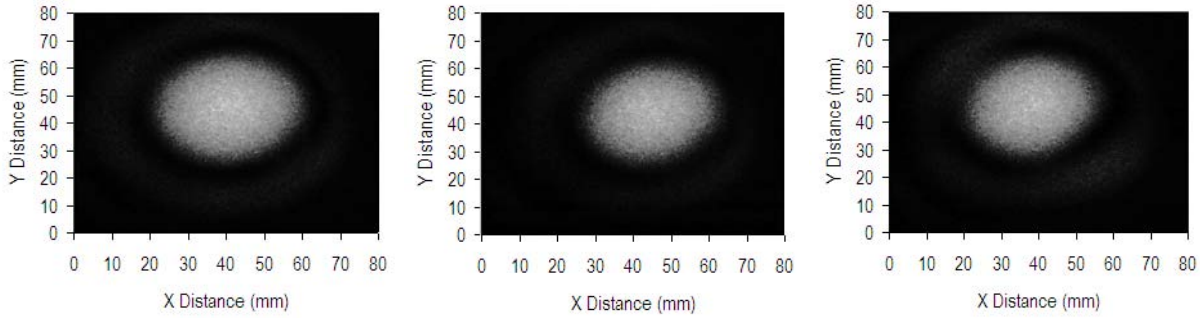

Figure G - 14: Three consecutive images of the 4.67 µm beam recorded after propagating through turbulent flow (Re=10,000) with peak temperature 310°C.

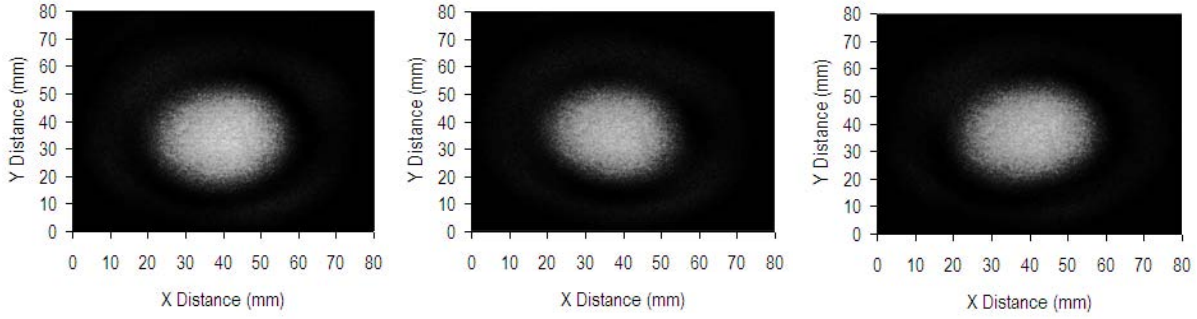

Figure G - 15: Three consecutive images of the 4.67 µm beam recorded after propagating through turbulent flow (Re=10,000) with peak temperature 430°C.

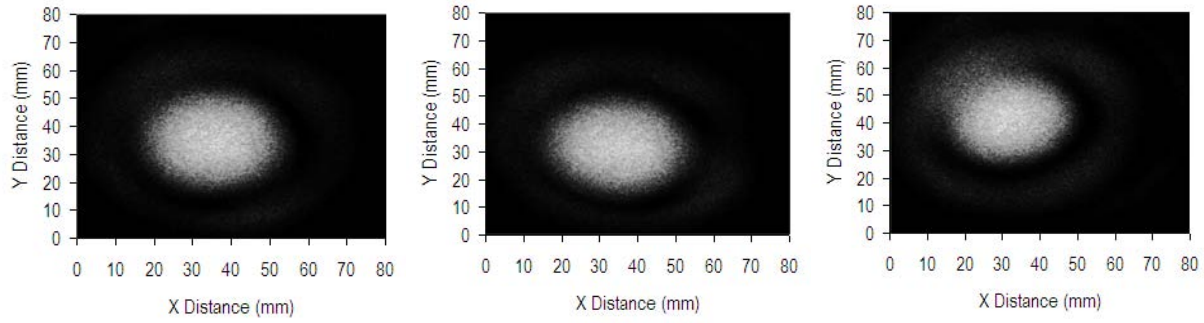

Figure G - 16: Three consecutive images of the 4.67 µm beam recorded after propagating through turbulent flow (Re=10,000) with peak temperature 520°C.

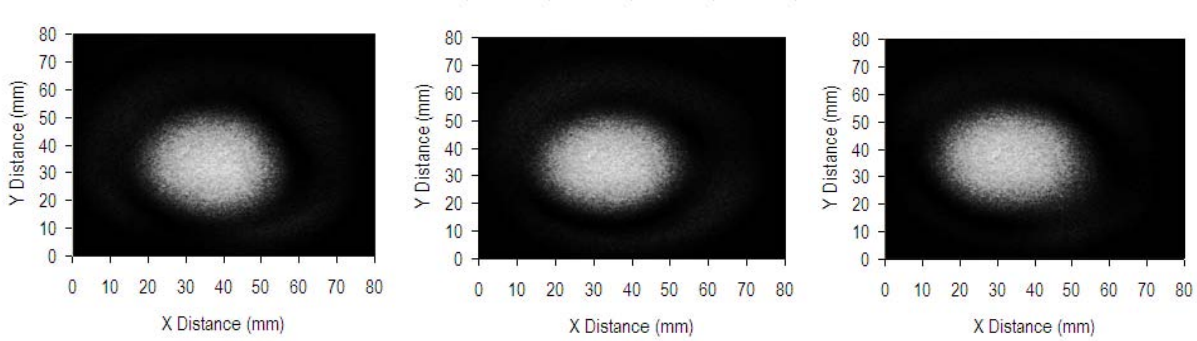

Figure G - 17: Three consecutive images of the 4.67 µm beam recorded after propagating through turbulent flow (Re=10,000) with peak temperature 600°C.

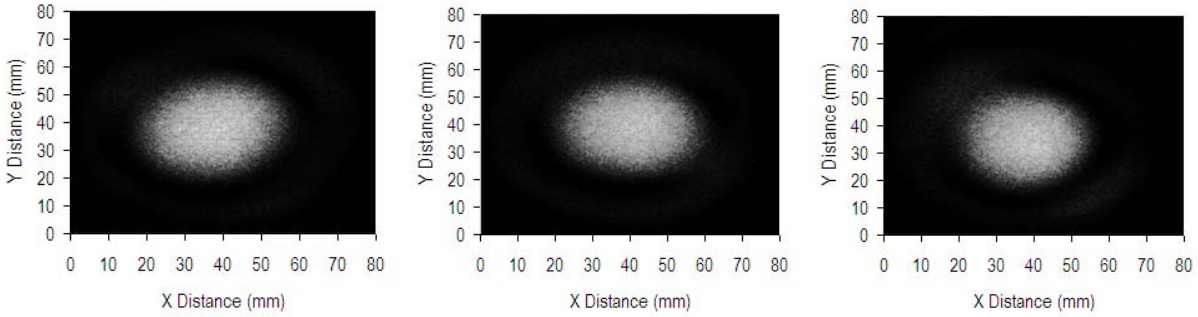

Figure G - 18: Three consecutive images of the 4.67 µm beam recorded after propagating through turbulent flow (Re=10,000) with peak temperature 710°C.

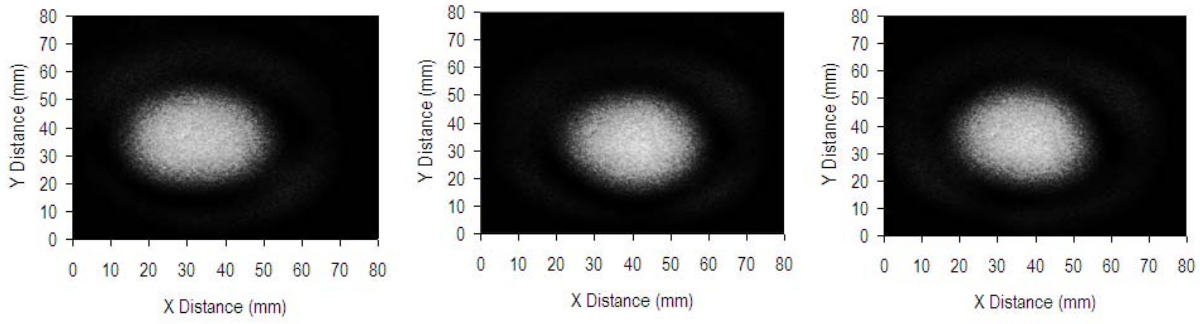

Figure G - 19: Three consecutive images of the 4.67 µm beam recorded after propagating through turbulent flow (Re=10,000) with peak temperature 810°C.

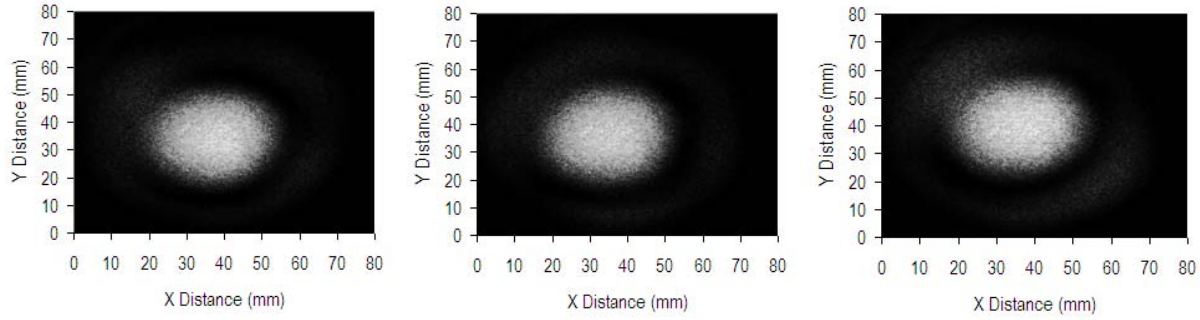

Figure G - 20: Three consecutive images of the 4.67 µm beam recorded after propagating through turbulent flow (Re=10,000) with peak temperature 1030°C.

Appendix H

Publications

Publications arising from this thesis

Isterling, W.M., Dally, B.D., Alwahabi, Z., Dubovinsky, M. and Wright, D. "Laser beam propagation through combustion of Hydrogen and Air", Fifth Australian Conference on Laser Diagnostics in Fluid Mechanics and Combustion, Perth, Dec. (2008).

Isterling, W.M., Dally, B.D., Alwahabi, Z., Dubovinsky, M. and Wright, D. “Propagation of 632.8 nm and 4.67 μm laser beams in a turbulent flow containing CO2 and H2O at high temperature”, SPIE, Europe Security and Defence 2008, Cardiff, 14-18, Sept. (2008).

Isterling, W.M., Dally, B.D., Alwahabi, Z., Dubovinsky, M. and Wright, D. “On the interaction of turbulence intensity and its scales with various diameter laser beams at high temperatures”, SPIE, Europe Security and Defence 2008, Cardiff, 14-18, Sept. (2008).

Isterling, W.M., Cox, L.J., Dubovinsky, M., Titterton, D.H. and Porter, T. (2006), Laser Beam Propagation through a Jet Engine Exhaust, AOC International Symposium and Exhibition 2006, Adelaide 13-14 February.

Isterling, W.M., Cox, L.J., Dubovinsky, M., Titterton, D.H. and Porter, T. (2005), Laser Interaction with Jet Engine Exhaust Induced Turbulence, Fourth Australian Conference on Laser Diagnostics in Fluid Mechanics and Combustion, pp 65-68.